Accretion Variability in Young Stellar Objects

A dissertation submitted to Queen's University Belfast
for the degree of Doctor of Philosophy

Gráinne Costigan
B.A.(mod) TCD
MSc. Cambridge University
September 2013

School of Mathematics and Physics
Queen's University Belfast

Dublin Institute of Advanced Studies
Armagh Observatory
European Southern Observartory

To Mum, Dad, Meadhbh and Jack, for giving me every opportunity, supporting me in every decision and keeping me on my toes. To Anna, for her big heart. To Mathias, for acting the maggot. To Carlo, for the lessons in Italian. To Rachael for bringing southern sunshine to Dublin. To the Mexicans and Pedro, the best gold fish that was. To all the coffees with my cohorts at ESO. To all the cups of tea with the family at DIAS. To all who have kept me going with chats and pints along the way. To Aleks for his support. To everyone who proof read, Peter, Tim, Meadhbhie, Mathias, Adrià, Carlo and Roberto. And finally to Adrià for being himself and for knowing when I am not.

Grazie mille. Merci beaucoup. Muchas Gracias. Danke Schön. Moltes Gràcies. Go raibh míle maith agaibh. Thank you.

Acknowledgments

I would like to acknowledge the fantastic help, guidance, motivation and support that was given to me by my four supervisors, Aleks Scholz, Jorick Vink, Leonardo Testi and Tom Ray, over the course of my PhD. Special thanks to Aleks for his patience, support, straight talk and accessibility. Thanks to Jorick for taking me on and dealing with the long distance for the whole PhD. Thanks to Leonardo for the wonderful ESO experience and support. Thanks for Tom for always having time for a question or a chat. I could not have asked for a better team by my side.

I would like to acknowledge the support, suggestions and comments that have come from a great many people along the way in particular those who have been part of this work, Antonella Natta, Beate Stelzer, Giacommo Beccari and Subu Mohanty.

A special thank you to Carlo Manara for the daily talks and bouncing around of ideas that have kept my enthusiasm going right to the end of the thesis.

I have been lucky enough to be part of three great research institutes over the course of the Phd, DIAS, Armagh Observatory and ESO. I would like to acknowledge the funding that was provided by the Lindsay scholarship from DIAS and Armagh observatory which gave me the chance to start down the astronomy path, and also the student scholarship from ESO for the last two years of support.

Abstract

Accretion is one of the dominant sources of radiation from a low mass young stellar object for the first few million years. This process regulates the flow of material and angular momentum from the surroundings to the central object, and is thought to play an important role in the definition of the long term stellar properties. Variability is a well documented attribute of accretion, and has been observed on time-scales ranging from days to years. However it is not clear where these variations come. The current model for accretion is magnetospheric accretion, where the stellar magnetic field truncates the disc, allowing the matter to flow from the disc onto the surface of the star. This model allows for variations in the accretion rate to come from many different sources, such as the magnetic field, the circumstellar disc or the interaction of the different parts of the system.

This thesis sets out to use the intrinsic accretion variability to probe the inner regions of these systems. Two spectroscopic surveys were utilised that concentrated on the Hα emission line, which is known to be closely connected to the accretion process. Together, these surveys covered 24 object including low mass T Tauri, intermediate mass T Tauri stars and Herbig Ae stars, on time-scales of minutes, days, weeks, months to years. These two studies found the accretion variations to be less than $1\,M_{\odot}/yr$ and dominated by time-scales close to the rotation period. A further photometric monitoring campaign was undertaken to confirm the short term variations found in the low mass sample. The results from all three of these works are in agreement with each other, and they suggest that the majority of the variations in typical accreting objects are the result of an asymmetric accretion flow.

Contents

List of Figures

List of Tables

Publications

Costigan, G., Vink, J. S., Scholz, A., Ray, T., Testi, L., 2013, MNRAS, *submitted*, 'Temperments of young stars: Rapid mass-accretion rate changes in T Tauri and Herbig Ae stars'

Joergens, V., Herczeg,G., Liu, Y., Pascucci, I., Whelan, E., Alcala, J., Biazzo, K., **Costigan, G.**, Gully-Santiago, M., Henning, Th., Natta, A., Rigliaco, E., Rodriguez-Ledesma, M. V., Sicilia-Aguilar, A., Tottle, J., Wolf, S., 2013, Astronomische Nachrichten, 334, 1-2, p. 159 , 'Disks, accretion and outflows of brown dwarfs'

Costigan, G, Scholz, A., Stelzer, B., Ray, T., Vink, J. S., Mohanty, S., 2012, MNRAS, 427, 2, pp.1344, 'LAMP: The Long-term Accretion Monitoring Program of T Tauri stars in Chamaeleon-I'

Scholz, A., Stealzer, B., **Costigan, G.**, Barrado, D., Eislöffel, J., Lillo-Box, J., Riviere-Marichalar, P. Stoev, H., 2012, MNRAS, 419, 2 pp.1271, 'Magnetic activity and accretion on FU Tau A: clues from variability'

List of Acronyms

AU	**A**stronomical **U**nit
CCD	**C**harge **C**oupled **D**evice
CTTS	**C**lassical **T** **T**auri **S**tar
EW	**E**quivalent **W**idth
FLAMES	**F**ibre **L**arge **A**rray **M**ulti **E**lement **S**pectrograph
IR	**I**nfra- **R**ed
IRAF	**I**mage **R**eduction and **A**nalysis **F**acility
ISIS	**I**ntermediate dispersion **S**pectrograph and **I**maging **S**ystem
MIR	**M**agneto **R**otational **I**nstabilities
MHD	**M**agneto **H**ydro **D**ynamics
NIR	**N**ear **I**nfrared
SED	**S**pectral **E**nergy **D**istribution
VLT	**V**ery **L**arge **T**elescope
WFI	**W**ide **F**ield **I**mager
WHT	**W**illiam **H**erschel **T**elescope
WTTS	**W**eak-lined **T** **T**auri **S**tar
YSO	**Y**oung **S**tellar **O**bject

'All men have the stars,' he answered, 'but they are not the same things for different people. For some, who are travellers, the stars are guides. For others they are no more than little lights in the sky. For others, who are scholars, they are problems.'

★ *The Little Prince, Antoine de Saint-Exupéry*

1 Introduction

1.1 The Story of Star formation

For millennia, the stars have been used to navigate, distinguish the seasons, give significant meaning to certain times of the year and as part of the folklore. For the most part, we have seen them as immovable, eternal celestial objects, reliable and unchanging. However, over time we have learnt that these celestial bodies have limited life times too, albeit orders longer than we can observe. It is through the study of our local star forming regions such as Taurus that we have learnt the most about the formation of these stars. We cannot follow a single star through its lifetime, or even the initial stages of formation, the time-scales are too long. However in these star forming regions we can observe different objects at all stages of star formation, which allows us to connect the different stages of lifetimes. Through this we have learnt that they are dynamic, evolving objects in the early stages. The first sections of this chapter will briefly present the process through which these star forming regions develop from molecular clouds over a few million years to main sequence stars such as our sun. The remainder of the chapter will be dedicated to accretion: from observations of accreting sources (Sect. 1.2) and the accretion mechanism (Sect. 1.3), to the modelling (Sect. 1.4) and measurements of accretion rates (Sect. 1.5). Finally the dependencies of

accretion and its variability will be addressed in Sect. 1.6, 1.7 and 1.8.

1.1.1 Fragmentation of the Cloud

Star forming regions begin as large molecular clouds that can be light years across and are loosely bound together with low column densities of $\sim 10^{-20}$g cm^{-2} (Schulz 2005). As these clouds collapse slowly under their own weight, gravitationally bound regions form that are initially supported by various processes such as magnetic fields, turbulence and thermal energy. Eventually these over-densities will begin to gravitationally collapse into cores when the gravitational energy is greater than the thermal energy i.e. when the mass within a radius reaches the Jeans limit given by $M_J \propto \sqrt{\frac{\rho}{T^3}}$, where ρ is the density and T is the temperature. The gravitational energy is radiated away which allows for a free fall collapse.

Large surveys of molecular clouds and star forming regions can identify these cores through molecular lines (e.g. Chamaeleon: Mizuno et al. (1999), Taurus: Onishi et al. (1998)). Depending on the initial conditions these cores will vary in mass and dimension, and they can be in clusters or isolated. The lifetimes of these cores will depend on their densities but is on the order of 10^5 years (Ward-Thompson et al. 2007).

These cores are the seeds in which stars form, and are expected to gradually evolve towards becoming a main sequence star. The typical classification system of this evolution is based on the slope of the spectral energy distribution (SED) in the wavelength range of $\sim$ 2.2 to 10 - 25 µm (Lada & Wilking 1984).

$$\alpha = \frac{dlog\lambda F_\lambda}{dlog\lambda} \tag{1.1}$$

There were originally three stages of evolution Class I, II, and III. Class I objects have a positive slope ($\alpha >$0.3) indicating the presence of a lot of surrounding dust, Class II have a negative slope in the infrared (-1.6 $< \alpha <$ -0.3) and Class III have a steeply negative slope ($\alpha <$-1.5), indicative of a bare star with no surrounding dust (Greene et al. 1994). An earlier stage of evolution, Class 0, was then proposed by Andre et al. (1993), when hydrostatic cores showing no infrared (IR) emission were discovered through submm continuum maps of star forming regions. The following sections describe the observed properties of each of the evolutionary stages. However, this evolution is a gradual process and so the observational divides between the classes are not definitive.

1.1.2 Class 0

Gravitational energy in these cloud cores is radiated away until enough density builds up and the material becomes opaque. Here a hydro-statically stable core forms - a protostar. The central object then continues to grow in mass through the infall of material from the surrounding envelope. These protostars are referred to as Class 0 objects - deeply embedded protostars with envelopes that are larger in mass than the central protostar (Andre et al. 1993).

There is no optical or near-infrared emission from these sources due to the high extinction and they are often difficult to detect and can be mistaken for starless cores. The bolometric temperatures[1] for these objects is typically less than 70K (Chen et al. 1997, 1995). Identification is often dependent on indirect detections such as an outflow from the core, some source of central heating within the core or as compact radio sources (Andre et al. 1993). In the last years submm/mm interferometers have begun to disentangle the emission in these objects, discovering structure within the envelopes in the form of discs (Jørgensen et al. 2009).

1.1.3 Class I objects

When the protostar's mass has grown to a similar mass as that remaining in the envelope, it can be classified as a Class I object (Andre et al. 1993). More quantitatively, when the bolometric temperature is between 650 - 2880 K (Chen et al. 1997, 1995) or using the IR spectral slope ($\alpha > 0.3$).

The vast majority of molecular clouds will have some rotation, which is carried through during the collapse into cores. This angular momentum results in a disc forming around the protostar, which is continuously fed with material from the surrounding envelope. These discs form very quickly after the core begins to collapse, and at the Class I phase the mass in the disc is larger than the depleted envelope. Due to the difficulty in discriminating the disc from the envelope, they are not easily observable. However sub-/millimetre continuum interferometric observations have found disc masses of $0.3\,M_{\odot}$ (Chandler et al. 1995; Pudritz et al. 1996). This means these discs are massive enough to develop gravitational instabilities through which spiral arms can form, allowing for the transport of angular momentum outwards through the disc, and the infall of material onto

[1]The bolometric temperature is defined as the temperature of a black body with the same mean frequency as the observed continuum spectrum. This is used in place of the effective temperature as a pre-main squence star has a broader and redder spectral energy distribution than a black body i.e. $T_{bol} < T_{eff}$.

the proto-stellar surface (Laughlin & Bodenheimer 1994; Vorobyov & Basu 2010). The growth of these instabilities will lead to sporadic accretion events (Vorobyov & Basu 2010), which have been observed in objects such as FU Orionis, which has been undergoing a large accretion event for the past century (Herbig 1977). It is also possible that massive planet formation begins at this stage, with planet growth through gravitational instabilities (Boss 2000).

Accurate determinations of the rate at which material is accreted from the circumstellar discs onto the source is hampered by the heavy extinction associated with these systems. IR observations of some accretion related emission lines have been carried out, but these studies are often heavily biased towards less embedded objects and there are many uncertainties in deriving stellar parameters at this evolutionary stage. This has lead to accretion rates of $\sim 10^{-7}$ - $10^{-8}\,M_{\odot}.yr^{-1}$ (Muzerolle et al. 1998a; Salyk et al. 2013), where as average accretion rates of $\sim 10^{-6}\,M_{\odot}.yr^{-1}$ on time-scales of 10^{5} yrs are necessary to grow to the observed masses (Hartmann 1998). With accretion rates on this level, the excess luminosity from the accretion flow should make up a substantial fraction of the observed luminosity (Kenyon et al. 1990). However they are observed to have similar luminosities as more evolved objects (White & Hillenbrand 2004). Episodic accretion, such as that seen in FU Orinis, is often used to explain these discrepancies between theoretical expectations and observations of these embedded protostars.

Another mechanism through which the envelope material is cleared is outflows. These large collimated jets of material extend over large distances and are often more readily visible than the embedded sources (Eisloffel et al. 1994). They are thought to be a direct consequence of the ongoing accretion in these systems (Cabrit et al. 1990; Reipurth & Bally 2001; Shu et al. 2000) and as these systems develop and the envelope is cleared, both the accretion rate and the outflow rate fall.

1.1.4 Class II objects

When the circumstellar envelope has been depleted of mass, the circumstellar disc falls below the mass where it can become gravitationally unstable and the final stages of disc accretion begin. These Class II objects can be recognised has having an SED with an IR slope of -1.5 $< \alpha <$0 (Lada & Wilking 1984) and a bolometric luminosity >2880 K (Chen et al. 1997, 1995). (See Fig. 1.1). Class II objects that are actively accreting are often referred to as Classical T Tauri Stars (CTTS), where as Class II objects that have ceased accreting are referred to as Weak-lined T Tauri Stars (WTTS).

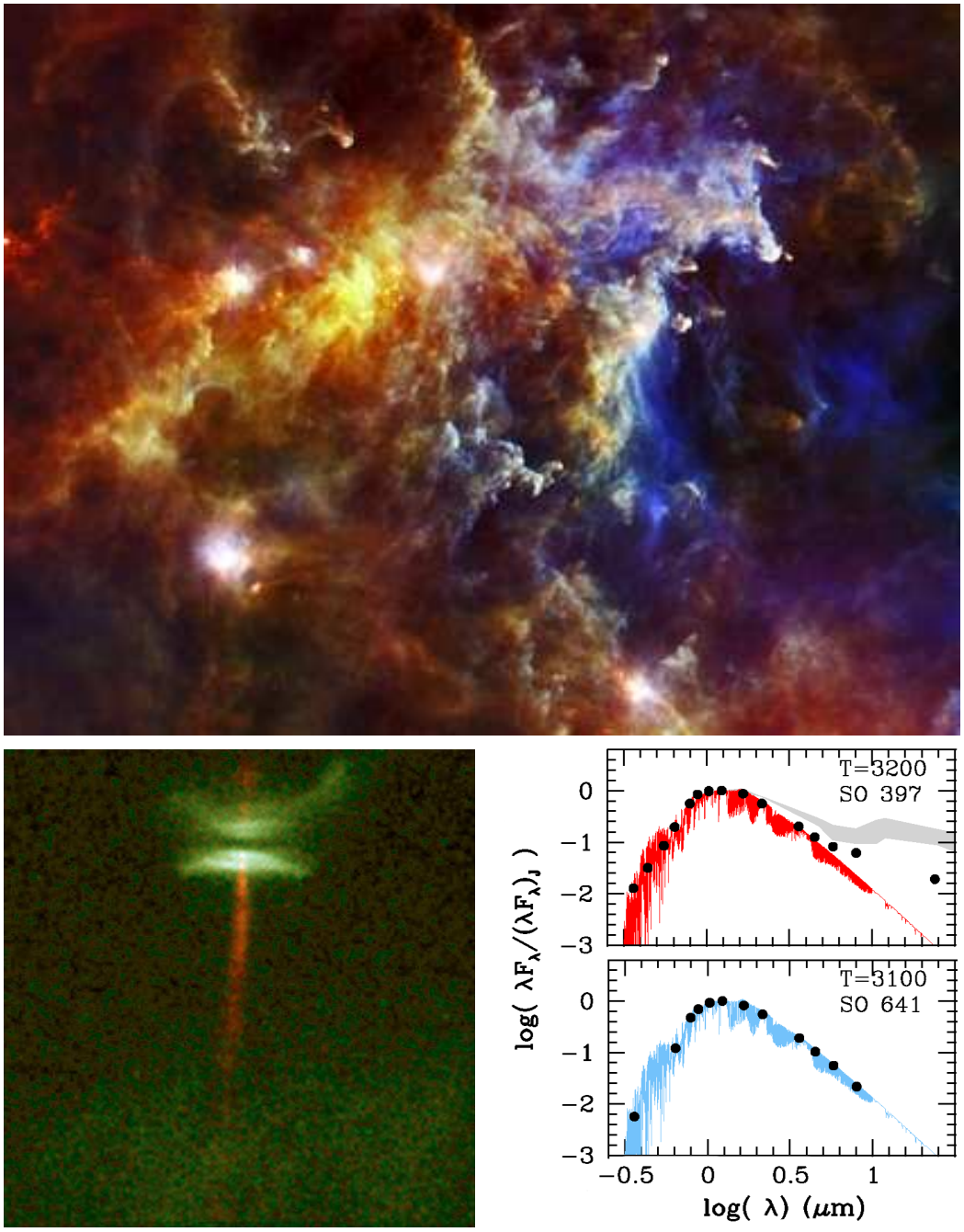

Figure 1.1: *Top Panel: Hershel image of the Rosette star forming region showing embedded protostars in the process of formation. Bottom Panel Left: HST image of T Tauri star HH-30 showing edge-on disc and jet. The central object here is masked by circumstellar disc. Credit: C. Burrows (STScI & ESA), the WFPC 2 Investigation Definition Team, and NASA. Bottom Panel Right: SED of a Class II (top) and a Class III (bottom) young stellar object in the σ Ori star-forming region. Effective temperatures of the adopted photospheric template are indicated as well as the name of the target. For the Class II, the median disk SED in Taurus (grey region) is also displayed. Black points are the photometric data. Taken from Rigliaco et al. (2012)*

Free from the envelope the central object, outflows, accretion flows and disc are readily observable for the first time across the entire wavelength range, from X-rays, UV, optical and infra-red. This allows for the direct measurement of the accretion rate using UV excess emission from the base of the accretion flow. The accretion rate at this stage is on average 10^{-9} - 10^{-7} $M_{\odot}.yr^{-1}$ (Gullbring et al. 1998). By now the star has accreted $\sim 90\%$ of the stellar mass, and the accretion rate continues to fall as the disc evolves.

The mass loss rate from these targets can be measured using optical forbidden emission lines that are now visible such as [OI] 6300$\lambda\lambda$. Part of this mass loss takes the form of a collimated outflow referred to as a jet. The jet launching mechanism is still not very well understood, but for a long time it has been associated with accretion (Cabrit et al. 1990; Hartigan et al. 1994). For most CTTS, the ratio between the mass loss and the accretion rate has been found to be $\sim 10\%$ demonstrating the close connection between the two (Cabrit & Andre 1991; Cabrit et al. 1990; Hartigan et al. 1995; Konigl & Pudritz 2000). Evidence for additional mass loss through warm stellar wind has been found in such lines as He 10708 Å (Edwards et al. 2003).

The ongoing accretion and the outflows both contribute to the dissipation of the circumstellar disc. Another important process at this stage in the disc is grain growth and planet formation through core accretion. Planets that do form at this stage are thought to sweep out cavities in the disc, this can allow for further grain growth through the creation of pressure gradients in the disc, and hence further planet formation (Chatterjee & Tan 2013). Another process that is thought to dominate the disc evolution at this stage is photo-evaporation of the gas and dust in the disc by the radiation from the central star (Clarke et al. 2001).

1.1.5 Class III objects

The number of young stellar objects (YSOs) showing near-IR (NIR) excess decreases as the age of the region increases (Bouwman et al. 2006; Haisch et al. 2005; Hillenbrand 2008). This is thought to be due to a gradual clearing of the inner disc material. The majority of YSOs have lost their disc at the age of 10 Myr (Fedele et al. 2010), this is referred to as the Class III phase. However it is still not clear what is the dominant cause of the disc dispersal. Compared to Class II objects these are very inactive and show little variability as there is no longer any accretion, no longer any jets and very little circumstellar material left. Mass loss still occurs through spherical stellar winds such as that from

the surface of our Sun. These Class III objects do still have some remaining magnetic fields and chromospheric activity (e.g. Phillips et al. 1991). However, though activity signatures are observed, they rapidly drop off as these targets evolve towards the main sequence (Scholz et al. 2007).

As has been shown, the star formation process is very dynamic, and one in which the physical attributes of a protostar can change drastically in a few million years, from a barely detectable deeply embedded core, to an energetic T Tauri star emitting from the UV to the far-IR. Accretion is a vital feature in the process of star formation. It controls the flow of matter and angular momentum from the circumstellar environment on to the YSO. This thesis is focused on disc accretion in Class II stage objects when their envelope has been dispersed and the disc mass has fallen below the gravitationally unstable limit. It is at this stage that the central object can be well classified as it is directly observable for the first time.

1.2 Components of Accreting YSOs

Accretors at this stage of their evolution (Class II) are systems with multiple interdependent components i.e. central star, magnetic field, circumstellar disc, outflows (See Fig. 1.2). The following section describes these components, their connection and some of their properties as derived from observations.

The young stellar object at this stage is comprised of a central opaque core surrounded by an atmosphere composed of layers of gas. The radiation emitted from the core is affected by the different temperatures, densities and compositions of the layers it passes through. For instance, atoms in the photosphere will absorb light at specific wavelengths corresponding to the energy levels in that atom. The outer layer of the chromosphere is hotter, so similarly the atoms are heated, excited and emit photons at specific wavelengths. This composition of atmospheric layers results in a spectrum with both absorption lines and emission lines, which carry the signatures of the atmospheric layers from which they come from. The spectral classification of stars is based on these spectral features which identify the temperature of the photosphere.

The first measurements of the magnetic fields on the surface of T Tauri stars found them to be quite strong, ~ 1 kG (Basri et al. 1992; Johnstone & Penston 1986). The fact that X-ray emission is found in many YSOs attests to the

presence of strong fields in the majority of the young stellar population (Feigelson & Montmerle 1999). Magnetic activity in young stars acts to further heat the chromosphere, resulting in more pronounced emission lines in the spectrum. This enhanced emission is one of the most common methods of identifying young stellar objects in star formation regions, and is particularly strong in Hα .

Another distinguishing feature of YSOs and in particular accretors is their variability, which has also been used to identify young populations (Hoffmeister 1962). Photometric monitoring reveal irregularities on the surface of Class II objects in the form of cool spots. These are analogous to the sunspots on the surface of our sun, and are a result of the magnetic field interacting with the stellar photosphere. As the cold spots move across the surface of the star they modulate the luminosity of the star, and provide a way to measure the stellar rotation rates with accuracies of 1% (Herbst et al. 2007).

Actively accreting Class II objects will also have hot spots on their surface where the infalling accretion material heats the photosphere to a higher temperature than the surroundings (Bertout et al. 1988). The temperature of cold spots is about 10 - 30% lower than the photosphere, however hot spots are thought to be a few 100 to a few 1000 K hotter than the photosphere (Bouvier et al. 1995). Hence, small hot spots can cause much larger variations in the light curves than cool spots. Through modelling of the color variations the two can be distinguished.

Through rotation rate measurements it has been found that accreting T Tauri stars are slow rotators compared to stars with no accretion disc (Bouvier et al. 1986; Vogel & Kuhi 1981). As the protostellar object accretes material it is also accreting angular momentum, so it is expected to spin up making it necessary to have some process to slow the rotation of the central star while it is accreting. The key difference between these two populations of rotators is the presence of a circumstellar disc, indicating it has a strong role to play in the rotational braking.

Observations of these objects have revealed large scale collimated outflows called jets, that are thought to be launched from the disc, and also stellar winds launched from the surface of the star. As both these processes contribute to the mass loss in the system, they could be key ingredients to the spinning down of the star (Matt & Pudritz 2005, 2008).

The mass reservoir for accretion at this evolutionary stage is the circumstellar disc. The NIR emission from these objects is dominated by the reprocessing of the stellar radiation by the dust in the disc. The level of emission suggests many of the discs have a high degree of flaring, exposing more surface area to the

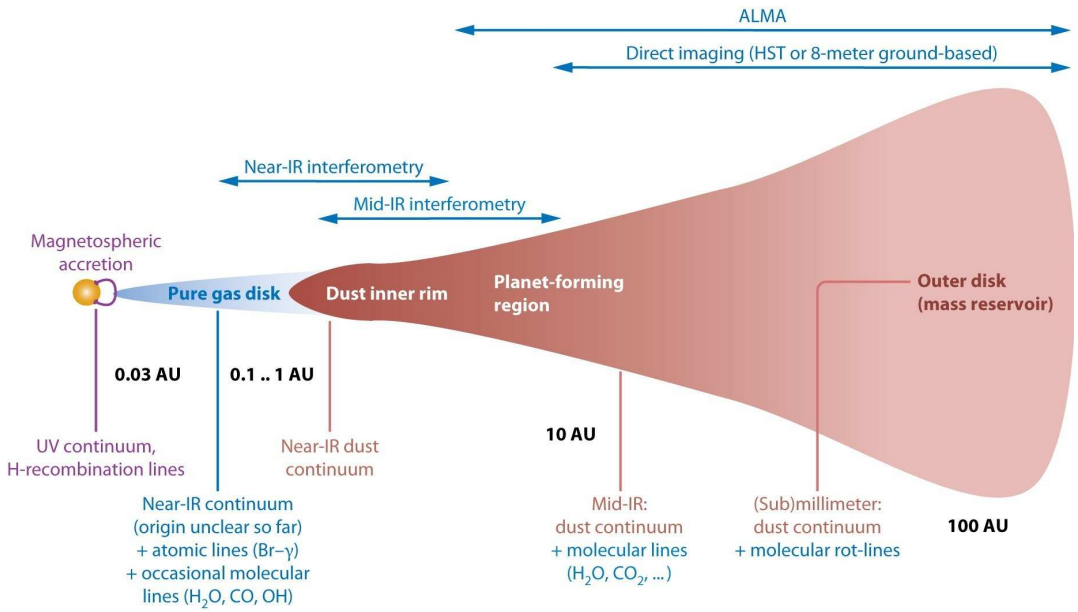

Figure 1.2: *Cartoon showing different components of an accreting Class II source. Also indicated are the wavelengths used to observe these different components. Taken from (Dullemond & Monnier 2010)*

stellar radiation, allowing for a more efficient absorption of the light which in turn increases the flaring in the disc (Kenyon & Hartmann 1987). Some objects show high degree of variability in the NIR emission and this is probably due to changes in the structure of the disc (Flaherty et al. 2012). Whether there is a single source for all the objects variations or if it changes from source to source is not clear.

The above processes all come from the inner AUs of these systems, making them highly likely to be sensitive to changes in each of them. One process that does connect them all is accretion.

1.3 What is Accretion?

T Tauri stars are first identified as a different class of object by the excess emission observed in a certain emission lines such has Hα and its variability (Joy 1945). Later it was found that high levels of Hα emission was strongly correlated with the presence of a UV excess (Haro & Herbig 1955). A number of models have been put forward to explain this emission.

It was first postulated that this emission was a result of the accretion of material from the circumstellar disc through a boundary layer. In this picture the disc extends all the way to the surface of the star. The excess energy in the

disc is dissipated through shearing forces between slowly rotating star and the disc following Keplerian rotation (Lynden-Bell & Pringle 1974). The observed NIR excess in the spectra of YSOs then originates in a self luminous disc and the UV excess comes from the energy released in the boundary layer between the disc and star.

However there were a number of observations that were contradictory to the physics in this model. The associated emission lines were shown to be very broad, with high velocities of $\sim 100\,\mathrm{km\,s^{-1}}$. This is indicative of acceleration of material from large distances to the stellar surface which is inconsistent with the boundary layer model. As the resolution of spectrographs improved many of these highly broadened emission lines were also seen to contain reverse P-Cygni profiles, which is a signature of infalling material at high velocities (Walker 1972).

Under the boundary layer model there is no mechanism under which the star can loose the angular momentum it gains during accretion, meaning the stars would continuously spin up. At the time there was also mounting evidence that the stellar discs do not extend all the way to the surface of the star (Bertout et al. 1988). The surface hotspots that are revealed through photometric monitoring suggest the origin of the UV emission is not axisymmetric as needed in the boundary layer model, but in confined regions that come in and out of view as the star rotates.

As the quality and amount of observations of these targets increased, it became apparent that this model was not reflective of the physics in these systems. Königl (1991) suggested that the presence of magnetic field could regulate the accretion flow as was first proposed as a model of accretion in neutron stars by Ghosh & Lamb (1978).

In this magnetospheric accretion model the inner disc is partially ionised by the stellar radiation and collisions, allowing for a stellar magnetic field to couple to the disc. At some point in the disc, if the magnetic field is strong enough, the kinetic and ram pressure of the accreting material moving through the disc will equal the magnetic pressure. This point is referred to as the truncation radius R_T. Here, if the disc material is sufficiently ionised, its motion will be controlled by the magnetic field. Due to the pressure gradient the material is lifted from the disc and can free-fall onto the surface of the star following the magnetic field lines. Based on simple spherical infall models and a dipolar field, the truncation radius can be found to be proportional to the strength of the magnetic field (B_*),

stellar mass (M_*) and stellar radius (R_*) (Bouvier et al. 2007b):

$$\frac{R_T}{R_*} = \frac{B_*^{4/7} R_*^{5/7}}{\dot{M}^2 (2GM_*)^{1/7}} \tag{1.2}$$

In reality the disc truncation radii are much smaller than this, as the higher disc densities mean the ram pressure in the disc is larger than ram pressure due to spherical infall accretion.

The magnetic field intersects the disc at a series of radii. The point at which the angular velocity of the star ($\Omega_* = \frac{2\pi}{P}$) equals the Keplerian velocity in the disc ($\Omega_K = \left(\frac{GM_*}{R^3}\right)^2$), is called the co-rotation radius (R_c) i.e.

$$R_c = \left(\frac{GM_*}{\Omega_*}\right)^{\frac{1}{3}} \tag{1.3}$$

Any magnetic field lines that couple to the disc outside the corotation radius will act to slow the stellar rotation. In the same way, any field lines coupled inside the corotation radius will act to spin the star up. This process allows for a disc braking mechanism, which coupled with the angular momentum loss through outflows, could account for the spin down of accreting stars (Romanova et al. 2005; Ustyugova et al. 2006).

Accretion shocks form at the base of the accretion flows near the surface of the star, which cool through X-ray emission, most of which is absorbed and reprocessed as UV emission. These shocks are similar to the classical boundary layers in their basic geometry, but instead occur at high latitudes which increases the visibility of the emission regions, and allows for an efficient heating of the disc by stellar radiation.

The geometry of this system would mean that the central star would, for the most part be masked by the accretion curtains. However, the density and temperatures in the flows fall off rapidly as the distance from the star increases, which allows for the stellar UV and optical emission to be observed.

This magnetospheric accretion model has held up well against the modern observations. The application of this model to observations has lead to insights into the make up of the inner AUs of these systems, and gives us a further understanding of the physics in the inner regions that would not be attainable otherwise. The following section describes one of the early models, and some conclusions that can be drawn from the application of more sophisticated models to individual objects.

1.4 Modelling of Accretion

The first models of magnetospheric accretion used a strong symmetric dipolar field and radiative transfer methods to model emission lines from accreting T Tauri stars (Hartmann et al. 1994). Many of these models concentrated on the emission lines in particular as they hold a lot of information on the structure and velocities of the accretion flow, the geometry of the magnetosphere and the interaction between the magnetosphere and disc.

Hartmann et al. (1994) focused on the production of the Balmer series, which is one of the most readily observable series in these accreting objects. These emission lines are thought to originate in the hot accretion flows. Hartmann adopted a simple approximation for the temperature profile in these flows that was inversely proportional to the density within the flows. This meant the accretion material was cool as it left the disc, warmed as it reached higher velocities and lower densities and cooled again as it reached the stellar surface and the density increased and enhanced the radiative cooling. The line source functions were then calculated using the Sobolev approximation, which assumes that conditions in the flow are resonant over length scales proportional to the velocity in gas. This is likely to only be valid in the fastest part of the accretion flow, where the velocity gradient is at its largest. It has been found that Stark broadening is an important factor in the optically thick Hα line which means the Sobolev approximation is not valid in this case (Muzerolle et al. 2001). However this approximation is still used in the majority of radiative transfer calculations, albeit with some caution for the Hα emission line in particular.

The Balmer lines are seen in non-accreting stars at this evolutionary stage due to the active magnetic fields these stars harbour. The emission that this model produces however is much stronger and broader than chromospheric activity alone. The enhanced emission comes from the hot accretion flows exciting the Hydrogen atoms. The broadened emission lines also reflects the range of velocities from zero to free fall within the accretion flow. Within the Hartmann model the higher Balmer emission lines (Hγ) also showed overlying red-shifted absorption features which occur when the hot inner parts of the accretion flow are viewed through the cooler tail of the flow.

In reality the emission profiles are more complex than these simplified models can reproduce. For instance, comparing the model with observations Hartmann et al. (1994) noted that the model does not show the blue-shifted absorption that is seen in the profiles of BP Tau and UY Aur. This blue-shifted absorption

is commonly, but not always seen in the Balmer profiles, and is indicative of a cold wind outside of the accretion emission region, reabsorbing the emission (Giampapa et al. 1993). It has been later found that warm winds originating close to the star, can contribute to the emission in these Balmer lines (Whelan et al. 2009). Particularly for Hα, which is the strongest and most readily observable emission line in these accreting objects, a hybrid code incorporating accretion and wind is necessary to model this line properly.

Many accretion related emission lines have also been observed to contain a broad component consistent with free-fall velocities, with an overlying narrow emission component attributed to emission directly from the accretion shock (Basri 1987; Hamann & Persson 1992). This demonstrates that to properly model the emission the different components of the accretion flow have to be considered.

One of the weaknesses that still remains in modern models, is the temperature structure in the magnetosphere. The Hartmann et al. (1994) temperature approximation for the accretion flows has an arbitrary normalisation to fit observations. More consistent temperature structure calculations have yet to fit observations (Martin 1996), but it has been suggested that the line profiles are only sensitive to the mean temperature in the flow rather that the detailed temperature structure (Kurosawa et al. 2008).

The simplistic geometries of the first models have been improved on and made more realistic to better model the observed emission. In recent years the magnetic fields of a number of accreting T Tauri stars have been mapped. This is done using spectro-polarimetric observations, and monitoring of the rotational modulation of the Zeeman signal. Photospheric lines are used to map the magnetic field across the surface of the star, but also accretion related emission lines are used to estimate the magnetic field strength at that base of the accretion flow. Very complex fields have been found in accreting stars, differing greatly from a simple dipolar field (e.g. V2046 Sgr (Donati et al. 2011b)). However, for the majority of T Tauri stars, a combined dipolar and octupole magnetic field has been found to fit the observations (e.g. BP Tau (Donati et al. 2008), V2129 Oph (Donati et al. 2011a) and AA Tau (Donati et al. 2010)). The presence of the octupole field is thought to force the accretion flows into a smaller area to higher latitudes. As the octupole is only dominant on the surface, the dipolar field still determines the truncations radius (Adams & Gregory 2012). Most recently, the limitation of the assumed dipole magnetic field has been addressed by combining magnetohydrodynamics (MHD) and radiative transfer codes to model more

realistic accreting systems. These models can allow for more complex magnetic fields with multiple components, misalignments between rotation axis and field axis (Kurosawa et al. 2008) and instabilities in system (Kurosawa & Romanova 2013). These models are coming much closer to reproducing observations and can provide very detailed pictures of what is happening in these systems.

Models of these accreting systems have also lead to a better understanding of how the geometry and structure of the accretion flows. A small misalignment in the magnetic field and rotation axis will also lead to structured accretion funnels (rather than a curtain of material in classical model). There is strong evidence for this from photometric monitoring of accreting objects which is more conducive to distinct hot spots on the surface rather than a continuous circumstellar hot ring. Romanova et al. (2003) showed there exists density gradients in the cross sections of these flows, where a narrow dense column is surrounded by a much larger low density flow that can cover most of the magnetosphere. This is then reflected in the hot spots on the surface of the star, which can also have pressure, velocity and density gradients across them, peaking in the centre. The size of the accretion flows, and the size of the accretion shock are also dependent on the accretion rate. At higher accretion rates, the shock and flow expand, so that the energy flux in the flows remain equal for different accretion rates (Gullbring et al. 2000). This has been observed in BP Tau (Ardila & Basri 2000). Also when the accretion rate increase, the truncation radius decreases. This leads to a higher angular velocity at the base of the accretion funnel, which then changes the position of the accretion spot on the surface (Romanova et al. 2004).

As our understanding of accretion improves, and more observations are gathered on the different components in the system, the models can be developed to become closer to reality. The above examples show that the current state of the models do allow us to derive strong constraints on the geometry in these systems. However this is usually restricted to specific objects for which a lot of observational data is available to constrain the properties of the accretion flows. The most successful applications of models to accreting systems have used the observed spectroscopic variability to narrow down the model parameter space (See Sect. 1.7 for more).

The necessity of large amount of observations is a weakness that needs to be overcome in order to expand our understanding of accreting systems to more than a handful of targets. One possible way to do this is through the measurement of the accretion rate across many targets. This allows for the comparison between the physical properties of these systems and accretion rates to understand which

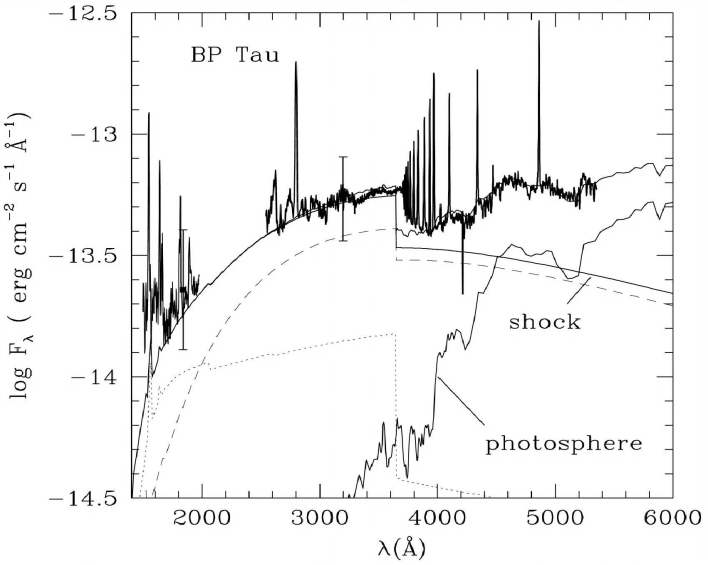

Figure 1.3: *Observed spectrum of accreting star BP Tau (thick black line). The narrow line shows the model excess continuum emission which is a combination of the post-shock and pre-shock continuum emission (dotted line) and the continuum emission originating in the heated photosphere (dashed line). From Gullbring et al. (2000).*

are the defining properties in the accretion process.

1.5 Measuring Accretion Rates

Disentangling the accretion emission from the stellar or other sources of emission is non-trivial. The following section goes through the most common methods of deriving accretion rates from observations.

The 'gold standard' of accretion rate measurements and the most direct, is to use the accretion shock emission at wavelengths >3700Å. The material falling along the magnetic field lines will reach the surface of the star at free-fall velocity. A shock front forms just above the photosphere, as the kinetic energy of the infalling material is released as it meets the surface of the star. The energy is released as soft X-rays, which are quickly absorbed by the stellar atmosphere in one direction, and the accretion flow in the other. This emission is then readmitted in the optical and the UV.

Originally a simple slab model of hot hydrogen with strong emission peaking in the UV was used to reproduce the excess emission from this region (Basri & Bertout 1989; Gullbring et al. 1998; Valenti et al. 1993). The excess emission in UV is due to the Balmer continuum emission which peaks in the UV ($<$3700Å)

where the majority of low mass stars do not emit strongly. The Balmer jump can be defined as the ratio of the continuum emission at 3600Å to the that at 4000Å. For non-accretors this can be as low as 0.35 whereas for actively accreting objects it can be as high as 6 (Herczeg & Hillenbrand 2008). Excess continuum emission long-ward of 4000Å is classified as Paschen continuum emission. This excess is observed as a filling in of the stellar photospheric absorption lines, and is usually referred to as veiling. The amount of veiling in a spectrum can be found by comparing the depth of photospheric absorption lines in accreting and non-accreting stars (Hartigan et al. 1991).

Valenti et al. (1993) used a pure hydrogen isothermal slab in LTE to reproduce this Balmer and Paschen emission. The luminosity of this slab model is dependent on five parameters, the emitting surface area, the temperature, density, macroturbulance, and the depth of the slab. Through this simple model the Balmer jump, and veiling due to the Paschen continuum emission can be estimated. This was first developed for the boundary layer model where the range of temperatures and densities is low compared to the magnetospheric accretion model. Calvet & Gullbring (1998) proposed a multicomponent shock model to be more appropriate for the case of magnetospheric accretion. However comparisons between the slab model and the multicomponent shock model have shown very little difference between the predicted emission (Herczeg & Hillenbrand 2008). So although the slab model makes very simplified assumptions on the shock geometry, it is considered the best way to estimate accretion rates.

This slab model method does very well in reproducing the emission that is observed at these wavelengths (See Fig. 1.3). The accretion luminosity can then be converted to an accretion rate using the stellar radius R_*, the infall radius R_{in}, stellar mass M_* and the following equation from Herczeg & Hillenbrand (2008):

$$\dot{M} = \left(1 - \frac{R_*}{R_{\rm in}}\right)^{-1} \cdot \frac{L_{\rm acc} R_*}{G M_*} \tag{1.4}$$

This UV excess is difficult to observe in many objects with low accretion rates, and due to extinction or obscuration it is not possible to obtain UV spectroscopy for many more objects. Instrument limitations (CCDs are not very sensitive at wavelengths <4000Å) also limit the feasibility of large UV surveys of accreting objects.

For this reason, the accretion rates derived from the UV excess emission, have been used to find empirical relations between accretion rates and certain emission line luminosities. This allows for the measurement of accretion rates

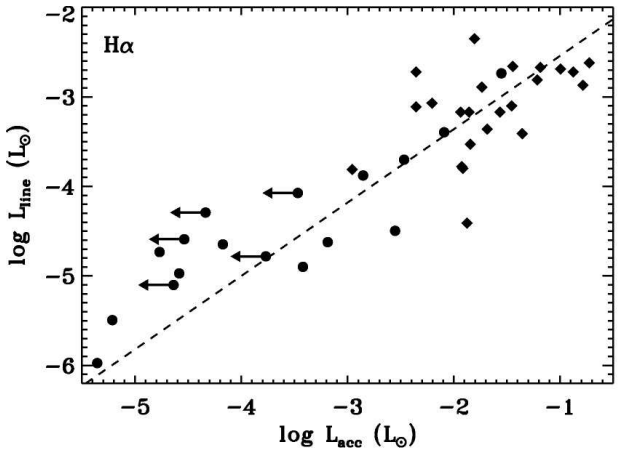

Figure 1.4: *Relation between Hα line luminosity and the accretion luminosity derived from the Balmer continuum excess. The dashed line represents the linear fit to the data. From Herczeg & Hillenbrand (2008).*

from readily observable emission lines such as Hα, Br γ, Ca II (λ8542 and 8662), He I λ5876 (Hartigan & Kenyon 2003; Herczeg & Hillenbrand 2008; Mohanty et al. 2005; Muzerolle et al. 1998a), and also for line profile properties (e.g. Hα 10% width Natta et al. (2004)). Fig. 1.4 shows the relation derived by Herczeg & Hillenbrand (2008) between the accretion luminosity and Hα line luminosity.

These relations are empirically derived and though there is a strong correlation found between these line luminosities and accretion luminosities, the physics connecting the line emission and the excess continuum emission is not well defined. These relations use the entire line emission, which as in the case of Hα, can contain emission from other sources such as chromospheric or wind emission. For this reason, large samples are used to derive these relations, in an attempt to limit the effect of these issues. It has also been found that these luminosity relations do not to hold across very large mass ranges. For example, Mohanty et al. (2005) found on deriving a relation between Ca II line luminosity and the accretion rate, that there was an offset between the relation derived for the low mass (~ 0.1 M$_\odot$) and the higher mass (~ 0.7 M$_\odot$) T Tauri stars in their sample.

There have been efforts to extend these relations to higher mass Herbig AeBe stars (2 - 5 M$_\odot$). For example, Mendigutía et al. (2011) found a slightly shallower relation between Hα line emission and the accretion luminosity than was found in the lower mass (<1 M$_\odot$) sample of Herczeg & Hillenbrand (2008). Though there is inconclusive evidence of strong magnetic fields on Herbig stars, the fact that a very similar relation is found for these larger mass T Tauri stars suggests they are undergoing the same accretion process.

These relations have created many more opportunities to measure accretion

rates in different systems than was previously allowed with the UV excess emission. Accretion models are developed somewhat 'blindly' to fit the data available. Infalling material at free-fall velocity is used to estimate the energy released, the luminosity and hence the accretion rate. This relies on simple assumptions on the geometry and the physics of the inner system, but it does well to reproduce the emission observed. One way to test the reliability of these accretion measurements and models is to apply them to a wide range of accreting objects to test the dependence on such things as mass, age and disc properties. Another very powerful method, and one which is used in this thesis, is to use the intrinsic variability of the accretion process to do the same.

1.6 Accreting Objects as Dynamic Systems

These systems are very dynamic and this is reflected in the observed variable emission at X-Ray (Gagné et al. 2004), UV (Herbst et al. 1994), optical (Grankin et al. 2007), NIR (Scholz et al. 2009) and radio (Feigelson et al. 1994) wavelengths. This section explores the variations that are observed in accretors and their connection to the different components of T Tauri stellar systems.

The original classification of T Tauri stars was based on their irregular photometric variability (Joy 1945). Photometric variability is seen in all pre-main sequence stars at some level, and is a diverse phenomenon occurring on all timescales. A large fraction of this variability is caused by cool spots on the surface. On top of these variations, CTTS are more likely to show more significant variability than WTTS due to the ongoing accretion and hot spots on their surface (Herbst et al. 1994).

Long term photometric monitoring of CTTS suggest that typical T Tauri stars show low levels of variations over time periods of $\sim$20 yrs (Grankin et al. 2007). Only a fraction of the sample of Grankin et al. (2007) showed significant changes over time-scales of months to years, whereas the majority showed variations on time-scales of weeks suggesting that the short term time-scales are more important in these systems.

At early evolutionary stages large photometric changes have been found, reflecting an evolution in the variability in these objects. This is most likely due to a transformation in the accretion process itself as it changes from being driven by infall from the envelope to solely disc accretion (See Fig. 1.5). FU Ori objects, show increases from luminosities of normal accreting T Tauri stars to a few 100 $L_\odot$. These jumps in emission correspond to accretion rate changes of

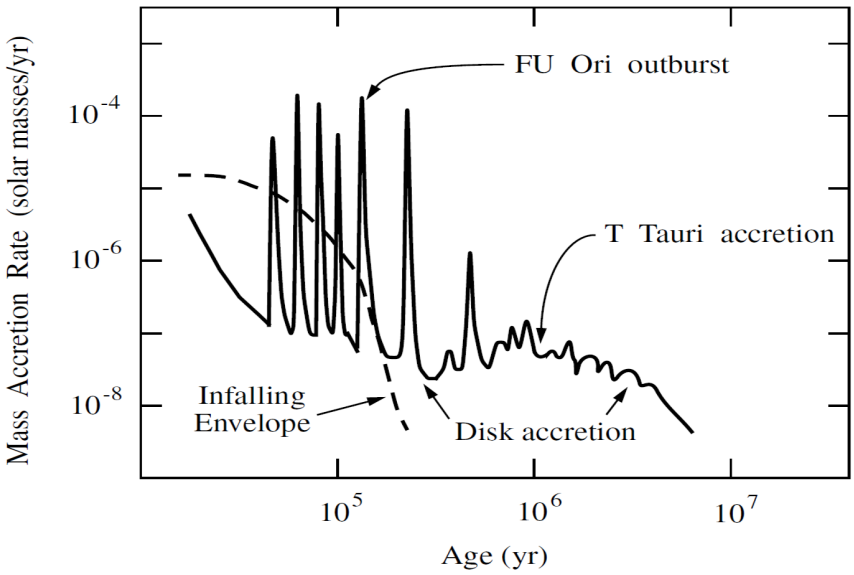

Figure 1.5: *Speculative evolution of the accretion rate onto the star over time. In the beginning large accretion rate variations occur while the disc is gravitationally unstable, then when the envelope mass has been exhausted the disc mass falls below the gravitationally unstable limit and disc accretion begins. EXors are thought to lie between the FU Ori and T Tauri phase. From Calvet et al. (2000).*

three orders of magnitude, from 10^{-7} up to $10^{-4}\,M_\odot\ yr^{-1}$. The increase takes months or years, and remains high for centuries (Hartmann & Kenyon 1996). It is not clear if all FU Ori objects are at the same stage of evolution. FU Ori itself appears to have cleared its envelope (Malbet et al. 1998, 2005), where as emission from other FU Ori objects is consistent with envelope emission (Kenyon & Hartmann 1991). However, one likely mechanism for this process is that these targets still have massive enough discs to allow gravitational instabilities to form which would dump huge amounts of material onto the central star (Vorobyov & Basu 2010). Another possibility is that these large changes are a result of binary interaction (Reipurth & Aspin 2004), but it has yet to be confirmed that FU Ori outbursts occur preferentially in close binary systems.

Slightly less dramatic accretion changes occur in EXors type objects, which can show 1 - 3 magnitude flare ups every few years for a period of weeks (Herbig 2007) which could be a result of instabilities in the inner disc (D'Angelo & Spruit 2012). These objects probably represent the transit between FU Ori type accretion to the T Tauri disc accretion phase.

Observations of accreting T Tauri stars in multiple star forming regions of different ages give strong evidence that there is an evolution to the accretion rate as these systems gets older. Fedele et al. (2010) find that at 1.5 - 2 Myr the

fraction of accreting stars in star forming regions is 60%, this drops to only 2% at 10 Myr. These are similar time-scales for disc clearing, however the number of accretors is found to drop off much faster than the number of YSOs harbouring discs which suggests that the point at which accretion ceases is dependent on the disappearance of the disc.

Fig. 1.5 shows the hypothetical connection between the different phases of accretion in a system i.e. large episodic accretion in the FU Ori stage evolving to lower levels of accretion and variability in the EXors stage, which further evolves to disc accretion in the T Tauri phase, which decays gradually as the system evolves. This connection is still speculative. One of the aims of this thesis is to study the variations in the T Tauri stage to quantify their magnitudes in order to better compare the accretion processes at the different stages, and the connection between them.

As was indicated in the cases of FU Oris and EXors, the presence, geometry and amount of circumstellar material is thought to play an important role in the accretion process. Evidence has been found for changes in the inner disc of T Tauri systems. Eiroa et al. (2002) found variations in the NIR emission of 1 mag. on time-scales of days for a number of objects, suggesting changes in the structure of the inner disc on short time-scales. Any changes to the inner structure due to changes in the accretion rate through the disc will occur on viscous time-scales which in T Tauri discs are on the order of months and years (Pringle 1981). These short term variations are thus more likely to come from a change in the magnetic field (Armitage 1995) or some instability in the inner disc (Lai 1999), which can cause changes in the structure of the inner disc on time-scales of days. These kind of variations in the inner disc structure could induce changes in the accretion rate onto the star.

Conversely, changes in the accretion rate can also affect the inner disc. A change in the accretion rate and hence accretion luminosity, will change the sublimation radius in the disc and cause the inner edge to move in or out. Observations of this occurring have been made in a few cases (Carpenter et al. 2001; Skrutskie et al. 1996).

The magnetic fields in these accretors channel the flow of material from the disc to the surface of the star. Donati et al. (2011a) found changes in magnetic topology of the accreting star V2129 Oph over the time-scales of years. A change of 0.3 kG in the magnetic field, coincided with a half an order of magnitude change in the logarithmic accretion rate. This kind of change in the magnetic field will also have an effect on the inner disc, as the truncation radius changes.

The variability seen in other parts of the accreting system is also seen in accretion. The excess emission and emission lines from the accretion shock and flows are all found to be variable on time-scales from hours, to weeks, and to years (Mohanty et al. 2005; Nguyen et al. 2009b; Scholz & Jayawardhana 2006). Although the current models of magnetospheric accretion fit the emission we observe in these objects, it is as of yet unclear where the variations come from.

This variability can and has been used to probe the inner regions of these accreting systems, to find the source of the variations and to provide stringent constraints on the nature of the accretion process itself (Dupree et al. 2012). The time-scale of accretion variations and the magnitude of the variations will depend on their source. This thesis sets out to monitoring typical accreting systems over different time-scales, in order to identify where these variations originate. This allows for constraints to be put on the stability of the different parts of the accreting system i.e. the magnetic field, the inner disc and the accretion flows themselves.

1.7 Accretion Variability

Spectral lines are particularly useful when investigating accretion due to the velocity information they contain and the multiple components within them. In particular spectroscopic variability studies can provide information on the spatial structure and dynamics of the accretion flow (Bouvier et al. 2003).

The majority of the spectroscopic monitoring studies of YSOs have focused on either single target or a small number of targets, specifically selected for their known variability. Some of these studies have led to a detailed close-up view on the disc-accretion system (e.g, Bouvier et al. 1999; Giampapa et al. 1993) and provided unique insights into the magnetospheric accretion/ejection scenario (e.g. Bouvier et al. 2007a; Johns & Basri 1995a). In other cases the changes in the variability patterns are highly complex and difficult to interpret (e.g. Alencar et al. 2005). This thesis makes use of these spectral lines to monitor the accretion rates in YSOs and in the following sections some examples are given as to what can be found by doing this.

From the basic model of steady disc accretion through a dipolar magnetic field, there have been a number of variations on these models put forward to explain the variations seen in T Tauri objects. One of the first models to be investigated was the case of an asymmetric accretion flows, as is suggested by the photometric variability seen in these objects. Simulations of magnetospheric

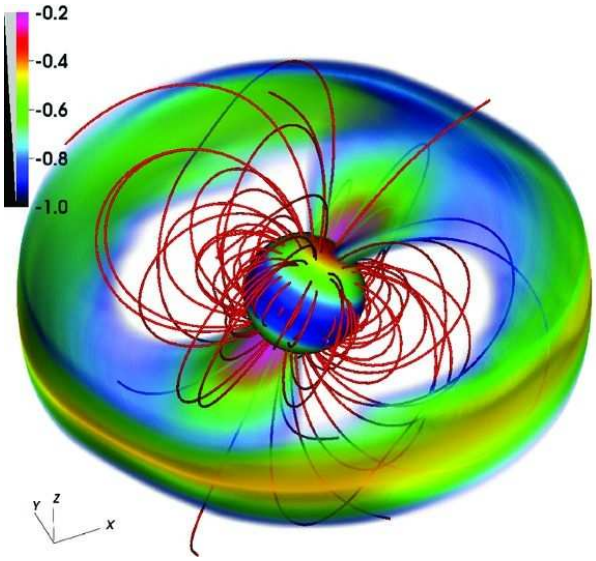

Figure 1.6: *MHD simulation of accreting star with a 30° offset between rotation axis and magnetic field axis which results in an asymmetric accretion flow. Volume density is colour coded on a logarithmic scale, and sample magnetic field lines are shown in red. From Kurosawa & Romanova (2013)*

accretion have found that even a slight offset (2 - 5°) between the rotation axis of the star and the magnetic field will result in an asymmetry in an accretion flow (Romanova et al. 2003). Different parts of the flow will then come into view as the star rotates, changing the emission signature we observe on the time-scale of the rotation period (Kurosawa et al. 2008). This will result in an apparent accretion rate change (See Fig. 1.6), and take the form of a smooth variation in the emission line and its features. An example of such a asymmetric flow was found in SU Aur where the accretion emission features (red-shifted absorption in Hβ) and the wind emission (blue-shifted absorption in Hα) were found to vary on rotational time-scales in anti-phase (Johns & Basri 1995b). If both the rotation and the magnetic field axis were aligned, these signatures would be expected to vary in phase, but even a slight offset between the two will result in anti-phase correlation.

An asymmetric accretion flow is thought to be responsible for the variations observed in the spectra of V2129 Oph (Alencar et al. 2012). The authors used MHD simulations of the observed magnetic octupole and dipolar fields of V2129 Oph, and radiative transfer codes to reproduce the observed line profiles. Earlier observations of the magnetic field found an offset between the octupole and dipole fields (15 and 25°) and the rotation axis (Donati et al. 2011a). The modelling of these fields result in two ordered flows of material onto the star very close to the poles. The derived profile variations are similar in magnitude to the observed

profiles, however the changes in the profile shape are not. The presence of higher order fields, as has been observed in a number of targets, will also disrupt the symmetry in the system making it more likely for asymmetric accretion flows to form.

Observations indicative of an azimuthally twisted accretion column have been found on SU Aur. Oliveira et al. (2000) found a delay in variations and features in a number of emission lines. The authors argue that these emission lines form in different parts of the accretion flow, and the offset is due to an azimuthally twisted accretion flow. This could occur in the case of differential rotation between the disc and the star, which will lead to a trailing of the magnetic field anchored in the disc and disrupt the symmetry of the accretion flow. Differential rotation can also lead to expanding field lines, which could radically reduce the mass accretion rate as the magnetic field lines open, and will then cause it to increase again upon reconnection (Goodson et al. 1998). These magnetic reconnection led variations are expected to occur on the time-scales on the order of the rotation period of the circumstellar disc (Hayashi et al. 1996). If this process is seen to occur, it can provide important constraints for the rotational braking problem. If the magnetic field is not stable on these time-scales, it would mean that disk locking alone cannot account for the slow rotators observed, and so another mechanism is needs to be evoked to carry away the extra angular momentum such as accretion powered stellar wind (Matt et al. 2012).

Additionally, inhomogeneities in the disc will cause the observed accretion rate to vary, as is the case with an accreting T Tauri star found by Bouvier et al. (1999). AA Tau was found to have a light curve with roughly constant brightness, broken by a quasi-periodic fading. This was attributed to a wall in the inner circumstellar disc which obscures the light from the central source periodically as it rotates. In the same way, such a wall could be a source of apparent accretion variability on a much longer time-scale if placed further out in the circumstellar disc.

These walls are thought to occur in the event of an offset between the rotational and magnetic field axis. The interaction between the magnetic field and the disc is thought to lead to an accumulation of matter in the inner disc (Romanova et al. 2002), forming a denser ring of material at the truncation radius. If a misalignment exists between the magnetic field and rotation axis, the material from the disc would preferentially be loaded onto the shorter field lines, making it likely for a warp in the disc to form with the possibility of trailing spiral arms (Terquem & Papaloizou 2000).

The examples above show the quality and resolution of the 3D MHD modelling has reached a level of sophistication that allows us to follow variations in the features of the emission lines as different aspects of the accreting system change. However, so far only a few individual objects have the temporally resolved spectroscopic observations that are needed to match these simulations.

Apart from a few benchmark objects, observations have yet to distinguish a dominant source of variations. Each of the sources of variations discussed above will show different amplitudes and time-scales of variations, which provides a robust way to determine their origins.

1.8 Accretion Rate Dependencies

It is still not clear what drives accretion through the circumstellar disc. At the T Tauri phase the discs are no longer massive enough to be gravitationally unstable. One of the more likely methods of transporting material and momentum through the disc is via magneto-rotational instabilities (MRI). However for MRI to play a significant role the disc must be sufficiently ionised, which is probably not the case in the inner, densest part of the disc where the matter is shielded from cosmic rays and X-rays (Mohanty et al. 2013) Recently, simulations have found that both ohmic resistivity and ambipolar diffusion could dominate in the inner AU and act to completely suppress the MRI, allowing for a disc wind driven accretion of matter through the disc (Bai 2013).

If MRI is the driving force for matter through the disc, we would expect the accretion rate onto the star to show some dependence on it. However, one of the only correlations that has been found when measuring the accretion rates in large samples of objects is a dependency on stellar mass (M_*). Conversely, MRI is strongly dependent on the active surface layer density in the disc, and shows no explicit dependence on stellar mass.

A wide range in exponents have been derived for this $\dot{M}$ - M_* relation, and a defining feature of these plots is the spread around the relations. Mohanty et al. (2005) derived a correlation $\dot{M} \propto M_*^2$ for a sample with a mass range of $0.15\,M_\odot$ to $\sim 2\,M_\odot$ and age range from $\gtrsim 1$ Myr to 10 Myr (See Fig. 1.7). Apart from the correlation, there is a ± 1.5 order of magnitude spread in accretion rates at any given mass. Natta et al. (2006) found a similar trend for a sample of (0.03 - $3M_\odot$) in Ophiuchus, which has an age of about ($\gtrsim$0.5 Myr - 1 Myr). For this single region there is still a spread of $\sim$2 dex at least for any given mass.

Several explanations have been put forward to explain this scatter in accretion

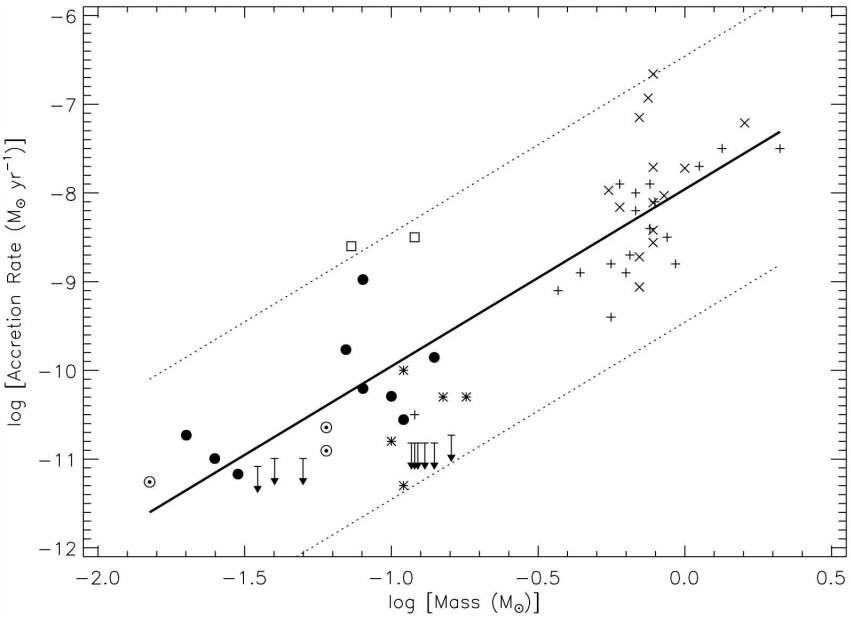

Figure 1.7: *Accretion rates versus stellar mass. Upper limits in measurements are given in downward pointing arrows. The fit to the data, $\dot{M}$ - M_*^2, is represented by the thick black line. The two dashed lines are the ± 1.5 dex offset to the fit and are over-plotted to represent the upper and lower envelopes of the trend. Accretion rates are compiled from a number of different sources, see Mohanty et al. (2005) for details.*

rates at a given mass such as environmental or initial conditions (Dullemond et al. 2006) or uncertainties in the determinations of stellar parameters such as radius and mass (Antoniucci et al. 2011). It has also been put forward that this relation is simply an attribute of limited sample sizes and detectability (Barentsen et al. 2011; Clarke & Pringle 2006). (See Chapt. 3 for further discussion). One of the most promising ways to explain the scatter in this relation is through accretion variability. If the majority of the accreting population regularly go through accretion variations of $\sim$ 1 - 2 dex then the correlation holds. However, if the variations are smaller than the spread in the correlation, it is likely that the accretion rate is not directly related to the stellar mass, but it is an indirect correlation due to some other ongoing process.

1.9 Variability as a Tool

There has been a limited number of spectroscopic studies in larger samples of T Tauri stars (See Fig. 1.8). These studies are vital if we expect to determine the characteristic magnitudes of accretion variations in typical accreting objects.

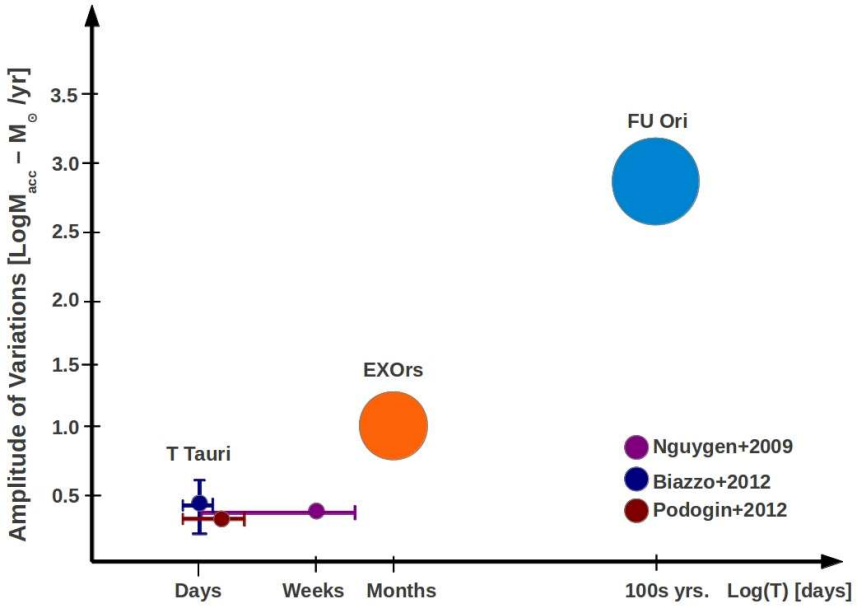

Figure 1.8: *Amplitudes of accretion rate variations versus the time-scales over which they occur. Average numbers are taken in the case of EXors and FU Ori objects. Error bars here indicate the spread in accretion rates, and time coverage in each bin. (Biazzo et al. 2012; Nguyen et al. 2009b; Pogodin et al. 2012)*

Nguyen et al. (2009b) monitored a sample of YSOs over time-scales of days, weeks and months and found that the variability in accretion rates of a sample of YSOs is dominated by variations on time-scales. The amplitudes of variations found to be much lower than the spread in the $\dot{M}$-M_* relation. A small number of observations were taken over a period 48 hours of 29 accreting objects in Chamaeleon II, from which Biazzo et al. (2012) found an similar accretion rate spread of 0.2 - 0.4 dex. These works suggest that typical accretion variability on the time-scales of weeks is not enough to explain the spread in the $\dot{M}$-M_* relation, but longer term variations could play a role. To derive conclusive results a wider range of time-scales needs to be probed.

To understand where the origins of the variations lie, a unbiased sample needs to be studied over all time-scales. Published results are often difficult to compare as accretion rates and variations are derived using different methods and different emission lines. The goal of this thesis is to encompass as many sources as possible while performing the same observations and analysis throughout. Only by doing this can the dominant time-scales and magnitudes of variations be identified in typical accreting systems. This will further allow for a better understanding of the dependencies of the accretion process. These results can also provide

constraints for the dominant processes at work in the disc, which is important for disc evolution and planet formation. Also the stability and geometry of the magnetic field can be probed through variability monitoring.

This aim of this thesis is to address this issue of accretion variability in an unbiased sample, in order to probe the inner workings of typical accreting systems. It is laid out as follows: The observations, instruments used and the reduction methods are described in Chapt. 2. Two spectroscopic monitoring studies covering complementary time-scales of accreting targets are presented in Chapt. 3 and 4. Finally a photometric monitoring campaign is described in Chapt. 5 before the summary in Chapt. 6.

2 Methods

2.1 About this Chapter

To address the issue of accretion variability the two most important requirements were to spectroscopically monitor accreting targets in order to accurately follow the accretion variations over time, and identify the rotation periods of the accretors - an important time-scale in the inner regions of these systems. To complete these two targets high resolution spectroscopy is needed, for which FLAMES (Fibre Large Array Multi Element Spectrograph) on the VLT (Very Large Telescope) and ISIS (Intermediate dispersion Spectrograph and Imaging System) on the WHT (William Herschel Telescope) were used. A photometric monitoring campaign was also undertaken with WFI (Wide Field Imager) on the 2.2 m at La Silla Observatory. Another important aspect of these studies was to get as large a sample as possible. For this reason we began our studies with the multi-object spectrograph FLAMES, and completed them with the large field of view of WFI.

The data is based on targets from the Chamaeleon I region, the Taurus-Auriga association and the Orion complex. The first part of the chapter will be dedicated to the description of these regions, the data sets, and the timing of the observations. The second part of the chapter introduces the instruments and

telescopes used to obtain these data sets and the reduction methods.

2.2 Chamaeleon I

The Chamaeleon I sample forms the core of this thesis, and in the following section the region is briefly introduced and the spectroscopic and photometric observations are presented.

Chamaeleon is a relatively close star forming region (d $\sim$ 160 - 170 pc, Bertout et al. 1999; Whittet et al. 1997) that is split into three main clouds Cha I, Cha II and Cha III. All three clouds are relatively compact with an angular size of a few degrees and masses and stellar densities that are low compared to other star forming regions. At a high galactic latitude, it is an isolated region which makes it attractive for star formation studies as contamination of the membership is limited. The mean age of the region is $\sim$2Myr, and it holds members of every evolutionary stage from embedded Class 0 protostars to main sequence stars.

The first members of the cloud where found through Hα objective prism surveys (e.g. Henize 1963). Since then deep X-ray surveys have been carried out with a number of telescopes ROSAT, XMM-Newton and Chandra (Feigelson & Lawson 2004). The modest extinction in Chamaeleon (A_v <5) means many of the optical and NIR surveys have been successful in identifying members (e.g. Luhman 2007; Spezzi et al. 2007). For the identification of the youngest, most embedded and for the lowest mass stars in the region mid- and far-IR surveys are necessary. The region has been mapped with IRAS, ISO and Spitzer resulting in a near complete survey of the disc bearing members (Baud et al. 1984; Persi et al. 1999; Young et al. 2005).

Most of the star formation is concentrated in Cha I, which has 237 confirmed members (Luhman 2008), as opposed to 50 members in Cha II. The initial mass function (IMF) of the Cha I region peaks at 0.1 - 0.15 $M_\odot$, and 33 members are likely brown dwarfs with spectral types >M6.

The Cha I cloud is further split into a northern (δ >-77°) and southern cluster (δ <-77°) that have mean ages of 3 - 4 Myr and 5 - 6 Myr respectively. The spectroscopic study used in this work was centred on the highest density of stars which lies in the southern part of the Cha I cloud.

Figure 2.1: *Composite image of the Chamaeleon I region obtained with FORS1 at VLT (11'.2 x 6'.8). The image is made using V, I and R photometry. Image has been rotated so that east is up, and north is right. Credit: ESO.*

2.2.1 Spectroscopy in Cha I

The spectroscopic observations of Chamaeleon were carried out using the multi-object fibre spectrograph FLAMES/GIRAFFE at the ESO/VLT under the ESO programmes 082.C-0005(A) and 084.C-0094(A) (See Section 2.5.3 for instrument description).

Targets were chosen from the census by Luhman (2007). For the fibre positioning the UCAC catalogue (Zacharias et al. 2004) coordinates were used when available, however for the faintest targets (spectral type later than $\sim$ M4) the less accurate 2MASS coordinates were used as these are not covered by the UCAC catalogue.

There are 130 fibres on the FLAMES/GIRAFFE spectrograph. In the preparation of the observations, and the configuration of the fibres, priority was given to objects with a) evidence for accretion from emission lines and b) evidence for a circumstellar disc from mid-IR excess (e.g. Class II objects). No other selection criteria were used. A single field was observed with a central pointing of α $11^h08^m20.0^s$, δ -77^{o}36$'$10$''$ (J2000).

The final sample of targets contained 50 objects, however twenty five of these objects were dropped from the analysis because no measurable stellar continuum was observed above the sky background emission. A brief description of the 25 targets are given in Table. 2.1. The spectral type distribution for the objects

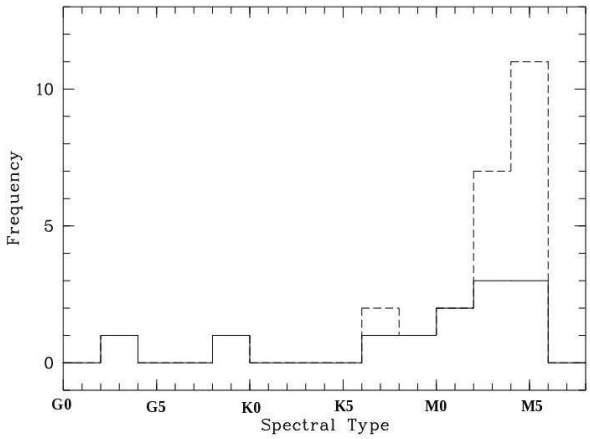

Figure 2.2: *Histogram of spectral type distribution within Chamaeleon I spectroscopic sample. The dashed line indicates all objects and the solid line indicates the objects with discs.*

with and without discs in this sample is shown in Fig. 2.2. The remaining working fibres (35 for the first run and 58 for the second) were placed on the sky.

We observed this sample 6 times in each of the two campaigns. The observations cover the time span from January 2009 to March 2009 and from December 2009 to April 2010. The minimum separation between consecutive observations is $\sim$ 1 week. The exact dates of the observations are given in Table 2.2. These observations were performed using two grisms, HR15 (6470 - 6790 Å) and HR21 (8480 - 9000 Å) which cover the Hα emission line and the Ca II infra-red triplet respectively.

Please note that the proposal and preparation of these observations should not be considered part of the thesis work as they were completed by others.

2.2.2 Photometry in Cha I

The photometric monitoring of the Chamaeleon region was performed using the WFI on the MPG-ESO 2.2 m telescope. The central pointing of the telescope was roughly the same as our FLAMES pointing (α $11^h07^m08.7^s$, δ -$77^o37'13.3''$) so all targets in the spectroscopic sample are within the field of view of WFI. (See Section 2.4 for details on instrument and telescope).

The photometric observations took place over seven nights in April 2012, from the 18^{th} to the 25^{th}. Due to poor weather during the observation run, the awarded 11 half nights of monitoring were not completed. The two filters used in this analysis were R_c/162 with a central wavelength of 6517.25 Å, and Ic/lwp with a central wavelength of 7838.5 Å. Exposure times of 10 s were used for both

Object	Spectral Type	SED Class	α [hh:mm:ss]	δ [° ' "]
CHXR28	K6	III	11:07:55.8	-77:27:25.5
CHXR20	K6	II	11:06:45.1	-77:27:02.3
T22	M3	III	11:06:43.5	-77:26:34.5
ISO143	M5	II	11:08:22.4	-77:30:27.7
T33A	G7	II	11:08:15.2	-77:33:53.1
T39A	M2	III	11:09:11.6	-77:29:12.7
ChaHα2	M5.25	II	11:07:42.5	-77:33:59.3
B43	M3.25	II	11:09:47.4	-77:26:29.0
T45	M1.25	II	11:09:58.7	-77:37:09.0
ChaHα6	M5.75	II	11:08:39.5	-77:34:16.6
ISO126	M1.25	II	11:08:2.97	-77:38:42.5
ChaHα8	M5.75	III	11:07:46.1	-77:40:08.9
ChaHα5	M5.5	III	11:08:24.1	-77:41:47.3
ESOHa566	M5.75	III	11:09:45.2	-77:40:33.2
T30	M2.5	II	11:07:58.1	-77:42:41.3
T34	M3.75	III	11:08:16.5	-77:44:37.2
ChaHα3	M5.5	III	11:07:52.3	-77:36:56.9
T26	G2	II	11:07:20.7	-77:38:07.3
ESOHa560	M4.5	III	11:07:38.3	-77:47:16.8
LM04 429	M5.75	III	11:07:24.4	-77:43:48.9
CHXR22E	M3.5	II	11:07:13.3	-77:43:49.8
CHXR21	M3	III	11:07:11.5	-77:46:39.4
T31	K8	II	11:08:01.5	-77:42:28.8
CHXR76	M4.25	III	11:07:35.2	-77:34:49.3
CHXR74	M4.25	III	11:06:57.3	-77:42:10.6

Table 2.1: *Data on Chamaeleon sample observed spectroscopically. Spectral types from Luhman (2007), SED classes from Luhman et al. (2008). Coordinates are for epoch J2000.*

Obs. Period 1 Obs. Date	Time UTC	Obs. Period 2 Obs. Date	Time UTC	Grism
04-Jan-2009	05:10	09-Dec-2009	07:06	HR21
04-Jan-2009	05:26	09-Dec-2009	07:21	HR15
16-Jan-2009	04:35	03-Jan-2010	06:30	HR21
16-Jan-2009	04:51	03-Jan-2010	06:46	HR15
03-Feb-2009	04:40	15-Jan-2010	07:26	HR21
03-Feb-2009	04:56	15-Jan-2010	07:42	HR15
11-Feb-2009	05:30	27-Jan-2010	04:11	HR21
11-Feb-2009	05:46	27-Jan-2010	04:26	HR15
19-Feb-2009	05:38	10-Feb-2010	06:30	HR21
19-Feb-2009	05:54	10-Feb-2010	06:45	HR15
01-Mar-2009	02:42	07-Mar-2010	06:20	HR21
01-Mar-2009	02:59	07-Mar-2010	06:36	HR15

Table 2.2: *Observing log of spectroscopic observations of Chamaeleon I region. These observations were taken using the FLAMES/GIRAFFE instrument.*

filters. Priority was given to the I band over the course of the observations to ensure that an extensive light curve could be achieved in at least one band. Details of the timing and filters used are given in Table 2.3.

2.3 Taurus-Auriga and Orion

The second sample of stars used in this thesis is not as uniform as that in the Chamaeleon I region. Most of the sample lie in the Taurus-Auriga region, while three objects are from the Orion complex. The following is a short description of both regions and the observations.

The parental molecular cloud of Taurus-Auriga is highly structured. Spread over 30 pc and with a mass of $3 \times 10^4\,M_\odot$ (Ungerechts & Thaddeus 1987), most of the star formation in the region follows the filaments in this cloud. Kenyon et al. (2008) report the young stellar and brown dwarf population of this region to be ~ 380. At a distance of 140 - 145 pc it is the closest region with ongoing star formation of both massive and low mass stars.

The Orion complex is the nearest giant molecular cloud, hosting everything from massive O stars ($\sim 40\,M_\odot$) to the low mass end beyond the hydrogen burning limit ($\sim 0.08\,M_\odot$). Orion's high galactic latitude means there is limited foreground confusion, and large extinction in the clouds limits the background confusion. This makes it a very attractive region to study star formation at all ages, and across a very wide mass range. The full membership of Orion is not yet known, it is likely that 5,000 - 20,000 stars have formed in the region in the

Date	Time	Filter	Date	Time	Filter	Date	Time	Filter
18	02:53:54	I	21	00:22:52	I	22	00:22:24	I
19	00:34:26	I	21	00:34:54	R	22	00:34:37	R
19	00:55:16	R	21	00:49:14	I	22	00:46:59	I
19	01:09:07	I	21	01:12:24	I	22	01:05:53	I
19	01:34:22	I	21	01:25:22	I	22	01:21:31	I
20	00:14:42	I	21	01:37:18	I	22	01:33:45	R
20	01:04:48	I	21	01:50:32	R	22	01:46:04	I
20	01:22:15	R	21	02:03:37	I	22	02:09:19	I
20	01:36:27	I	21	02:31:33	I	22	02:36:02	I
20	01:56:17	I	21	03:25:52	I	22	02:59:28	I
20	02:08:05	I	21	03:37:52	R	22	03:14:48	I
20	02:20:07	R	21	03:57:16	I	22	03:29:17	R
20	02:32:23	I				23	03:54:27	I
20	02:50:20	I				24	03:57:15	R
20	03:01:24	I				25	00:47:46	I
20	03:19:48	R				25	01:47:42	I
20	03:31:53	I						
20	03:55:43	I						

Table 2.3: *Observing log of photometric observations in Chamaeleon I taken with the WFI instrument on the ESO-MPG 2.2 m at La Silla. All observations took place in April 2012. The time is given in UTC. Exposure times of I band and R band images were 10 seconds.*

last 15 Myr (Bally 2008). The whole Orion complex lies at about $\sim$ 400 pc, and is comprised of many different regions that formed at different ages.

One of the targets, BF Ori, is in the southern part of the Orion complex, in the Lynds 1541 molecular cloud which makes up the bulk of Cloud A. It lies at a distance of about 400 pc, with an age of $\sim$ 1 - 2 Myr.

Both CO Ori and GW Ori lie in the λ-Ori at a distance of 440 ± 40 pc (Murdin & Penston 1977). This region is centred on the star λ-Ori and is surrounded by a ring of gas and dust. The low mass population is spread over about 16 pc radius from λ-Ori. Star formation began in this region $\sim$ 6 - 8 Myrs ago and has been continuing since (Mathieu 2008).

Our targets were originally observed for a linear spectro-polarimetry study (Vink et al. 2005) to probe the circumstellar structures around Herbig Ae/Be and T Tauri stars. The sample was chosen from Herbig & Bell (1988), based on their relative brightness ($V \lesssim 11$), and their position on the sky, but not on any known circumstellar geometries, or T Tauri/Herbig Ae type. A general overview of the targets is given in Table 2.4. Individual targets will be discussed in more detail in Chapt. 4 and Appendix A. The observations where taken in 2001 and 2003, and for the most part take the form of $\sim$ hour block observations of a single target. This provided very dense sampling with only minutes separating spectra. The majority of the targets were observed more than once, and half the sample was observed in both 2001 and 2003. See Table 2.3 for more details on the break down of the observations.

The following sections introduce the instruments and telescopes used to obtain the above described data, as well as the reduction steps performed on each of the data sets.

2.4 Photometry with WFI

Monitoring of a star forming region with high cadence needs an instrument with a large field of view and one that is sensitive enough to allow for short exposures. The Wide Field Imager (WFI) on the ESO-MPG 2.2 m fulfils these requirements, and provided the monitoring needed in Chamaeleon to derive rotation rates. In this section the instrument and telescope are first described, followed by an introduction to CCDs and CCD reduction and finally the specific reduction steps

Name	Mag.	SpT	Ref.	Type	Date	Exposures	Total [hrs]
RY Tau	10.1	K1	3	CTTS	26-12-01	4x120,12x180	4.0
					10-12-03	8x120, 20x240	
					12-12-03	8x90, 12x180	
					13-12-03	8x120, 12x180	
AB Aur	7.1	A0	3		27-12-01	20x30,16x30,16x30	1.83
					10-12-03	12x90	
					11-12-03	20x60	
					12-12-03	20x60	
					13-12-03	4x120,12x90	
T Tau	10.3	K1	3	CTTS	12-12-01	8x45,16x120	1.37
					12-12-03	4x60, 18x150	
SU Aur	9.0	G2	3	SU AUR	27-12-01	12x180	2.30
					10-12-03	8x90,16x150	
					11-12-03	4x90,5x240	
					13-12-03	12x120	
DR Tau	11.43	K5	2,1	CTTS	27-12-01	16x180	1.87
					12-12-03	4x60,20x180	
RW Aur A	10.36	K1	2,7	CTTS	26-12-01	11x180	1.40
					10-12-03	12x150	
					13-12-03	4x60,20x150	
GW Ori	11.1	G5	3	CTTS	11-12-03	4x60,20x240	1.40
V773 Tau	10.35	K2	4	CTTS	13-12-03	4x60,16x240	1.13
UX Tau A	11.3	K2	3	WTTS	13-12-03	1x120,24x240	1.63
BP Tau	12.1	K7	3	CTTS	12-12-03	4x90	2.13
					13-12-03	4x30,24x300	
BF Ori	12.2	A0	3	HAe	27-12-01	16x180	0.80
LKha 215	10.8	B1	3	HAe	12-12-01	16x120	0.53
MWC 480	7.6	A3	5	HAe	26-12-01	16x75,16x30	1.03
					27-12-01	16x45,8x45,16x60	
CO Ori	9.83	F8	6	SU AUR	27-12-01	8x120,8x180	
					24-12-01	8x12,8x180	1.09

Table 2.4: *Target list and observing log for spectroscopic observations in Taurus-Auriga and Orion. Magnitudes are given in the V-band. The T Tauri type is taken from Herbig & Bell (1988), where a SU Aur type is given as 'A star like SU Aur: type late F to K, weak emission at H-alpha and Ca II, very broad absorption lines (v sin i >50 km/s), and relatively high luminosity'. Exposures are given as number of exposures times the exposure time in seconds. References: 1: Mora et al. (2001), 2: Høg et al. (2000), 3: Cohen & Kuhi (1979), 4: Rydgren et al. (1976), 5: Jaschek et al. (1988), 6: Herbig & Bell (1988), 7: Basri & Bertout (1989).*

Figure 2.3: *Image of the ESO-MPG 2.2 m telescope (silver dome in foreground) at La Silla Observatory, Chile.*

taken with the WFI Chamaeleon data set are presented.

The ESO-MPG 2.2 m telescope was built by the Max Planck Gesellschaft, and has been in operation at La Silla observatory since 1984. The optical design of the telescope is Ritchey-Chretien, with a 2200 mm free aperture and a Cassegrain focus. WFI is mounted permanently on the Cassegrain focus, and has a field of view of 34' x 34'. WFI contains a f/5.90 focal reducer by way of two triplets of lenses to flatten and reduce the intrinsic telescope scale from 0.0351" per 15μm pixel to 0.238"/pix. The instrument contains a large roughly semi circular rotating shutter, that allows exposures of less than 2 seconds. It also contains a filter wheel that can hold up to 46 filters, allowing WFI to cover wavelength ranges from 350 nm- near-IR.

The detector is comprised of 4 x 2 mosaic of 2k x 4k CCDs (see Section 2.4.1 for further explanation of CCD technology). On the eastern side of the detector in the same plane lies the tracker chip. Both filters used in the science observations were circular in shape and cover both the science mosaic and the tracker chip. The two filters were R_c/162 with a central wavelength of 6517.25 Å, and Ic/lwp with a central wavelength of 7838.5 Å. The gaps between each chip in the mosaic are of 98$\pm$2 pixels on the long side and 30 $\pm$ 2 on the short side of each chip. The surface of each chip is confined to two planes within 80 μm from each other, where the mean plane is aligned with the focus.

2.4.1 Introduction to CCDs

CCD or charge-coupled device is the modern detector used in optical astronomy. CCDs are made up of arrays of capacitors. These capacitors are mainly made

of silicon, which has a band gap energy of 1.41 eV. When the CCD is exposed, photons that strike the CCD are easily absorbed if they are at the right energy, i.e. from 1.1 to 4 eV (11,000 to 3,000 Å). As the silicon absorbs a photon, it is forced to give up a valence electron and move it into the conduction band. Here the free electrons are trapped by an applied voltage called a gate. A typical CCD will have three gates per pixel. At the end of the exposure, the voltages of the three gates in a pixel are manipulated so that all of the electrons are in the deepest potential well. Then the voltages across all the pixels are cycled through so that one by one the charge moves from one pixel to the next. There remains one unexposed column at the end, in which the charges collect. From here each charge that has collected in each pixel is amplified by an output amplifier and converted to a digital number. These digital numbers are often referred to as ADUs (analogue-to-digital units). The number of electrons per ADU is called the gain of the device.

If too many electrons are gathered in one pixel, it can lead to an overflow of charge into neighbouring pixels. This is often called blooming, and can lead to bleeding of charge in both directions along the row away from the overexposed pixel. This can be countered by exposing for a shorter amount of time or by the use of anti-blooming CCDs.

The dark current of a CCD is a result of thermally excited photons within the CCD. At high enough temperatures (room temperatures) electrons can be freed from the valence band and collect along with the science electrons. This problem is tackled by cooling the CCD with, for instance, liquid nitrogen. It is also important to keep the CCD at a stable temperature as the dark current is highly temperature dependent.

Due to noise in the electronics, an unexposed pixel will have a distribution of readings around zero. In order to avoid negative numbers, and avoid reducing the dynamical range of the CCD, a positive bias is applied to the CCD. This zero level and it's uncertainty can be estimated using a bias frame, which is simply an unexposed image of the CCD, which consists of the bias level of photons only.

2.4.1.1 Basics of CCD reduction

Before any readout from the CCD can be used for science, a few steps need to be taken into account to address some of the issues mentioned above.

The first thing that is done to the science frames, is to subtract the zero level offset, i.e. the bias frame. The quantum efficiency differs from pixel to pixel, so in order to get a uniform response across the CCD a flat field needs to be

taken. This is normally achieved with the use of an illuminated screen on the inside of the telescope dome. This screen is brighter than the science image, and so produces a calibration frame that has a high signal-noise ratio. The early evening sky is also often used in place of an illuminated screen as it provides a more uniform image. Flat field images need to be produced for every filter used. The bias image is first extracted from the flat field image and then the flat field image is divided into the biased science images.

A dark frame can be obtained to estimate the dark current, by 'exposing' the CCD with the shutter closed. The exposure time in this case should be approximately the same as for the science frames. In most cases the dark current does not need to be considered, if the CCD is cooled. However if the dark is non-negligible it should be used in place of the bias.

No CCD is perfect, and all contain some dead pixels or hot pixels. Before carrying out the WFI observations, the archive CCD images were checked for bad pixels. On finding that the eastern four CCDs had significantly less dead columns and pixels, the science targets were positioned primarily on these four CCDs.

2.4.2 Reduction of WFI Photometry

The basic reduction steps of the WFI data were performed using IRAF. All the steps below were followed for both the I and R band observations separately. Firstly the fits files are unpacked with *mscsplit*, as the mosaic is delivered as a single fits file. This also requires the header to be rewritten with the command *esohdr* (in the *esowfi* package). Then the standard bias frames and evening sky flats were used along with *zerocombine*, *flatcombine* and *imarith* to produce the science images.

The photometry was computed for the four eastern most chips using the IRAF package *daophot* taking the following steps:

- The first step was to choose an image in which to identify the targets. This image should not have the best seeing in the series, but the majority of stars should be visible i.e. not the worst night of weather. A list of targets is then compiled using *daofind*.

- This list was then manually cleaned for false detections due to bad pixels or cosmic rays.

- As the tracking of WFI is not perfect, there were some small offsets between

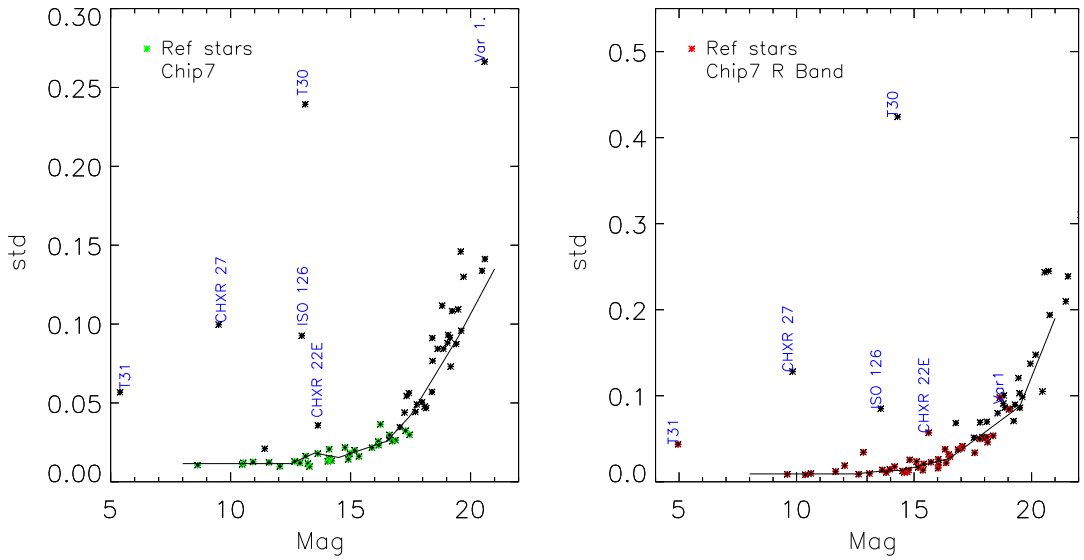

Figure 2.4: *Left: Standard deviation of magnitudes versus average magnitudes for all objects for which I-band photometry was extracted on chip 7 of WFI. Right: The same for the R-band photometry. In both cases the reference stars are marked in colour. The black line shows a mean standard deviation for each magnitude bin (excluding outliers).*

frames. The offsets were identified for half the chips using the eclipse script *jitter*, which was designed to be used for IR observations with ISACC and SOFI, and for half the chips manually. Two of the chips contained diffuse emission, allowing *jitter* to register the frames. The resulting offsets were then applied to each frame using *imshift*. For the other two chips with no diffuse emission, the target list was manually adjusted for each frame.

- Photometry was found using the *phot* function along with a range of apertures. The output files for each frame were then edited to select stellar IDs, coordinates and magnitudes.

- A suitable aperture size was selected by plotting the aperture sizes and the magnitudes measured in them. The aperture at which the magnitude turns over and stops rising was taken as the most suitable. This ensures that the aperture is large enough to contain all the flux while limiting the contribution from the background. The same aperture was then used for the analysis on all the chips.

To derive the relative photometry a script in IDL was written following the method of Scholz & Eislöffel (2004). In the following a 'frame' refers to an

Object	RA	DEC	SpT.	SED	LAMP
Chip1					
B43	11:09:47.4	-77:26:29.0	M3.25	II	✓
Chip2					
T33	11:08:15.2	-77:33:53.1	G7	II	✓
ChaHα2	11:07:42.5	-77:33:59.3	M5.25	II	✓
ChaHα6	11:08:39.5	-77:34:16.6	M5.75	II	✓
ISO 143	11:08:22.4	-77:30:27.7	M5	II	✓
ChaHα1	11:07:16.7	-77:35:53.3	M7.75	II	X
Chip7					
T31	11:08:01.5	-77:42:28.8	K8	II	✓
CHXR 27	11:07:43.7	-77:39:41.2	M0	II	X
ISO126	11:08:2.97	-77:38:42.5	M1.25	II	✓
T30	11:07:58.1	-77:42:41.3	M2.5	II	✓
CHXR 22E	11:07:13.3	-77:43:49.8	M3.5	II	✓
Chip8					
T45	11:09:58.7	-77:37:09.0	M1.25	II	✓

Table 2.5: *Variable targets found during photometric monitoring campaign in Chamaeleon I. Coordinates are for epoch J2000. Spectral types and SED classes are taken from Luhman (2007) and Luhman et al. (2008). The targets which were studied in the LAMP sample are indicated in the last column.*

observation frame. In total, the data set contains 35 I-band frames and 11 R-band frames. In most cases the numbers below refer to the I-band images.

- First this script identified a number of stars that were detected in the majority of frames (i.e. 34 out of 35 frames for I-band). This was done to make sure all targets were well sampled, and to remove any remaining false detections. The stars that are not well sampled were thrown out.

- The average magnitude ($\overline{m}_i$) was found for each star

$$\overline{m}_i = \frac{1}{N_F} \sum_{j=1}^{N_F} m_i(t_j) \tag{2.1}$$

  where $j = 1 - N_F$ is the frame number, and $i = 1 - N_*$ is the star number.

- The average magnitude of that star was then removed from its magnitude in each individual frame to give a normalised magnitude (m_i^o)

$$m_i^o(t_j) = m_i(t_j) - \overline{m}_i \tag{2.2}$$

- The mean magnitude and standard deviation of magnitudes in each frame

was calculated.

$$\overline{m}_i^o = \frac{1}{N_*}\sum_{i=1}^{N_*} m_i^o(t_j) \qquad \sigma_j = \sqrt{\frac{1}{N_*}\sum_{i=1}^{N_*}(m_i^o(t_j) - \overline{m}_j)^2} \tag{2.3}$$

- The frame with the highest standard deviation was rejected and the process repeated. This is done until the standard deviations of all frames are roughly the same.

- The next step was to find non-variable stars within the sample to use as reference stars, using only the 'good' frames that passed the above test. The difference between the normalised magnitude of a star and the average magnitude in that frame was found for each star. If this value was larger than the standard deviation in the frame, the star was considered to vary in that frame.

$$if\ |m_i^o(t_j) - \overline{m}_j^o| \geq \sigma_j\ \ then\ var_{ij} = 1 \tag{2.4}$$

  This was repeated for all frames and stars. Any star for which $var_i = \sum_{j=1}^{N_F} var_{ij}$ was greater than 2 was not considered to be a reference star. This left approximately 20 - 30 reference stars for each chip.

- For each frame the average magnitude of the reference stars was determined. (Including those frames rejected as being too variable above).

$$\overline{m}^{ref}(t_j) = \frac{1}{N_{ref}}\sum_{i=1}^{N_{ref}} m_i^{ref}(t_j) \tag{2.5}$$

- This average frame magnitude of the reference stars was then removed from the magnitude of each star in that frame.

$$m^{rel}(t_j) = m(t_j) - \overline{m}^{ref}(t_j) \tag{2.6}$$

- Finally the frame with the lowest standard deviation was chosen as the reference offset for the magnitudes. The magnitude of each star in this frame was added to the relative magnitudes calculated above.

$$m^{final}(t_j) = m^{rel}(t_j) + m(t_{offset}) \tag{2.7}$$

The standard deviation of the resulting magnitudes versus the average magnitude for all stars on chip 7 of the WFI mosaic are shown in Fig. 2.4. These plots show that the mean standard deviation within the sample is small (0.015 for I-band and 0.012 for R-band in Chip 7). As we do not expect the majority of stars to show variations, the mean standard deviation is reflectant of the errors in the derived photometry. However there are variable stars which have large standard deviation (See Table 2.5 for lists). For these stars we investigate their light curves further and attempt to find periods in each of them (See Chapt. 5 for more).

2.5 Spectroscopy

In order to get accurate measurements of the changes in the emission line profiles associated with accretion, high resolution spectroscopy is needed. Spectroscopic observations in Chamaeleon, Taurus-Auriga and Orion were taken using two different instruments, ISIS on the William Herschel Telescope and FLAMES on the ESO-VLT. Here a brief general description of spectrographs is given, followed by a more detailed description of ISIS and FLAMES and the reduction steps taken on each data set.

Spectrographs are designed to split light into wavelength bins the size of which are dependent on the instrument and the instrumental set-up. Most spectrographs begin with a slit entrance, which is used to focus the light entering from the telescope, to reduce the amount of stray light entering and to set the spectral resolution. The thinner the entrance slit is the higher the spectral resolution will be i.e. the narrower the wavelength bins. However a narrower entrance slit also results in less counts per wavelength bin, so if the observing target is dim this needs to be taken into consideration. After passing through the slit, the light is dispersed by a grating, a prism or a combination of the two (a grism). Further optics are then necessary to focus the light on the CCD. It is considered preferable to align the emergent spectra with either the columns or rows of the CDD. Within the spectrograph there is also a light source to provide flat fields and wavelength calibration.

The first steps of CCD reduction for spectroscopy take the same form as those discussed above i.e. bias, flat field and darks (see Sect 2.4.1). These steps then produce an image of the 1-dimensional spectrum on the surface of the CCD. This spectrum then needs to be extracted from the image. Due to flaws and imperfections in the optics of these spectrographs the light will not

fall perfectly on a single column of pixels in the CCD. The spectrum will have some curvature and spread which can be due to a number of reasons, optic imperfections, misalignment in the spectrograph or differential refraction of the spectral light by the atmosphere. This makes it necessary to sum the light across a number of pixels along the slit axis, and trace the the path of the light along the dispersion axis.

In slit spectroscopy, the sky background contribution to the resultant spectrum can also be estimated by measuring the counts either side of the traced path and subtracting the mean. This is not the case with fibre spectroscopy (see Sect. 2.5.4).

2.5.1 ISIS @ WHT

The Intermediate dispersion Spectrograph and Imaging System (ISIS) is mounted on the Cassegrain focus of the 4.2 m William Herschel Telescope on La Palma, Canary Islands.

ISIS comprises of two standard spectrographs built in a horizontal layout, where the upper arm is optimised to operate in the wavelength range 3000 - 6000 Å, and hence is called the blue arm. The lower red arm, is optimised to operate in the range 5000 - 10000 Å. A dichroic allows for observations in both arms simultaneously or individually.

The light from the entrance slit (4' slit length and 22" slit width) is fed, via a 45° mirror or prism in the optical path of the telescope, into the collimators in each of the spectrographs. Above these components lie the polarimetry optics which are composed of: a quarter wave plate which converts linearly polarised light to circular, a half wave plate which rotates the polarised light to a specific angle, a Savart plate which splits the light beam into two orthogonally polarised beams and a polaroid filter.

The CCD for the red arm, which was used for the observations in this thesis, has 4096 x 2048 pixels. ISIS has nine gratings in all, four for the red arm and five for the blue arm. In the case of these observations, a single grating was used R1200R, along with a slit width of 1.0 arcsec. This grating has a spectral range of 1000 Å centred on 6500 Å, with a spectral resolution of $\simeq 35\,\mathrm{kms}^{-1}$ around Hα. During the observations the rotating quarter-wave plate and a calcite block where in place, which split the light into two incoming beams.

2.5.2 ISIS Reduction

The standard reduction steps were taken to reduce the ISIS data using *IRAF* routines. To bias and flat field the images *zerocombine* and *imarith* where used. The *apall* routine was used to extract the spectra. In this case there were two apertures per image, as the incoming beam was split into two beams of oppositely polarized light. The windows for the sky estimation had to be carefully chosen, as the two resulting spectra lie very close on the CCD (∼10 pixels apart). To perform the wavelength calibration *identify* was used on the nearest (in time) arc spectrum to the science observations, and the wavelength solution was applied using *dispcor*. The two apertures were then separated using *scopy*. Before performing any science, the two extracted spectra were added, and the continuum normalised. The measurements, analysis and results from these spectra are given in Chapt. 5.

2.5.3 FLAMES @ VLT

The Very Large Telescope (VLT) is composed of four 8 m Unit Telescopes (UTs) that can be used separately or combined. The Fibre Large Array Multi Element Spectrograph (FLAMES) is a multi-object spectrograph mounted on the Nasmyth foscus of UT2.

FLAMES has a large a field of view (25 arcmin) and is composed of three main parts: a fibre positioner consisting of two plates, a medium-high resolution spectrograph GIRAFFE, and a link to the high resolution spectrograph UVES. The two spectrographs GIRAFFE and UVES are fibre fed and can used simultaneously. For the observations in this thesis GIRAFFE was used. It contains a 2k x 4k CCD with a scale of 0.19 arcsec/pixel. It can be used in three fibre modes: MEDUSA and two IFU modes called ARGUS and IFU. For this work the MEDUSA mode was used, allowing the observation of up to 130 objects simultaneously. GIRAFFE is a medium to high resolution spectrograph R = 7500 - 45000 and covers the entire visible range from 3700 - 9500 Å. It contains two grisms, high and medium resolution. Order sorting filters are used to select the relevant spectral range for the observations.

FLAMES has two fibre positioner plates, allowing observations with one while the fibres on the other plate are being positioned for the next observation. Each of these plates hosts 132 MEDUSA fibres, where each fibre has an aperture on the sky of 1.2 arcsecs. These fibres are then fed to one of two slit units, one for each plate. The slits are split into sub-slits of two types: 1) eight sub-slits hosting

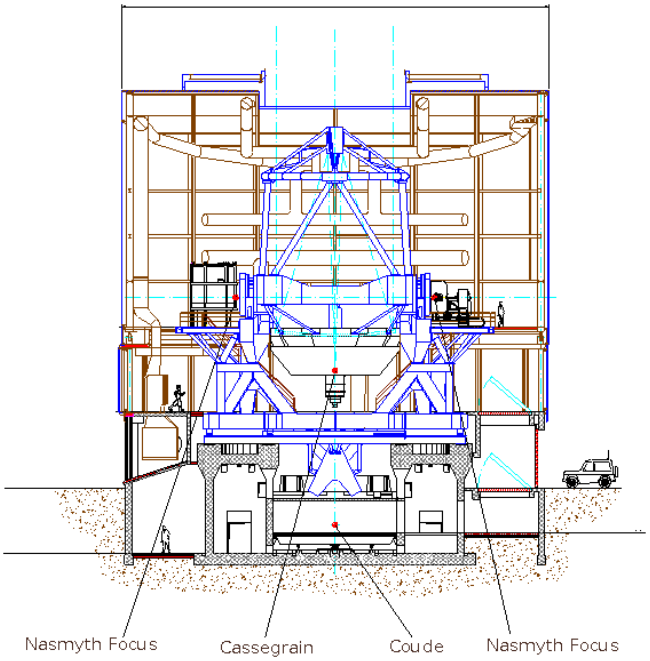

Figure 2.5: *Schematic of VLT unit telescope with Nasmyth and Cassegrain focus indicated. Credit: ESO*

9 fibres and 2) five sub-slits hosting 13 fibres, one of which is for simultaneous wavelength calibration. After this slit unit the light passes into GIRAFFE and through the order sorting filters to a collimator, dispersed by the grism (high or low) and through another collimator before landing on the CCD.

Two high-resolution GIRAFFE grisms were used in these observations, R15N and HR21, with a wavelength coverage of 6470 - 6790 Å and 8480 - 9000 Å respectively (See Table 2.2). These settings were selected because they cover the accretion-related emission lines Hα, He I, and the Ca infrared triplet. The nominal resolution for these grisms is in the range of $R \sim 16000$ - 17000. For each epoch and setting a long exposure (800 s for HR21 and 1000 s for HR15N) was obtained and in addition a short exposure (30 s) in case of saturation. As saturation was not an issue even for the brightest objects the short exposures were only used for consistency checks.

2.5.4 FLAMES reduction

The FLAMES analysis was based on the fully processed science frames as provided by the ESO-GIRAFFE pipeline ('SRBS' files). The pipeline reduction includes bias correction, extraction, flatfielding, transmission correction and wavelength calibration. The spectral response is not corrected, because no standard

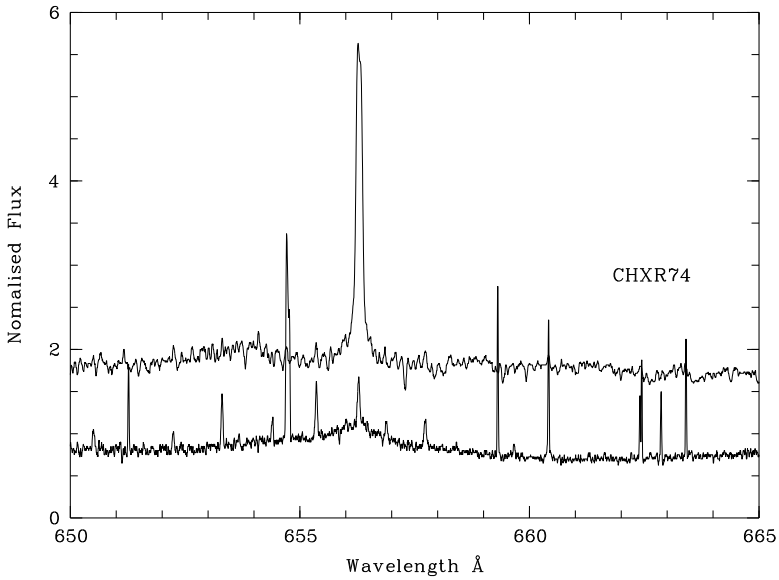

Figure 2.6: *FLAMES observations in Cha I. A spatially averaged spectrum of the sky background Hα emission, and a single epoch spectrum from a non-accretor in the sample, CHXR74, which is offset by 1 for clarity.*

stars were observed, i.e. absolute flux measurements are not feasible with this data set. In the standard pipeline reduction, sky subtraction and scattered light subtraction does not take place.

Spectra taken in molecular cloud regions are affected by emission line flux from the nebular background (e.g. Sicilia-Aguilar et al. 2005). For fibre spectrographs this can be problematic. The light collected in the fibre is a combination of both sky and target, and cannot be separated. So a measurement of the background close to the target is usually not feasible as it is for the slit spectrometers. To be able to assess the background contamination, a number of additional fibres were placed on empty sky across the field (35 and 58 sky fibres for the first and second observation periods). Fig. 2.6 shows an averaged spectrum from eight sky fibres, with a single epoch spectrum from an object in the sample, CHXR74. Here we see that the amount the sky emission contributes to the Hα flux is small (here CHXR74 has a Hα equivalent width ~ 8.6 Å).

Two different methods were used to remove the sky background continuum levels from the object spectra. For the majority of objects, a spatially averaged sky continuum value was derived for each epoch, and was removed from their spectra. To increase the spatial resolution and the reliability of our background subtraction, in addition to the sky fibres, 18 target spectra were used that showed no continuum emission above the sky background. This method was found to be insufficient for four objects' shorter wavelength spectra (6470 - 6790 Å), and so a

further step in the sky subtraction was taken. When a range of sky continuum values from across the field of view was removed from these objects, it was found that their Hα equivalent width (EW) measurements for a single epoch varied by 20 - 50 Å (which resulted in an order of magnitude change in the calculated accretion rate). For these four objects (ISO143, ChaHα2, ChaHα6 and B43) 3 - 4 nearest neighbour fibres were used to estimate the local sky background continuum. Again by varying this local sky continuum value within the range given by the neighbouring sky fibres, the EW measurements were found to stay stable for ISO143 and ChaHα6. However objects B43 and ChaHα2 still showed very large variations in EW. For these objects the EW measurements cannot be trusted, so in the following chapter only measurements based on the Hα line width are given.

A number of spectra were effected by cosmic rays. These were removed using a sigma-clipping script that was written in *MIDAS*. The cosmic rays appear in the spectra as large, sharp jumps in the counts. By removing any pixels that are 5-sigma above the average continuum around them the cosmic rays are cleaned from the spectra. These pixels are then set to zero so that they would not be included in any further analysis.

The three data sets discussed here, photometric monitoring from WFI and spectroscopy from ISIS and FLAMES together cover many different time-scales, from minutes, hours, days, weeks, months and years. They represent a powerful tool to probe the accretion in these young stellar objects. The following three chapters present the analysis and results from these data sets, and discuss the implications for the magnetospheric accretion model.

3

The **L**ong-term **A**ccretion **M**onitoring **P**rogram: LAMP

3.1 About this Chapter

The majority of accretion rate monitoring programs focus on individual targets known for their variability. There are very few unbiased studies. The LAMP project was designed to investigate the extent and characteristics of accretion-related variability in YSOs in an unbiased sample of objects, not chosen for their variability. In total 25 low-mass YSOs were observed in the Chamaeleon I star forming region (age $\sim$ 2 Myr) using the multi-object fibre spectrograph FLAMES at the ESO/VLT. For each target, 12 epochs were obtained, covering time-scales from $\sim$ 1 week to 15 months. The observations and reduction have been discussed in Chapt. 2. Rather than focusing on individually selected targets, the main goal was to constrain long-term accretion variability for *typical* YSOs. Three accretion-related emission lines (Hα 6563 Å, He I 6678 Å, Ca II 8662 Å) were used to investigate possible accretion within these systems. In this chapter the analysis of the data will be presented in Sect. 3.2. The origin of the Hα and Ca II emission and the derivation of the accretion rates from this emission are given in Sect. 3.4 and 3.5. The measurements of accretion rate variations and the

time-scales over which they occur are then presented and discussed in Sect. 3.7.

3.2 Emission Lines

The two high-resolution GIRAFFE grisms used in this data set (R15N and HR21) cover a narrow wavelength range of 6470 - 6790 Å and 8480 - 9000 Å respectively. The most prominent emission line within this wavelength range is the is Hα (6562.81 Å) and is present in almost all targets within sample. In addition, both the He I (6678.2 Å) and Ca II triplet emission lines (8498, 8542, 8662.1 Å) are covered and are present in the spectra of a few objects.

3.2.1 Hα emission

Fig. 3.1, 3.2 and 3.3 show average line profiles for a selection of objects in the sample. Based on the shape of the Hα profiles, the objects clearly fall in two groups. Ten of them show strong, broad Hα emission (see Fig. 3.1 and 3.2), often asymmetric and accompanied by absorption features. In this case 7 out of 10 show obvious absorption superimposed on the emission line, 5 have blue-shifted and 1 has red-shifted absorption. Most of the remaining 15 objects have weak, symmetric Hα emission as seen in the two upper panels of Fig. 3.3. A small subgroup of these objects, show broad wings in their Hα profiles (See lower panels of Fig. 3.3).

Under each average profile in Fig. 3.1, 3.2 and 3.3 the normalised variance profile is plotted in blue. This can be used to assess the variability as a function of wavelength. The variance at a certain wavelength is given by:

$$\sigma^2(\lambda) = \frac{1}{n-1}\sum_{i=1}^{n}(I_{\lambda,i} - \bar{I}_\lambda)^2 \tag{3.1}$$

where $I_{\lambda,i}$ is the flux at wavelength λ for spectrum number i, $\bar{I}_\lambda$ is the average flux at that wavelength and n is the total number of spectra for a given object (Johns & Basri 1995a). The normalised variance is then given by $\sigma_N^2(\lambda) = \sigma^2(\lambda)/\bar{I}_\lambda$.

The horizontal navy dashed line in these plots indicates the zero variability level, which is given by

$$\sigma_N^2(\lambda) = \sigma_{N,0}^2\left(\frac{\sqrt{\bar{I}_\lambda}}{\bar{I}_\lambda}\right)^2 \tag{3.2}$$

where $\sigma_{N,0}^2$ is the normalised variance in the continuum (Scholz & Jayawardhana 2006; Stelzer et al. 2007).

The variance profiles in Fig. 3.1 and 3.2 reveal that the variability is not uniform across the line profile. Seven of these objects show multiple peaks of enhanced variations. (Two objects B43 and ChaHα2 are shown without variance profiles, as they have weak continuum emission compared to the sky background emission).

In all spectra the Hα equivalent widths (EW) and 10% widths (10%w) were measured. The 10%w is simply the full width of the emission line at 10% of the peak height, and is measured in $\mathrm{km\,s^{-1}}$. The equivalent width of a line is given by

$$EW = \sum \frac{F_c - F_\lambda}{F_c} \Delta\lambda \tag{3.3}$$

where F_c is the continuum flux and F_λ is the monochromatic flux and the units of EW are Å. Three different integration window sizes were used, depending on the emission line width (25, 15 or 7.5 Å). The continuum was found by averaging measurements from two 10 Å windows either side of the integration window. To determine the 10%w of the Hα line, the same continuum was used to find the peak height above the continuum. Given in Table 3.1 are the average and the spread in EW and 10%w for all objects as well as the window sizes and an estimate of the measurement errors. A brief explanation of how the measurement errors where estimated is given in Sect. 3.3.

Due to the low signal to noise ratio in some spectra, a number of the 10%w measurements are considered to be upper limits. In these cases the Hα wings are not clearly distinguishable from the continuum due to the noise. This does not affect the EW measurements in the same way, as the full line is integrated over to calculate the EW. For the objects with more measurements than upper limits, the measurements only are taken in calculating the average 10%w given in Table 3.1.

As previously mentioned in Chapt. 2, when the sky subtraction was preformed for two objects (ChaHα2 and B43) it was found that they have no discernible continuum above the sky background. For this reason no EW values are given for these targets, and only 10%w measurements which are not affected by low continuum counts are quoted.

Plotted in Fig. 3.4 is the average 10%w against EW for all 23 well measured objects, one panel for each of the two observing periods. Over-plotted on these two panels is the often adopted cut off between CTTS and WTTS, an EW of 10 Å and a 10%w of $270\,\mathrm{km\,s^{-1}}$ (White & Basri 2003). Barrado y Navascués & Martín (2003) have introduced a more precise CTTS/WTTS division based

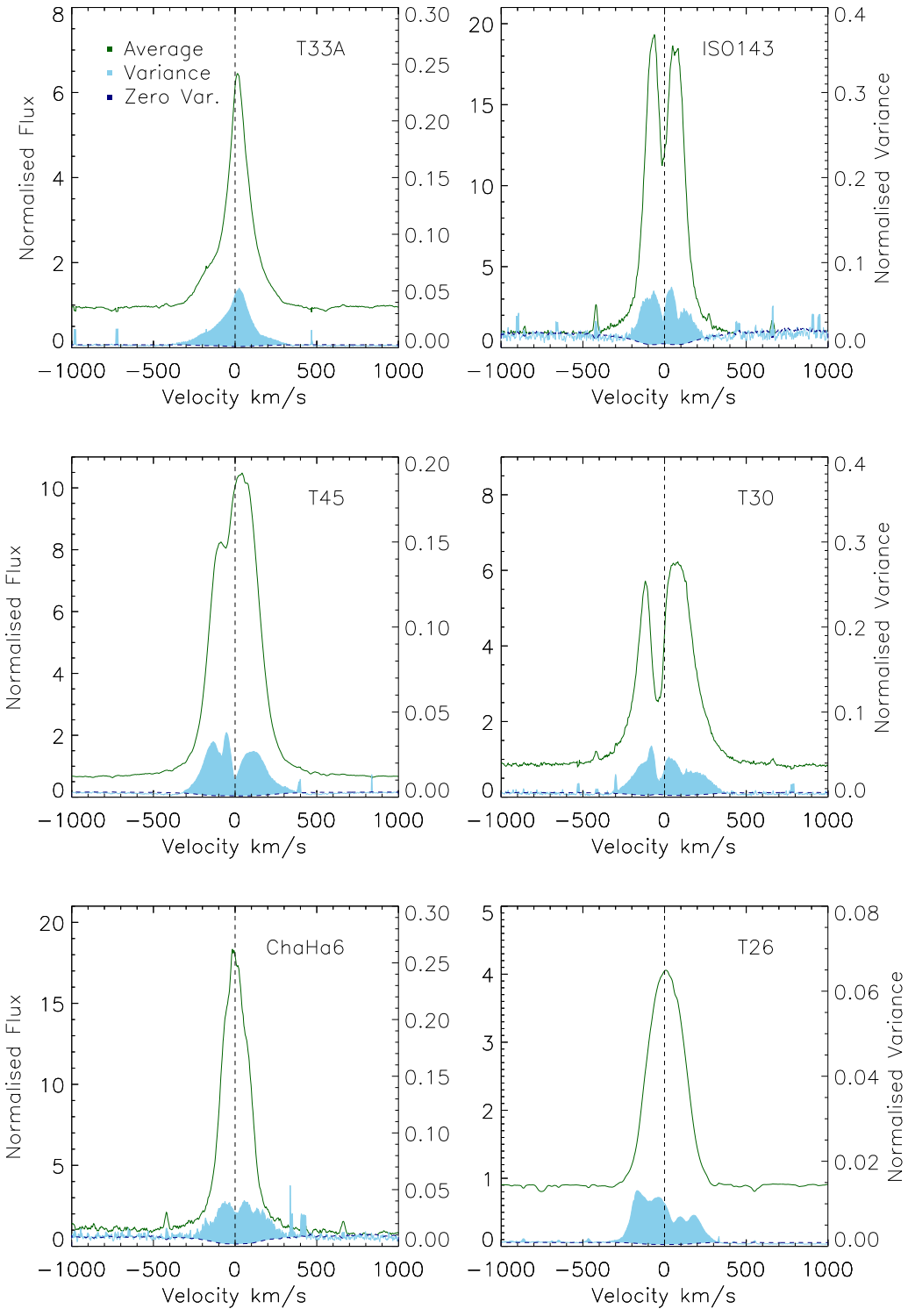

Figure 3.1: *Average profiles of Hα emission for 6 of the 10 objects with strongest Hα emission (see Sect. 3.2.1). The name of the object is given in each frame. Vertical lines mark the central wavelength for Hα emission (6562.81Å). The blue region in each plot shows the variance profile. The horizontal navy dashed line is the zero variability level. Only variations above this line can be considered significant, these are shaded in blue.*

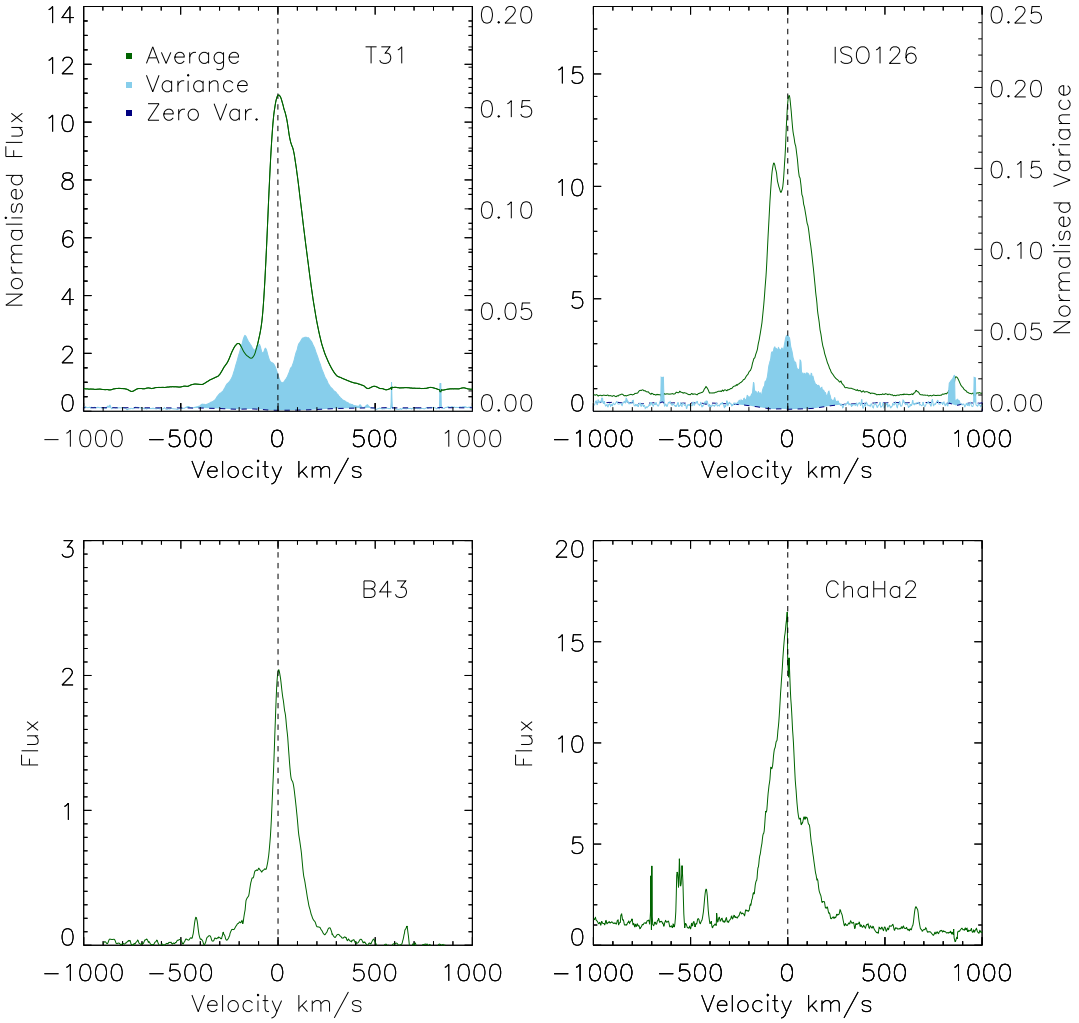

Figure 3.2: *Same as Fig. 3.1. Average profiles of Hα emission feature for the remaining 4 of the 10 objects with strongest Hα emission. B43 and ChaHα2 are shown without variance profiles, as their continua were not measurable.*

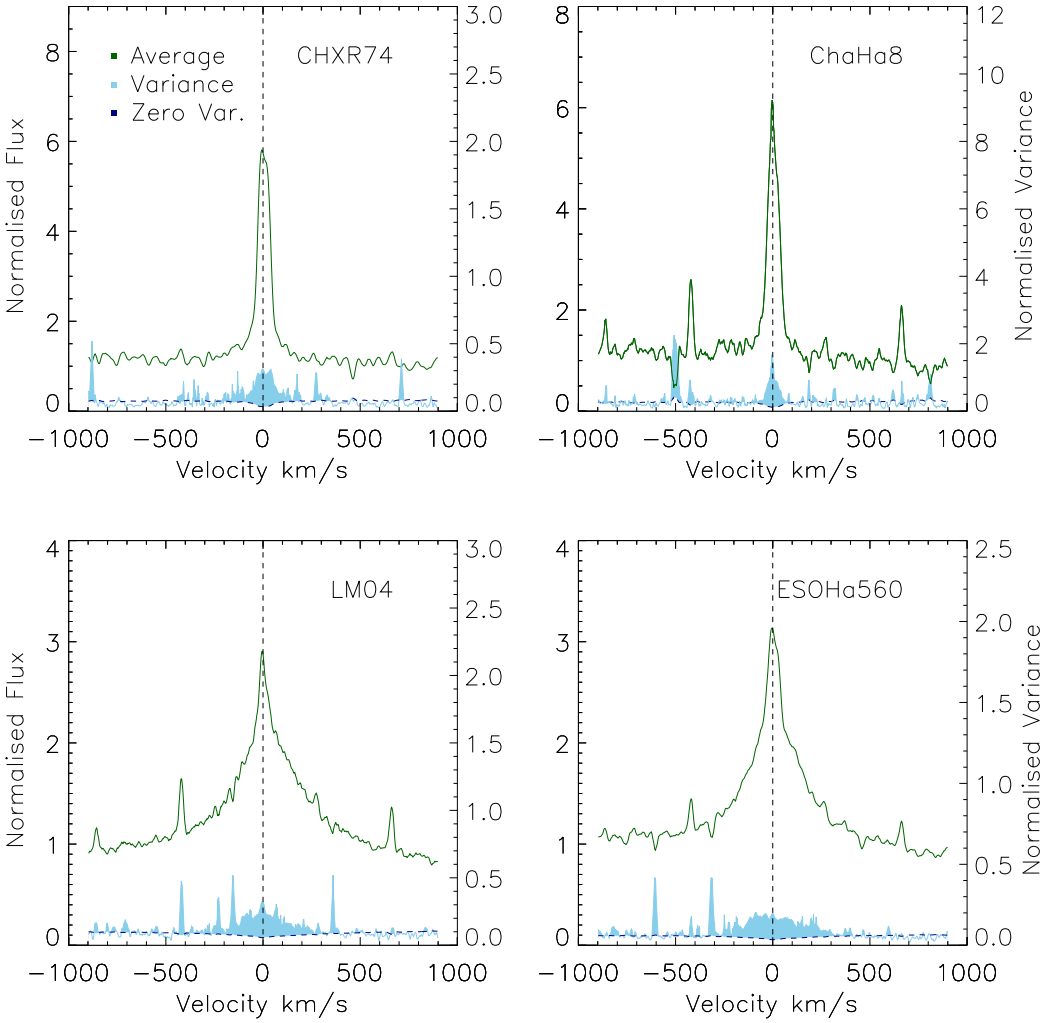

Figure 3.3: *Same as Fig. 3.1. Top Panels: Average Hα profiles for two objects classified as non-accretors. Bottom panels: Average Hα profiles for two objects with weak emission but broad profiles. These are also classified as non-accretors.*

Object	SpT	SED	EW Å	ΔEW	Er.	10% $km\,s^{-1}$	Δ10%	Er.	Win (Å)
CHXR28	K6	III	0.6	0.8	(0.1)	<194	-	(36)	7.5
CHXR20	K6	II	0.3 *	0.7	(0.1)	<255	-	(24)	7.5
T22	M3	III	3.0	1.3	(0.1)	419*	384	(29)	15
ISO143	M5	II	138.2*	172.2	(13.6)	395	66	(5)	25
T33A	G7	II	25.9	19.7	(0.4)	433 *	158	(1)	15
T39A	M2	III	5.3	4.2	(0.1)	197	86	(3)	15
ChaHα2	M5.25	II	-	-	-	349	74	(6)	25
B43	M3.25	II	-	-	-	398 *	68	(5)	25
T45	M1.25	II	104.4	64.8	(1.3)	506	69	(1)	25
ChaHα6	M5.75	II	81.7	55.7	(3.8)	350	118	(6)	25
ISO126	M1.25	II	79.9	72.1	(4.0)	386	68	(1)	25
ChaHα8	M5.75	III	6.7	9.1	(1.3)	170*	108	(24)	15
ChaHα5	M5.5	III	7.3*	4.5	(1.4)	168*	116	(12)	15
ESOHa566	M5.75	III	7.5*	3.1	(1.6)	158*	75	(3)	15
T30	M2.5	II	59.0	53.9	(2.2)	561	213	(1)	25
T34	M3.75	III	3.0	2.6	(0.2)	194*	78	(11)	15
ChaHα3	M5.5	III	6.9	10.6	(0.5)	222*	146	(12)	15
T26	G2	II	20.7	7.6	(0.2)	430	90	(1)	25
ESOHa560	M4.5	III	10.2	8.0	(0.7)	526*	179	(7)	15
LM04 429	M5.75	III	11.7*	11.2	(1.6)	<618	-	(23)	25
CHXR22E	M3.5	II	9.5*	8.1	(0.7)	412*	357	(37)	25
CHXR21	M3	III	9.1*	7.5	(0.2)	425*	211	(4)	25
T31	K8	II	68.9	36.7	(0.4)	470	214	(1)	25
CHXR76	M4.25	III	12.6	6.4	(1.3)	153	58	(2)	15
CHXR74	M4.25	III	8.6	3.5	(0.4)	174*	74	(1)	15

Table 3.1: *Data for observed sample. Spectral types from Luhman (2007), SED classes from Luhman et al. (2008). EW and 10%w measurements listed are the averages from all 12 epochs. (*: In these cases the mean is not based on 12 measurements. See Tables 3.8 and 3.9). The ΔEW and Δ10%w are the max - min measurements for the 12 epochs, unless otherwise indicated.* Win *is the integration Window over which the EW and 10%w are calculated. Error estimates are given for EW and 10%w measurements (See Sect. 3.3 for more). Note: Sky subtraction was not possible for B43 or ChaHα2 so measurements are not given (See Chapt. 2, Sect. 2.5.4).*

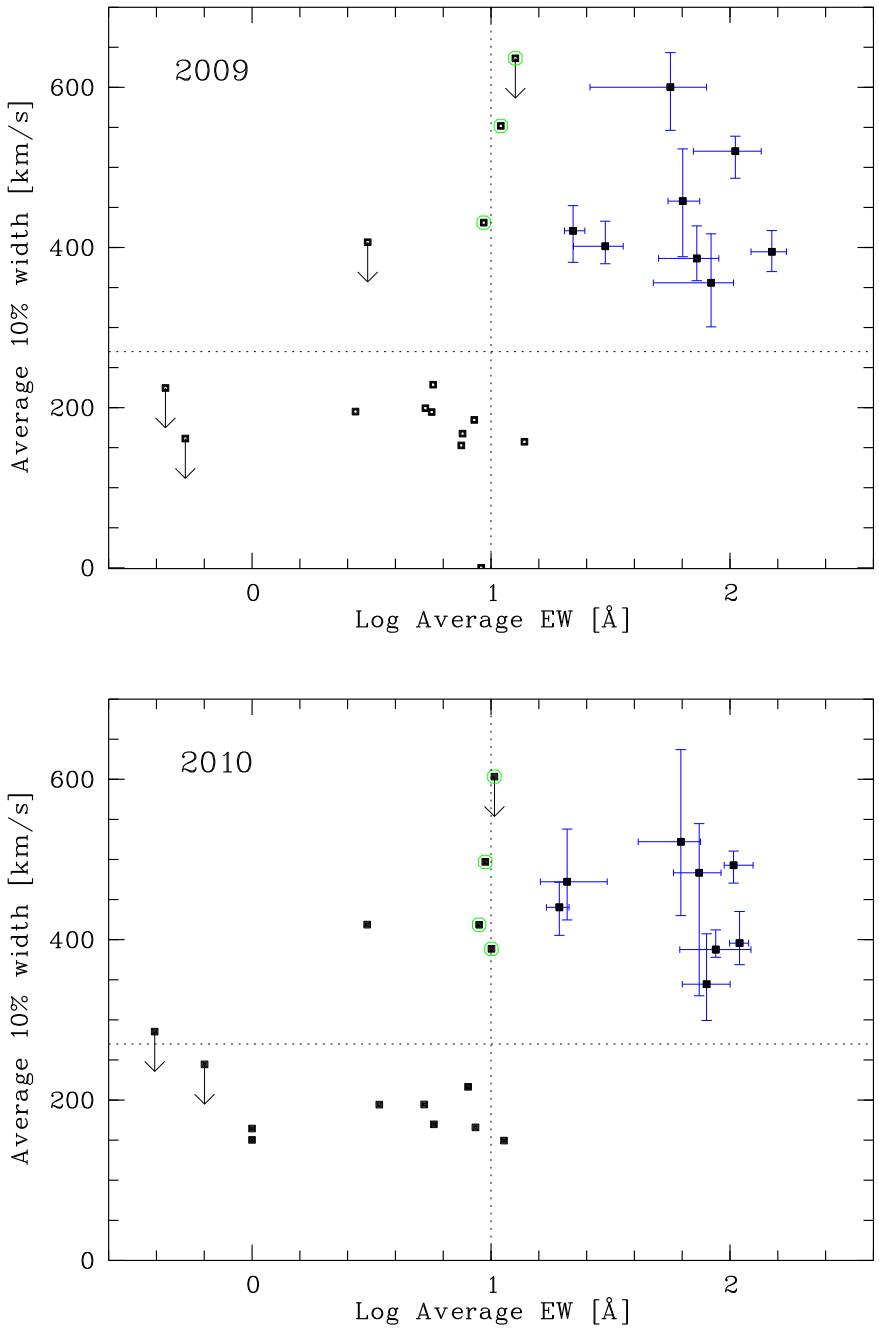

Figure 3.4: *Average Hα 10%w versus Hα EW for the first and second observation periods on the upper and lower panel respectively. The horizontal line is at 270 km s^{-1} and the vertical line is at 10 Å, which are the standard limits to differentiate between WTTS and CTTS. The spread (max - min) in measurements for objects with the broadest Hα profiles are indicated by the over-plotted horizontal and vertical bars (shown in blue). The arrows pointing down indicate upper limits in 10%w. The green ringed objects have weak but broad Hα emission and are discussed in Sect. 3.4.1.*

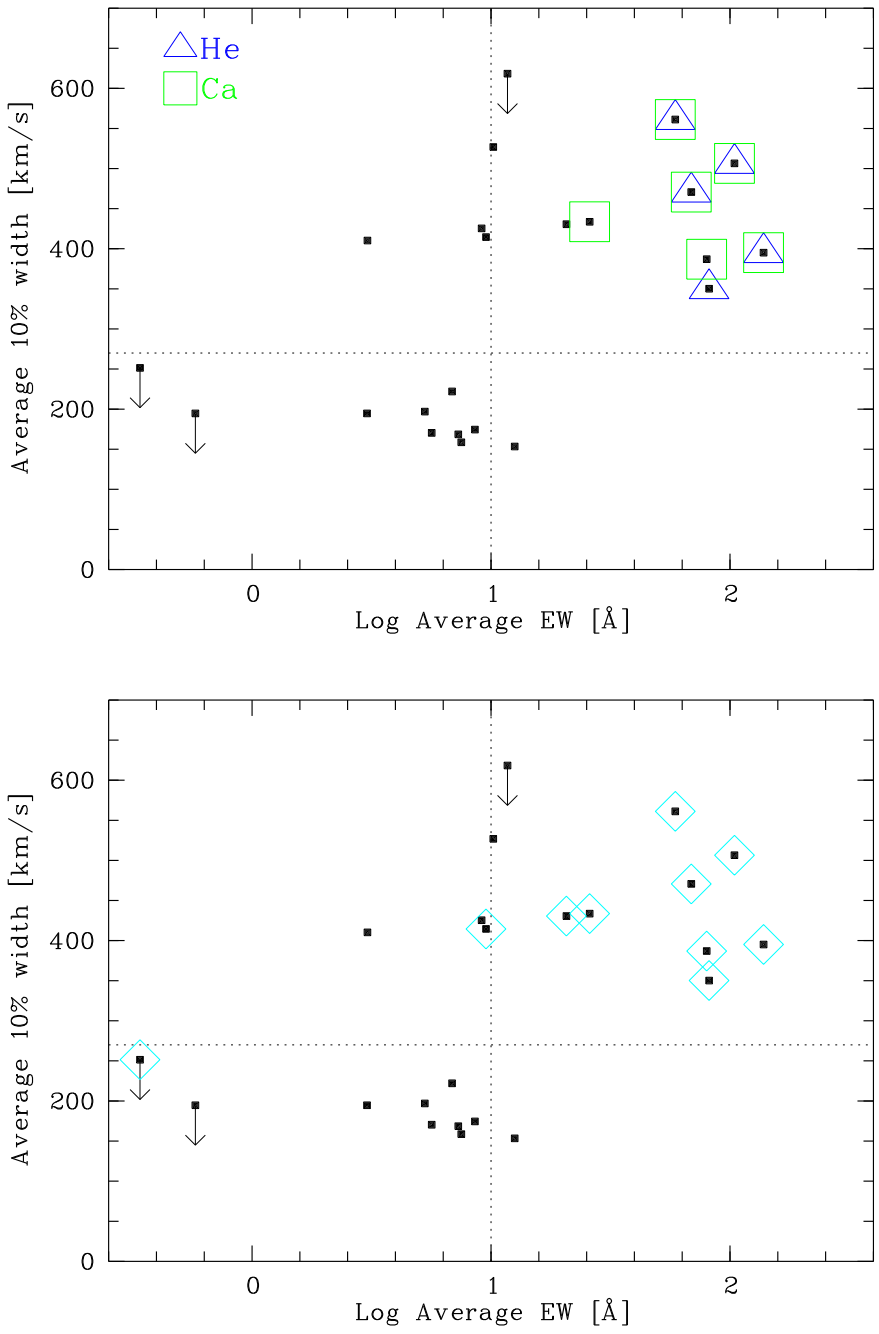

Figure 3.5: *Top Panel: Average Hα 10%w and EW for all observations, showing objects with Helium emission (blue triangles) and Calcium emission (green squares). Lower Panel: Average Hα 10%w and EW for all observations where objects marked with (cyan) diamonds are Class II YSOs according to Luhman et al. (2008).*

on spectral type: for K6 stars it is 5.9 Å, for M1 stars it is 10.1 Å and for M6 objects 24.1 Å. The mean spectral type in the sample is M1, making the 10 Å a reasonable value to take, as the three K and two G type stars in the sample, either have very high EW or an EW well below the cut off for their spectral type.

Eight objects stand out with EW > 20 Å and 10%w $> 350\,\mathrm{km\,s^{-1}}$ (two objects, B43 and ChaHα2 have 10%w $> 270\,\mathrm{km\,s^{-1}}$ but no EW measurements). They appear in the upper right quadrant and coincide with the objects found to have highly variable, mostly asymmetric line profiles (see above). Defining the spread as the maximum - minimum value measured during one observation season, the spread in Hα EW and 10%w measurements are indicated by the over-plotted horizontal and vertical bars. Although variability is clearly present, the objects in the right upper quadrant have continuous strong Hα emission over both observation periods and remain a separate group. Objects with 10%w $< 270\,\mathrm{km\,s^{-1}}$ also show some variations but are not shown in the plot for clarity.

The subgroup of objects mentioned above with weak Hα emission but broad wings, are ringed in Fig. 3.4, with EW$<$ 20 Å and 10%w$>$ $270\,\mathrm{km\,s^{-1}}$. These objects show significant variability over the course of the observations; in two cases their 10%w fall below $270\,\mathrm{km\,s^{-1}}$ in some epochs.

It is worth noting that the changes in EW and 10%w both show erratic behaviour, with no recognisable pattern across the time period of observations. However it is possible that the temporal resolution of the observations was not high enough to resolve any periodic or quasi-periodic variations in these quantities.

3.2.2 Other emission lines

In the spectra for which He I (6678.2 Å) and Ca II (8662.1 Å) emission lines were detected, the EW of these lines were measured. For the He I line a 6 Å integration window was used and the average of two 10 Å windows on either side of the integration window was taken to measure the continuum. For Ca II an integration window of either 12 Å or 20 Å is used depending on the line strength. To estimate the continuum, the average of three different continuum measurements is taken, two 10 Å windows centred at 8605 and 8585 Å and a 20 Å window centred at 8670 Å. Table 3.2 and 3.3 shows the EW measurements for both lines. Estimates of the measurement errors for both lines are also given in Table 3.2 and 3.3. (See Sect. 3.3 for an explanation of how these were derived).

In the upper panel of Fig. 3.5, the objects with Ca II or He I emission are

	Ca II Emission				
Object	Obs.1 EW [Å]	ΔCa EW	Obs. 2 EW [Å]	Δ EW	Error
ISO143	4.6	5.0	3.2	3.5	(0.30)
T33A	2.0*	2.5	-	-	(0.07)
ChaHα2	-	-	-	-	
B43	12.4	15.8	19.3	7.0	(0.90)
T45	21.6	24.7	19.8	16.3	(0.05)
ChaHα6	-	-	-	-	
ISO126	6.2	5.6	6.7	4.3	(0.10)
T30	11.4	17.1	7.4	12.4	(0.10)
T26	-	-	-	-	-
T31	3.3	6.2	7.4	8.4	(0.01)

Table 3.2: *Emission line measurements for objects with Ca emission in their spectra. EW measurements listed are the averages from each observation period, ΔEW is the max - min measurement in an observation period. Estimate of measurement errors are given in parentheses. (* : Ca II in emission in only four epochs for this object.)*

	He I Emission		
	Obs.1 EW [Å]	Obs.2 EW [Å]	Error
ISO143	7.7	10.0	(3.00)
T33A	-	-	-
ChaHα2	-	-	-
B43	X	-	-
T45	1.2	1.1	(0.05)
ChaHα6	1.4	1.3	(0.20)
ISO126	-	-	-
T30	1.7	1.5	(0.20)
T26	-	-	-
T31	0.6	1.0	(0.06)

Table 3.3: *Emission line measurements for objects with He in their spectra. EW measurements listed are the averages from each observation period, ΔEW is the max - min measurement in an observation period. Estimates of measurement errors are given in parentheses. (X : He I present in spectra, but no continuum for measurements.)*

marked with squares and triangles respectively. It clearly shows that these emission lines are found along with strong and variable Hα emission. Calcium absorption increases in earlier types, correspondingly, the two earliest type stars in the sample, T33A and T26, show Ca II in absorption. (For four epochs in the first observation period T33A does show weak Ca II emission). Individual epoch Ca II EW measurements for the accretors are given in Table 3.10. The average Ca II profiles for all 10 accretors are given in Fig. 3.6 and 3.7. Fig. 3.8 shows the average He I profiles for the five objects that show He I emission and one which does not.

3.3 Error Estimation

In order to get an estimate of the measurement errors of the emission lines both the sky removal and emission line measurement parameters were varied. Specifically the parameters used were (i) three different sky continuum estimates, the spatially averaged sky continuum and the average sky continuum $\pm$ standard deviation (ii) five different window sizes around the chosen window size given within the text, and (iii) five different window positions around the line centre. The ranges in parameters were chosen to allow for reasonable measurements of the emission line, while still differing from the correct parameters. These three sets of parameters were separately varied for each measurement of the Hα, Ca II and He I emission lines.

The mean difference in the correct line measurement and the perturbed line measurement was found for each of the three parameter variations. After these mean differences were added in quadrature, the square root of the sum was taken to get an estimate of the total error in each line measurement (see Tables 3.1, 3.2 and 3.3).

These total error estimates were then carried through to the accretion rate estimates, giving the error estimates in Table 3.5.

3.4 Origin of Emission

3.4.1 Accretion

Based on the emission lines in the spectra, the sample shows a clear division into two groups (see Sect.3.2). In this section it is argued that 10 objects in the sample are accreting from a disc for the following reasons: (i) Strength and

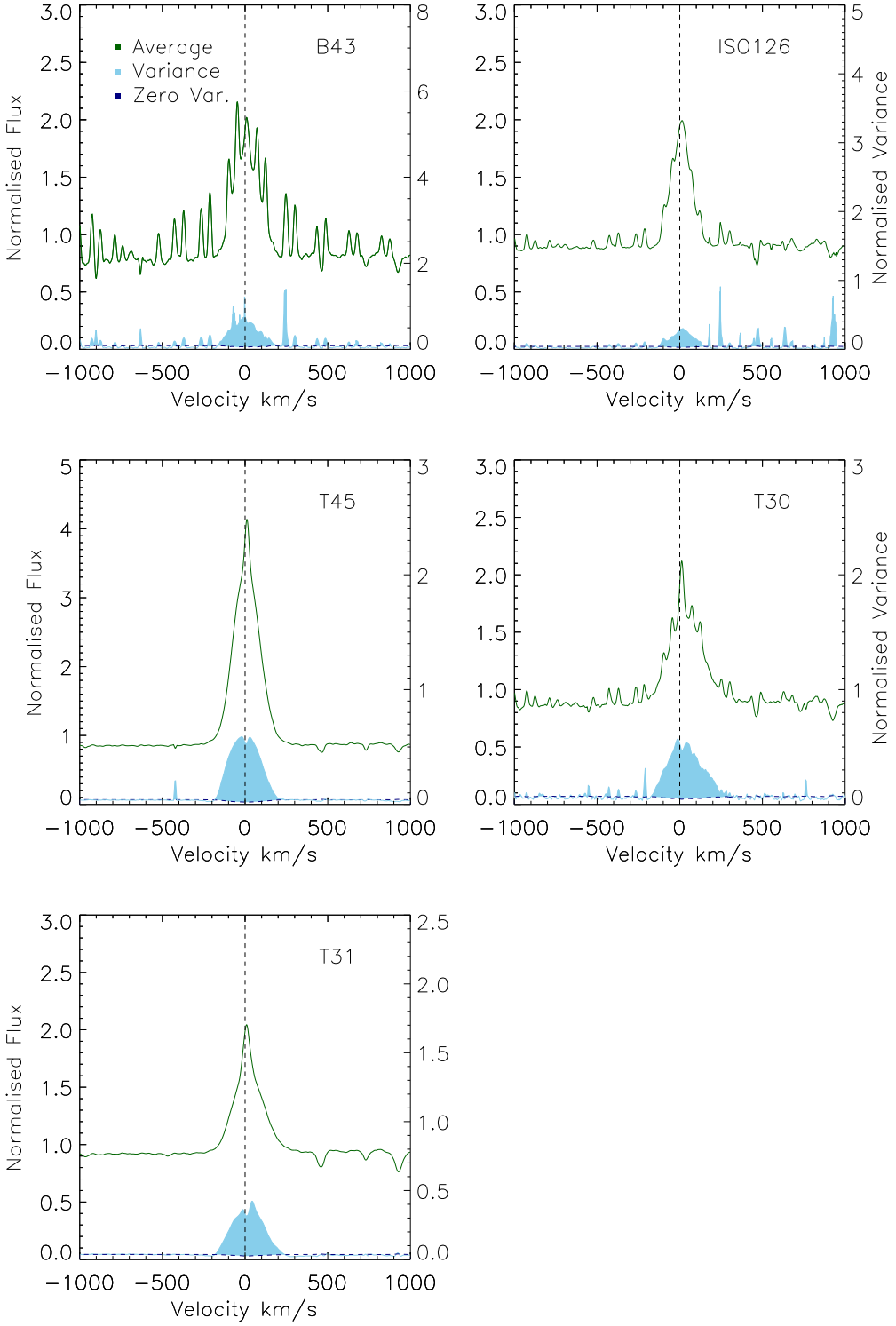

Figure 3.6: *Average and Variance profiles for the 5 accretors that show the strongest Ca II emission.*

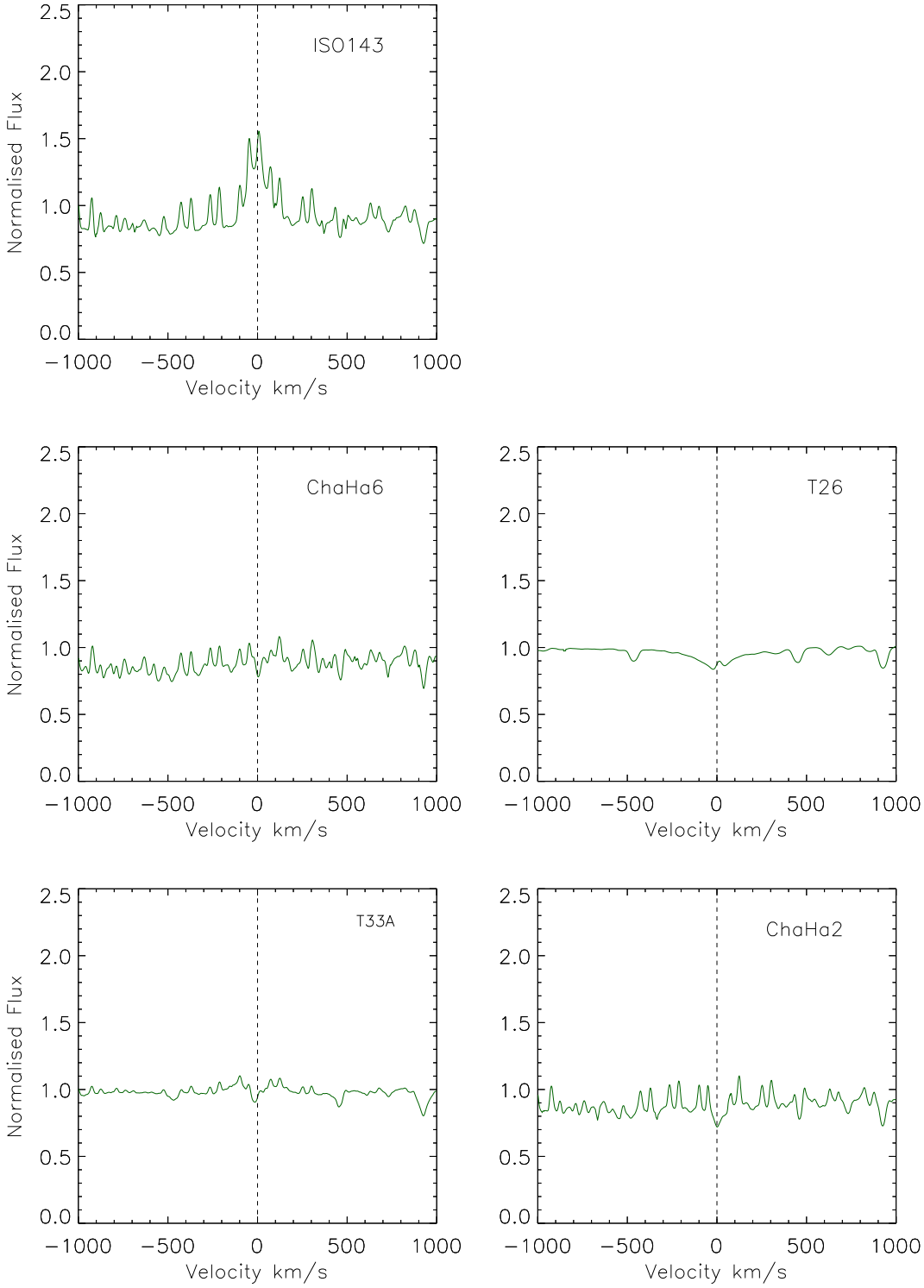

Figure 3.7: *Average profiles for Ca II emission for the remaining 5 accretors. Note for T33A, the average profile does not show any Ca II emission, but this object does show weak Ca II emission in four epochs.*

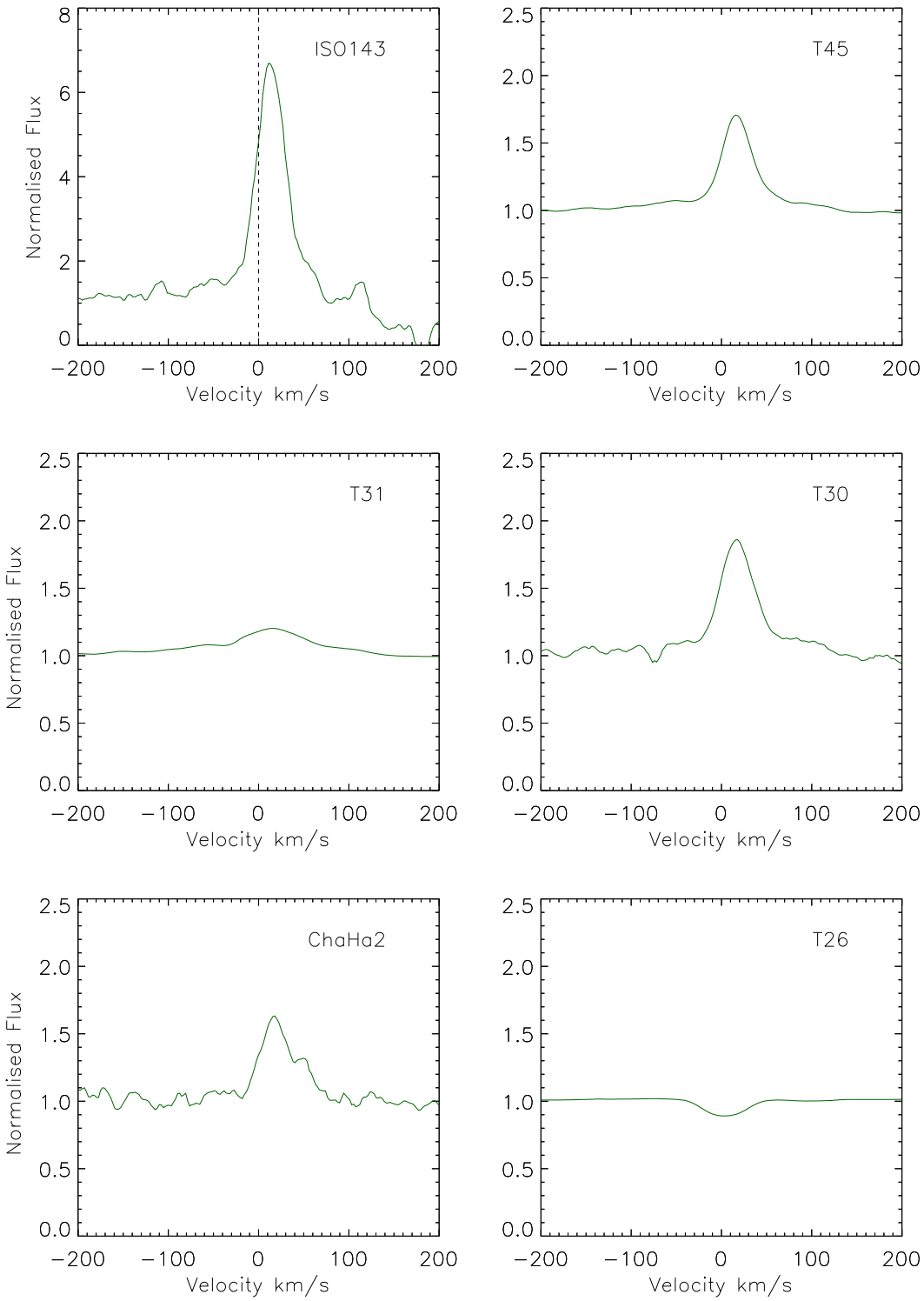

Figure 3.8: *Average profiles for 5 objects with He I emission and one without.*

width of Hα emission lines (ii) Shape of Hα profiles (iii) Presence of Calcium and Helium and (iv) Presence of circumstellar discs in the sample.

1. Hα 10%w versus EW: Eight objects show Hα emission with average EW > 20 Å and 10%w $> 340\,\mathrm{km\,s^{-1}}$ (see Fig. 3.4) (Two further objects, B43 and ChaHα2, which are classified as accretors have strong Hα emission with 10%w $> 340\,\mathrm{km\,s^{-1}}$, but do not have a continuum for measurement of the Hα EW). In the case of accretion, the line velocities should correspond to the typical velocities in an accretion flow. Taking the mass range in the sample to be around $0.1M_{\odot}$-$1M_{\odot}$, free fall velocities should be in the region of $\sim$160 - 300 $\mathrm{km\,s^{-1}}$, which would correspond to a range in 10%w of $\sim$320 - 600 $\mathrm{km\,s^{-1}}$. The apparent free-fall velocities will be smaller than this range in most cases due to the inclination of the stellar system with respect to us. For example taking an inclination of 45° this 10%w range becomes $\sim$ 225 - 425 $\mathrm{km\,s^{-1}}$. The line widths for the 10 accretors are consistent with these ranges (see Fig. 3.4 and Table 3.1). In contrast, the rotational velocities of M-type stars in Cha-I have on average $v\sin i$ $\sim$11 $\mathrm{km\,s^{-1}}$ (Nguyen et al. 2009a), which cannot account for the broadening that is observed .

2. Shape of the Hα profiles: The accretors' Hα profiles are almost all asymmetric, often with more than one peak and an overlying absorption feature (see Fig. 3.1 and 3.2). Therefore the emission is likely to originate from a structured flow. One possible explanation of the asymmetry is absorption by stellar wind or material in the inner disc (Edwards et al. 1994; Hartmann et al. 1994).

3. Hα Variability: The accretors show distinctively different variations across the emission line compared to the non-accretors. The variance profiles seen in Fig. 3.1 show multiple peaks of variations across the emission line and are much stronger than those of the non-accretors (see Fig. 3.3).

4. Presence of Calcium and Helium emission: Strong emission of these lines is thought to originate in the infall region of a magnetosphere (Jayawardhana et al. 2003; Muzerolle et al. 1998b). As seen in the top panel of Fig. 3.5 and from Tables 3.3 and 3.2, 8 out of 10 of the accretors show signs of either He I or Ca II emission. None of the non-accretors show the presence of Ca II or He I. Both of these emission lines can be produced in the chromospheres of active M-type objects, however it is either at low levels compared with

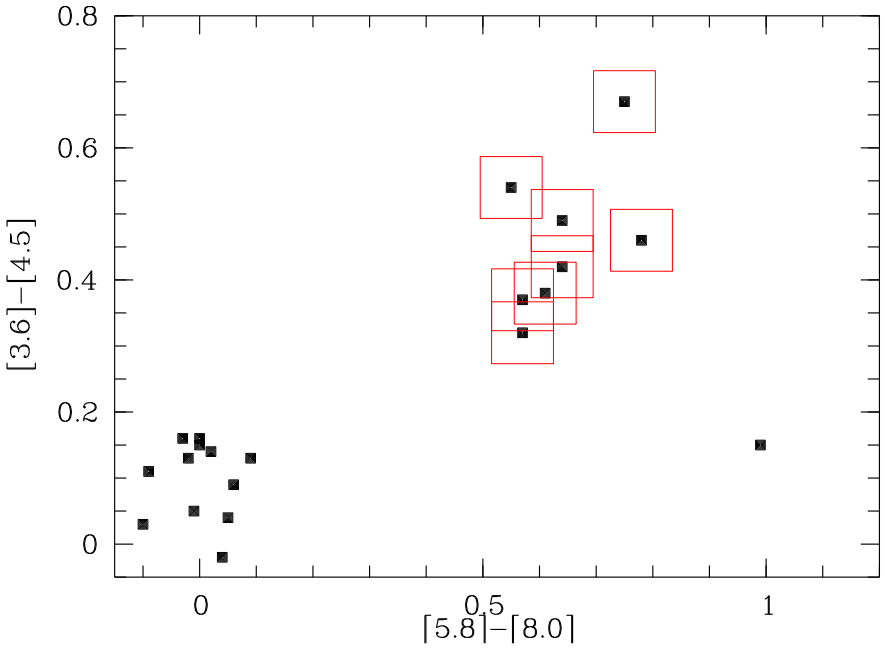

Figure 3.9: *Colour plot for the sample based on Spitzer photometry from Luhman et al. (2008). Here the accreting objects are indicated with a red box. Four objects are not shown as not all of the 4 IRAC magnitudes were available for them (T26, T33A, ESOHa560 and CHXR21).*

the accretors or in transitory flare events (Gizis et al. 2002; Jayawardhana et al. 2006; Montes et al. 1998).

5. Discs: The lower panel of Fig. 3.5 shows a plot of 10%w versus EW of the Hα emission in the sample, where the objects with discs are marked with a diamond. This is based on the SED classification by Luhman et al. (2008) from Spitzer photometry (see Fig. 3.9). All of the objects in the sample are either Class II, which are considered to have inner discs, or Class III objects. All 10 accretors are Class II objects.

The above arguments strongly suggest that these 10 objects are actively accreting. This accretion is further discussed in Sect. 3.5 and 3.7. The 15 remaining objects are defined as non-accretors (further discussed below). There is a possibility that some are weakly accreting objects that fall below the detection limits. However, the distinctive difference in Hα emission between the accretors and non-accretors is strong evidence that they are two separate populations, with different physical processes determining the Hα emission.

There are four objects that do show Hα EW of ~ 10 Å and have large Hα wings (these are ringed in Fig. 3.4). Apart from these broad wings, they do not share the other characteristics with the accretors. Most notably, only one object

has any evidence of having a disc and none have Ca II or He I in emission. The Hα emission profiles are quite different to the accretors, they are centrally peaked and show with no overlying absorption or other structures within the profile. Their Hα EWs are also below the cut-offs for accretors (Barrado y Navascués & Martín 2003), and they do not show the same amplitude of variations in EW (4.8 Å on average) as seen in the accretors (36 Å). This can also be seen by comparing the variance profiles of the non-accretors, Fig. 3.3, with the strength of those of the accretors, Fig. 3.1. The origin of this emission remains unclear.

3.4.2 Magnetic Activity

The 15 non-accretors in the sample all show an average Hα EW of $\lesssim 13$ Å, which is consistent with chromospheric emission from young M-type stars caused by magnetic activity (Scholz et al. 2007). They mostly show narrow, symmetric Hα profiles (see Fig. 3.3), which is expected for chromospheric emission.

3.5 Accretion Rate Estimates

The Ca II EW (at 8662.1 Å), Hα 10%w and the Hα EW were used to estimate mass accretion rates. The He I emission was not further examined due to the fact that the line was very weak and noisy or else not observed at all.

1. Ca II: To derive $\dot{M}$ from the Ca II EW, the method of Mohanty et al. (2005) was followed. Firstly, the underlying continuum flux is determined around the Ca II emission line from the AMES-Dusty synthetic spectra by Allard et al. (2001), which are available for a range of effective temperatures, gravities and metallicities. The appropriate model spectrum is selected using the effective temperature from Luhman (2007). In each case the lowest $\log g$ available was used, which for $T_{\rm eff} < 3100$K was $\log g = 3.5$, $T_{\rm eff} < 4000$K was $\log g = 4$ and $T_{\rm eff} > 4000$K was $\log g = 5$. Considering a small range of $\log g$ values will not adversely affect the results as the continuum flux is only negligibly dependent on $\log g$, and primarily determined by $T_{\rm eff}$ (Mohanty et al. 2005). The average continuum flux ($F_{\rm cont}$) was then computed from the model over the range 8600 - 8700 Å.

   The Calcium flux $F_{\rm CaII}$ (per unit area on the stellar surface [ergs sec^{-1}cm^{-2}]) was calculated from the EW, using the following equation:

$$F_{\rm CaII} = F_{\rm cont} \cdot (1 + r_{\lambda({\rm CaII})}) \cdot {\rm EW}_{\rm CaII} \qquad (3.4)$$

where $r_{\lambda(\mathrm{CaII})}$ is a measure of excess continuum emission produced by the accretion shock relative to the photospheric emission, and is given by $r_{\lambda(\mathrm{CaII})} = \frac{F_{\mathrm{excess}}(\lambda)}{F_{\mathrm{cont}}(\lambda)}$. Following Mohanty et al. (2005), it is assumed that $r_{\lambda(\mathrm{CaII})} \sim 0$, which is a reasonable approximation for the red part of the spectrum and at low accretion rates. If this is not the case, and $r_{\lambda(\mathrm{CaII})}$ is not close to zero, the accretion rates will have been underestimated. (See Sect. 3.6 for a test of this statement).

Using accretion rates derived from UV veiling measurements and detailed modeling of the Hα profiles in a sample with a mass range of $\sim$0.02 $M_{\odot}$ to $\sim$2 $M_{\odot}$), Mohanty et al. (2005) found the following relation between accretion rates and Ca II fluxes.

$$log(\dot{M}) = 1.06 \cdot \log(F_{\mathrm{CaII}}) - 15.40 \tag{3.5}$$

where the units of $\dot{M}$ are $M_{\odot} yr^{-1}$. (Note Herczeg & Hillenbrand (2008) found a very similar relation $log(\dot{M}) = 1.03 \cdot \log(F_{\mathrm{CaII}}) - 15.2$).

2. Hα 10%w: Using veiling measurements for calibration purposes and Hα line modeling from a few different studies with a sample mass range of 0.04 $M_{\odot}$ to 0.8 $M_{\odot}$, Natta et al. (2004) found that the 10%w of the Hα emission line correlates with the mass accretion rate:

$$\log(\dot{\mathrm{M}}) = \mathrm{A} + \mathrm{B} \cdot (\mathrm{H}\alpha\ 10\%\ \mathrm{width}) \tag{3.6}$$

where A = -12.89 ± 0.03 and B = 0.0097 ± 0.0007. Units of $\dot{\mathrm{M}}$ are $M_{\odot} yr^{-1}$. The spread in the coefficients is not propagated through the calculations, as it is the variations that are relevant in this case rather than the absolute accretion rate.

3. Hα EW: To estimate the accretion rate using the Hα EW, firstly the the Hα EW is converted to a flux per unit area on the stellar surface [ergs sec^{-1}cm^{-2}]. As with Ca II and following Eq. 3.4, the AMES-Dusty models are used to compute the continuum flux in the range 6554 - 6572 Å. Note that the AMES-Dusty models do not go to high enough temperatures to cover the T_{eff} of two objects T26 and T33A. In these two cases the Kurucz (1993) atmosphere models are used to convert the Hα EW to a flux. Veiling is not taken into account (see Appendix 3.6 for further details). Using the published stellar luminosities and effective temperatures from Luhman (2007) stellar radii (R_*) are determined for each accretor. The Hα fluxes

are then converted to luminosities by multiplying by $4\pi R^2$.

By fitting models to accretion continuum emission to objects in the range $0.02\mathrm{M}_\odot \lesssim \mathrm{M} \lesssim 1\mathrm{M}_\odot$, Herczeg & Hillenbrand (2008) derived a series of relations between accretion luminosity and the luminosity of certain emission lines associated with accretion. They derived the following relation for Hα:

$$\log(L_{\mathrm{acc}}) = \mathrm{A} + \mathrm{B} \cdot \log(L_{\mathrm{H}\alpha}) \tag{3.7}$$

where $\mathrm{A} = 2.0 \pm 0.4$ and $\mathrm{B} = 1.20 \pm 0.11$. $L_{\mathrm{H}\alpha}, L_{\mathrm{acc}}$ are in units of $L_\odot$. This equation is used to to determine accretion luminosities but again, the spread in the coefficients are not taken into account. Assuming that all the gravitational energy from the accretion is converted into luminosity, the accretion luminosity is related to the accretion rate as follows (Herczeg & Hillenbrand 2008):

$$\dot{M} = \left(1 - \frac{R_*}{R_{\mathrm{in}}}\right)^{-1} \cdot \frac{L_{\mathrm{acc}} R_*}{G M_*} \tag{3.8}$$

Here R_* is the stellar radius, R_{in} is the infall radius and M_* is the stellar mass. Following Herczeg & Hillenbrand (2008), the approximation of $(1 - \frac{R_*}{R_{\mathrm{in}}})^{-1} \sim 1.25$ is taken, assuming $R_{\mathrm{in}} \sim 5R_*$ (Gullbring et al. 1998).

To get an estimate of the stellar mass, the published effective temperatures of the targets (Luhman 2007) were compared with a 2 Myr isochrone from the BCAH98 evolutionary models by Baraffe et al. (1998). Two objects in the sample have temperatures that are higher than those covered by the Baraffe models (T26 and T33A); for these objects there masses are estimated to be $M \sim 2.5\,M_\odot$ based on the D'Antona & Mazzitelli (1997) isochrones. The Baraffe et al. (1998) models have been found to systematically overestimate masses compared to the D'Antona & Mazzitelli (1997) models (Muzerolle et al. 2003). Therefore the Hα EW derived accretion rates of T26 and T33A are underestimated compared to those of the other accretors. This means that although these accretion rates are not fully comparable, the relative spread in accretion rates are.

The time-averaged accretion rates and the spread (max - min) in accretion rates for all three diagnostic are given in Tables 3.5 and 3.6. The parameters such as F_{cont}, M_* and R_* that were used in the derivation of these accretion rates are given in Table 3.4.

Object	$F_{cont}(H\alpha)$	$F_{cont}(Ca)$	M_* $[M_\odot]$	R_* $[R_\odot]$
ISO143	1.369	3.600	0.175	1.02
T33A	58.89*	-	2.5	1.77
ChaHα2	-	-	0.15	1.17
B43	-	5.731	0.35	1.38
T45	4.383	8.073	0.75	2.29
ChaHα6	0.879	2.797	0.11	0.87
ISO126	4.383	8.073	0.75	1.43
T30	3.055	6.467	0.50	1.07
T26	70.16*	-	2.5	3.39
T31	10.295	11.567	1.15	3.71

Table 3.4: *Parameters used in the derivation of accretion rates. Fluxes are in units of [ergs $sec^{-1}cm^{-2}\AA^{-1}]x10^5$. (*: Estimates from Kurucz (1993) models.)*

	Log($\dot{M}$) Ca EW		Log($\dot{M}$) Hα EW		Log($\dot{M}$) Hα 10%w	
	Av. [Sprd]	Er.	Av. [Sprd]	Er.	Av. [Sprd]	Er.
ISO143	-8.97 [0.67]	(0.07)	-8.82 [0.29]	(0.10)	-9.06 [0.64]	(0.10)
T33A	-	-	-8.09 [0.42]	(0.01)	-8.68 [1.53]	(0.01)
ChaHα2	-	-	-	-	-9.54 [0.68]	(0.12)
B43	-8.39 [1.04]	(0.09)	-	-	-9.02 [0.70]	(0.09)
T45	-7.85 [0.68]	(0.003)	-7.82 [0.34]	(0.01)	-7.98 [0.66]	(0.01)
ChaHα6	<-9.16	(0.08)	-9.37 [0.40]	(0.05)	-9.49 [1.14]	(0.12)
ISO126	-8.39 [0.73]	(0.04)	-8.65 [0.46]	(0.06)	-9.14 [0.66]	(0.01)
T30	-8.39 [1.11]	(0.03)	-9.24 [0.59]	(0.04)	-7.45 [2.07]	(0.02)
T26	-	-	-7.16 [0.19]	(0.01)	-8.71 [0.88]	(0.01)
T31	-8.20 [0.76]	(0.03)	-7.06 [0.27]	(0.01)	-8.32 [2.08]	(0.01)
Av. Spread	[0.83]		[0.37]		[1.11]	

Table 3.5: *Derived time-averaged accretion rates for the sample in Table 3.4. Following each average is the max - min spread in accretion rates over the 12 epochs of observations. An estimate of measurement errors are give in parentheses. Units: Log($M_\odot yr^{-1}$). A 2σ upper limit is given for the object with no discernible Ca II emission in its spectrum (ChaHα6). No Ca II accretion rate estimates are given for the 3 objects in the sample with Ca II in absorption. For B43 and ChaHα2 no Hα EW estimates are given as they have no measurable continuum at that wavelength.*

	Observation Period 1					
	Log($\dot{M}$) Ca EW		Log($\dot{M}$) Hα EW		Log($\dot{M}$) Hα 10%w	
	Av.	[Sprd]	Av.	[Sprd]	Av.	[Sprd]
ISO143	-8.89	[0.58]	-8.80	[0.18]	-9.06	[0.50]
T33A	-		-8.02	[0.25]	-9.00	[0.52]
ChaHα2	-		-		-9.65	[0.42]
B43	-8.24	[0.64]	-		-8.91	[0.23]
T45	-7.78	[0.68]	-7.82	[0.34]	-7.84	[0.51]
ChaHα6	<-9.26		-9.36	[0.40]	-9.44	[1.12]
ISO126	-8.45	[0.64]	-8.70	[0.30]	-9.14	[0.66]
T30	-8.28	[1.10]	-9.28	[0.59]	-7.07	[0.94]
T26	-		-7.13	[0.10]	-8.81	[0.69]
T31	-8.36	[0.50]	-7.10	[0.16]	-8.45	[1.31]
Av. Spread		[0.69]		[0.29]		[0.69]
	Observation Period 2					
	Log($\dot{M}$) Ca EW		Log($\dot{M}$) Hα EW		Log($\dot{M}$) Hα 10%w	
	Av.	[Sprd]	Av.	[Sprd]	Av.	[Sprd]
ISO143	-9.04	[0.44]	-8.96	[0.01]	-9.05	[0.64]
T33A	-		-8.20	[0.34]	-8.31	[1.10]
ChaHα2	-		-		-9.45	[0.47]
B43	-8.60	[0.50]	-		-9.26	[0.65]
T45	-7.88	[0.54]	-7.83	[0.14]	-8.11	[0.39]
ChaHα6	<-9.11		-9.38	[0.24]	-9.55	[1.05]
ISO126	-8.35	[0.64]	-8.61	[0.36]	-9.13	[0.33]
T30	-8.49	[1.10]	-9.23	[0.31]	-7.83	[2.01]
T26	-		-7.20	[0.11]	-8.62	[0.64]
T31	-8.06	[0.59]	-7.02	[0.24]	-8.20	[2.08]
Av. Spread		[0.54]		[0.22]		[0.94]

Table 3.6: *Derived average accretion rates shown separately for observation periods 1 and 2. Units: Log($M_{\odot}yr^{-1}$). The 2σ upper limits are given for the object with no discernible Ca II emission in its spectrum (ChaHα6). For B43 and ChaHα2 no Hα EW estimates are given as they have no measurable continuum at that wavelength. No Ca II accretion rate estimates are given for the 3 objects in the sample with Ca II in absorption.*

3.6 Test for Veiling

The accretion process not only results in excess line emission, but also produces continuum emission, which fills in and 'veils' any photospheric absorption lines, making these lines appear shallower. One method of estimating the accretion rate is to compare a veiled spectrum of an accreting star to that of a non-accreting star of similar spectral type and age.

The strongest photospheric absorption line that lies within the observation spectral range is Li (6708.1 Å). In order to accurately determine the depth of the Li line it is necessary to have smooth, distinct and clearly visible absorption profiles. It is also important to have a spectral match for each of the accretors in order to estimate the amount of veiling. Due to these restrictions, the veiling analysis was limited to four accretors with distinct Li absorption in their spectra for all 12 epochs, ISO126, T45, T30 with spectral types M1.25, M1.25, M2.5 respectively and T31 with a spectral type of K8. Two non-accretors with suitable spectral types and strong Li absorption were used for comparison, T39A (M2) and CHXR20 (K6). The Li EW were measured in all epochs for these six objects, and the measurement for the accretors and their non-accretor spectral match are shown in Fig. 3.10. The non-accretors both show steady deep Li absorption, indicative of photospheric absorption. All four accretors show shallower and more variable Li absorption, which is what one would expect when there is variable veiling present in the continuum. (Note: only 11 epochs are considered in the case of ISO126 due to an increase in noise in the second last epoch.)

In the calculations of the accretion rates it is assumed that veiling was negligible. Since the Li (6708.1 Å) absorption line is close to the Hα (6562.81 Å) emission line, the estimate of the veiling derived at the wavelength of Li can be considered a good estimate of the veiling around the Hα line. This veiling estimate was then used to correct the measurements for the Hα EW, as the measured continuum is actually veiled continuum and not true continuum. To find the veiling factor the equation following equation is used

$$r = \frac{EW_P}{EW_V} - 1 \tag{3.9}$$

where EW_P is the photospheric Li EW, and EW_V is the veiled EW. (For definition of the veiling factor r see Sect. 3.5). In this case the EW_P is the EW of the Li absorption line in the reference non-accretor, and EW_V is the EW of the veiled Li line in the accretor. The same equation is then used with the calculated veiling factor, to derive an unveiled EW for Hα and recalculate the accretion

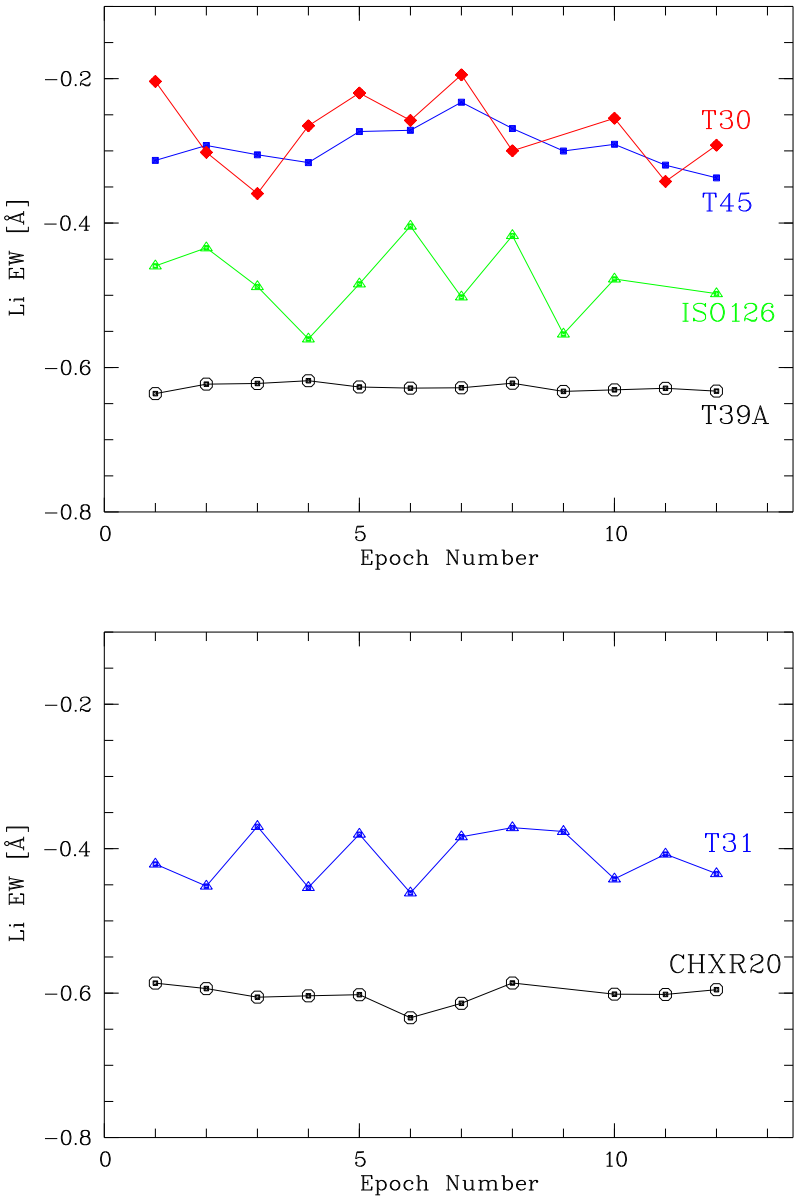

Figure 3.10: *Top Panel: Li EW measurements of three accretors and a non-accretor (T39A) used as a reference. Bottom Panel: Li EW of the remaining accretor for which this analysis was carried out and a non-accretor (CHXR20).*

Object	Log($\dot{M}$) Corrected		Log($\dot{M}$) Uncorrected		r
	Av.	[Sprd]	Av.	[Sprd]	
T45	-7.42	[0.38]	-7.82	[0.34]	1.16
ISO126	-8.53	[0.36]	-8.65	[0.46]	0.32
T30	-8.78	[0.71]	-9.25	[0.59]	1.39
T31	-6.86	[0.36]	-7.06	[0.27]	0.47

Table 3.7: *Accretion rate estimates derived from Hα EW with and without veiling correction for four accretors, and calculated average veiling factor, r. Units of* $\dot{M}$ *are* $[M_{\odot} yr^{-1}]$

rates. This was done for all epoch measurements, and so the new accretion rate estimates also take into account the variations in veiling. These measurements are presented in Table 3.7.

There are a number of sources of uncertainty using this method. The veiling factors were derived to give an estimate of how much veiling there is in the spectra and hence allow for the evaluation of the affect of veiling on the results. Ideally to reduce the spread and errors in the veiling estimate, a number of lines are used, however since there is only a single line available, these calculations can only provide a rough estimate of the veiling. The abundance of lithium in YSOs decreases with age, so an older star will have shallower Li absorption. Previous studies have found stellar clusters, such as TW Hydrae and η Chamaeleontis with ages of $\sim$ 12 Myr, to have a range of Li EW of 0.4 - 0.6 Å (Mentuch et al. 2008). However at $\sim$ 2 Myr, ChaI is a younger region, where an even smaller range in Li EWs can be expected. Similarly, a fast rotator will have a broadened Li absorption line, making it appear shallower, and will lead to an overestimation of the veiling. In this sample all the accretors have narrow Li absorption, so this is unlikely to be a significant factor.

On average when the veiling in the continuum is accounted for, the accretion rate for all four objects increases by 0.30 dex. However, more importantly for the results is that the variations in the veiling have little effect on the amplitude of variations in the accretion rates, there is only a 0.09 dex increase on average in the spread. Extrapolating from this figure to hypothesize that on average, the spread in all the accretors will increase by the same amount. This will increase the average spread in accretion rates derived from Hα EW to 0.46 dex. The same can most likely be said for the accretion rates derived from Ca II EW, however veiling tends to be less at longer wavelengths. Therefore, although the veiling present in the continuum may have caused the underestimation of the accretion rates and spread slightly, it does not affect the conclusions.

3.7 Discussion

3.7.1 Comparing accretion rate indicators

In Fig. 3.11 and 3.12 a graphical comparison of the three accretion rate estimates can be seen, with the 1-1 relation indicated by the dotted line. The over-plotted horizontal and vertical bars do not show the errors in measurements, which are substantially smaller (see Table 3.5). These bars denote the max - min spread in derived accretion rates from the 12 epochs of observations. The data points with arrows mark the 2σ upper limit for the object with no discernible calcium in its spectrum. Three further objects had Ca II in absorption, and so there are no Ca II measurements for these three objects. Taking into account the spread in derived accretion rates of individual objects, there is a reasonable agreement between the three accretion rate estimates. Some more additional trends can be seen by comparing the average accretion rates and the amplitude of variations.

On average the Ca EW and the Hα EW give the lowest variations in accretion rates over the course of the observations (see top panel of Fig. 3.11). For a given object the Ca EW estimates show greater variations than the Hα EW estimates do. This could possibly be explained by the presence of telluric emission lines in the wavelength domain of Ca II, which could contaminate the EWs (Osterbrock et al. 1996). The telluric lines are drowned out by the Ca II emission when it is strong (e.g. in the case of T31 and T45, see Fig. 3.6), but they can clearly be seen in objects with weak Ca II emission. These telluric lines will change over the course of the observations, and increase the variability measured in the Ca EW. This does not account for all of the variability though, as some of the objects with the largest spread in Ca EW (e.g. T45 and T31) show no sign of telluric lines in their spectra.

The variations in individual object's accretion rates are larger when derived from the Hα 10%w ($\sim$1.11 dex) than they are when derived from the other two signatures. (Note: 1 dex means there is an order of magnitude spread in measurements). These results suggest that the Hα 10%w does not give reliable estimates of average accretion rates, especially with single epoch observations.

The fact that the amplitude of variations for individual accretion rates derived from Hα 10%w is on average greater than what it is for the other two accretion rate estimates implies there is another contributor to the 10%w changes. It has been shown that outflows do contribute to the Hα emission in the wings in some cases (Alencar et al. 2001; Whelan et al. 2009). Looking at the average and variance profiles in Fig 3.1, it can be seen that much of the variability in the Hα

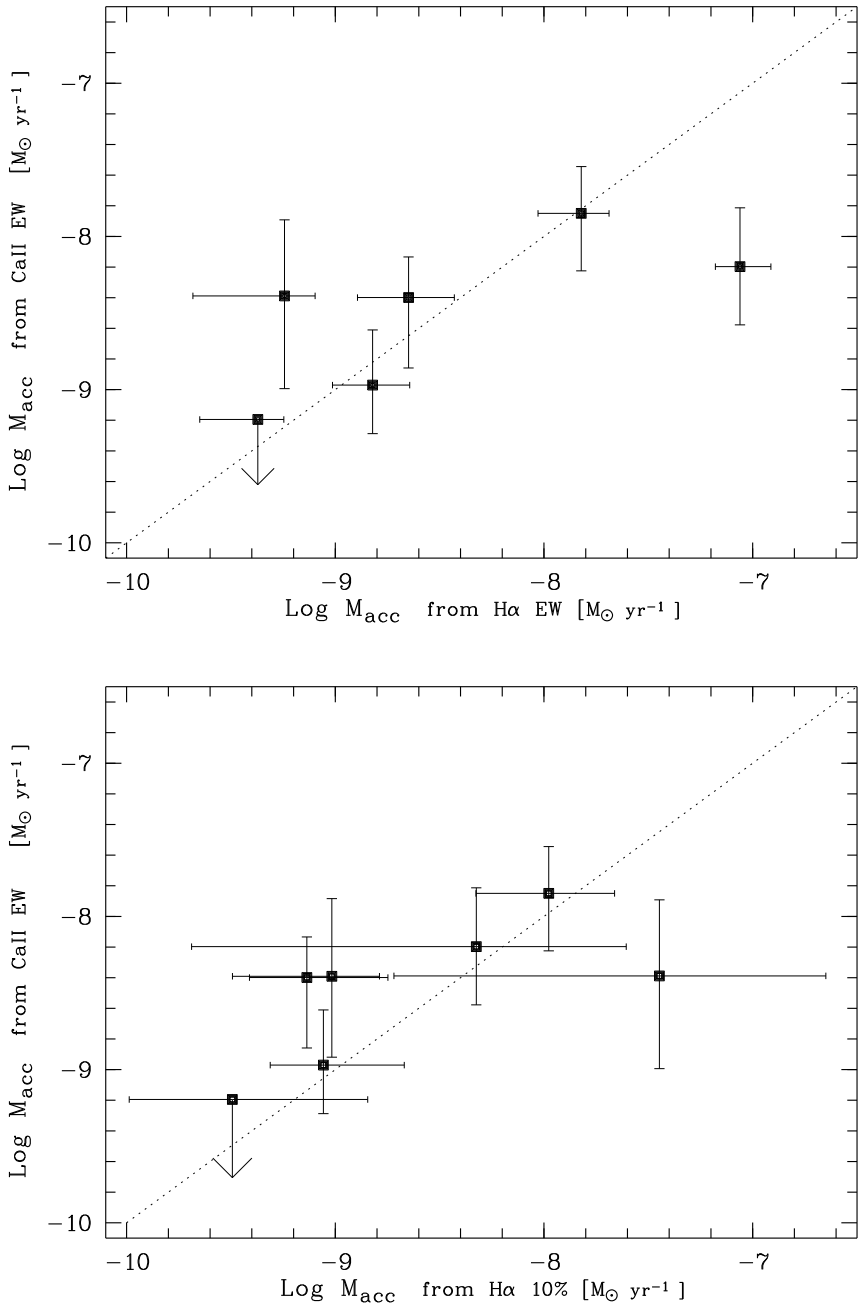

Figure 3.11: *Top Panel: Calculated accretion rates from Ca EW and Hα EW. Over-plotted horizontal and vertical bars indicate spread in measurements for all 12 epochs. The object with a downwards pointing arrow is the 2σ upper limit for the Ca EW accretion rates as this object has no discernible calcium in its spectrum. Lower Panel: Calculated accretion rates from Hα EW and Hα 10%w. The dotted line in both plots indicates the 1-1 relation between the two indicators.*

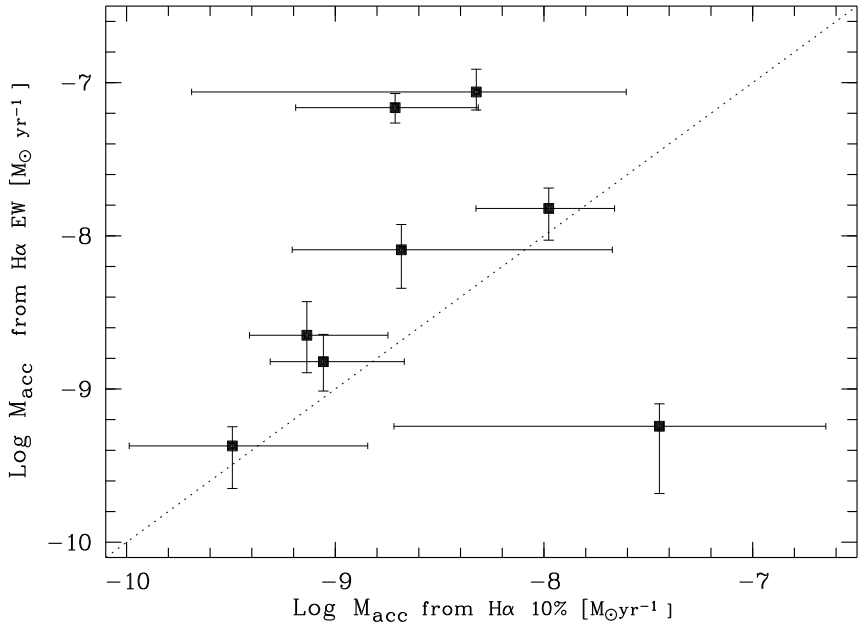

Figure 3.12: *Continued from Fig. 3.11: Calculated accretion rates from Ca EW and Hα 10%w. Over-plotted horizontal and vertical bars indicate spread in measurements for all 12 epochs. The dotted line indicates the 1-1 relation between the two indicators.*

line is found in the wings. The calcium emission lines show a different behaviour where the line emission varies all across the profile and not just in the wings (see Fig. 3.6).

Most of the accretors show blue- or red-shifted absorption in their Hα profiles. The blue absorption is unlikely to be associated with accretion and more likely to be a consequence of a stellar wind. Over the course of the observations these absorption features change in strength and wavelength. This will contribute to the variability in the 10%w, but it could also reduce the peak height of the Hα emission line, which would lead to an overestimation of the 10%w and the accretion rate. Hence, the absorption features could explain the fact that accretion rates derived from the 10%w are more variable. Furthermore, in a number of profiles there is evidence of high velocity absorption in the wings, which the 10%w measurements are far more sensitive to than the EW measurements. From these results it is considered that the Ca EW and Hα EW estimates to reflect the accretion rates more accurately. In the following the discussion is focused on these two quantities and the Hα 10%w measurements are not considered.

The variability cannot entirely be due to measurement errors. Estimate of the measurements errors are given in Tables 3.1, 3.2 and 3.3. These have been

carried through to the accretion rate estimates and are given in Table 3.5. In all cases these errors are less than the variations in accretion rates.

3.7.2 Spread in $\dot{M} \propto M_*$ relation

The average spread in accretion rates is ~ 0.83 dex for the values derived from the Ca EW and ~ 0.37 dex for the Hα EW. This can be taken as the maximum spread in accretion rates for young objects (~ 2 Myr) over a time period of 15 months. This spread is an upper limit as it is likely that emission from the wind and the chromosphere both contribute to these lines.

This spread is relevant in the context of the $\dot{M} - M_*$ relation (see Chapt. 1). As the size of this sample is small, a derivation of such a relation is not attempted. However, it is found that when these two stellar properties are plotted against each other the dominant feature is the large spread in accretion rates for any given mass. These multi-epoch observations are designed to probe this significant attribute of the $\dot{M} - M_*$ relation.

Mohanty et al. (2005) derived a correlation $\dot{M} \propto M_*^2$ for a sample with a mass range of $0.15\,M_\odot$ to $\sim 2\,M_\odot$ and age range from $\gtrsim 1$ Myr to 10 Myr. The striking feature of this correlation is the ± 1.5 order of magnitude spread in accretion rates at any given mass.

The accretion rate variations derived here show that this spread cannot be due to variations of individual objects on the time-scale of about a year. This statement was also checked using the standard deviation of the accretion rates within the sample, which on average for the Hα EW derived accretion rates is 0.16, for the Hα 10%w derived accretion rates it is 0.61 and for the Ca II EW derived accretion rate it is 0.25.

To illustrate this, Fig. 3.13 shows the mean Hα EW and Ca EW derived accretion rates versus mass for the sample. The over-plotted vertical bars in this plot indicate the spread in measurements over the 12 epochs of observations. The dotted line on both of these plots is the $\dot{M}$-M_*^2 relation found by Mohanty et al. (2005). Also plotted as a dashed line is the linear fit derived from the data set using standard linear regression. The relation derived from this Cha I sample is much shallower for the Ca EW derived accretion rates than the Hα EW derived accretion rate. Significantly, this plot shows that the spread around the relation is much larger than any spread is seen in accretion rates over the observations.

Several alternative explanations for the scatter in $\dot{M}$ have been suggested in the literature. It could be accounted for by evolutionary differences between sources, as $\dot{M}$ is expected to change with time. However, in Ophiuchus which has

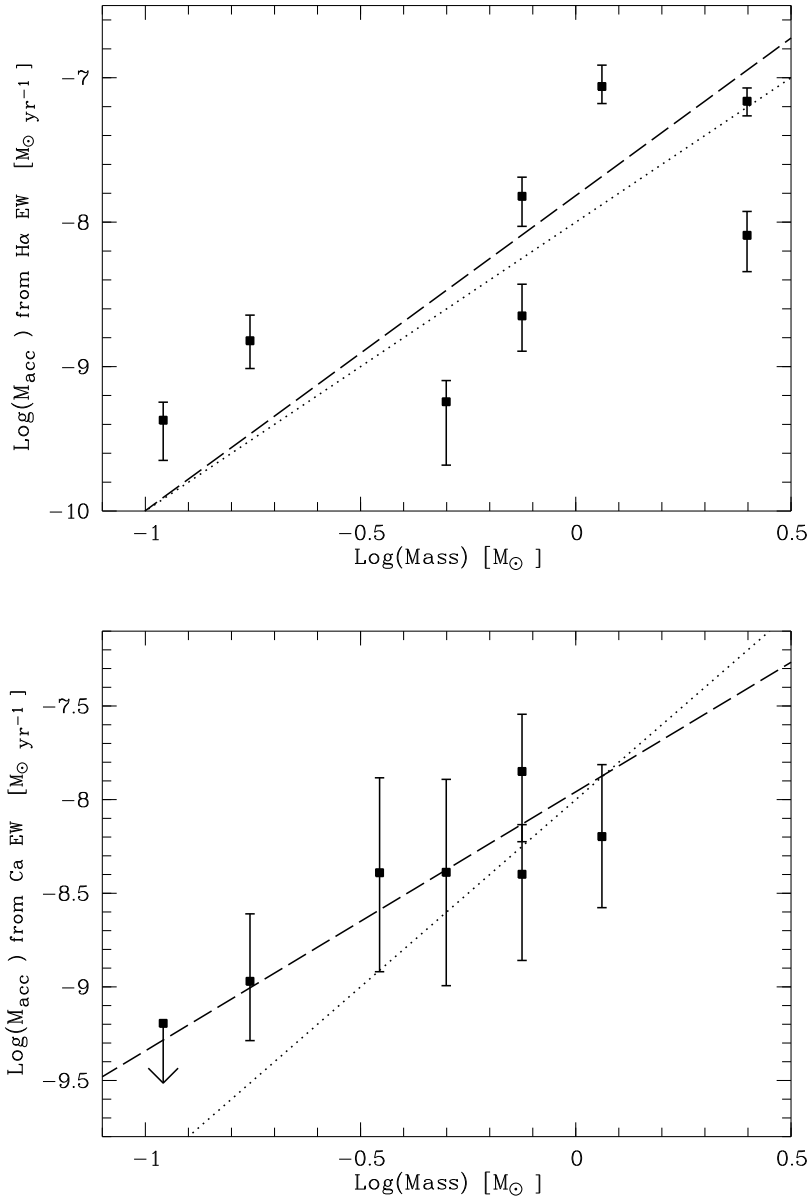

Figure 3.13: *Top Panel: Hα EW derived accretion rates versus object mass. Lower Panel: Ca EW derived accretion rates versus object mass. The dotted line represents the $\dot{M}$-M_*^2 relation found by Mohanty et al. (2005). The dashed line represents the linear fit derived from the measurements. The over-plotted vertical bars indicate max - min spread in measurements. Upper limits are indicated by arrows.*

an age of about ($\gtrsim$0.5 Myr - 1 Myr), Natta et al. (2006) found a spread of $\sim$2 dex at least for any given mass. Large spreads in accretion rates within single star formation regions suggests that evolutionary effects are unlikely to explain the full spread. Differences in initial conditions or environmental conditions between objects could also result in a variety of accretion rates (Dullemond et al. 2006). For instance, as a result of different initial disc conditions Alexander & Armitage (2006) have predicted a 2 dex spread in accretion rates for stars in the mass range 0.02 - 0.2 $M_{\odot}$ and a 2.8 dex range for masses 0.4 - 4.0 $M_{\odot}$. Observations such as those by Rigliaco et al. (2011) have provided evidence for a mass dependent evolution in the accretion rates, with very low mass stars and brown dwarfs evolving faster, steepening the slope of the $\dot{M} \propto M_*$ relation at the low mass end. Furthermore, it cannot be ruled out that a significant portion of the scatter in the $\dot{M}$ - M_* plots could be due to uncertainties in the determination of the stellar masses (Antoniucci et al. 2011), stellar radius, infall radius or from the veiling calibrations themselves.

The exponent in this relation is also poorly defined and there has been a range of values found, from $\dot{M}$ - $M_*^{1.1}$ (Barentsen et al. 2011), $\dot{M}$ - $M_*^{1.8}$ (Natta et al. 2006) and up to $\dot{M}$ - $M_*^{3.1}$ (Fang et al. 2009). There are also suggestions that a close to quadratic relation is a result of limited sample size and detectability (Barentsen et al. 2011; Clarke & Pringle 2006), although some relation between mass and accretion rate is expected. However, all these relations have a large spread of at least 1 order of magnitude in accretion rates for a given mass.

3.7.3 Time-scales of Variations

In the first observation period, the mean amplitude of variations in $\dot{M}$ is $\sim$ 0.69 dex when derived from Ca II and $\sim$ 0.29 when derived from Hα EW. For the second observation period they are $\sim$ 0.54 and $\sim$ 0.22 dex respectively. The total variations over 15 months (0.83 and 0.37 dex, see above) are not significantly different. The slight increase in the amplitude of variations in the full sample shows there is some variability on the longer time-scales. However, the fact that it does not increase by much means the dominant variations occur in a single observation period i.e. it is shorter than 8 weeks.

Fig. 3.14 shows the average difference in accretion rates on different time-scales within the sample. The accretion rates are those derived from the Hα EW (B43 and ChaHα2 are not included due to the lack of continuum around Hα). In order to cover all the possible time-scales in the sample, every accretion rate estimate is compared to every other accretion rate estimate for that object. The

differences in accretion rates ($\dot{M}_1$-$\dot{M}_2$) are then placed into three different time bins, depending on the time difference between measurements, (i) T $<$ 25 d(ays) (ii) 40 d $<$ T $<$ 90 d (iii) T $>$ 1 yr. The mean accretion rate difference in each bin is then plotted for each object. For two objects the largest variations occur on the shortest time-scales. Five more objects show a roughly even distribution over the three time bins, and one object shows the largest variations on the longest time-scales, T33A. This could be a true increase in accretion rate, or it could also come from the incomplete sampling of the variations. Although long term variations are seen in the sample, for all, excluding T33A, the amplitude of variations have reached a maximum or are within 70% of the maximum after 25 days.

Nguyen et al. (2009b) observed spectroscopically a number of low-mass pre-main sequence stars over a series of time-scales of days, weeks and months, with the majority of the observations taking place on shorter time-scales than the LAMP observations. They found that the amplitude of variations increases on time-scales from hours to several days, after which it saturates. The LAMP observations are able to test if there are any larger variations when the period of observations is extended. The results suggest that observations on time-scales of a few of weeks are sufficient to limit the majority of the extent of accretion rate variations in typical young stars over the time period of $\sim$ 1 year.

A previous long term photometric monitoring program also found low levels of variability in a large sample 72 CTTS over the course of $\sim$20 yrs (Grankin et al. 2007). Only a fraction of their sample showed significant changes over time-scale of months to years, suggesting that T Tauri photometric variability is dominated by short term variations.

A major proportion of the variations occur on the time-scale of 8-25 days, which is on the same order as the rotation period of young stellar objects, 1-10 days (Herbst et al. 2007). Note only two objects in the sample have known periods, ChaHα2 at 3.21 days and ChaHα6 at 3.6 days (Joergens et al. 2003). This suggests the origin of the variations is close to the surface of the star, possibly within the co-rotation radius. If rotation is the underlying mechanism that causes the observed accretion variability, than the variations could be tracing structural asymmetries in the accretion flow rather than actual accretion rate changes. These time-scales could also be in agreement with magnetic reconnection events (Goodson et al. 1998; Hayashi et al. 1996), but this data set does not not have the temporal resolution to distinguish what is occurring on these shorter time-scales.

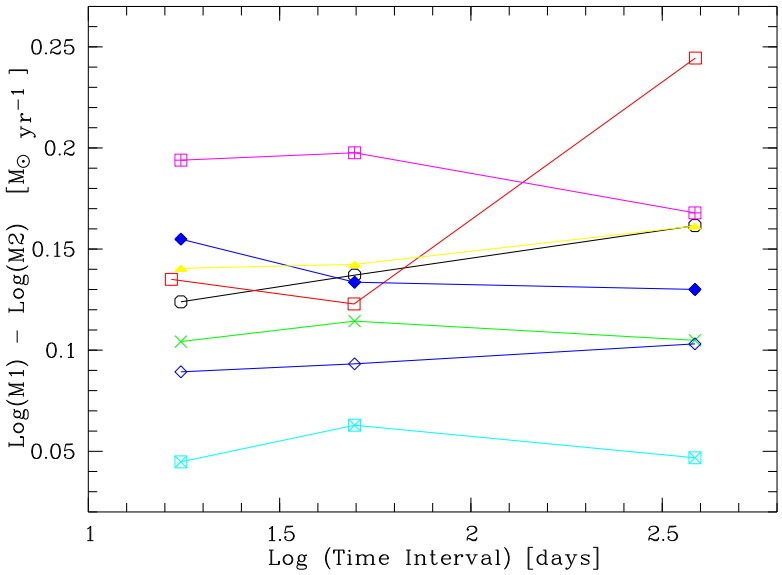

Figure 3.14: *Average spread in accretion rate over different time-scales for accretors in the sample, excluding B43 and ChaHα2, as these accretion rates were derived from Hα EW. Three different time bins were used (i)8 d(ays) < T < 25 d (ii) 40 d < T < 90 d (iii) T > 1 yr. Seven out of the eight accretors here show very little increase in variations across the three time bins, demonstrating that the variations are dominated by short term variability.*

As can be seen in Fig. 3.4 the accreting objects are steadily accreting through all epochs in the observations. No radical changes are seen in the emission lines of the non-accretors over the course of the observations, they always have much weaker Hα emission than the accretors. This demonstrates that if they are accreting it is below the detection levels, and never accrete at the same levels as the 10 accretors in the sample. Extreme variations in accretion or episodic accretion is thought to be necessary for YSOs to gain the masses that are observed (Evans et al. 2009). There have now been a number of observations of FU Ori events where an object will suddenly jump from having an accretion rate of 10^{-7} to $10^{-4}\,M_{\odot}yr^{-1}$ in a very short amount of time, and then decay slowly over the course of 20-100 yrs (Hartmann & Kenyon 1996). However these are rare events, only a handful have been found, and they are expected to occur at the early stages of stellar evolution when the infall is still occurring to the disc. Slightly less dramatic accretion changes occur in EXors type objects, which can show 1 - 3 magnitude flare ups every few years for a period of weeks (Herbig 2007).

Highly variable, sporadic accretion rate changes have also been found in older objects such as in the 8 Myr old η Cha cluster (Jayawardhana et al. 2006; Murphy et al. 2011). Murphy et al. (2011) suggest that such sporadic accretion could

occur at 'the critical age range of 5 - 10 Myr when inner discs are being cleared and giant planet formation takes place'. The T Tauri star, T Chamaeleontis, shows very large changes in Hα EW, increasing from 0 Å to 30 Å and falling again, Schisano et al. (2009) infer these variations to be a result of an evolved, clumpy disc. Furthermore Jayawardhana et al. (2006) have also found evidence to suggest that inner disc clearing and/or grain growth might indeed affect two accretors in η Cha.

The sample does not show signs of episodic or sporadic accretion like the cases discussed above. The fact that at 2 Myr the younger stars in Cha I are continuously accreting, supports the results of Murphy et al. (2011) that the sporadic accretion is likely related to the older age of the population and the evolutionary stage of the disc.

3.8 Conclusions

This study was designed to investigate the accretion variability of YSOs based on multi-epoch optical spectra of 25 targets in the Chamaeleon I region. The observations took place over a total of 15 months. They were split into two separate periods, of 8 weeks each. In each of these periods 6 observations were made, evenly spread across the 8 weeks. The high resolution spectra from the FLAMES/GIRAFFE spectrograph on the ESO-VLT covered the Hα (6562.81 Å), He I (6678.2 Å) and Ca II (8662.1 Å) emission lines which were used to identify 10 accretors in the sample. Accretion rates for these objects were derived from the Hα EW, Hα 10%w and the Ca EW.

When the amplitude of variations in accretion rates from all three accretion rate estimators are considered, it is seen that Hα 10%w accretion rate estimates of individual objects show much greater variability than the other two estimators. For this reasons the Hα 10%w is not considered a good quantitative accretion rate estimator.

Considering the full observation period the average spread in accretion rate was found to be 0.83 dex for Ca EW estimates and 0.37 dex for the Hα EW estimates. These variations demonstrate that over $\lesssim$ 15 months, the accretion rate changes are 0.37 - 0.83 dex or less. Mohanty et al. (2005), using the Ca II (8662Å) emission line, found the spread for a single mass in the $\dot{M}$-M_* relation to be 1-2.5 orders of magnitude. Bearing in mind that the Ca II sample is small, these results show that the spread in the $\dot{M}$-M_* relation is probably not due to the variability of individual objects on the time-scales of years. They also suggest

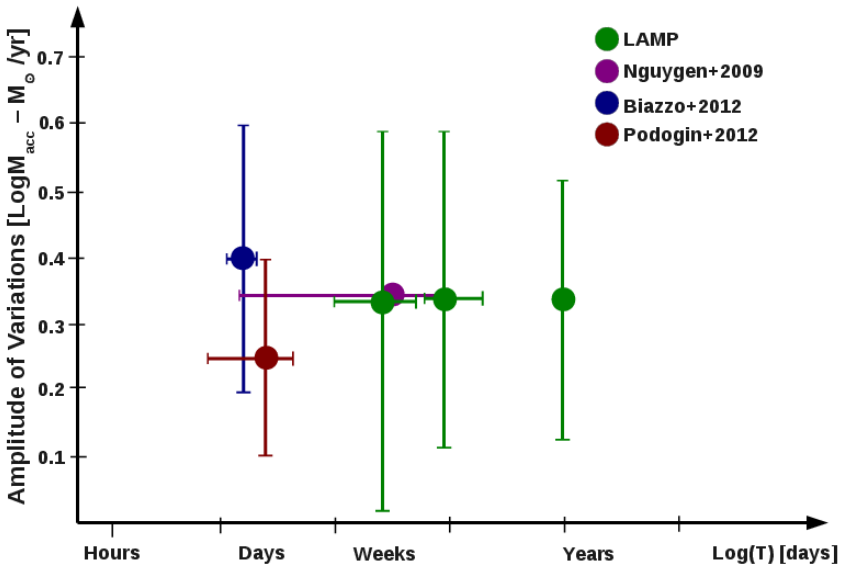

Figure 3.15: *Accretion rate variations versus the time-scales over which they were observed. This plot represents a comparison between LAMP data and accretion rates derived in comparable data sets using comparable methods. Note error bars here indicate the spread in accretion rates, and time coverage in each bin.*

that this spread is not entirely due to evolutionary differences within a sample, but is more likely due to environment or initial conditions or uncertainties in the derived parameters.

The dominant time-scales of the variations found in this data agree with those found in other studies. Fig. 3.15 is a graphical comparison of accretion variations found in different samples. The error bars within the plot, represent the parameter space covered by each data set, not the errors. This is not a complete sample of variability studies, but as these studies used similar similar accretion indicators, they are more comparable. For example, Pogodin et al. (2012) used a number of emission lines associated with accretion to estimate accretion rates in 8 Herbig Ae stars. For half the sample they have multiple observations covering time-scales of tens of days. By averaging across the accretion indicators, including Hα they found variations of 0.1 - 0.4 dex for these four objects. Biazzo et al. (2012), with a sample of 12 objects, found variations of 0.2 - 0.6 dex over the two days separating observations. The last data set in this comparison was covered by Nguyen et al. (2009b), who found variations from Ca II emission of 0.35 dex on average over time-scales of days to months.

The accretion rate variability within the LAMP sample reached a maximum

or was within 70% of the maximum within $\sim$ 8 - 25 days, for 7 out of 8 accretors (based on Hα EW derived accretion rate, and hence excluding two accretors B43 and ChaHα2). This period of variations roughly corresponds to the typical rotation period of these types of objects, suggesting the rotation could be modulating the observed accretion in these systems. One such model is the asymmetric accretion flow hypothesis due to misaligned rotation and field axes or complex field topologies. In this case we would be probing the structural asymmetries in the accretion flow as different parts of the flow come into view. Differential rotation between the disc and the star has been shown to produce magnetic field line expansion and reconnection over the course of a few days (Hayashi et al. 1996), and could also account for the variations. Further studies with greater temporal resolution are needed to discriminate between such hypotheses.

	EW														
Object	1	2	3	4	5	6	7	8	9	10	11	12	Mean	ΔEW	σ
CHXR28	0.4	0.7	0.6	0.5	0.7	0.4	0.6	0.6	1.2	0.4	0.5	0.6	0.6	0.8	0.2
CHXR20	0.1	-	0.7	0.6	0.2	0.7	0.8	-	0.2	0.2	-	0.5	0.3	0.7	0.3
T22	3.1	2.2	3.1	3.4	3.3	3.2	3.2	2.7	-	3.1	2.7	3.5	3.0	1.3	0.4
ISO143	172.2	129.2	122.5	163.4	-	160.6	119.6	-	-	-	-	9.6	138.2	72.6	27.2
T33A	35.7	22.1	26.0	30.9	30.8	34.8	17.0	30.6	21.1	19.2	3.1	6.1	25.9	19.7	9.4
T39A	4.5	4.8	5.1	8.6	4.7	4.4	7.0	4.7	4.8	4.7	5.3	4.9	5.3	4.2	1.3
T45	94.2	70.3	93.7	121.7	116.6	135.1	107.6	97.9	101.1	124.8	94.6	5.1	104.4	64.8	17.7
ChaHα6	97.5	83.2	74.4	103.4	47.7	93.9	78.2	94.4	63.3	100.1	-	3.1	81.7	55.7	18.1
ISO126	50.2	81.4	82.9	89.8	60.7	70.7	76.2	79.2	122.4	61.7	104.8	8.8	79.9	72.1	19.6
ChaHα8	6.4	9.0	-	-	2.7	4.6	-	-	-	-	-	-	5.6	6.3	2.7
ChaHα5	10.2	-	8.2	7.1	6.7	5.8	-	-	-	5.8	-	-	7.3	4.5	1.7
ESOHa566	9.3	-	-	7.1	6.2	7.5	-	-	-	-	-	-	7.5	3.1	1.3
T30	79.5	52.8	43.8	56.0	79.8	26.0	53.8	41.3	-	74.7	75.3	6.2	59.0	53.9	17.7
T34	3.0	3.8	3.1	2.0	1.8	2.6	3.0	3.1	-	2.6	4.4	4.0	3.0	2.6	0.8
ChaHα3	5.4	10.5	6.4	4.4	2.1	5.5	5.7	4.0	12.2	2.7	12.7	0.8	6.9	10.6	3.7
T26	20.4	24.7	22.0	20.3	22.3	22.6	17.2	17.1	20.9	19.4	20.2	1.2	20.7	7.6	2.2
ESOHa560	11.4	14.6	13.2	9.9	7.9	8.9	6.6	8.3	11.4	9.0	11.4	0.1	10.2	8.0	2.3
LM04 429	13.9	17.8	14.4	13.4	6.6	9.7	12.5	-	-	6.8	11.8	0.3	11.7	11.2	3.5
CHXR22E	11.8	9.4	11.1	8.7	4.6	9.1	5.8	11.0	-	9.2	12.7	1.4	9.5	8.1	2.5
CHXR21	12.3	7.3	12.2	10.0	4.8	9.2	5.7	11.9	-	10.2	11.2	5.6	9.1	7.5	2.8
T31	74.7	59.1	62.2	55.1	67.4	62.1	79.2	72.9	91.7	58.0	60.6	3.4	68.9	36.7	11.5
CHXR76	12.2	12.7	16.7	11.7	15.0	14.6	11.2	10.8	10.8	10.6	14.3	0.3	12.6	6.4	2.1
CHXR74	7.4	-	10.1	9.3	7.3	8.6	10.0	8.2	9.9	8.5	8.5	6.6	8.6	3.5	1.2

Table 3.8: *List of Hα EW values for all observations. Here Δ EW is the max EW - min EW measurement. Also given are the mean EW and RMS (σ) values which are calculated over the entire sample. B43 and ChaHα2 Hα EW measurements are not included here as they have no measurable continuum at that wavelength.*

	10%w [km s^{-1}]														
Object	1	2	3	4	5	6	7	8	9	10	11	12	Mean	Δ10%	σ
CHXR28	<115	<219	<130	<121	<258	<122	336	257	<252	<206	<266	<252	<194	-	-
CHXR20	<119	<324	<216	<175	<336	<175	<338	<293	<221	<219	<298	<339	<255	-	-
T22	393	<492	<370	<362	384	<400	407	438	<145	415	416	414	418*	54	17
ISO143	381	369	391	387	421	416	409	395	368	435	390	374	395	66	21
T33A	430	391	392	432	379	381	430	537	475	424	<380	492	433*	158	50
T39A	174	212	177	261	182	187	213	188	193	188	178	204	196	86	24
T45	526	486	521	527	539	519	496	510	477	502	470	499	506	68	21
ChaHα6	361	300	360	381	313	417	308	385	308	407	358	299	350	117	42
ISO126	427	403	380	358	379	370	412	379	378	385	380	390	386	68	18
ChaHα8	203	178	195	192	<221	202	159	186	95	187	161	112	170*	108	36
ChaHα5	154	131	195	155	213	154	149	154	163	133	248	<115	168*	116	36
ESOHa566	164	<133	174	146	124	154	144	198	-	162	176	140	158*	74	21
T30	612	623	643	610	546	564	429	509	522	637	534	499	561	213	65
T34	176	<254	188	214	195	200	149	201	154	226	223	209	194*	226	26
ChaHα3	265	217	267	269	<245	122	218	241	166	207	247	216	222*	146	45
T26	408	452	437	439	381	405	405	451	412	471	435	465	430	90	27
ESOHa560	517	645	578	497	516	555	465	478	<535	515	491	533	526*	179	51
LM04 429	<721	701	<635	<633	<463	<726	<786	<731	<465	<574	<564	<497	<618	-	-
CHXR22E	572	393	539	427	214	469	274	542	<168	410	444	270	412*	357	199
CHXR21	494	371	485	420	378	436	284	492	<327	479	443	393	425*	494	283
T31	478	436	477	443	523	388	514	528	495	487	330	544	470	214	62
CHXR76	151	148	149	171	167	156	146	148	125	148	142	184	153	58	15
CHXR74	186	-	155	185	187	207	162	133	201	150	177	170	174	74	22
B43	403	-	422	399	-	416	-	417	-	386	350	-	399	72	25
ChaHα2	317	339	336	361	326	324	388	346	339	356	342	357	344	70	19

Table 3.9: *List of Hα 10%w values for all observations. Here Δ10% is the max - min 10% width measurement. Also given are the mean 10%w and RMS (σ) values which are calculated over the entire sample.(*:Indicates the cases where the mean 10%w is not based on all 12 epochs due to some measurements being upper limits.)*

	EW														
Object	1	2	3	4	5	6	7	8	9	10	11	12	Mean	ΔEW	σ
ISO143	4.0	2.6	2.0	4.2	4.8	7.1	3.6	1.6	4.6	4.1	2.0	2.3	3.6	5.5	1.6
T33A+B	2.3	1.7	1.1	-	-	1.4	-		-	-	-	-	1.6	1.2	1.0
ChaHα2	-	-	-	-	-	-	-	-	-	-	-	-	-	-	-
B43	14.4	-	21.5	6.0	-	5.4	-	6.5	-	6.1	2.3	-	8.9	19.2	6.5
T45	16.3	7.3	12.1	22.3	31.9	26.9	21.7	21.6	23.9	17.2	10.2	7.3	18.2	24.6	7.8
ChaHα6	-	-	-	-	-	-	-	-	-	-	-	-	-	-	-
ISO126	2.7	6.5	5.1	6.4	1.8	7.3	4.9	4.3	9.9	4.9	7.0	4.6	5.5	8.0	2.3
T30	18.7	5.8	8.2	11.3	15.1	1.7	3.7	2.2	19.3	15.4	5.3	3.0	9.2	17.6	6.8
T26	-	-	-	-	-	-	-	-	-	-	-	-	-	-	-
T31	6.9	2.7	3.1	2.4	5.7	-	12.4	10.8	6.0	3.5	5.2	9.8	6.2	10.1	3.0

Table 3.10: *All Ca II EW measurements for the accretors with discernible Ca II emission. ΔEW is the max - min measurements. The RMS (σ) and the mean are calculated across the entire observation period.*

4

Temperaments of Young Stellar Objects

4.1 About this Chapter

Building on the results from the LAMP sample, the next logical step was to study the shorter time-scales (days and less) in these accreting objects. The high signal-to-noise and high-cadence linear spectro-polarimetry data set of Vink et al. (2005) on a sample of T Tauri and Herbig Ae stars provided the necessary sample. The 14 targets in the sample were observed over time-scales of hours and days, and were spread between two observing periods 2001 and 2003 (See Chapt. 2 for details).

In order to distinguish between possible causes of accretion variations on short time-scales, it is necessary to monitor these systems on time-scales close to the rotation period (multiple days) as well as on time-scales of hours. This allows one to distinguish between the case where the mass-accretion rate variations are a result of a slow and gradual changes in accretion emission across the rotation period, or when they take the form of stochastic and rapid changes.

Furthermore, this sample allows the work to be extended to higher stellar masses (up to 2-3 $M_{\odot}$ for Herbig Ae stars). It has been suggested that the accretion process in Herbig Ae stars might be similar to that in lower mass T Tauri stars (Eisner et al. 2004; Garcia Lopez et al. 2006; Natta et al. 2001; Vink

et al. 2002, 2003). Whilst there has been claims of observations of magnetic fields in Herbig Ae stars (Hubrig et al. 2004; Wade et al. 2005), the number found is similarly low to that found in post-main sequence objects (e.g. Alecian et al. 2012) which casts doubts over the extension of the magnetospheric accretion scenario towards higher masses. Therefore the issue of the fundamental accretion process in Herbig Ae stars remains open, and can be tested with this data set.

The sample consists of 14 objects which were introduced in Chapt. 2. The stellar parameters are given here in Table 4.1. This chapter begins with the description of the typical Hα emission changes in this sample, using a single object AB Aur, as an example (Sect. 4.2). Each individual object is discussed in Appendix A. The different origins of Hα emission in these objects are presented and are examined with respect to this data set in Sect. 4.3. The derived accretion rates are presented in Sect. 4.4, and the implications of the accretion variations observed are discussed in Sect. 4.5.

4.2 Behaviour of the Hα Emission

In the following section, AB Aur is used to represent the typical behaviour of the line emission in the sample. This section will concentrate on the 2003 observations of this object as an example, all of the observations for the remaining 13 targets and the 2001 observations of AB Aur are discussed in Appendix A.

4.2.1 Hα Profiles

For each block of observations of each object there are about 20 different exposures over the course of $\sim$ 1 hour (see Table 2.4). This provides very close temporal coverage of the Hα emission. The top left panel in Fig. 4.1, 4.2, 4.3 and 4.4 shows a time series of profiles across the four nights of observations for AB Aur in 2003. These four nights were the 10^{th}, 11^{th}, 12^{th} and 13^{th} of December, and for simplicity these will be referred to Night 1, 2, 3 and 4 respectively. Each profile is off-set from the previous one for clarity. The minute of the hour in which the spectrum is observed is given to the right of each profile. The spectra are selected from across the full observation block.

The changes in the profiles during Nights 1, 2 and 4, are typical of what is seen in the majority of objects of this sample. These changes will be referred to as *slow variations*. During each of these nights, AB Aur shows a strong central emission with a large blue-shifted absorption in the wing. Within this blue-

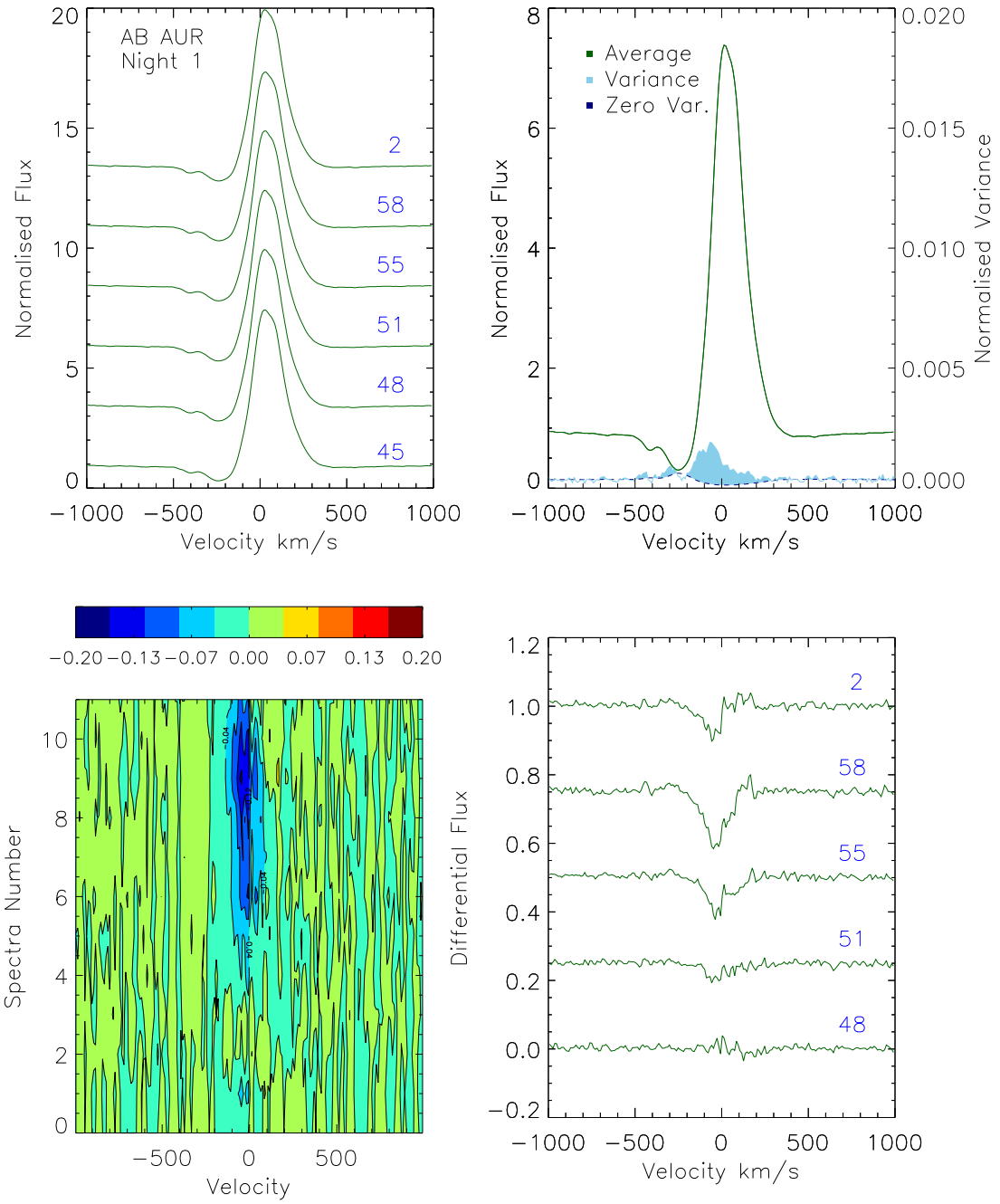

Figure 4.1: *Top Left: Sample of Hα profiles across the first night of observations of AB Aur in 2003. Each profile is off-set from the previous one for clarity. The minute of the hour in which each spectrum was observed is given to the right of each profile. Top Right: Average and variance profiles. Bottom Left: A differential surface plot. This plot shows the color coded difference between the first spectra of that night and the preceding spectra. Bottom Right: Time-series of cuts in differential flux plots. This was done in the same way as the surface plots, where the first spectrum of that night was removed from all the rest of the spectra. These are the same profiles as chosen for the profile time series.*

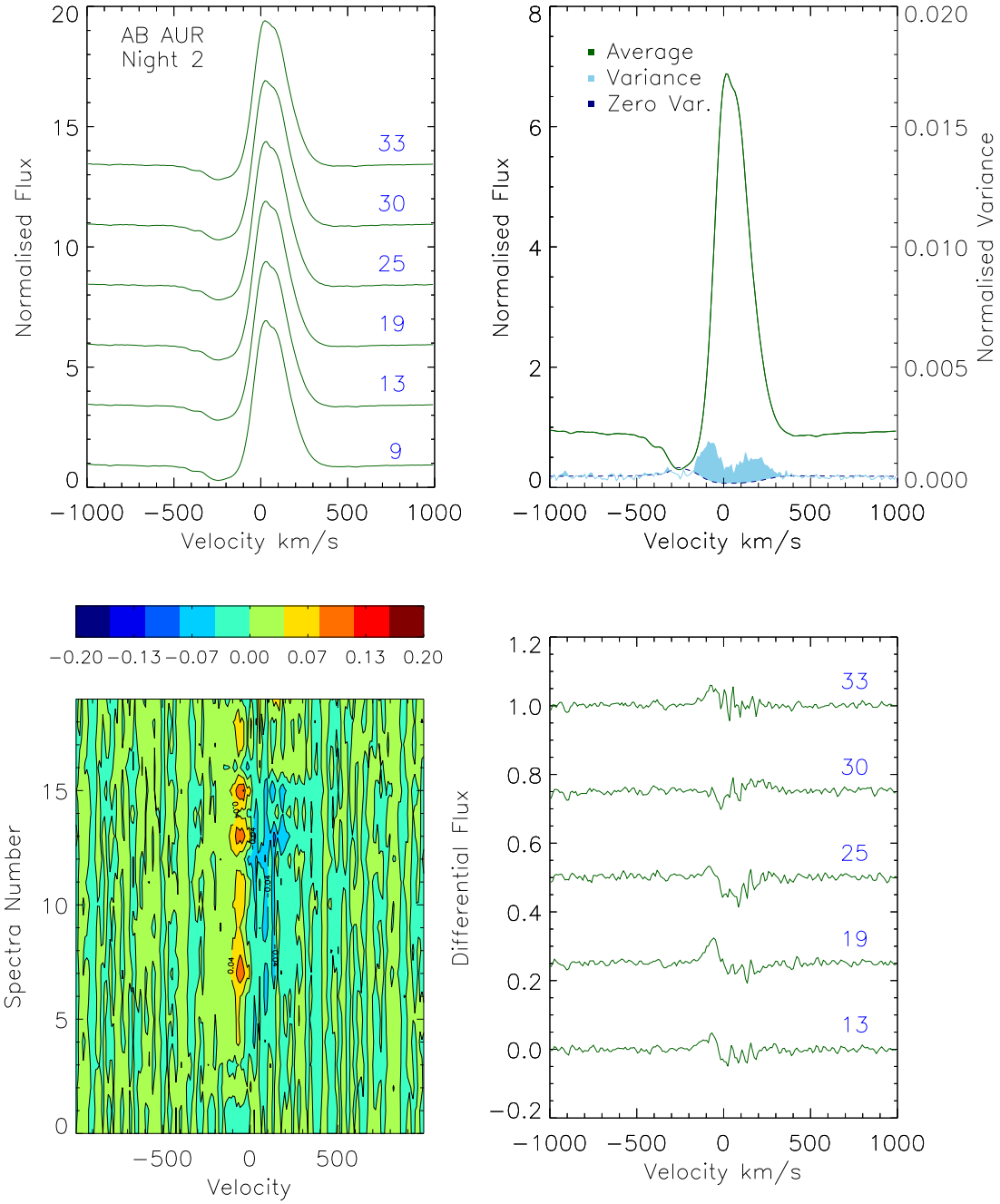

Figure 4.2: *Night 2 of the 2003 observations of AB Aur. Caption the same as Fig. 4.1.*

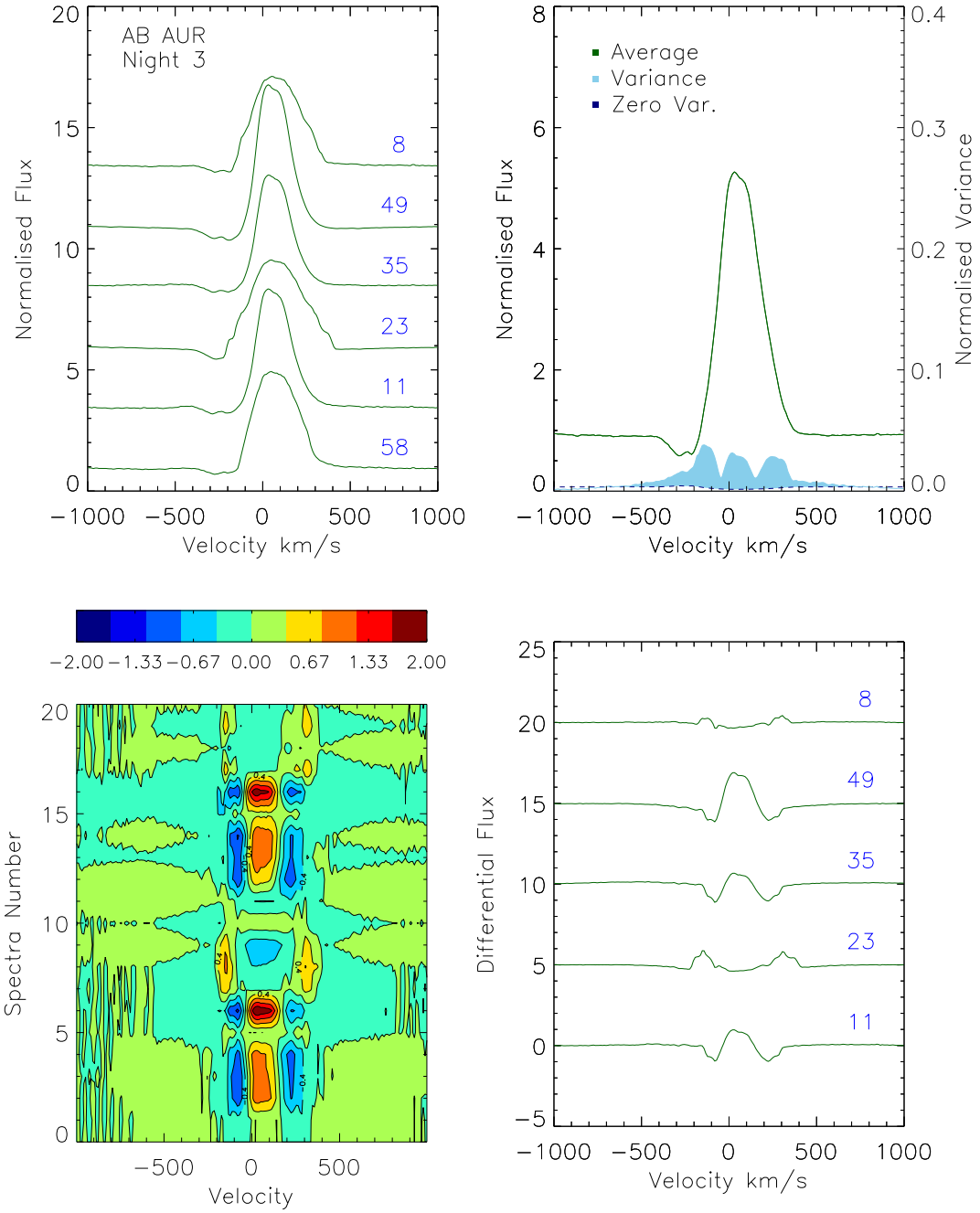

Figure 4.3: *Night 3 of the 2003 observations of AB Aur. Note scale change in the surface plot in bottom left panel. Caption the same as Fig. 4.1.*

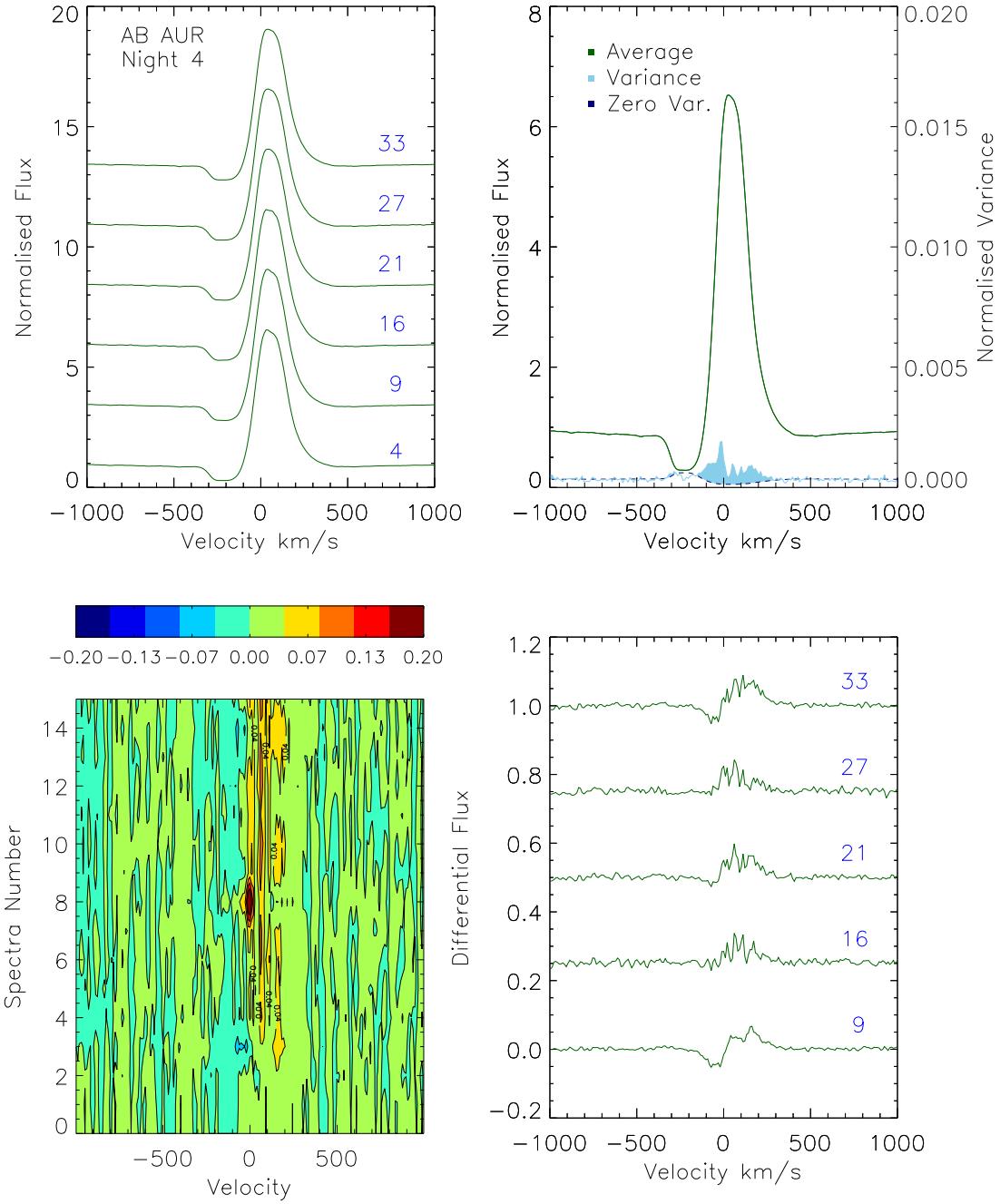

Figure 4.4: *Night 4 of the 2003 observations of AB Aur. Caption the same as Fig. 4.1.*

shifted absorption there is also a small emission peak. Within a single night's observation there is very little change seen within the profile.

Larger changes in the profile can be seen from night to night. For example in the case of AB Aur, the small emission peak within the blue absorption noticeably changes in wavelength. The strength of the emission, the depth of the absorption, and the red wing also change between the nights observations.

It is only on Night 3 of the observations that large changes in the profile are seen from one exposure to the next. These changes occur on the time-scales of *minutes*, and they take the form of a drop in intensity across the line, and a broadening of the emission. These changes will be referred to as *rapid events*. They are not common in the sample. These *rapid events* also occur in the spectra of RY Tau and RW Aur, however they are much weaker than those seen in AB Aur, and show different behaviour.

Object	M_* $[M_\odot]$	Teff [K]	R_* $[R_\odot]$	P_{rot} [days]	$v \sin i$ [km s^{-1}]	Inclin.	Determination of Inclination	Ref.
RY Tau	2.0	6300	2.7	5.6	55±3	30°	Inteferometric	1,33,7,6,5
AB Aur	2.5	9332	2.5	1.4	-	30°	H-Band Imaging	2,4,5,31,16
T Tau	2.0	5250	3.3	2.8	19.5±2.5	29°	Inteferometric	1,19,6,32
SU Aur	2.0	5550	3.1	1.7 - 2.7	59 ± 1	63°	Inteferometric	1,3,7,6
DR Tau	1.0	4060	1.2	5.1	<10	-	-	1,20,7
RW Aur	1.0	4700	2.7	5.6	16 - 40	45°	Jet Inclination	1,17,33
GW Ori	3.7	5700	2.5	3.2	40 - 43	15°	Inteferometric	9,21,22,10,25
V773 Tau	1.2	4900	2.4	3.43	41.4	-	-	10,27,23,11,12
UX Tau	1.3	4900	2.0	2.7	25	50°	Photometry	10,24,13,25
BP Tau	0.8	4000	3.0	7.6	<10	30°	Inteferometric	1,19,1,26,8,34
BF Ori	2.5	8912	1.3	-	37 ± 2	-	-	9,27,14
LkHα 215	4.8	14125	5.4	-	<200	-	-	18,9,27
MWC 480	2.3	8890	2.1	0.5	90	30°	Interferometric	15,29,15
CO Ori	2.5	6030	4.3	-	40 - 50	-	-	28

Table 4.1: *Published Stellar parameters. References: 1: Bertout et al. (1988), 2: Praderie et al. (1986), 3: DeWarf et al. (2003), 4: Bohm & Catala (1993), 5: Mora et al. (2001), 6: Herbst & Layden (1987), 7: Johns & Basri (1995a), 8: Hartmann et al. (1986), 9: Manoj et al. (2006), 10: Kraus & Hillenbrand (2009), 11: Welty (1995), 12: Rydgren & Vrba (1983), 13: Espaillat et al. (2007), 14: Mora et al. (2001), 15: Mannings & Sargent (1997), 16: Catala et al. (1999), 17: Petrov et al. (2001a), 18: Hernández et al. (2004), 19: White & Ghez (2001), 20: Gullbring et al. (1998), 21: Mathieu et al. (1991), 22: Bouvier et al. (1986), 23: Boden et al. (2007), 24: Kenyon & Hartmann (1995), 25: Bouvier & Bertout (1989), 26: Vrba et al. (1984), 27: Hillenbrand et al. (1992), 28: Calvet et al. (2004), 29: Hubrig et al. (2011), 30: Akeson et al. (2003), 31: Fukagawa et al. (2004), 32: Akeson et al. (2002), 33: López-Martín et al. (2003), 34: Simon et al. (2000)*

4.2.2 Average and Variance Profiles

In order to better discern the where the changes in the emission profiles occur, average and variance profiles are utilised. The average profile in this case is simply the average flux at each wavelength and is calculated for observation block separately. The variance profile allows one to distinguish which parts of the emission profile are changing, and which are remaining the same. The equation for the variance and the zero variability level are given as Eq. (3.1) and Eq. (3.2) in Chapt. 3. The zero variability level can be considered the level below which variations are not significant.

The average and normalised variance profiles for AB Aur are given in the top right panels of Fig. 4.1, 4.2, 4.3 and 4.4. The area in the variance profile above the zero variability level i.e. significant peaks of variations are shown as a filled (blue) colour.

Across the four nights there different parts of the Hα profile change. A constant change in intensity across the entire line would result in a variance profile that had the same shape as the emission profile. However for AB Aur there are distinct structures within the variance profile for each night.

For Nights 1 and 2, the changes are concentrated in the wings of the profile. This behaviour is representative of the slow variations seen in the majority of the sample, where most of the changes occur in the line wings rather than the line centre.

On the third night of observations, the rapid variations noted in the time series of the Hα profile manifest themselves as three distinct regions of variations: one peak in the blue wing, one peak in the line centre, and another one in the red wing. (Note the scale change for the variance profile on the third night). This is unusual behaviour within this sample, these large changes are only seen in three observation blocks for three separate objects over the course of these observations. However, no other object shows such strong, distinct peaks in the variance profile as AB Aur.

4.2.3 Distinguishing Variations

The majority of the variations in the profiles are small. So in order to perceive these changes more clearly, differential surface plots and differential time series of the profiles are given for each observation block. (See bottom left and right panel of Fig. 4.1, 4.2, 4.3 and 4.4). The surface plots were created by finding the difference between the first spectrum of that observation block and all the

preceding spectra. These are then plotted as a surface where the difference in flux is color coded. As you move from the bottom of the plot to the top, you are moving through the observation block, and the changes in the surface plot correspond to the differential changes in the profiles across the block.

The bottom right panel in Fig. 4.1, 4.2, 4.3 and 4.4 represents cuts across these surface plots. As with the profiles given in the top left panels, the minute of the hour in which the spectra were observed are given to the right of each differential spectrum.

4.2.4 Line Measurements

In order to quantify the changes in the Hα emission, two measurements of the emission line were taken, the Hα equivalent width (EW), and the Hα 10% width (10%w). (See Sect. 3.2.1, Chapt. 3 for definitions). The integration windows for each source differ and are chosen on the basis of the breadth of the Hα emission. The window size for each object is given in Table 4.3, along with the average, max, min and standard deviation of both the Hα EW and 10%w measurements.

From these measurements it can be noted that the *slow variations* observed across the entire sample do result in small changes in the EW and the 10%w. Much more significant variations occur between each nights observations.

Error analysis was performed by varying the measurement parameters for the EW. The integration window was varied by $\pm$0.5, 1, 1.5, 2, 2.5, 3 Å and continuum measurements were varied by $\pm$1, 2, 3 σ. The mean differences between each of these variations and the 'real' measurement were added in quadrature. The square root of this sum was taken as the error estimate for that spectrum. This was performed on a sub-sample of spectra for each object, and then averaged across the sub-sample of spectra to give an estimate of the errors in the EW measurements. The 10%w is not as sensitive to changes in the continuum as the EW is, and is more difficult to get an proper estimate of the measurement errors using this method. In this case twice the spectral resolution (10 km s^{-1}) can be taken as a rough estimate of the 10%w errors. These EW errors are given in Table. 4.2 and Table 4.3.

Object	Night	*EW* [Å]	Max	Min.	σ	Er.	10%w [km s^{-1}]	Max	Min.	σ	Win [Å]
RY Tau	ALL	10.38	10.64	10.21	0.12	(0.08)	650	660	640	6	25
AB Aur	ALL	24.80	26.81	24.80	0.56	(0.28)	360	360	350	4	25
	1	26.55	26.81	26.35	0.14		360	360	355	2	
	2.1	25.89	26.36	25.60	0.16		360	360	350	4	
	2.2	25.81	26.03	25.51	0.17		360	360	360	0	
	2.3	24.97	25.15	24.80	0.11		360	360	350	4	
T Tau	ALL	71.42	86.51	55.96	12.22	(0.55)	520	525	510	6	25
	1	86.10	86.51	85.79	0.18		520	525	510	8	
	2	61.64	64.28	55.96	1.93		515	525	510	4	
SU Aur	ALL	4.65	5.43	3.91	0.69	(0.08)	550	560	535	6	20
	1	3.98	4.05	3.93	0.04		555	560	545	5	
	2	5.33	5.43	5.24	0.06		545	555	535	7	
DR Tau	ALL	65.32	78.69	58.50	7.53	(0.68)	659	689	625	20	25
	1	78.16	78.69	77.49	0.43		685	690	670	8	
	2	61.31	63.45	58.50	1.86		650	680	625	15	
RW Aur	ALL	74.04	81.11	67.88	3.95	(3.6)	720	725	715	5	40
GW Ori	ALL	19.33	19.52	19.06	0.14	(0.16)	505	505	490	6	25
BF Ori	ALL	3.88	4.21	3.44	0.23	(0.86)	495	505	490	5	25
LkHα 215	ALL	30.45	30.72	29.87	0.22	(0.22)	690	700	680	5	30
MWC480	ALL	11.85	15.11	9.65	1.87	(0.36)	-	-	-	-	30
	1	11.21	11.74	10.48	0.37		-	-	-	-	
	2	10.53	11.54	9.65	0.74		-	-	-	-	
	3	14.86	15.11	14.65	0.13		-	-	-	-	
	4	10.71	11.75	9.85	0.78		-	-	-	-	
CO Ori	ALL	7.57	7.91	7.22	0.19	(0.1)	585	600	560	10	20

Table 4.2: *Average Hα EW and 10%w measurements for 2001 observations. Also given are the max, min measurements and the standard deviations (σ) across the range of measurements. Window is the integration window over which EW and 10%w were calculated. No 10%w measurements are given for MWC 480 as the entire blue wing is in absorption.*

Object	Night	*EW* [Å]	Max	Min.	σ	Er.	10%w [km s^{-1}]	Max	Min.	σ	Win [Å]
RY Tau	ALL	17.62	24.52	14.85	3.59	(0.11)	670	710	640	18	25
	1	23.08	24.52	20.37	1.43		690	710	680	8	
	2	14.98	15.16	14.85	0.11		675	680	665	4	
	3	15.90	16.02	15.73	0.08		655	660	640	5	
AB Aur	ALL	22.87	25.92	19.99	1.84	(0.21)	385	550	340	54	25
	1	25.56	25.92	25.30	0.21		370	370	370	0	
	2	23.65	23.78	23.47	0.09		360	360	360	0	
	3	22.72	23.49	21.17	0.60		445	550	345	62	
	4	20.10	20.26	19.99	0.08		345	345	340	2	
T Tau	ALL	47.03	48.02	46.51	0.47	(0.39)	445	450	445	2	25
SU Aur	ALL	5.71	8.09	3.60	1.91	(0.09)	575	610	540	23	20
	1	7.96	8.09	7.56	0.13		590	600	580	4	
	2	4.34	4.49	3.93	0.16		550	565	540	6	
	3	3.68	3.95	3.60	0.09		560	610	585	8	
DR Tau	ALL	80.48	81.47	78.74	0.70	(0.29)	640	645	630	5	50
RW Aur	ALL	64.66	77.13	34.57	13.54	(3.18)	720	740	705	9	40
	1	48.54	52.32	36.57	3.67		730	740	720	5	
	2	75.41	77.13	73.34	0.93		715	720	705	5	
GW Ori	ALL	33.16	33.32	32.99	0.07	(0.12)	405	410	400	3	25
V773	ALL	1.85	1.98	1.73	0.06	(0.04)	455	475	440	7	25
UX Tau	ALL	8.72	9.23	8.28	0.29	(0.05)	440	455	425	9	25
BP Tau	ALL	92.57	103.49	88.63	4.50	(0.44)	480	500	450	13	30
	1	103.25	103.49	102.97	0.22		455	460	450	5	
	2	91.04	94.42	88.63	1.97		485	500	470	9	

Table 4.3: *Average Hα EW and 10%w measurements for 2003 observations. Also given are the max, min measurements and the standard deviations (σ) across the range of measurements. Window is the integration window over which EW and 10%w were calculated.*

4.2.5 Plausibility Checks

A number of tests were performed to determine whether the *slow variations* observed in the sample are real changes within the line profile, and not because of some changes in the instrumental set up or weather. These are listed below.

- The changes in the line measurements were compared to the changes in the signal-to-noise (S/N) in each observations. In the majority of cases, the changes in the EW or 10%w do not follow the changes in the S/N. There is one object, RY Tau for which changes in the intensity across the line correspond to changes in the S/N (See Appendix A, Fig. A.14). This occurs in the first nights observations in 2003, but there is a similar change in S/N during the second night without any corresponding change to the EW measurement, so the two events are not considered to be connected.

- With regards to the *rapid events* in the profile of AB Aur, tests were also run on the sky subtraction around Hα. This was found not to be the cause of these changes.

- Instrumental set-up was checked for any changes between observations, no differences were found. The dispersion axis changed between the 2001 and 2003 observations, and as a result the wavelength range is smaller ($\sim$ 200Å) in the 2001 observations. However this does not effect our observations of the Hα emission line.

- There were changes in the weather conditions across the four nights, but these would result in a change in the intensity across the entire profile rather than a change in the profile structure.

As a result of these checks, the variations observed in the profiles are believed to be true variations in the emission from these objects.

4.3 Origin of Hα Emission

The most dominant known sources of Hα emission in young stellar objects are chromospheric activity and accretion. All the objects are likely candidates for accretion, as they are all thought to have circumstellar discs at sufficiently young ages. There is a number of ways to determine whether the emission is solely from chromospheric activity or not.

4.3.1 Hα Measurements

The most common method to determine whether a stellar object is accreting or not is to use the Hα EW and 10%w measurements. The standard limits between an accreting and a non-accreting T Tauri star are EW of 10 Å and a 10%w of 270 kms^{-1} (White & Basri 2003). The limits in the EW come from the fact that these young stars are active and show some level of Hα emission from chromospheric activity alone. This activity is much weaker than the emission we expect from accretion especially in the case of T Tauri and Herbig Ae/Be stars (e.g. Manara et al. 2013). As chromospheric Hα emission depends strongly on spectral type, for the T Tauri stars in the sample we use a a spectral type dependent cut-off as given by Barrado y Navascués & Martín (2003).

The 10%w provides a measure of the broadening of the emission line. As the material in the accretion flows is free-falling to the stellar surface, it can reach velocities of 100s of km s^{-1}. These high velocities are then reflected in the broadening of the Hα line, and can be estimated by the 10%w of the emission line.

Using the EW cut-off based on spectral types by Barrado y Navascués & Martín (2003), and from Hα 10%w >270 km s^{-1} we can classify all of our sample objects as accretors. The mean Hα EW and 10%w measurements for each object are given in Table 4.3.

For Herbig Ae objects, the chromospheric contribution to the Hα emission is likely to be very insignificant, as the emission decreases in earlier spectral types. In fact, it is more important to take consideration of the photospheric absorption in these objects. For example, in comparison to main sequence objects of the same spectral type, Pickles (1998) give an absorption strength of 98 Å for A0, 93 Å for B1, 32 Å for F8, 25 Å for G2 and 0 Å for K5. This is quite significant compared to the emission measured in some of the early targets, and hence the EW measurements are underestimating the strength of the Hα emission in the sample. To account for this photospheric absorption, it is common to fit the observed spectrum with a main sequence spectrum to estimate the photospheric contribution. Mendigutía et al. (2011) removed the photospheric absorption in this way for a number of objects in this sample. For BF Ori, Mendigutía et al. (2011) measured a mean EW of 9.9 Å compared to 3.8 Å here, for CO Ori they found 21.3 Å compared to 7.6 Å here and for RY Tau 15.3 Å compared to 10.4 Å in 2001 and 17.6 Å in 2003 here.

This shows the removal of the absorption results in a significant difference for the weaker lines but not for the stronger emission lines. However the removal or

non-removal of the absorption will simply produce a systematic offset in the final measurement. As the photospheric absorption is considered to remain constant, it will not effect the variability measured in the line. Since this work is focused on the variations in these lines, and not on the absolute measurements, the photospheric absorption is not removed.

4.3.2 Average and Variance Profiles

A *typical* characteristic of an accreting system is an asymmetric Hα emission line, often with more than one emission peak and overlying absorption features. Under the magnetospheric accretion model, the Hα emission originates in a structured flow of material. This results in emission across a large velocity range. Stellar winds and jets are associated with accreting systems (Ray et al. 2007), and can contribute both in the form of excess emission to the Hα line and overlying absorption features (see next Sect. 4.3.4). This can been seen in many of Hα profiles in our sample. The average profiles for the sample show that the majority of the profiles are asymmetric, with many of them showing large absorption features.

Over-plotted in blue on each average profile in the top right panel of Fig. 4.1, 4.2, 4.3 and 4.4 are the variance profiles for each object and each observation block. These profiles indicate clearly which parts of the profiles show the most changes. In most cases where large changes occur they are confined to discrete wavelength ranges. This is also further evidence that there are multiple components within the emission lines and that it is not all from a single point i.e., the central star.

4.3.3 Chromospheric versus Accretion

There have been limited studies into the activity in accreting stars, mainly because both accretion and chromospheric activity cause similar emission in certain emission lines (Hα, Ca, He etc.) as well as UV and X-ray excess emission (Curran et al. 2011; Fuhrmeister et al. 2008). However there has been some recent work on chromospheric activity by Manara et al. (2013), focusing on lower mass objects than in this sample.

Flares have distinct rise and decay profiles by comparison to accretion events, making this one of the most commonly used attributes to distinguish between the two events. So, if a rapid rise in EW occurs, followed by a slow decay, it is usually attributed to a flare. Guenther & Ball (1998) found accretion and

flare events using spectroscopic monitoring of WTTS and CTTS. From $\sim$ 9500 spectra of CTTS, and 7200 of WTTS in Chamaeleon and Taurus they found 24 flares in WTTS and 15 in the CTTS. The largest flare was found in a WTTS. Whilst they claim that flare activity on T Tauri stars is more common than solar flares, these numbers show that these events do not occur very often in either CTTS or WTTS. Guenther & Ball (1998) also observed many slow variations in EW across a night's observation which they attribute to rotation, or variations in accretion rate.

One definitive attribute of flares is that the Hα emission associated with it is nearly entirely limited to the line centre with some extension in the wings up to $<$100 km s^{-1} (Robinson et al. 1990; Worden et al. 1981a). This can be seen in the observations of the CTTS by Guenther & Ball (1998), where the flaring produces relatively small symmetric emission peaks (20% above the continuum). In some cases small asymmetries in the emission lines were seen, which are thought to be connected to coronal mass ejections (CMEs). For Hα this took the form of excess emission in the blue wing which moved through the line as the material is ejected from the atmosphere of the star. However, in the case of the WTTS IM Lupi, the authors argued that the asymmetries observed in the Hα profile are more likely to be associated with accretion activity rather than a flare (Günther et al. 2010).

In T Tauri stars, the range of time-scales for flare events is 10^2 - 10^4 s (Worden et al. 1981b). Although the sample does not have exhaustive time coverage, the *rapid events* do not show the typical fast rise and slow exponential decay expected of flares. Stellar flares can rise to a peak within a few minutes, while the decay can also happen within half an hour or so (Liefke et al. 2010), but it is much more usual to have flares lasting hours to days (Favata et al. 2000; Kuerster & Schmitt 1996; Schmitt & Favata 1999).

Finally, the strength of the Hα emission from accretion is much larger than emission from the majority of flares. This, it is expected that any change in accretion rate will have a much stronger effect on the emission line profile than any flare activity.

Thus the variations and morphology of the emission seen in this sample, make it unlikely that the majority of the events are from chromospheric activity.

4.3.4 Emission from Outflows

The traditional tracers of outflows and jets in young stellar objects are forbidden emission lines such as [OI] λ6300, 6363 Å, [NII] λ6583 Å, and [SII] λ6716,

6731 Å (Hartigan et al. 1995). However, it has also been shown using spectro-astrometry that these outflows can contribute to the Hα emission. This mostly takes the form of additional emission on the blue side, but cases have been found in which there is excess emission from the outflows found in both the blue and the red wings (Takami et al. 2003; Whelan et al. 2009).

Within the sample, signatures of [OI] λ6300 and 6363 Å were found in many of the targets (see Table 4.4), indicating that there is an outflow from these objects. In the majority of cases the emission line was very narrow and weak ($\sim$ 1 Å). This suggests that though there is probably some wind emission contaminating the Hα line, it is going to be a weak contribution.

Since the density of the out-flowing material is much lower than the densities in the accretion flows, a small change in an accretion flow will produce the same change in emission as a large change in the outflow rate. This, along with the fact that the accretion emission will always be stronger in the Hα line than the outflow emission in an accreting object, makes it more likely that it is an accretion rate change. However, it cannot be ruled out that changes in the outflow have some contribution to the variations, so any accretion rate variations derived in this work are upper limits.

As a potential caveat, interferometric observations of the Herbig Be star, MWC 297 have found over 90% of the Brγ emission to originate in a disk wind (Malbet et al. 2007) . Further high-resolution spectra were taken, and modelling of the Brγ observed emission lead to the conclusion that the Brγ, Hα and Hβ all formed in a disc wind, with the majority of the Hα and Hβ emission originating in the polar regions. Optical spectra were taken of MWC 297 from which an EW of 649 Å was found for Hα (Drew et al. 1997). Note this is an order of magnitude higher than any Hα measured in this sample. Malbet et al. (2007) compared their wind model to these spectra and found the intensity of the Hα and Hβ lines to agree to within 10% of observed intensities, and also found a good agreement between the model line widths and those observed. Kraus et al. (2008) also found connections between Bγ emission and stellar wind in four out of five Herbig Ae/Be stars using interferometric data. In particular they find the emitting area of the Brγ emission line to be correlated with the Hα profile. If a star shows an inverse P-Cygni profile, and a high accretion rate, the Brγ line is more likely to come from the accretion column, whereas if the Hα emission line is single or double peaked, Brγ is emitted in a greater area consistent with a disc or stellar wind. These interferometry results (Kraus et al. 2008) are in line with the earlier Hα spectro-polarimetry work of Vink et al. (2002), where

Name	Year	[OI] λ6300Å	[OI] λ6363Å	HeI λ6678.2Å
RY Tau	2003	Yes	No	No
	2001	-	No	No
AB Aur	2003	Yes	Yes	Yes
	2001	-	Yes	Yes
T Tau	2003	Yes	No	No
	2001	-	No	No
SU Aur	2003	No	No	No
	2001	-	No	No
DR Tau	2003	Yes	Yes	Yes
	2001	-	Yes	Yes
RW Aur	2003	Yes	Yes	Yes
	2001	-	Yes	Yes
GW Ori	2003	Yes	Yes	No
	2001	-	No	No
V773 Tau	2003	Yes	No	No
UX Tau A	2003	Yes	No	No
BP Tau	2003	Yes	No	Yes
BF Ori	2001	-	Yes	No
LkHα 215	2001	-	No	No
MWC 480	2001	-	No	Yes
CO Ori	2001	-	No	Yes

Table 4.4: *Detections of other emission lines. [OI] λ6300 and λ6363 Å are associated with wind emission. The wavelength coverage is slightly smaller in the 2001 observations, so the [OI]λ6300 is not covered by these observations. No [SII] (λ6715, 6729Å) or [NII] (λ6548.4, 6583.4Å) emission were detected in any of the observations, are usually associated with stellar jets. The emission line HeI λ 6678.2Å which was detected in a number of targets, which is associated both with outflows and accretion.*

it was found that the later Herbig Ae stars have a compact line-forming region, similar to that seen in T Tauri stars (Vink et al. 2005, 2003), whilst the earlier type Herbig Be stars have a larger line-forming region.

As this sample does not contain Herbig Be stars, it can be argued that it is not necessary to be overly concerned about disk winds providing the line emission in the sample. Moreover, recent studies of accretion diagnostics in Herbig Ae/Be stars (F0 - O9) using the large wavelength coverage of X-Shooter (300 - 2500 nm) have also taken place. Pogodin et al. (2012) found that accretion rates derived from Hα to be in good agreement with accretion rates derived from indicators which can only originate in the high temperature region close to the stellar surface. The variations in the Hα accretion rate were also found to follow the accretion rates from the other indicators, and showed a similar magnitude of variations. This is a strong suggestion that the changes in the Hα emission of Herbig Ae/Be stars follow the changes in accretion rate, or if Hα is indeed primarily a wind indicator for all these objects, then the wind emission is very closely connected to the accretion emission as suggested by magnetospheric accretion models.

Similarly, Mendigutía et al. (2013) found a close agreement between the accretion rates derived from the Balmer excess and Hα emission in two Herbig Ae stars (one is also in this sample, MWC 480). Despite this agreement, they suggest the variations in the Hα line emission to be uncorrelated to the variations in the Balmer excess. This is an indication that there is either a time delay in the variations in the emission lines that is not seen in the low mass accretors, or the variations in the lines originate from some other process than accretion. Nonetheless, the level of the variations in these cases are low, so the correlation could be washed out by any noise in the observations. More sensitive observations are needed to confirm this.

Multi-wavelength studies with X-shooter have also been undertaken with T Tauri stars (Rigliaco et al. 2012), which again find the Hα emission to be correlated with the UV excess and other indicators. There is substantial evidence confirming the effectiveness of using the Hα emission as an accretion rate estimator across the whole mass range of this sample, even if it is partially contaminated by wind emission.

4.3.5 Variations from Continuum Changes

Changes in the accretion rate will lead to changes in the veiling in the stellar continuum. This can lead to measured changes in the EW while the line emission

remains steady. As the spectra in this work are not flux calibrated, changes in the continuum cannot be accounted for. The majority of the targets in this sample are optically variable (i.e. see Grankin et al. (2007) for light curves of 8 targets), and so it can be expected that some changes in the continuum level occur over the course of these observations.

However a change in the continuum will lead to a change in the emission across the whole line. This is not what is seen in this sample (i.e. see Fig. 4.1). The variance profiles attest to the fact that the variations measured originate in a narrow wavelength ranges within the profiles. This strongly suggests that even if there are continuum changes during the observations they are not significant compared to those changes that occur within the profile emission.

It has been reported that continuum changes in these objects are also likely to come from occultations of the star by orbiting circumstellar clouds (Grinin et al. 1994; Mendigutía et al. 2011). However these occultations will cause both a fall in the continuum and line emission, and so need not be taken into account here.

4.3.6 Previous Observations

The objects within the sample are mostly well studied objects. Many of them have previous observations of other accretion related emission lines, as well as confirmed accretion with UV excess measurements, which is considered to be the most direct indicator of ongoing accretion. These detections are discussed on an individual object basis in Appendix A.

The above arguments point towards accretion being the primary source of the emission observed and the variations in the emission lines. Through the following sections, it is assumed that the contribution of chromospheric and wind emission to the Hα line is negligible, and that any variations observed are the result of changes in the accretion rate.

4.4 Accretion Rates

Making the assumption that all of the Hα emission originates in accretion flows, the accretion rates can be calculated from the Hα EW measurements for all objects in the sample.

As in the LAMP sample (See Chapt. 3) the relation derived by Herczeg & Hillenbrand (2008) between the luminosity of Hα ($L_{H\alpha}$) and accretion luminosity

(L_{acc}) is used. In order to convert an Hα EW to luminosity, it is first necessary to convert the EW to a flux. This was done by using the Kurucz models (Kurucz 1979) to compute the continuum flux in the range 6450 - 6500 and 6620 - 6720 Å. Using these continuum estimates the EW can be transformed to a flux per unit area on the stellar surface ([ergs sec^{-1}cm^{-2}]), which is then converted to a luminosity using the published stellar radii given in Table 4.1. The relation derived by Herczeg & Hillenbrand (2008) for Hα is then given by

$$\log(L_{\rm acc}) = {\rm A} + {\rm B} \cdot \log(L_{\rm H\alpha}) \tag{4.1}$$

where A = 2.0 ± 0.4 and B = 1.20 ± 0.11. $L_{\rm H\alpha}, L_{\rm acc}$ are in units of $L_{\odot}$. This equation is used to determine accretion luminosities but the spread coefficients is not taken into account as they originate from the empirical derivation of this relation. Assuming that all the gravitational energy from the accretion is converted into luminosity, the accretion luminosity is related to the accretion rate ($\dot{M}$) as follows (Herczeg & Hillenbrand 2008):

$$\dot{M} = \left(1 - \frac{R_*}{R_{\rm in}}\right)^{-1} \cdot \frac{L_{\rm acc} R_*}{G M_*} \tag{4.2}$$

Here R_* is the stellar radius, $R_{\rm in}$ is the in-fall radius and M_* is the stellar mass. Gullbring et al. (1998) approximates the factor $(1 - \frac{R_*}{R_{\rm in}})^{-1} \sim 1.25$, assuming $R_{\rm in} \sim 5R_*$, which is appropriate for T Tauri stars. An infall radius of $R_{\rm in} \sim 2.5R_*$ has been calculated to be more suitable for the higher rotation velocities in Herbig Ae stars (Muzerolle et al. 2004). Observations of inner hole sizes were provided in the linear spectro-polarimetry study of Vink et al. (2005), these were used where possible, along with other published values. For the rest of the sample, an infall radius of $5R_*$ was assumed for the lower mass stars, and in keeping with observations of Herbig Ae stars, an infall radius of $3R_*$ was assumed for the higher mass objects. The assumed infall radii, continuum estimates from the models, and the published stellar mass and stellar radii used in the accretion calculations are all given in Table 4.5.

The mean accretion measurements for each object and for each night are give in Table 4.6. Also given, are error estimates, calculated by carrying the Hα EW estimated errors through the accretion relations.

Object	M_* $[M_\odot]$	R_* $[R_\odot]$	$F_{cont}(H\alpha)$ $[10^6]$	R_{in} $[R_*]$	Ref.
RY Tau	2.0	2.7	8.35499	10	1
AB Aur	2.5	2.5	34.2899	5	2
T Tau	2.0	3.3	4.87506	5	A
SU Aur	2.0	1.0	8.35499	3	2,3
DR Tau	1.0	1.2	1.60352	10	1
RW Aur	1.0	2.7	2.99850	5	A
GW Ori	3.7	2.5	8.35499	3	2
BF Ori	2.5	1.3	27.3585	3	A
LkHα 215	4.8	5.4	57.8910	3	A
MWC 480	2.3	2.1	27.3585	3	A
CO Ori	2.5	4.3	9.73760	5	A
V773 Tau	1.2	2.4	4.87506	5	A
UX Tau	1.3	2.7	4.87506	5	A
BP Tau	0.8	7.6	1.60352	5	A

Table 4.5: *Parameters used in the derivation of accretion rates. The continuum under the Hα line was estimated from the Kurucz (1993) stellar atmosphere models. Fluxes are in units of [ergs sec^{-1}cm^{-2}Å^{-1}]. References for stellar masses and radii are given in Table. 4.1. For some objects in the sample, estimates of inner radii from observations were available. For the majority of the sample, an inner radii was assumed (indicated by A). References for infall radii: 1: Kitamura et al. (2002). 2: Vink et al. (2005) 3: Akeson et al. (2002). See Sect. 4.4 for more.*

2001	Log($\dot{M}$)		Night 1		Night 2		2.2		2.3		Error
	Av.	[Sprd]	Av.	[Sprd]	Av.	[Sprd]	Av.	[Sprd]	Av.	[Sprd]	
RY Tau	-7.720	[0.022]									(0.004)
AB Aur	-6.669	[0.041]	-6.654	[0.009]	-6.668	[0.009]	-6.669	[0.010]	-6.686	[0.007]	(0.006)
T Tau	-6.612	[0.227]	-6.507	[0.004]	-6.681	[0.007]					(0.004)
SU Aur	-7.810	[0.169]	-7.885	[0.016]	-7.734	[0.019]					(0.009)
DR Tau	-7.804	[0.154]	-7.708	[0.008]	-7.835	[0.042]					(0.005)
RW Aur	-7.322	[0.093]									(0.020)
GW Ori	-7.647	[0.012]									(0.004)
BF Ori	-8.285	[0.062]									(0.050)
LkHα 215	-5.541	[0.015]									(0.004)
MWC 480	-7.341	[0.233]	-7.364	[0.059]	-7.397	[0.093]	-7.217	[0.016]	-7.388	[0.092]	(0.016)
CO Ori	-6.036	[0.048]									(0.007)
2003	Log($\dot{M}$)		Night 1		Night 2		Night 3		Night 4		Error
	Av.	[Sprd]	Av.	[Sprd]	Av.	[Sprd]	Av.	[Sprd]	Av.	[Sprd]	
RY Tau	-7.454	[0.261]	-7.305	[0.097]	-7.529	[0.011]	-7.498	[0.010]			(0.003)
AB Aur	-6.732	[0.128]	-6.676	[0.011]	-6.716	[0.007]	-6.734	[0.057]	-6.795	[0.007]	(0.005)
T Tau	-6.822	[0.017]									(0.004)
SU Aur	-7.726	[0.421]	-7.524	[0.035]	-7.841	[0.07]	-7.927	[0.047]			(0.009)
DR Tau	-7.693	[0.017]									(0.002)
RW Aur	-7.405	[0.341]	-7.546	[0.133]	-7.312	[0.026]					(0.030)
GW Ori	-7.365	[0.005]									(0.002)
V773 Tau	-8.788	[0.007]									(0.011)
UX Tau	-8.297	[0.057]									(0.003)
BP Tau	-7.418	[0.084]	-7.357	[0.026]	-7.426	[0.033]					(0.002)

Table 4.6: *Accretion rates derived from Hα EW. The average for all observations in 2001 and 2003 campaign is given, as well as the average for each observation block in the cases of multiple observations. Following each average is the [max - min] spread in accretion rates over the observation period. Units are $M_{\odot}.yr^{-1}$. Errors are calculated by carrying the Hα EW errors through the accretion rate calculation.*

Object	Log($\dot{M}$) 2001		Log($\dot{M}$) 2003		Both	
	Av.	[Sprd]	Av.	[Sprd]	Av.	[Sprd]
AB Aur	-6.669	[0.041]	-6.732	[0.128]	-6.701	[0.149]
RY Tau	-7.720	[0.022]	-7.454	[0.261]	-7.513	[0.457]
SU Aur	-7.810	[0.169]	-7.726	[0.421]	-7.748	[0.421]
RW Aur	-7.322	[0.093]	-7.405	[0.341]	-7.387	[0.367]
DR Tau	-7.804	[0.154]	-7.693	[0.017]	-7.745	[0.172]
T Tau	-6.612	[0.227]	-6.822	[0.017]	-6.659	[0.323]
GW Ori	-7.647	[0.012]	-7.365	[0.005]	-7.442	[0.291]

Table 4.7: *Comparison of Accretion rates from 2003 and 2001 observations. Here the average for each years observations are given, along with the spread [max - min]. Also given is the average over both periods and the spread in accretion rate estimates. Units are* $M_{\odot}.yr^{-1}$.

Note, this relation (Eq. 4.1) was derived using the entire line emission. Therefore it includes excess emission from wind and chromosphere, the effects of which will have been averaged out over the calibrating sample. The absolute value is then close to what would be measured from the UV excess, but the variations can still be affected by these extra sources of emission.

The mean accretion rate spread for a single night for Hα EW is 0.01 - 0.03 dex. Half of the sample have multiple nights observations so a measure of the spread in accretion rates from one night's observation to the next could be obtained. This inter night spread, 0.1 - 0.4 dex, is an order of magnitude larger than the spread on a single night. There are 7 targets that have observations in both 2001 and 2003 (See Table 4.7), when comparing the accretion rates for these 7 objects over the 2 years the spread is 0.15 - 0.46 dex.

4.4.1 Comparison with Other Accretion Rate Relations

The Herczeg & Hillenbrand (2008) accretion rate relation was empirically derived in a sample of low mass stars that reached up to 1 $M_{\odot}$. As the sample in this work includes objects with greater masses, the differences between the relation of Herczeg & Hillenbrand (2008) and another covering Herbig Ae/Be stars was examined.

Mendigutía et al. (2011) derive a relation of the same form as Eq. 4.1, with coefficients $A = 2.28\,(\pm 0.25)$ and $B = +1.09\,(\pm 0.16)$. The sample used in this case was focused on higher mass objects from $\sim$ 1.5 - 5 $M_{\odot}$, but was derived using photospheric corrected Hα emission (See Sect. 4.3.1).

The accretion rates derived using the Herczeg & Hillenbrand (2008) relation $\log(L_{\rm acc}) = (2.0 \pm 0.4) + (1.20 \pm 0.11) \cdot \log(L_{\rm H\alpha})$ and the Mendigutía et al. (2011)

relation $\log(L_{\rm acc}) = (2.28 \pm 0.25) + (1.09 \pm 0.16) \cdot \log(L_{\rm H\alpha})$ are compared in Table 4.8.

It can be seen that the absolute accretion rates for each of the relations differ. The Mendigutía et al. (2011) relation consistently gives higher accretion rates than the Herczeg & Hillenbrand (2008) relation. This was pointed out by Pogodin et al. (2012), who also found the accretion rates derived by Mendigutía et al. (2011) to be consistently higher than those derived by Donehew & Brittain (2011) and Garcia Lopez et al. (2006).

However the variations derived are very similar, in the majority of cases the differences lie within the estimated errors. For this reason it is argued that using the relation of Herczeg & Hillenbrand (2008), even though it is derived using lower mass objects, it does not produce any systematics when we consider the variations in accretion rates of the higher mass objects. It also allows for a consistent comparison across the entire sample, and with the previous LAMP sample.

The Hα 10%w has also been used to estimate the accretion rate (see Sect. 3.4.1, Chapt. 3). A relation for low mass T Tauri and brown dwarfs was derived by Natta et al. (2004), and is useful in the cases where little or no stellar continuum can be detected. It has been proved to be a very good indicator of accretion (White & Basri 2003), as was shown with the LAMP sample (See Chapt. 3), however its accuracy as a measurement of accretion has been called into question. In the LAMP sample it was shown to have much larger variations than the two other accretion indicators, Hα EW and Ca II EW, demonstrating it is more likely to be affect by wind emission and line broadening processes other than the free-fall velocities within the accretion flow. Mendigutía et al. (2011) show that in higher mass Herbig AeBe stars, the 10%w is strongly correlated with rotational velocities, and no correlation is found between the accretion rate and 10%w measurements. To test for this within this sample, the derived Hα EW derived accretion rate is plotted against the corresponding 10%w in Fig. 4.5. This plot again confirms that there is very little correlation between the two accretion indicators, and for this reason no accretion rates derived from the 10%w are discussed in this work.

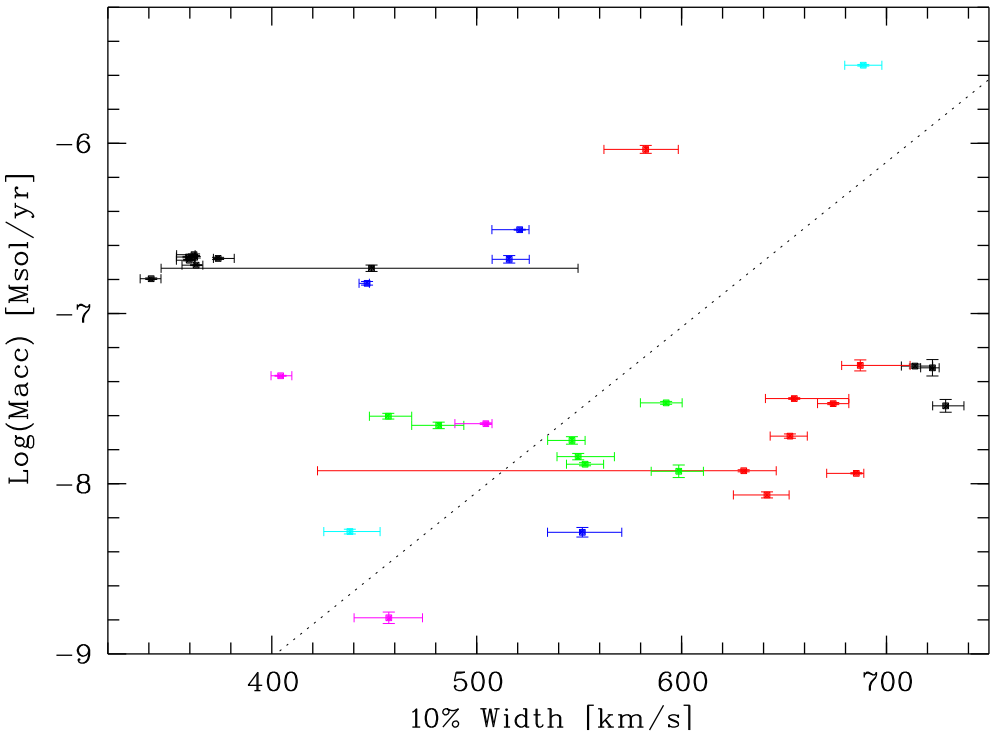

Figure 4.5: *Average Hα EW derived accretion rate versus the average Hα 10%w. Error bars represent the max - min spread in each. Measurements for each observation block of each object are compared, and the colours represent different objects. The over-plotted dashed line is the accretion rate to 10%w relation* $Log(M_{acc}) \sim -12.9 + 0.0097 \cdot (10\%w)$ *empirically derived by Natta et al. (2004) for brown dwarf and T Tauri objects. As found previously by Mendigutía et al. (2011), this plot shows that the two measurements are not correlated in the higher mass regime.*

Relation	Average Log($\dot{M}$)		Night 1		Night 2		Night 3		Night 4		Error
	Av.	[Sprd]	Av.	[Sprd]	Av.	[Sprd]	Av.	[Sprd]	Av.	[Sprd]	
2001 AB Aur											
H&H	-6.669	[0.041]	-6.654	[0.009]	-6.668	[0.009]	-6.669	[0.010]	-6.686	[0.007]	(0.006)
Mend	-6.272	[0.037]	-6.259	[0.008]	-6.271	[0.009]	-6.272	[0.009]	-6.288	[0.007]	
2003 AB Aur											
H&H	-6.732	[0.128]	-6.676	[0.011]	-6.716	[0.007]	-6.734	[0.057]	-6.795	[0.007]	(0.005)
Mend	-6.330	[0.116]	-6.289	[0.010]	-6.315	[0.007]	-6.331	[0.052]	-6.387	[0.007]	
2001 MWC 480											
H&H	-7.341	[0.233]	-7.364	[0.059]	-7.397	[0.093]	-7.217	[0.016]	-7.388	[0.092]	(0.016)
Mend	-6.879	[0.212]	-6.900	[0.054]	-6.930	[0.085]	-6.766	[0.015]	-6.922	[0.084]	
LkHα 215											
H&H	-5.541	[0.015]									(0.004)
Mend	-5.251	[0.013]									

Table 4.8: *Comparison of the accretion rates derived for the largest targets in sample, using two different accretion rate relations. H&H: $log(L_{acc}) = (2.0 \pm 0.4) + (1.20 \pm 0.11) \cdot log(L_{H\alpha})$, Herczeg & Hillenbrand (2008) and Mend: $log(L_{acc}) = (2.28 \pm 0.25) + (1.09 \pm 0.16) \cdot log(L_{H\alpha})$, Mendigutía et al. (2011). The absolute accretion rate changes in each case, but the variations are relatively unchanged and any differences are on the same scale as the estimated errors.*

4.5 Discussion

As previously mentioned, there are two distinct types of behaviour observed in this sample, *slow variations* and *rapid events*. In the following section possible origins of each are discussed.

4.5.1 Slow Variations: Rotational Modulation of the Accretion Rate

In the majority of the cases in this sample, small changes are seen in the profiles across the time-scale of our observation blocks. These variations are referred to as *slow variations*. These occur in discrete wavelength ranges, and take the form of a gradual change in the profile emission. These variations do not translate to large accretion rate changes and on average they result in changes of the accretion rate derived from Hα EW of 0.01 - 0.09 dex. When the changes between different nights of observations are examined in this sample, the spread in accretion rate variations increases slightly to 0.1 - 0.4 dex (see Table 4.6). Comparing the difference in derived accretion rates for the objects with observations in 2001 and 2003 this spread does not increase from the individual observation periods remaining at 0.15 - 0.46 dex. This is a strong indication that the time-scales of days are the dominant time-scales for these variations.

Fig. 4.6 shows a comparison of accretion rate variations on all the time-scales in the sample. For each object every accretion rate measurement is compared with every other accretion rate measurement for that object. In this way all the time-scales available in the sample can be exploited. The mean accretion rate is then plotted for each time bin for that object. In all cases but two, the variations reach a maximum after the first few days of observations. It shows that the dominant time-scale of variations in this sample is on the order of days. Two objects do show a rise in variations on the year time-scales, GW Ori and RY Tau. In the case of GW Ori, the sharp rise could be due to the lack of observations over consecutive days, and is probably not a real increase in accretion variations on the longer time-scales (see Fig. 4.6). For RY Tau, it could be a real rise in accretion variations, but it is more likely to be a single event observed at the end of the time-series. (See Fig. 4.7 and Fig. 4.8 for un-binned comparison of accretion variations and time-scales for all objects.)

The time-scales over which the accretion rate variations reach a maximum are comparable to the rotation periods within this sample, which all lie between $1 \sim 5$ days (see Table 4.1). These *slow variations* in the profiles are consistent

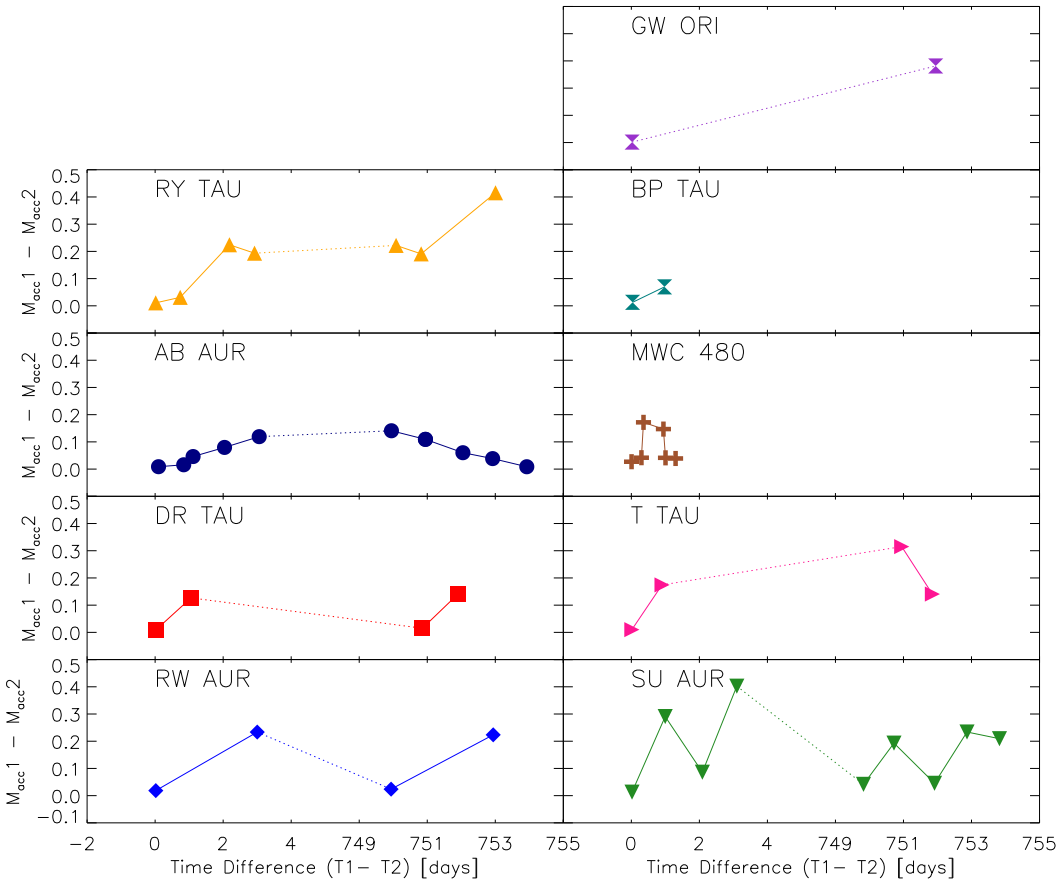

Figure 4.6: *Mean differences in accretion rates [Log($M_\odot$ yr^{-1})] versus the time difference [days]. In this case we compare all accretion rates for each object, in order to cover all time-scales within the sample. The difference between all accretion rates was calculated, and the mean is plotted for each time bin. The time bins vary from object to object depending on the number of observations blocks. The same plot for all objects where the accretion rate differences are not binned can be seen in Fig. 4.7 and Fig. 4.8.*

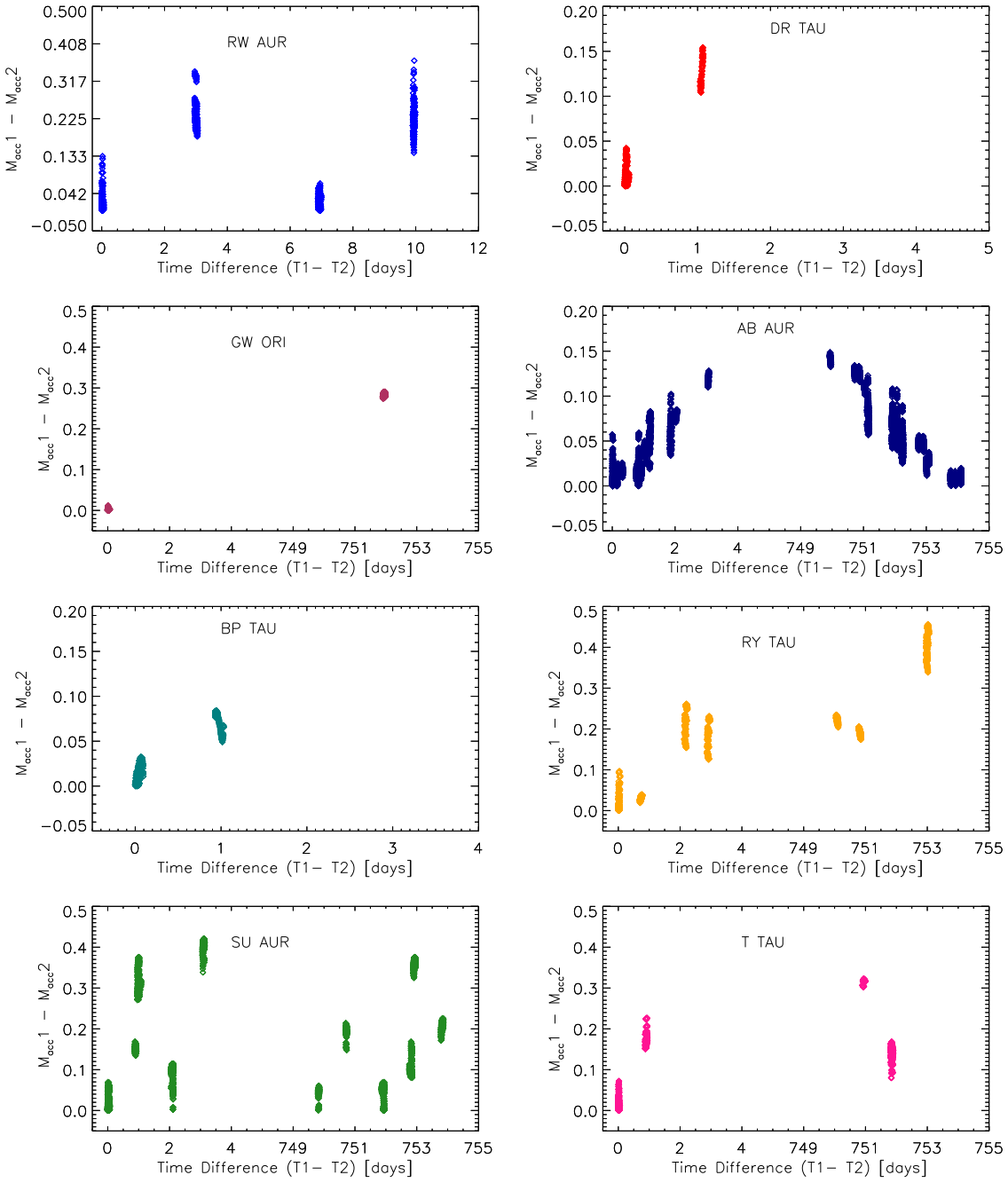

Figure 4.7: *Difference between two accretion rate measurements versus their time difference. This is done for every measurement for each object in order to cover all the possible time-scales in the sample. The mean accretion rate difference in each time bin is plotted in Fig. 4.6 for half of the sample.*

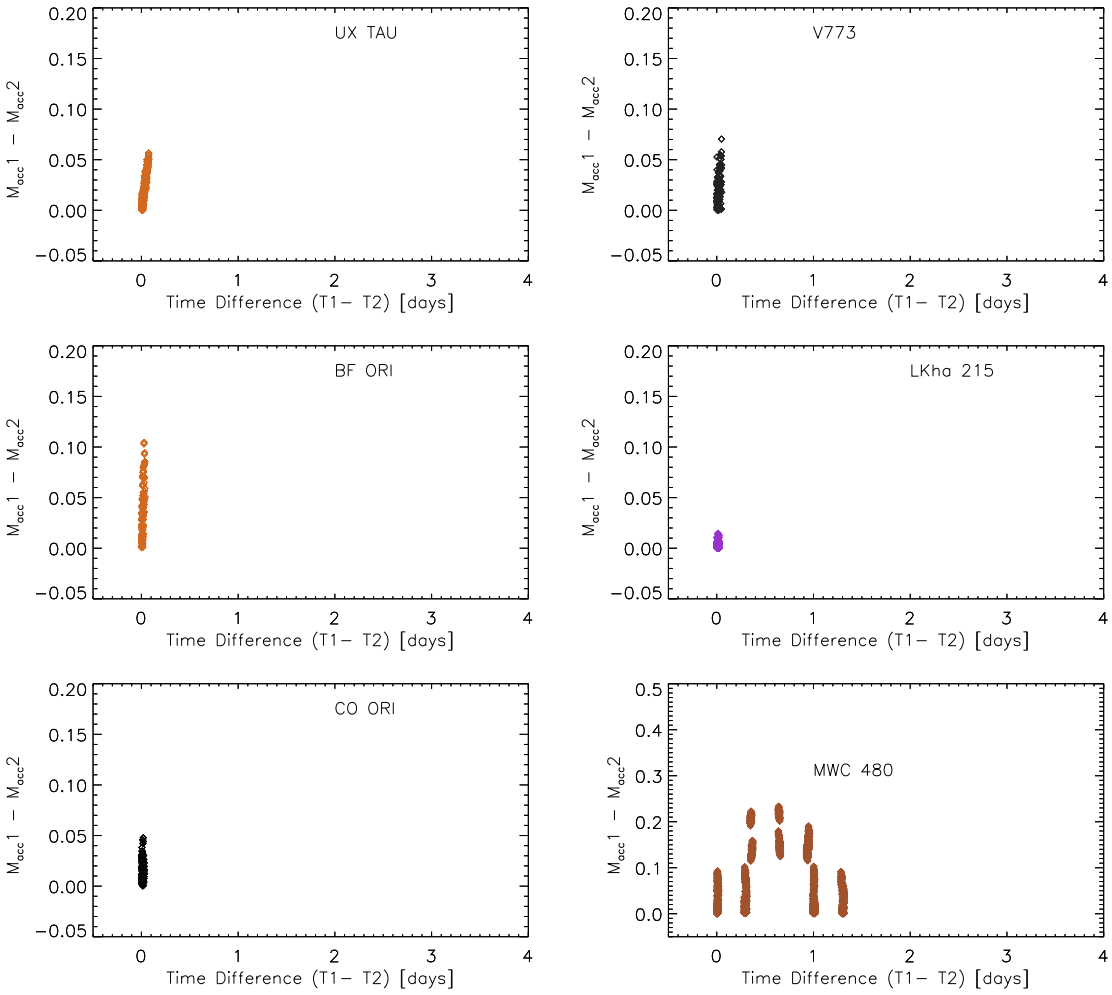

Figure 4.8: *Continuation of Fig. 4.7. Difference between two accretion rate measurements versus their time difference. See Fig. 4.7 for full caption.*

with what one would expect from a rotational modulation of the accretion rate. In the case of an asymmetric accretion flow, as the star rotates, different parts of the accretion flow will come into view, changing how much of the accretion flow is visible and what velocities within the flow are visible. Apart from three cases, no major changes are seen in the profiles within the single blocks of observations. These blocks represent time-scales of about an hour or less. In this sample it appears that the small, gradual changes we see within these observation blocks accumulate to larger variations between the different nights of observations.

The previous work on the LAMP sample supports this result (See LAMP sample Chapt. 3), where it was also found that it was the short time-scales, of a few weeks or less, that were the dominant time-scales within the sample (Costigan et al. 2012). In Chamaeleon, the average spread in accretion rates was found to be 0.37 dex, which is very close to the variations found in this sample of both T Tauri and Herbig Ae stars.

Simulations of magnetospheric accretion have found that even a slight offset (2 - 5°) will result in an asymmetry in the accretion flow (Romanova et al. 2003). This is thought to be in the case for V2129 Oph (Alencar et al. 2012). The authors used MHD simulations of the observed magnetic octupole and dipolar fields of V2129 Oph, and radiative transfer codes to reproduce the observed spectral line profiles. Earlier observations of the magnetic field found an offset between the octupole and dipole fields (15 and 25°) and the rotation axis (Donati et al. 2011a). The modelling of these fields result in two ordered flows of material onto the star very close to the poles. The derived profile variations are similar in magnitude to the observed profiles, however the changes in the profile shape are not. At an inclination angle of 60° to the viewer, the models result in a change in 8 Å in Hα EW across the rotation period.

The changes that are observed in this sample over multiple days, are on the same order of magnitude as those modeled for V2129 Oph. For example AB Aur, RY Tau, SU Aur, BP Tau all have EW ranges of 5 - 15 Å between multiple nights observations. RW Aur has a much larger spread of 35 Å, which may mean that this model of two rotating flows is probably not sufficient to explain all of the variations seen in this object.

It is expected that rotationally-induced apparent accretion rate change will depend on the inclination of the systems to our line of sight. Kurosawa et al. (2006) showed through MHD simulations that as the inclination of an accreting system increases, the EW of the Hα emission decreases. This is due to the fact that we see less of the accretion flow at higher angles. In these models, as the

inclination increases from 10° to 80° the EW changes from 32 Å to 21 Å. One can also expect to see more changes in the Hα EW if the system is inclined to our line of sight, making it more likely that the accretion flow will move in and out of view. In the 2003 observations the three stars with the largest range in accretion rates in the sample are three of the most inclined systems. RY Tau, SU Aur, and RW Aur all have inclinations of 45° or over. DR Tau is also highly inclined, but does not show very large variations. However since the system is close to edge on, we may not have a full view of the accretion flow, and the disc may obscure a lot of the light coming from the accretion flows. The inclination angles are given in Table 4.1.

This assertion no longer holds true when the 2001 observations are considered. The three objects (RY Tau, SU Aur, and RW Aur) show much less variability than the other objects, whereas DR Tau shows some of the largest accretion-rate variations, and T Tau and MWC 480 with disc inclinations of $\sim 30°$ also show large variations. This suggests that a picture of a stable rotating asymmetric flow is probably too simplistic to describe the full variations in these objects.

Long term photometric monitoring of accreting objects also support the scenario of a more complicated accretion flow as irregular light curves have been observed in many accreting T Tauri stars (Grankin et al. 2007; Herbst et al. 1994; Scholz & Eislöffel 2004; Scholz et al. 2009). Over the time-scales of years multiple different types of variations can been seen in one object. In many of the cases were variations occur on the time-scales of days, the simple explanation of a rotational modulation cannot explain the full behaviour.

In their spectro-polarimetric observations of BP Tau, Donati et al. (2008) found strong signatures of rotational modulation in the accretion related emission lines. The narrow emission lines associated with accretion (He I, Fe II and narrow component of Ca II IR triplet) varied strongly with rotation period. However, the broad emission lines Hα, Hβ (and also the broad component of the Ca II IR triplet) were found to vary on the level of 10% - 20% with rotation, with the remainder of the variations coming from seemingly other sources. This could be explained by the narrow emission component originating close the base of the accretion flow, with the Hα emission originating in the bulk of the accretion flow, which may be more sensitive to instabilities. Excess contributions in the Hα emission from outflows could also play a role. The authors also suggest, that changes in the rotational modulation of the longitudinal magnetic field between the two observation periods in February and December 2006 implies that the large-scale field topology was distorted by variability in the system

between the two periods. This suggests though rotational modulation accounts for the majority of the variations, there are other ongoing processes.

There are many kinds of instabilities that can occur in the disc and accretion flow that may account for the changes in the variations observed over time, e.g.: the build up of material in the circumstellar disc (D'Angelo & Spruit 2012). Kurosawa & Romanova (2013) show that in the case where Rayleigh-Taylor instabilities exist in the inner disc, unstable accretion flows can form. These flows change in size, shape, and numbers, meaning there is always a accretion column visible. This results in a constantly observed red-shifted absorption in the Balmer lines, more particularly in the higher Balmer lines such as Hγ and Hδ. This has been observed in RW Aur (Edwards et al. 1994), where spectroscopic monitoring also confirmed the presence of an asymmetric accretion flow (Petrov et al. 2001a), as well as for SU Aur (Johns & Basri 1995b; Petrov et al. 1996).

It is possible that these instabilities exist in some if not all of the objects in this sample. Comparing the 2001 and the 2003 sample, some changes are seen in the Hα profiles, but also differences in the derived accretion rates and their variations. These instabilities could account for changes in the Hα emission if they change the form of the accretion flows.

4.5.2 Rapid Events

The *rapid events* observed in this sample do not fit into the frame of rotational modulation. AB Aur, and to a lesser extent RY Tau and RW Aur, show significant variations in the profile over the time-scale of 1 hour. In the case of each star, these changes only occur during a single night of observations (For AB Aur see Fig. 4.9). A number of short term rapid variations have previously been discovered in objects in our sample and these are presented in the following paragraphs.

Short term striking variations have been observed in the Hα profile of AB Aur previously, where changes occurred in both the intensity and profile shape. Beskrovnaya et al. (1995) described the changes as occurring during each observing night across the emission line but especially in the absorption feature of the P-Cygni profile and the emission peak. They attribute these variations to the motion of circumstellar inhomogeneities. This is similar to the changes observed in the Hα profile of AB Aur on night 3, where it oscillates between broad wings and low emission, and strong emission and with narrow wings. However in the case of Beskrovnaya et al. (1995), their observations take place with hour separations, so they do not have the short term cadence that we have in this

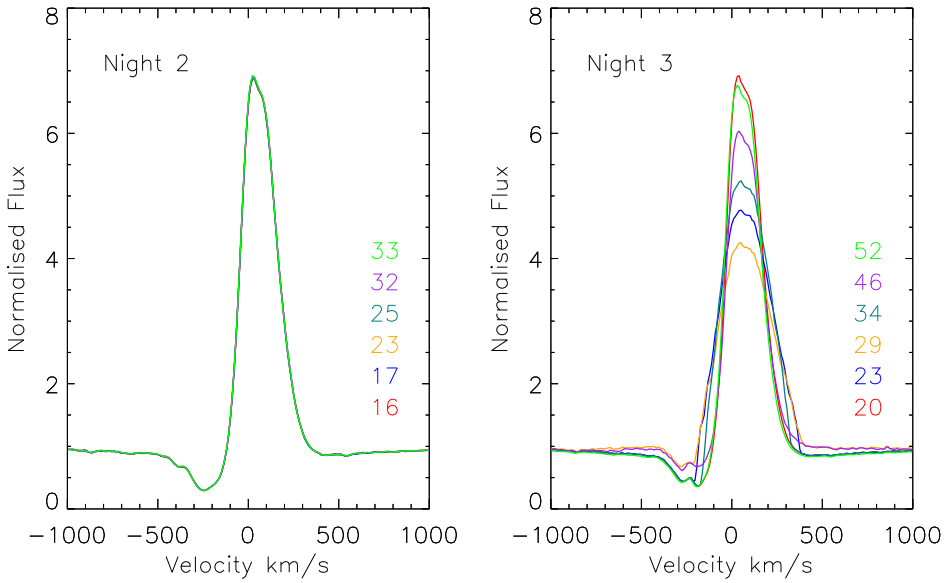

Figure 4.9: *A comparison between a sub-set of profiles on two separate nights of the 2003 observations for AB AUR. On the second night of observations in 2003, no significant change within the profile was observed. The minute of the hour in which the spectrum was observed is given to the right of the profiles in the corresponding colour. During the third night of observations there were large changes. Shown here is a sequence of spectra where the emission line falls in strength, and broadens, before returning to the initial strength.*

sample.

Rapid variations have been seen in the Hγ profile of RW Aur, occurring on time scales as short as 10 mins. OVer the course of the observations the central absorption component of the Hγ line increased in EW by a factor to 2 within an hour (Mundt & Giampapa 1982). These variations were not reflected in the Hα emission, which is thought to be a result of the high optical thickness in the surrounding envelope. Mundt & Giampapa (1982) found these variations to be consistent with both flaring and accretion events.

Variations in Hα profile of RY Tau were found on the time-scales of 10 - 20 mins without variations in the star's brightness (Kolotilov & Zajtseva 1975). Three separate nights observations took place covering time scales of a few hours each night. The profiles changed between nights, but in two out of three occasions they were stable throughout the night. The brightness of the star was lower on the night of the variations than on the other two nights, which is an indication that these variations came from magnetic activity (Gullbring et al. 1997).

With the short wavelength coverage in this sample and no simultaneous alter-

native observations, the behaviour seen in AB Aur, RY Tau or RW Aur cannot be properly defined, and the origin of these rapid variations is not clear. Gullbring (1994) argue that in the case of magnetospheric accretion short term variability is to be expected. The in-fall time-scale of gas towards the pole is less than one hour. Any instabilities that occur in the disc or the magnetic field at the point of their interaction will lead to a clumpy flow of material onto the surface.

The changes in RY Tau and RW Aur take the form of a drop in emission across both lines, but not within the line centre, which would be more indicative of a flare (see Sect. 4.3.3). However it is probable that the rapid events that are observed in RW Aur and RY Tau are due to a flare event. This is not the case with AB Aur. The *rapid variations* that occur in the profile of AB AUR are unique in the sample. In no other object do we see these changes in emission line strength, width and surrounding absorption.

It is possible that all the targets have these periods of *rapid variations*. Out of the total 22.6 hours of observations, these *rapid events* only take place with 3 observation blocks, which constitutes 2.4 hours or $\sim 10\%$ of our total observing time. This suggests they are not very common events and it rules out stochastic processes as the primary source of variations within the sample. However these stochastic events could be the cause of the *rapid variations* we see in a small number and probably take the form of instabilities in the magnetic field (Goodson et al. 1998), or inner disc (Kurosawa & Romanova 2013).

4.5.3 Comparison between Herbig Ae and T Tauri sample

Herbig Ae stars are the intermediate mass equivalent of T Tauri stars and are thought to go through a similar process of accretion as T Tauri stars. As they are higher mass, they are shorter lived, but retain their circumstellar disc for long enough to accrete material from them onto their surfaces.

Similar scalings of accretion rate to disc mass exist between T Tauri and Herbig Ae (Mendigutía et al. 2012). They also show that the NIR colour excess trend is the same across the T Tauri to Herbig Ae mass range, which can be explained by the reprocessing of both the stellar and accretion luminosities by the inner disc.

However there is inconclusive evidence whether Herbig Ae stars are host to strong magnetic fields. Under our current understanding of magnetospheric accretion these strong, stable fields are essential for maintaining a quasi-stable accretion flow.

Within this work a large mass range is covered (up to ~ 5 $M_{\odot}$) and similar

variations are seen in all objects. The largest mass target, LkHα 215 shows an accretion rate spread of 0.015 over a single observation block. Comparing to one of the smallest mass targets in the sample, DR Tau with 0.008, 0.042, 0.017, shows there is little difference between the two. Indeed, others have found similar accretion rate variations for Herbig Ae stars as is found in this work, and the LAMP sample. For example Pogodin et al. (2012) observed accretion variations of amplitude 0.4 dex over the time-scales of 10 days for one target, while multiple targets showed variations of 0.3 dex between consecutive days observations. From 38 Herbig Ae/Be stars, (Mendigutía et al. 2011) found a typical upper limit of accretion variations of 0.5 dex over time-scales from days to months.

Compiling the samples from both studies (this and the LAMP sample), of 10 low-mass T Tauri and 14 intermediate-mass T Tauri/Herbig Ae stars, suggests that it is the same process that produces the Hα variations in T Tauri and Herbig Ae stars, across the entire mass range up to ~ 5 M$_{\odot}$. This variability result is entirely consistent with earlier spectro-polarimetry surveys (Vink et al. 2002, 2005, 2003)

4.6 Summary

This study was undertaken to put a lower limit on the time-scales of accretion variability in T Tauri and Herbig Ae stars. The previous work, LAMP (Chapt. 3), used the Hα emission in low mass T Tauri stars as a proxy for accretion, through which an upper limit of 8 - 25 days for the time-scales of accretion variations was found (Costigan et al. 2012). These were the shortest time-scales in that sample.

This data studied in this chapter allowed to approach the problem from the other end of the scale, by studying the variations on the time-scales of minutes, hours, days and in a few cases years. The main findings of this work can be summarised as follows:

The majority of variations observed in this sample take the form of *slow variations*, where gradual changes in the Hα emission occur across the ~ 1 hour observation blocks. These *slow variations* are consistent with what we would expect from accretion rate changes rather than solely chromospheric activity or wind emission.

Calculating the mass accretion rate from the Hα emission, the average spread the accretion rate on time-scales of less $\lesssim 1$ hour is found to be 0.01 - 0.09 dex. The spread increases by an order of magnitude when different nights observations

are considered, 0.1 - 0.4 dex. However, when the variations are considered over 2 years, they have not increased and remain the same, 0.15 - 0.46 dex.

Therefore it is the period of days that is the dominant time-scales of these *slow variations*. These results are found to be consistent with a rotational modulation of the accretion rate and are supported by previous results.

Rapid events occur in 3 observation blocks, which constitute 2.4 hours or $\sim$ 10% of our total observing time. These events consist of fast changes within the Hα emission line on time-scales of less than an hour. They could be connected to instabilities in the magnetic field or inner disc, which would create more stochastic accretion events than we observe in the majority of the sample.

This data set covers a large range in masses, in which very similar variations and accretion rate changes are found. This strongly suggests that the same process is taking place across the full mass range, from low mass T Tauri stars up to Herbig Ae stars, and that the same model of accretion holds over large stellar mass range.

The results from this work, and the previous chapter are shown in Fig. 4.10, along with other published work. The trend from the LAMP sample continues in this sample, with a saturation in the accretion rate variations after a few days. For the majority of this sample, the rotation rates of the T Tauri and Herbig Ae stars are known. However, a large weakness in the conclusions drawn from these samples is the unknown rotation rates in the LAMP sample, and their behaviour on the shorter time-scales.

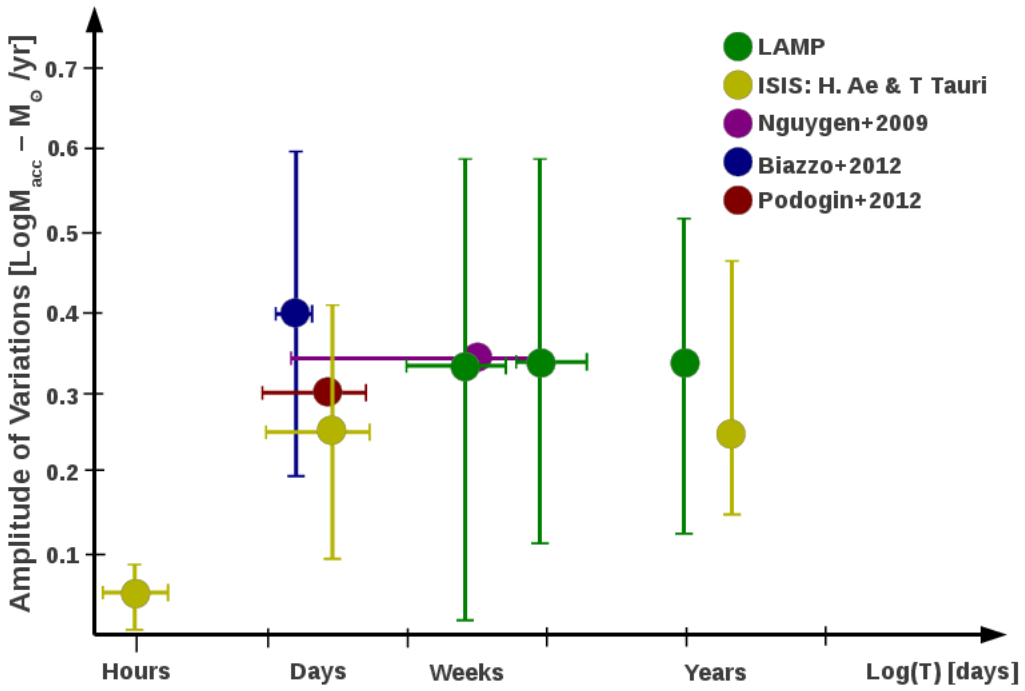

Figure 4.10: *Comparison of accretion variations versus time-scales found in different sample. The compilation of these data sets shows the accretion rate variations effectively saturate after a few days and do not increase when you go to longer time intervals. Note error bars here indicate the spread in accretion rates, and time coverage in each bin.*

5

Chamaeleon Photometry

5.1 About this Chapter

Spectroscopic observations of accreting sources are necessary to understand what is happening in these dynamic systems, as was shown in the previous chapters. However, these observations can be time consuming and the sample sizes are often small as a result. Although photometric observations do not contain the same level of information as the spectroscopic observations do, many more objects can be observed at once with higher cadence.

The previous two chapters described how the question of the origins of accretion variability was approached from two different ends of the time-scales. They both pointed to the intermediate time-scales of days as the most dominant time-scales in the variations of both samples. However the samples are not immediately comparable. For instance as mentioned in Chapt. 3, the LAMP sample is a relatively unbiased sample of young stars, chosen for showing infrared excess i.e. presence of a disc. On the other hand the ISIS sample, designed for spectropolarimetry, consists of some of the brightest targets in the sky, the majority of which are very well studied and are known variables. Nevertheless, both samples showed very similar behaviour with regard to the accretion variability.

To strengthen the conclusions drawn from these samples, photometric mon-

itoring was carried out of the Chamaeleon region over 8 days. This provides a robust method to determine the dominant time-scales in these systems that is independent of any accretion model. Utilising WFI's wide field of view to cover the entire Chamaeleon region in one pointing, allows for multiple observations of the region per night and provides the short term time sampling that is missing in the LAMP data. Also, the majority of photometric variations in typical YSOs are expected to be modulated by the rotation period, which provides a model independent method of determining the rotation rates of these objects. Thus sample provides complementary data to the previous two chapters, allowing for the reinforcement of the connection between them.

Sect. 5.2 describes different types of variability that may be observed in this sample. Sect. 5.3 presents the variable sources identified through the methods described in Chapt. 2. These variable sources are then fitted to find a possible rotation period in the light curve, the method of which is given in Sect. 5.4. The results of this fitting procedure are presented in Sect. 5.5 and Appendix B. The general trends in the sample are then discussed in Sect. 5.6.

5.2 Sources of Variations

The majority of the variations observed in this sample are expected to be caused by cool spots. The existence of these cool spots and their modulation of the light curves was first proposed by Hoffmeister (1965). Cool spots are thought to be very common in YSOs due to their high level of magnetic activity. They are analogous to sun spots and form as a result of the magnetic field interacting with the stellar photosphere. The typical manifestation of these spots in the observed light curves is a simple sinusoidal variation. This suggests that in the majority of cases these spots form at high latitudes, have an inhomogeneous distribution and exist in low numbers on the surface (Herbst et al. 1994; Rydgren & Vrba 1983).

The physical parameters of these spots can be constrained through models. Cool spots are 1000 - 1500 K colder than the surrounding photosphere (Carpenter et al. 2001) and have filling factors (percentage coverage of a hemisphere) of up to 30%. These spots result in changes of less than 0.5 mag. in the I band or 0.03 - 0.05 in V-band (Bouvier et al. 1995; Herbst et al. 1994). As these spots rotate with the surface of the star they are often used to determine the rotation periods of YSOs. The spots themselves are probably only stable over a number of rotation periods, and are likely to undergo changes on time-scales of weeks

(Hussain 2002). However, these spots have been successfully used to determine rotation periods based on observations years apart that are consistent with each other (e.g. Attridge & Herbst 1992 and Mandel & Herbst 1991).

Another source of light curve variations in accreting objects are hot spots, which form as the footprint of the accretion flow where the accretion shock heats the photosphere. These are typically smaller than cool spots, with surface filling factors of a few percent (Donati et al. 2008; Jardine et al. 2006), but there is a significant temperature difference between the photosphere and the hot spot. Typical temperatures are in the range of 7000 - 12,000 K (Herbst et al. 1994), and as a result can lead to large variations in the light curves (V band >0.8, Herbst et al. 1994). These hot spots are not as stable as the cool spots, but can survive over multiple rotations. Clear periodic signatures are observed on many accreting stars, showing the presence of cool spots (Bouvier & Bertout 1989; Vrba et al. 1986). These unstable hot spots will add additional irregular variations on top of those more stable cool spot variations (Herbst et al. 1994).

Small amplitude variations can be reproduced by both cool and hot spots with small filling factors, but variations greater than 0.5 mag. generally cannot be explained by cool spots alone, whereas variations of up to 1 mag. can be modelled with a hot spot with a high temperature or high filling factor (Carpenter et al. 2001).

These magnetically active stars will also flare, leading to a brightening of the star. These transient events will primarily cause more variations in the blue i.e. U and B bands (Herbst et al. 1994), rather than in the optical.

Further variations within the light curve can come from changes in the extinction. These changes can come from either variations in the molecular cloud lying between the target and the observer, or from variations in the circumstellar disc. These changes in extinction result in the targets getting redder as the object dims, much like for hot or cool spots, but the slope of the colour changes can be used to distinguish between these scenarios (Scholz et al. 2009). Observed velocities in molecular clouds suggest any variations to light curves would be on the order of weeks (Carpenter et al. 2001). Variations coming from inhomogeneities in the disc will depend on how far from the central source these inhomogeneities lie and can cause variations on time-scales from days to years.

Often stars will show signs of a combination of the above sources, and it can be hard to distinguish one source from another. Time-scales play an important role in distinguishing between them, as well as multi-wavelength observations. For example, hot and cool spots are expected to modulate the light curve on

time-scales of the rotation period, and they will exhibit larger amplitudes of variations at shorter wavelengths.

5.3 Sample

As previously discussed in Chpt. 2 these photometric observations were completed using the WFI on the 2.2 m telescope at La Silla Observatory. The pointing of the telescope was roughly centred on the FLAMES pointing used to observed the LAMP sample.

Variable stars were identified within the sample using the standard deviation versus magnitude plots shown in Fig. 5.2 and 5.3. The process of reducing the CCD images and extracting the photometry is described in Chapt. 2. The majority of the targets on each chip are not variable and in these cases the targets will have a low standard deviation in magnitudes across the observations. Any variable stars will have higher standard deviations and will sit above the field average.

The observational strategy was to obtain as many I-band images as possible across the observing period. On good weather nights, when it was possible to get multiple I-band images, R-band images were taken as well to constrain the origin of variations seen. In total, the data set contains 35 I-band images and 11 R-band images. As they are more numerous, and in general have a better S/N, the I-band frames were first used to identify the outstanding variables. These are identified in the plots with each of the target's identifiers. For example, the top panels of Fig. 5.2 show the standard deviation and average magnitudes for Chip 1. In this chip only one clear outlier was identified, B43. It has four times higher standard deviation than the other targets at that magnitude. When its light curve is examined variations can be seen between consecutive nights observations and within a single night. Fig. 5.1 shows a comparison between the light curve found for B43 and a non-variable star in Chip 1.

Other targets with variable light curves were not so clear. In Chip 2, T33 is clearly a variable star, however the other four targets identified in the plot do not stand far above the average standard deviation. Three of these targets were identified as accretors in the LAMP sample (ChaHα6, ChaHα6 and ISO 143), and so were of special interest. One target, ChaHα1 is not within the Chamaeleon sample. It is classified as a brown dwarf with a spectral type of M7.75 (Luhman 2007).

In Chip 7, (see Fig. 5.3), three of the variable star identified are accretors in

the LAMP sample (T31, T30 and ISO126). One star that was not identified as an accretor in the LAMP sample, CHXR22E, shows variations here. In the LAMP sample this object has an average EW of 9.5 Å and a 10%w of 412 km.s^{-1}. Though the EW is below the Barrado y Navascués & Martín (2003) cut-off for an M3 star (12.2 Å) the 10% width is large. It is possible that low levels of accretion are occurring in this object. A second object is not covered in the LAMP sample, CHXR27 which is classified as an M0 Luhman (2007). A further accretor, T45, was found to show large variations in Chip 8. Two further targets were found to show large variations in the I-band but not in the R-band. However these targets could not be identified and most probably are not members of Chamaeleon. Table 5.4 gives a quantitative measure of the variations in these targets. The column marked 'σ_O' gives the standard deviation in the observed I-band light curve for each of the variable targets. Alongside it, 'Er. I' gives the mean standard deviation of the non-variable sources at that magnitude. In all cases the standard deviation in the light curve is larger than the background non-variables.

A list of the variable stars mentioned here, along with their spectral types and SED classes are given in Table 2.5, Chapt. 2. All of the variable targets are classified as Class II objects, meaning they are all harbouring circumstellar discs. This is not surprising as IR surveys of young stellar regions have found 60% - 70% of YSOs with IR excess to be variable (Flaherty et al. 2012; Morales-Calderón et al. 2009). The light curves for each of these targets are examined in detail, and presented in Sect. 5.5 and Appendix B. In the non-variable sample 19 further targets were identified. According to the Chamaeleon catalogue of Luhman (2007), 11 were identified as candidate Chamaeleon I members and a further 8 were Class III objects. None of these disc-less targets show the same magnitude of variations that are observed in the Class II population.

5.4 Fitting Procedure

As confirmed members of the Chamaeleon I region, all of the targets are young, still harbour discs, and are very likely to still be magnetically active. Their spotted surfaces will allow us to determine likely rotation periods for these targets, while also providing estimates to any other variations occurring in the systems.

The typical rotation periods for these kinds of objects is 1 - 10 days (Herbst et al. 1994). Due to bad weather, only 8 nights observations were obtained, so a full coverage of all the rotation rates cannot be expected. Even so an attempt is made to identify rotation rates by fitting a simple sinusoid to the observed light

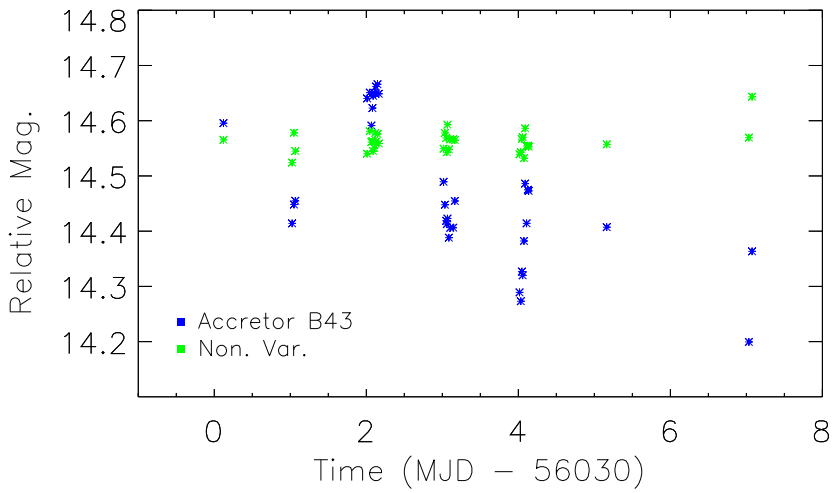

Figure 5.1: *Time series of a variable star (B43) compared to a non-variable star from the same chip (Chip 1).*

curves.

Using a least-mean square fitting python procedure (*leastsq* which comes under the package *optimize*), the I-band light curves are fitted for the mean magnitude, amplitude, period and phase. Initial guesses are provided for each, which are estimated by judging the light curve variations by eye. The fitting procedure uses the Levenberg-Marquardt method, which finds the local minimum and so is sensitive to the initial guess.

For this reason, the Lomb-Scargle method was used to indicate likely periods within the data (Lomb 1976; Scargle 1982). This spectra analysis method is well suited to finding weak periodic signals in unevenly sampled data. The *lomb.fasper* python script uses fast fourier transforms to decrease the computing time, and was used for each light curve to compute the Lomb-Scargle periodogram. In most cases the peaks in these periodograms are very broad and can only be used as a loose indication of a period. Each fit was checked by eye to ensure a reliable answer.

Assuming Gaussian uncertainties, the standard deviation in each of the fitted parameters is given by summing over the diagonal of the covariance matrix. In this case the *leastsq* method provides the fractional covariance matrix as an output and so needs to be multiplied by the reduced-χ^2 to get the full covariance matrix.

The reduced-χ^2 (χ^2_r) is given for each fit in Table 5.4. In the cases where the observed light curves are well described by the sinusoidal fit, the residuals of the fit will show lower variations than the observed data. The standard deviations for

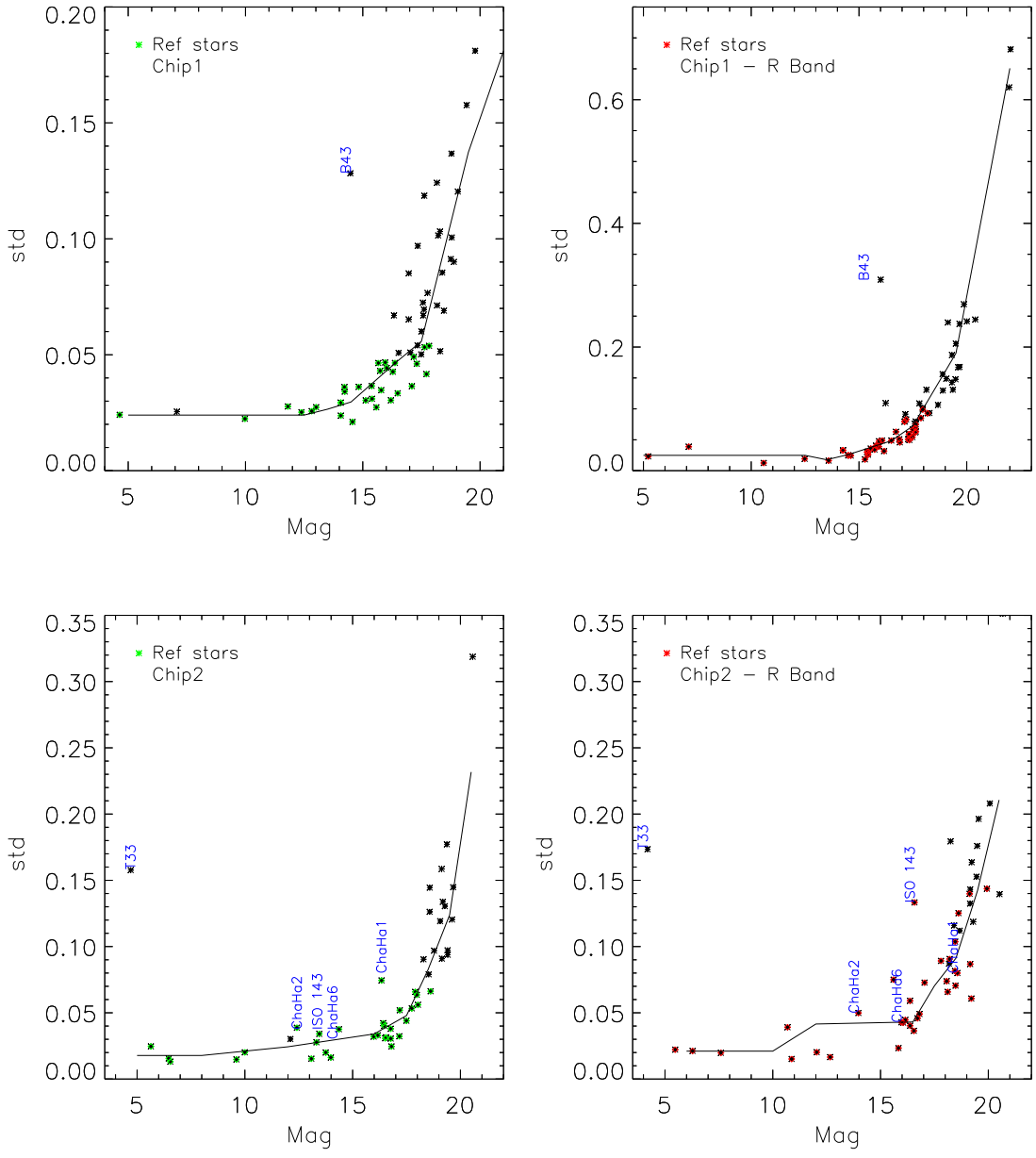

Figure 5.2: *Standard deviations for each target versus the mean magnitude for Chip 1 (Top panels) and Chip 2 (Bottom panels), in both I-band (left column) and R-band (right column).*

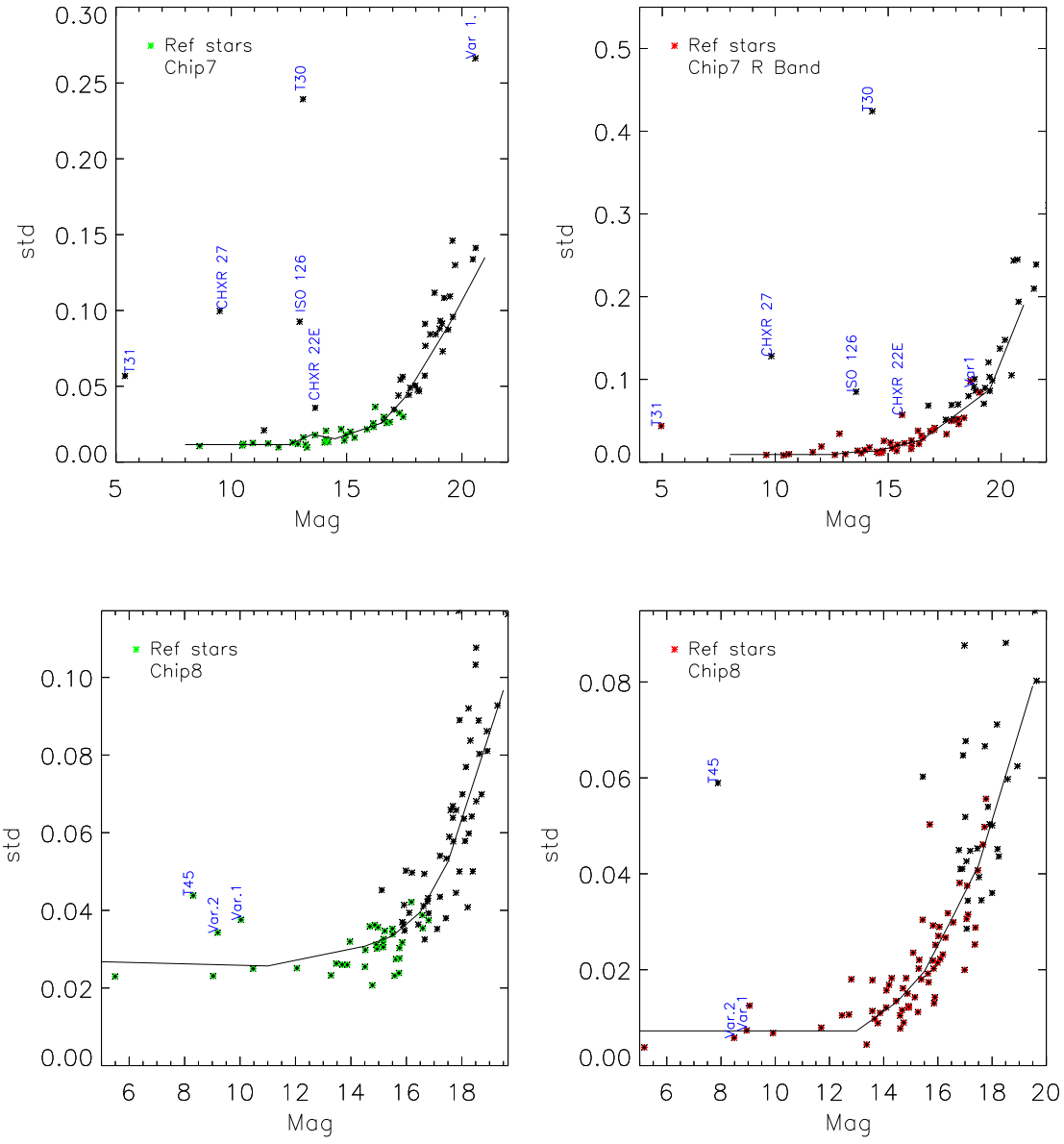

Figure 5.3: *Standard deviations for each target versus the mean magnitude for Chip 7 (Top panels) and Chip 8 (Bottom panels), in both I-band (left column) and R-band (right column)*

the observed light curves (σ_O) and the residuals of fit (σ_R) are also given in Table 5.4, along with the F-number for each fit. The F-number can be simply given by $F = \frac{\sigma_O^2}{\sigma_R^2}$, and is often used to represent the probability that both observed data and the residuals after the fit are drawn from the same population (e.g. Scholz et al. 2005). A large F-number indicates that the variations have been much reduced after the fit was preformed. The F-number false alarm threshold is set by the number of degrees of freedom of the data, which in the case of the I-band is 35. Therefore the 1% false alarm threshold for this sample is 2.2 - 2.3.

The R-band light curves were then also fitted using the least-mean square method taking the period and phase from the I band fit. This is done as the R-band sampling (11 data points) is significantly less than in the I-band (35 data points). So in the case of the R-band the light curved was fitted for the amplitude and mean magnitude only. This is a reasonable assumption to make as any cool or hot spot variations that do occur should appear with the same period and phase in both wavelength ranges.

Obj	Mid. I	Mid. R	P days	$\sigma_{\rm P}$	Amp. I	$\sigma_{\rm I}$	Amp. R	$\sigma_{\rm R}$	χ^2_r	σ_O	σ_F	Er.I	Er.R	F No.
ChaHα2	12.62	13.98	5.42	(0.30)	0.06	(0.003)	0.06	(0.02)	0.75	0.048	0.020	0.025	0.040	5.81
ChaHα6	13.66	15.95	4.27	(0.20)	0.04	(0.004)	0.05	(0.02)	0.74	0.041	0.020	0.025	0.040	4.36
T33	5.07	7.849	7.85	(0.08)	0.28	(0.003)	0.31	(0.05)	5.71	0.166	0.044	0.020	0.020	14.1
T31	5.44	4.97	4.09	(0.10)	0.07	(0.002)	0.07	(0.01)	13.76	0.042	0.048	0.015	0.010	0.76
T45	8.34	7.89	5.41	(0.09)	0.09	(0.004)	-	-	1.13	0.056	0.027	0.022	0.010	4.52
ISO143	14.61	16.69	8.82	(0.92)	0.05	(0.004)	0.17	(0.03)	1.00	0.127	0.023	0.025	0.040	30.84
ISO126	13.04	13.61	3.73	(0.02)	0.15	(0.002)	0.09	(0.01)	4.22	0.081	0.028	0.015	0.010	8.24
CHXR27	9.51	9.79	6.92	(0.06)	0.15	(0.002)	0.16	(0.004)	2.60	0.122	0.022	0.015	0.010	29.92
B43	14.47	15.92	3.08	(0.04)	0.11	(0.003)	0.23	(0.02)	10.23	0.216	0.079	0.027	0.050	7.42
CHXR22E	13.69	15.60	4.91	(0.19)	0.04	(0.002)	0.04	(0.003)	1.14	0.054	0.015	0.015	0.012	13.49
T30	13.11	14.141	4.82	(0.08)	0.28	(0.003)	0.37	(0.005)	79.46	0.404	0.123	0.015	0.012	10.78
ChaHα1	16.32	19.48	3.24	(0.07)	0.08	(0.004)	0.16	(0.06)	2.46	0.170	0.040	0.030	0.090	15.44

Table 5.1: *Table of fit parameters. The mean magnitudes for I and R band are given in first two columns. Given along side each of the other fitted parameters P (Period), Amp. I (Amplitude) and Amp R are estimates of the fitting errors, $\sigma_{\rm P}$, $\sigma_{\rm I}$ and $\sigma_{\rm R}$. σ_O is the standard deviation of the observed light curve, σ_F is the standard deviation of residuals after fit. 'Er. I' and 'Er. R' are the standard deviations of the reference stars in that field which can be taken as the photometric error. F-test threshold in these cases is 2.2 - 2.3 for a 1% false alarm probability.*

5.5 Results

The success of the fitting procedure and the parameters derived for each individual object are discussed in Appendix B. Here one target, ChaHα2 is presented to demonstrate the results obtained from this method.

Fig 5.4 shows the fitted light curves and Lomb-Scargle periodogram of ChaHα2. The three panels of the top figure show the I-band light curve, the R-band light curve and the residuals of the fit. The top panel shows the I-band light curve in blue, with photometric errors over-plotted. The solid red line indicates the sinusoidal fit to the light curve, and the derived period and amplitude of variations are also given in the panel. Below the R-band light curve is shown in green. The dashed red line indicates the fitted amplitude for the R-band, taking the period and phase from the I-band fit. The third panel shows the residuals to the I-band light curve fit, with the blue line indicating the zero point.

This figure shows that the I-band light curve of ChaHα2 is well fitted with a simple sine curve (See Fig. 5.4). The residuals of the fit are on the same level as the variations of the reference stars in the field. This shows that there is very little variations above those described by the model. The high F-number (5.81) and low reduced χ^2_r (0.75) also attest the fact that this simple model is a good description of the data. The period of 5.41 $\pm$ 0.3 days also fits the R-band data well. The periodogram peaks at 5.15 days, but has a very large peak width. This brown dwarf is classified as an accretor in the LAMP sample. As the amplitudes are small, 0.06 mag. in both R and I, it is likely that these variations come from a stable cool spot on the surface. Small variations occur in single nights of observations, but these are for the most part within the photometric error.

For 10 of the other 11 objects in the sample, a period was successfully extracted from the light curves (see Appendix B). These are given in Table 5.4, along with the fitted amplitudes. The errors estimates of the period and amplitudes are taken from the standard deviations in the fitted parameters.

For two objects in this sample, periods have been previously reported. Through photometric monitoring, Joergens et al. (2003) found a period of 3.21 $\pm$ 0.17 days for ChaHα2 and a period of 3.6 $\pm$ 0.19 days for ChaHα6. Joergens et al. (2003) also monitored ChaHα1 but no period was found. Both these periods are shorter than the period found here. The discrepancy between the two studies is addressed in Sect. 5.6.1.

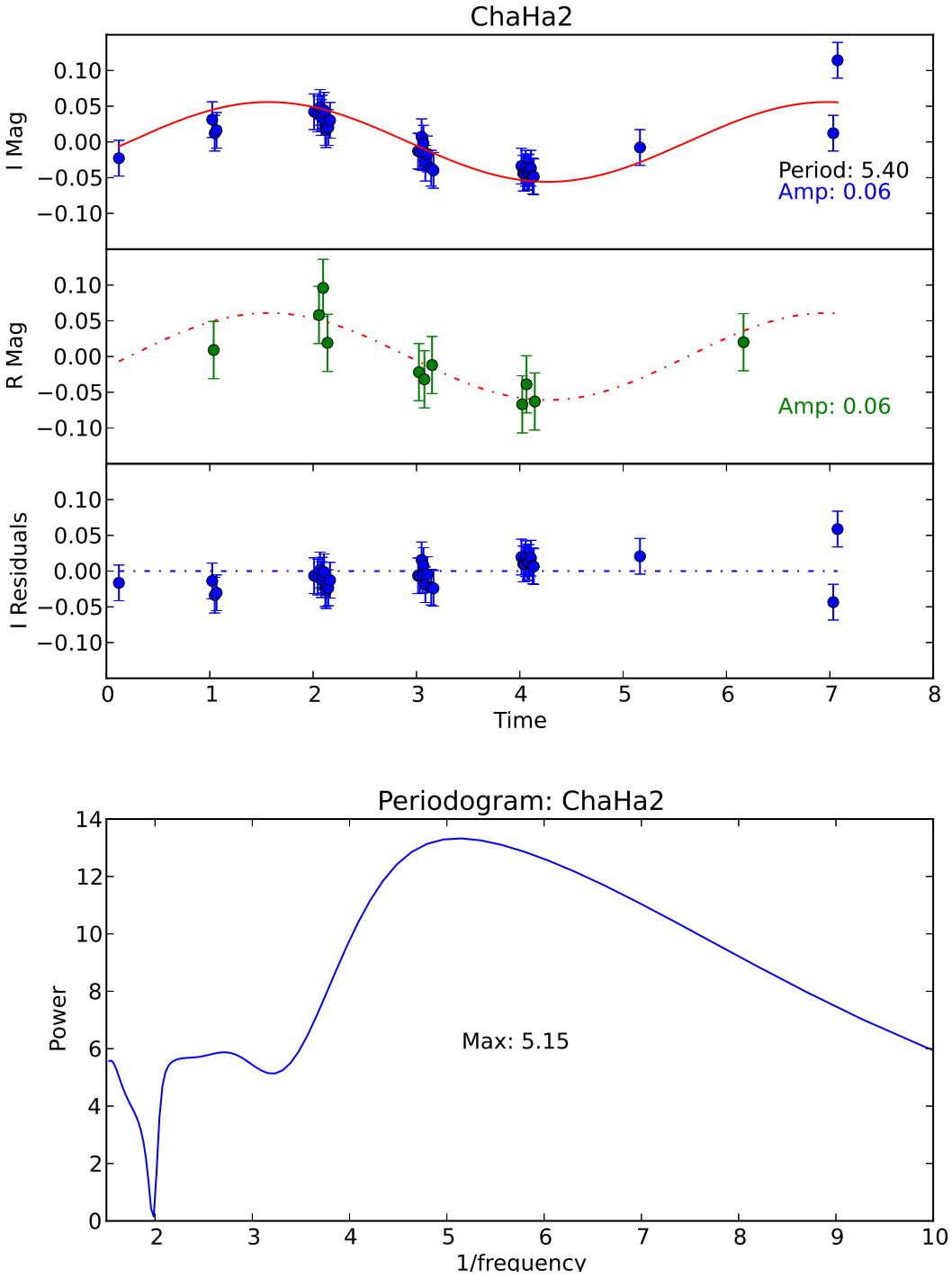

Figure 5.4: *Upper Plot: The first panel shows the I-band light curve (blue points) with the photometric errors. The light curve is normalised to the mean magnitude found by the fitting procedure. The sinusoidal fit to the light curve is over-plotted in red. Given within the panel is the derived period and amplitude of the light curve. The second panel shows the R-band light curve (green points), fit (red dashed line) and amplitude. The third panel shows the I-band residuals after the fit. Over-plotted in blue is the zero point. Lower Plot: Lomb Scargle periodogram with peak value indicated.*

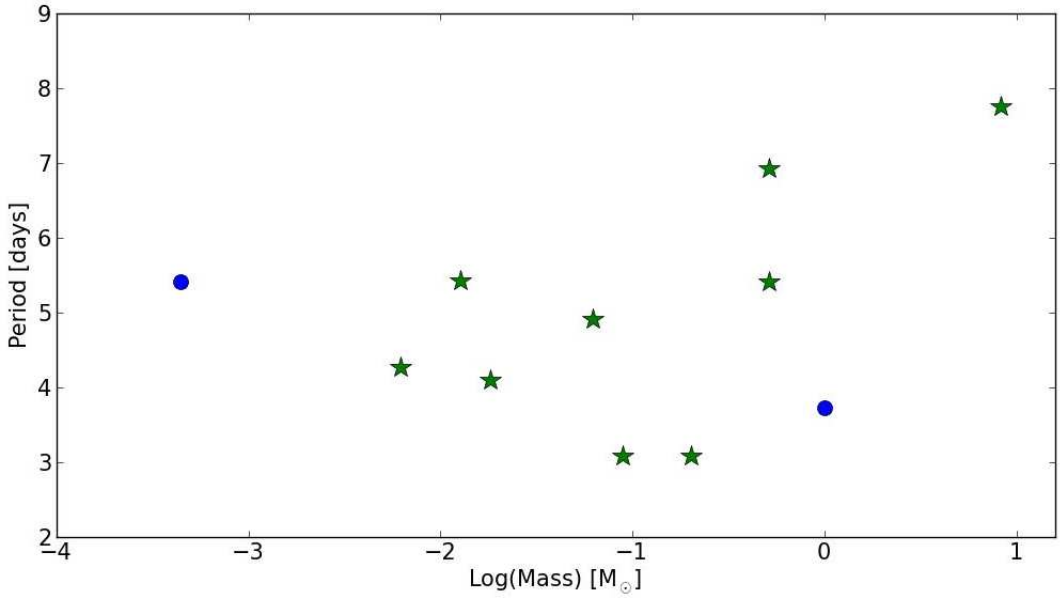

Figure 5.5: *Period versus mass for sample. Known accretors are shown in green, and the non-accretor (CHXR22E) and unclassified target (ChaHα1) are shown in blue. T31 is not included in this plot as it was not possible to derive a period for this star.*

5.6 Discussion

In the following, the periods, amplitudes and residuals that were found are discussed for the sample as a whole.

5.6.1 Periods

For the 12 targets mentioned likely periods were identified for 11, three of which are brown dwarfs candidates. Fig. 5.5 shows the derived periods versus sample masses. These masses were all derived from the published effective temperatures (Luhman 2007) and the Baraffe et al. (1998) 2 Myr isochrones. The derived periods all lie within the expected range for young stellar objects found through photometric monitoring (Herbst et al. 2002) and $v\sin i$ measurements (Bouvier et al. 1993b; Herbst et al. 1983).

There is a large spread in periods within the sample, and no strong dependency on spectral type is seen. Previous studies have found trends of lower masses having faster rotation rates which is consistent with what is observed here (e.g. Scholz & Eislöffel 2004).

Average rotation periods for brown dwarfs are usually shorter than one day (e.g. Scholz et al. 2005). However the rotation rates derived here for the three

Object	This Work	J+2003	Sine Fit to J+2003
ChaHα1	3.24 ± 0.07	No period found	-
ChaHα2	5.41 ± 0.3	3.21 ± 0.17	2.9 ± 0.1
ChaHα6	4.27 ± 0.2	3.6 ± 0.19	3.7 ± 0.1

Table 5.2: *Comparison between periods found in this work with those found in Joergens et al. (2003). Also given are the derived periods found by using our sine fitting method on the observational data of Joergens et al. (2003)*

brown dwarfs candidates are significantly higher than that. ChaHα1 was fitted with a period of 3.24 ± 0.07 days, ChaHα2 with a period of 5.41 ± 0.3 days and ChaHα6 with a period of 4.27 ± 0.2 days. This is in line with the periods derived by Joergens et al. (2003), who suggest the slower rotation rates are due to the relatively young ages of these target, and the presence of a circumstellar disc. They attest that the longer periods are due to ongoing rotational braking by interaction with the circumstellar disc.

Joergens et al. (2003) photometrically monitored the three brown dwarfs covered here. However, with a limited period coverage of six nights, the study faces the same restrictions as this work. The periods were found by using the more sophisticated string-length method (Dworetsky 1983), and folded J-band observations from Carpenter et al. (2001) into the I-band light curve in order to increase the phase coverage.

The periods found for the three brown dwarfs in both works are compared in Table 5.2. In the two cases for which Joergens et al. (2003) derive periods, they find significantly shorter periods than those derived here. In order to quantify how much of this discrepancy is due to the differences in fitting procedures, the sine fitting method was applied to the Joergens et al. (2003) data set. In both cases, the periods are in close agreement with those found by Joergens et al. (2003). This rules out the method as being a major contributor to the difference in periods.

Light curves have been seen to vary over time-scales as short as weeks to months as spot configurations change size, temperature or location. Longitudinal migrations of spots can also cause changes in the observed periods (Cohen et al. 2004). The time-scale between these two data sets is slightly over 10 years. These changes in light curves have been found to be more likely in accreting objects, where hot spots can play a significant role in concealing the rotational signatures. Both ChaHα2 and ChaHα6 are confirmed accretors (See Chapt. 2). Since the difference in the rotation periods is significant, it is more likely that hot spots are the cause rather than a reconfiguration of the cool spots.

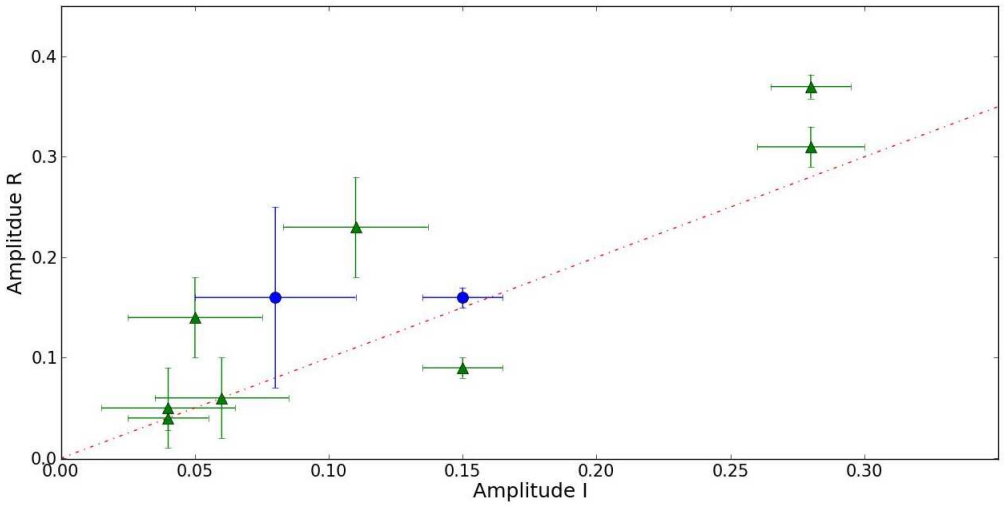

Figure 5.6: *I-band amplitudes versus R-band amplitudes. Over-plotted line represents the 1-to-1 line. Known accretors are shown in green, and the non-accretor (CHXR22E) and unclassified target (ChaHα1) are shown in blue. Note that T45 is not included in this plot as no amplitude for the R-band variations was found. T31 is also not included as neither the I-band or R-band could be fitted for periodic variations.*

The big limitation of this data set is the time-series coverage. At best two periods are covered for the fastest rotating objects in the sample, but in other cases not even a full period is covered. These light curves provide strong evidence for rotation periods on these time-scales, but further observations are needed to confirm them.

5.6.2 Amplitudes

It is clear that the majority of the sample shows periodic variations. One indication of the origins of these variations is their amplitudes and the comparison between amplitudes in different wavelength ranges. Fig. 5.6 shows a comparison between the fitted I-band and R-band observations. In most cases, the amplitudes either agree or the R-band amplitudes are larger. There is only one object which lies below the 1-to-1 line, ISO143, and in this case the R-band is very poorly fitted.

Larger amplitudes at shorter wavelengths are expected in the case of spots on the surface of the star. Considering that any small differences in the amplitudes could be hidden in the noise of the measurements, all our targets agree with this picture.

Photometric monitoring in the J,H and K band was undertaken in 2000 by

Carpenter et al. (2002). If we compare the variations found in this sample, with those observed in 2000 over the time-scales of months, we see in all cases but one, that the variations in the J-band are smaller than those in the I-band. The only object which shows twice as much variations in the J-band is T31. For this object no periodic signature was found, and the light curve took the form of a slow drop in brightness across the 8 nights of observations. This is another indication that spots are not the only source of variations in this object. Larger variations at longer wavelengths are suggestive of changes in the circumstellar disc emission, either due to an accretion event or a change in the inner disc structure (Carpenter et al. 2001).

As mentioned in Sect. 5.2, cool spots are not stable over the time-scales of years, however the rotation periods of these targets are. While definitive conclusions cannot be drawn on comparing variations in these objects from two samples that are a decade apart, the variations observed in 2000 are supportive of those found here.

5.6.3 Residual Variations

From the 11 objects with light curves that can be described by periodic variations, 4 accretors (T33, T45, B43, T30) show extra variations on top of the sinusoidal fit and significant structure in the residuals.

Accretors are more likely to be irregular variables then their non-accretor counterparts (Lamm et al. 2004). These variations occur on the time-scales of hours, on top of the periodic variations and are consistent with what would be expected in the case of short accretion rate changes on the time-scales of hours.

The fact that nearly half of the accretors in the Chamaeleon sample show these short term variations is complimentary to the findings in Chapt. 4, in which it was found that the rotational modulation cannot account for all the variations that were observed.

5.7 Conclusions

A photometric monitoring campaign was undertaken over an eight day period to identify variations of YSOs in the Chamaeleon I region. Of the objects for which light curves were extracted, 31 are members of the Chamaeleon region as classified by Luhman (2007). However 11 of these targets are only candidate members, while the remaining 20 are a mix of Class II and III objects. None

of the 8 Class III objects were seen to show variability above the background level, whereas the 12 Class II objects all showed variations. Nine of these class II objects are confirmed accretors from the LAMP sample (See. Chapt. 3).

The light curves of all Class II objects were fitted with a sinusoidal function to derive rotation periods. This method was successful in describing the majority of the variations in these light curves for 11 out of the 12 objects. The periods derived from this fit ranged from $\sim$ 3 to 7 days, with the shortest periods coinciding with the lower mass objects.

This period fitting method was found to agree with previous estimates of rotation period that employ more sophisticated algorithms. When applied to the data set of Joergens et al. (2003), the differences in derived periods lay within the errors.

The periods derived for the three brown dwarf candidates in this sample, are longer than the hours or day periods expected of them. The presence of the circumstellar disc suggests that their low rotation rates may be due to ongoing rotational braking through the magnetic field interacting with the disc.

The amplitudes and the colour variations in the majority of the sample are consistent with variations due to spots on the surface of the star. In all cases for which periods were derived, the magnitude of the variations agree with what is expected from cool spots alone. However this does not rule out the presence of hot spots on the surface.

Four of the accretors in the sample show further variations on top of the periodic variations. These additional variations occur on time-scales of hours and are consistent with what was observed in higher mass sample of T Tauri and Herbig stars in Chapt. 4. In both cases larger variations are observed over the time-scales of days, i.e. the rotation period, but on top of these variations low amplitude short term variations occur within a night's observation. This is an indication that there are short term accretion rate changes in these accretors, which could take the form of fluctuating density in the accretion flow or instabilities in the inner disc or magnetic field. Further observations are necessary at different wavelengths to firstly confirm these are accretion events and also to differentiate between these situations i.e. NIR monitoring of the inner disc or monitoring of magnetic sensitive photospheric lines in conjunction with accretion sensitive lines.

6 Summary

6.1 Motivation

Mass accretion is a key mechanism in the process of star formation. It controls the flow of matter and angular momentum from the circumstellar environment onto the YSOs, and can be the dominant source of emission from these objects. The current paradigm for this crucial process is magnetospheric accretion where the magnetic field of the young star truncates the inner part of the disk and channels the accretion flow from the edge of the disk to the star. These accreting objects are found to be the most variable members in young stellar populations (e.g. Herbst et al. 1994). Spectroscopic studies have identified this excess variability as coming from changes in the accretion rate (Nguyen et al. 2009b). For some individual objects, through extensive monitoring, the sources of accretion variations can be identified (e.g. AA Tau and Bouvier et al. 2007a, 1999, 2003). These objects are often targeted for their variability and it is not clear whether these variability mechanisms are common to all accreting objects, or are a result of a specific attributes of that system.

This thesis was focused on quantifying variations in *typical* accreting YSOs in order to identify their origins. Both spectroscopic and photometric observations were performed to disentangle the accretion variations from the intrinsic YSO

variability, and to identify time-scales and magnitudes of typical accretion rate changes.

6.2 Learning from LAMP

Th majority of variability studies suffer from low number statistics in biased samples with restricted time sampling. In an attempt to counter these weaknesses the Long Term Accretion Monitoring Program (LAMP) used the multi-object capabilities of the fibre spectrograph FLAMES to monitor as many targets as possible in the young star forming region Chamaeleon I. A single pointing was chosen in which a large number of targets with infrared excess (indicative of a circumstellar disc) could be covered. No other selection criteria were applied to this sample.

The final sample of well observed YSOs was composed of 25 objects ranging in spectral types from G2 to M5.75. These targets were observed 12 times over the course of 15 months (see Chapt. 2 for observing log). Using the emission lines Hα (6562.81 Å) and Ca II (8662.1 Å) as accretion indicators, 10 accreting objects were found. The mean amplitude of variations in derived accretion rates (measured as $Log(\dot{M}.yr^{-1})$) from Hα EW was $\sim$ 0.37 dex, from Ca II EW $\sim$ 0.83 dex and from Hα 10%w $\sim$ 1.1 dex.

The accretion rate measurements from the Hα 10%w are far more variable that those derived from the Hα EW and the Ca II EW. This implies there are contributions to this measurement that do not significantly affect the Hα EW and the Ca II EW. Thus it is considered that the 10%w is not only tracing the accretion rate changes, but something else as well i.e. stellar wind. For this reason the Hα 10%w is not considered a good measurement to derive accretion rates from.

The results from this study suggest that the accretion rates are stable within < 0.37 dex over time-scales of less than 15 months. All the accreting objects but one, were found to have reached a maximum amplitude of variations or were within 70% of the maximum on the shortest time-scales in the sample, 8 - 25 days. This means observations on time-scales of $\sim$ 2 weeks could be sufficient to limit the total extent of accretion rate variations in typical young stars.

Significantly these time-scales are comparable to the expected rotation periods of these young stellar objects, which is an indication that these variations are a result of a rotational modulation of the accretion rate. However without further observations it is not possible to discern what form these variations take.

6.3 Short Term Variations

Investigating these short term changes in accretion rates was made possible with a spectro-polarimetric data set observed by Vink et al. (2005). The sample is composed of 14 Herbig Ae and intermediate mass T Tauri stars. Compared to the previous sample, this one is very biased as all the targets are bright, known variables and in most cases very well studied.

These targets were observed over three nights in 2001 and four nights in 2003 with the ISIS spectrograph on the WHT. Timing and number of observations blocks differ between the targets (see Chapt. 2 for more), but time-scales of hours are covered for the full sample, while half the sample covers time-scales of days and years.

The observations were focused on the Hα emission, making any accretion rate variations derived directly comparable to those found in the LAMP sample. The variability in the emission line was assessed using line measurements and time series of line profiles. The majority of the sample shows low levels of variations within the $\sim$ hour block observations and, across multiple days observations the sample shows slow, gradual changes in the profiles.

However, in 3 observation blocks for 3 separate objects, there was evidence for rapid variations in the Hα emission with typical time-scales of $\sim$ 10 mins. This represents 10% of the total observing time. These rapid variations could occur in all targets, and possibly are a result of instabilities in the inner regions of the system such as a rearranging of the magnetic field, or a density change in the accretion flow.

Converting the changes in the Hα EW to accretion rates, the inferred mean accretion rate changes are 0.01 - 0.09 dex for time-scales of $<$ 1 hour, 0.1 - 0.4 dex for time-scales of days, and 0.15 - 0.46 dex for time-scales of years.

These results provide a lower limit to the accretion variability which is complementary to the upper-limit found in the LAMP sample. In fact the amplitude of variations derived in this sample over the time-scales of days, agrees with the mean amplitude of variations over time-scales of weeks and months found in the LAMP sample. The 7 objects with observations in both the 2001 and the 2003 data set also confirm this. Both the LAMP and the ISIS samples point towards days being the dominant time-scales in these samples which cover periods of years.

Significantly, even though both samples cover two very different mass ranges, both show the same level of variations. This is a strong indication that the same

accretion process and source of variations is occurring in stars from T Tauri to Herbig Ae stars, across the wide mass range of ~ 0.1 to $\sim 5\,M_{\odot}$.

The simplest explanation for these variations that occur on rotational time-scales is an asymmetric accretion flow. These have been shown to occur through MHD modelling in the cases when there is even a slight offset for a few degrees between the rotation axis and the magnetic field axis.

However not all variations in this sample can be explained by rotationally induced variations, i.e. the rapid variations seen on the time-scales of less than one hour. There was also one object in the Chamaeleon I sample, T33, that showed greater variations on the longer time-scales. These are indications that though rotationally modulated variations may dominate the observations, there are other active sources of variations in these systems, such as instabilities in the inner disc or magnetic reconnection events.

One of the weakness in this comparison between the samples is the heavy bias that exists in the ISIS sample. It was not clear that drawing the comparison between some of the brightest, well studied high mass objects and low mass T Tauri stars was reasonable, even if the two separate studies pointed towards the same time-scales. Constraining the rotation periods and short term variations in the LAMP sample makes the comparison definitively more robust.

6.4 Chamaeleon Photometry

One of the most reliable methods of determining rotation rates in YSOs is through photometric monitoring. This method relies on the fact that all YSOs are thought to be magnetically active, which results in cool spots on the surface where the field interacts with the stellar photosphere. These spots rotate with the star, and monitoring these objects reveals the change in emission as these spots come in and out of view allowing the rotation rates to be derived. However, changes in the light curve can also be caused by hot spots on the stellar surface, inner disc variations or changes in the accretion luminosity. This results in the accreting objects of young populations being the most variable.

Photometric monitoring of the Chamaeleon I region was undertaken in two wavelength ranges, I and R band, over a period of 8 consecutive nights. These observations were performed using the WFI on the ESO-MPG 2.2 m at La Silla, and were centred on the previous FLAMES field.

Twelve objects stood out from the non-variable background stars, and showed significant variations above the average. Nine of these objects were classified as

accretors in the LAMP sample, one was classified as a non-accretor, and the remaining two were not covered in the LAMP observations.

Likely periods were found for 11 of the 12 objects in the sample, and these range from $\sim$ 3 to 7 days. The majority of the variations in these 11 objects, can be explained by the presence of cool spots on the stellar surface and the derived rotation periods are consistent with what we would expect from these young objects. The upper-limit on the dominant time-scales for accretion variations in the LAMP sample is 8 - 25 days. The periods found here all lie within this upper-limit, proving that the variations found in the LAMP sample are consistent with what could be expected of rotationally modulated accretion variations.

Further significant residual variations were found in four of the accretors. In all cases the targets show clear periodic variations, but after fitting for this periodic signal strong residuals remain. As with the ISIS sample, there are short term variations occurring in these systems that cannot be accounted for by simple rotational modulation.

6.5 Putting the Pieces Together

The main findings in this thesis can be summarised under the following points:

- The LAMP program covered 10 low mass T Tauri stars and time-scales of weeks up to 15 months. During this period accretion rate variations of < 0.37 where found when derived from the Hα EW.

- For the majority of accretors in the sample, the variations had reached a maximum or were within 70% of their maximum after the shortest time period within the study (8 - 25 days).

- The ISIS sample covered 14 larger mass targets, ranging from intermediate T Tauri to Herbig Ae stars, for which time-scales of $\sim$ hour, days and years were covered.

- Most of the variations found in this sample took the form of slow variations in the Hα profile over the $\sim$ hour block of observations. However, in 10% of the observing time, rapid variations occur in the profiles, on time-scales of $\sim$ 10 mins.

- Using the same methods as the LAMP sample, accretion rates were derived from the Hα EW. The mean accretion rate variations were found to be 0.01 -

0.09 dex for time-scales of < 1 hour, 0.1 - 0.4 dex for time-scales of days, and 0.15 - 0.46 dex for time-scales of years.

- The accretion rate variations increased by an order of magnitude, from the time-scales of hour to days. However there was hardly any increase in the variations when the longer time-scales of years were considered, suggesting the time-scales of days to be the dominant period.

- Both samples together suggest that for a typical accreting object, the mean accretion rate variations will not be any greater than 0.5 dex over time-scales from hours to years.

- The similarity of the amplitude in the accretion rate variations found in the low mass end of the samples and the high mass end of the sample, suggest the same accretion process is occurring in both.

- The short term variations of the Chamaeleon sample were investigated with a photometric monitoring campaign over 8 days. Rotation rates were found for 8 of the accretors in the LAMP sample, which all lay within the derived upper-limit on the dominant time-scales for accretion rate variations,

- On top of the rotationally modulated variations in the light curves for 4 accretors, there were significant variations that could not be explained with a simple cool spot model.

Through the three studies in this thesis and others (i.e. Nguyen et al. 2009b), it has become clear that typical accretors do not go through large accretion bursts like EX Ors or even FU Ors (see Chapt. 1). Over the time-scales of days, months and years, no large variations in accretion rate were found in the samples of this thesis.

This work cannot rule out that large changes in the accretion could occur on time-scales of $\sim$ decades or longer (as is the case with FU Ori). However, it can be said that over the time-scales of years, the dominant variations occur on time-scales close to the rotation period. This suggests that observations over the time-scale of < 1 week in typical accreting objects are sufficient to put limits on the expected magnitudes of variations that occur over the time-scales of years.

These low levels of variations are also significant for the $\dot{M} - M_*^2$ relation. The mean amplitude of variations in the samples studied here is ~ 0.5 dex. This demonstrates that the 2 orders of magnitude scatter around the $\dot{M} - M_*^2$ relation at a given mass cannot be solely due to accretion variability. Studies of individual

star forming regions with low age spreads have shown that this spread is unlikely to be due to evolutionary effects (i.e. Natta et al. 2006). This strongly suggests that the $\dot{M} - M_*$ relation is due to either limitations in our detections of low accretion rates in high mass objects, initial conditions or is an indirect correlation where both the accretion rate and stellar mass are linked through a different process.

The dominant time-scales of variations in the LAMP sample were found to overlap with those found in the ISIS sample. In both cases the amplitude of variations saturated on time-scales close to the rotation period. This suggests that a large portion of the accretion rate variations in the vast majority of accreting objects are rotationally modulated. Simulations have shown that an asymmetric accretion flow can occur when there is a slight offset of a few degrees between the rotational and magnetic field axis (Romanova et al. 2003). Observations of BP Tau show that these offsets can and do exist (Donati et al. 2008). Along with the fact that the often observed higher order magnetic fields will also disrupt the symmetry, it is very likely that most accretors have asymmetric accretion flows. The observations in this thesis support this, and are consistent with what we would expect from an asymmetric accretion flow rotating with the star.

The smooth variations in accretion rates observed in this work rule out the presence of large scale instabilities in the accreting system. If magnetic reconnection events were common, more stochastic changes in the accretion rates would be observed. This suggests that the large scale structure and strength of these magnetic fields are roughly stable over the time-scales of years. This is an important point for the rotational braking paradigm, where the magnetic field needs to be stable over long enough periods to exert sufficient torque on the stellar disc to cause the spin down of the star. It remains to be seen if the magnetic fields remain stable over the longer time-scales of decades.

However, the rotational modulation of the accretion rate cannot explain all the variations that were observed in this work. For example, in 10% of the observing time in the ISIS sample, variations on shorter time-scales of hours were observed. Also in the Chamaeleon photometry, similar stochastic variations on the time-scales of hours were observed in part of the accreting sample. One likely cause for these variations is the existence of Rayleigh-Taylor instabilities in the inner disc (Kurosawa & Romanova 2013) which result in multiple temporary accretion flows existing in the system. In this unstable regime the red-shifted absorption is constantly observed, as there is always some accretion flow in view. However observations of higher order Balmer lines than Hα are needed to dis-

tinguish this feature. Multiple line monitoring is necessary to properly ascertain the nature of these variations, and the geometry of these accretion flows.

6.6 Looking to the Future

Within certain areas of astronomy, the new science is being achieved through monitoring studies (i.e. supernova, planet searching, gamma ray burst). However on modern telescopes there is little time for extensive monitoring campaigns for individual studies. There are a number of facilities now being built specifically for time domain studies. For example such large facilities like LSST have never before been dedicated to monitoring the night sky, others include the Palamar Transient Facility and VYSOS in Hawaii.

These surveys will provide far more opportunities than have been available before to monitor young star forming regions and gather extensive data sets, increasing the number of typical accretors with well defined variability and providing much better time-scale coverage than has been possible before. One of the main objectives of these studies, in the context of YSOs, is to identify more out-bursting events (i.e. FU Ori events) in order to find the connection between these outbursts and the typical accretion events seen in T Tauri stars. To date only 8 FU Ori targets have been identified, providing a small and non-uniform sample. To understand if these are common events in the lifetime of every star and what causes these events, the numbers of studied FU Ori objects needs to be drastically increased. These out burst events are thought to be stochastic, though the cause is still unknown. In order to catch these events, multiple star forming regions need to be monitored constantly. Not only will further observations of FU Ori events, increase our understanding of the long term evolution of the accretion process, but as a by product of monitoring for a FU Ori event, many T Tauri stars will also be monitored. This will provide a wealth of light curves for these targets, and in conjunction with archival data will help in the determination of any longer (decadal) term accretion rate variations.

ALMA will play a huge role in the coming years in pushing our understanding in disc processes and evolution. Already with the early science data evidence of asymmetric structure in circumstellar discs have been revealed, and are thought to be due to interaction with planets. ALMA will also allow for the temperature and density structure of these discs to be well mapped as well as disc dynamics such as gas flows and mixing within the disc layers. This will allow us to define the dominant accretion processes in these discs, whether it is gravitational

instabilities, disc winds or MRI turbulence. In the future, new interferometric instruments like GRAVITY will also provide key insights to the structure of the inner discs of accretors, and any variations that may occur within them.

To fully understand the accretion process it is vital to improve our knowledge of the magnetic field. ALMA will provide some constraints on magnetic fields, and their connection to the circumstellar discs in the future. There are also many large observations programs running on current instruments (e.g. CRIRES and HARPS) that have been successful in determining the structure and strength of magnetic fields in main sequence stars. However, more attempts are being made to expand these works and use the same methods in pre-main sequence objects, where variability and activity make the analysis more difficult.

Current instruments such as X-shooter which allow for simultaneous observations of the UV excess emission, accretion indicators, magnetic sensitive lines and outflow indicators. The demand is high on this instrument, but it is already improving our understanding of the relation between the emission lines and the accretion shock emission, and as the number of observations increase it will also go far in contributing to mapping of the geometry of these systems.

To complement the survey telescopes, there are many new and ground breaking multi-object spectrographs (FMOS at Subaru, KMOS at the VLT, Flamingos-2 at Gemini) which will make spectroscopic follow ups of the nearer star forming regions more efficient. The big weakness in this field is the poor statistics, and as it stands observations of accreting T Tauri stars are behind what the computational models can produce, leaving limited constraints on the system parameters that are used in these models. These multi-object spectrographs will allow for better time resolved observations in greater numbers of accreting sources, which will provide much needed physical constraints for the simulations.

This thesis lays the ground work for these future surveys. It shows that over the time-scales of years the majority of accretion rate variations occur over the period of days. This suggests a close connection to the rotation period of these accreting objects, and is a strong indication that the accretion rates are rotationally modulated. However, these studies cannot determine the long term variations of these targets that may occur over many years or decades. These future facilities will allow for the exploration of variations on the longer time-scales, and the physical processes that may occur over them.

A

Temperaments of Young Stellar Objects: Individual Objects

A.1 About this Appendix

In the following, the properties of the individual targets used in the analysis in Chapt. 4 are presented along with time series of the Hα profiles, average and variance profiles and differential surface and spectra plots.

The plots for each target take the same form. The top left panel is a time series of Hα profiles across the observation block. Each profile is off-set from the previous one for clarity. The minute of the hour in which each spectrum was observed is given to the right of each profile. The top right panel contains the average and variance profiles. The bottom left panel is a differential surface plot. This plot shows the difference between the first spectra of that night and the preceding spectra. The bottom right panel shows a time series of cuts in differential flux plots. This was done in the same way as the surface plots, where the first spectrum of that night was removed from all the rest of the spectra. These are the same profiles as chosen for the profile time series, and again the minute of the hour in which each spectrum was observed is given to the right of each profile.

A.2 RW Aur

Stellar Properties: RW Aur is a resolved triple system (Ghez et al. 1993). The primary has an estimated stellar radius of 1.3 - 1.5 $R_\odot$ and a stellar mass of 1.1 $M_\odot$ (Petrov et al. 2001a). A rotation period of 2.77 days has been reported for RW Aur A (Petrov et al. 2001a). However, measurements of the longitudinal magnetic field in the star, found the changes in B_z of -1.47 $\pm$ 0.15 to +1.10 $\pm$ 0.15 kG to be consistent with a rotation period of 5.6 days, and two rotating spots on the surface with opposite polarity. This is to be expected from an asymmetric accretion flow, where the two spots follow the base of the accretion flows.

Accretion Rates: Basri & Bertout (1989) have reported an accretion rate of $2\,\mathrm{x}\,10^{-7}$ $M_\odot.yr^{-1}$ derived by fitting a boundary layer model to the observed emission.

Outflows: This object is associated with a very large asymmetric outflow which was found to contribute to the Hα emission at $\sim$ -150 to -180 $\mathrm{km\,s^{-1}}$ and at $\sim$ 109 $\mathrm{km\,s^{-1}}$ (Hirth et al. 1994). López-Martín et al. (2003) found a bipolar jet with an inclination angle of 45°, in this work it is assumed that the stellar system has the same inclination.

Disc Properties: The inner disc radius is 2.7 R_* with a calculated co-rotation radius of 6.1 R_* (Gómez de Castro & Verdugo 2003), and an outer radius of $\leq$ 57 AU (Cabrit et al. 2006). The disc inclination is thought to lie between 45 - 60°, which is in agreement with the jet inclination (Cabrit et al. 2006). Submillimeter observations have revealed disc mass of $3\,\mathrm{x}\,10^{-4}\,M_\odot$ (Williams & Andrews 2006). At the end of 2010, RW Aur was observed to dim by $\sim$ 2 magnitudes over the course of $\sim$ 180 days. This is attributed to an occultation by a large tidally disrupted trailing arm from the disc (Rodriguez et al. 2013), which most likely formed through an interaction with RW Aur B (Cabrit et al. 2006).

ISIS Hα Observations: Over the course of the observations, RW Aur shows a double peaked emission line with a central absorption and extended wings. During the single observation block in 2001 (Fig. A.1) a double peaked profile is observed with a central absorption. Over the course of the observation block both peaks of emission strengthen with respect to the continuum.

During the first night of observations in 2003 there is very little change in the profile (Fig. A.2). A large change in the profile does take place between the first and second night's observations in 2003, where the red peak becomes much stronger the the blue emission peak (Fig A.3). The changes in the profile on the second night take the form of increased emission in the red side of each of the

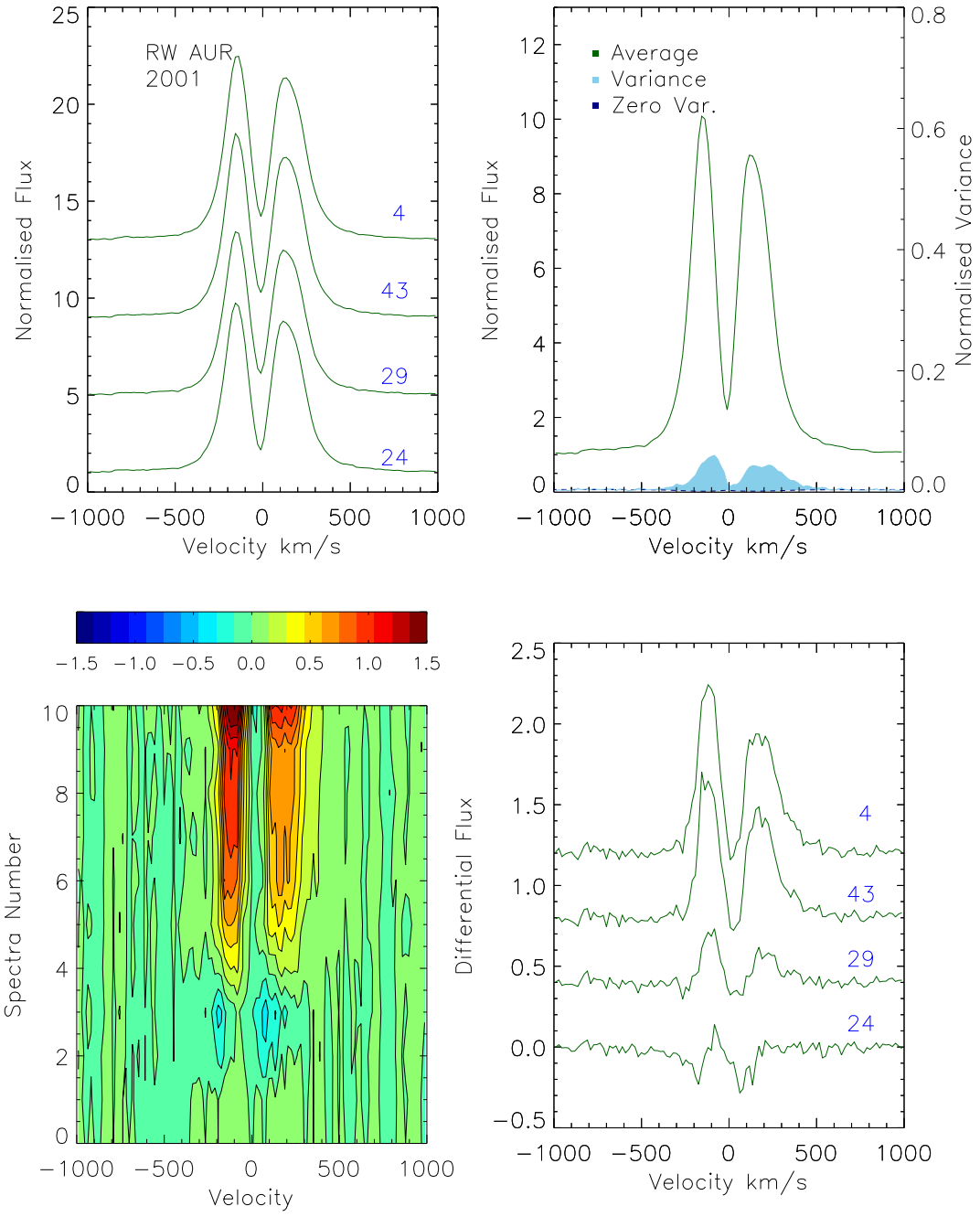

Figure A.1: *RW Aur 2001 observations.*

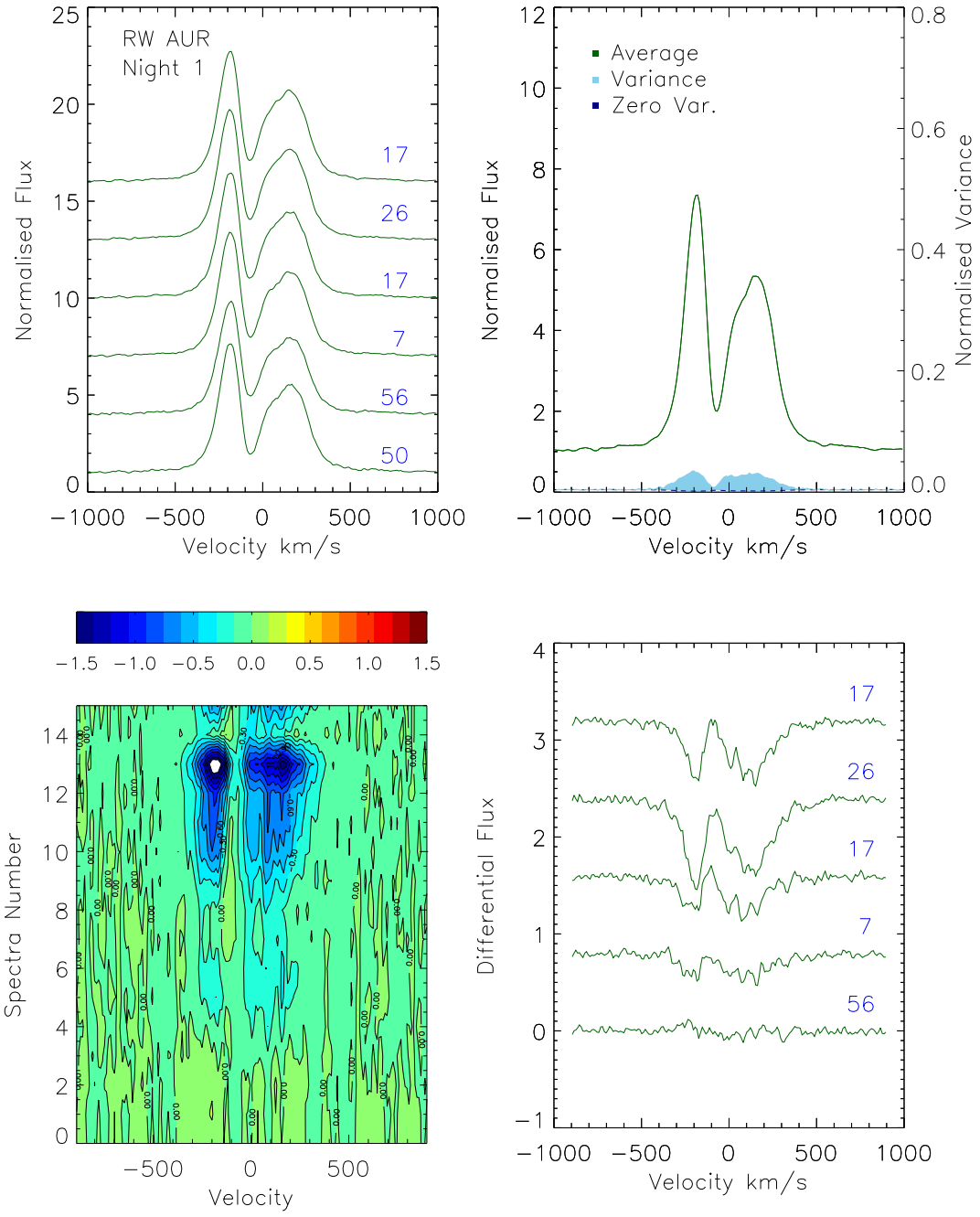

Figure A.2: *RW Aur 2003 observations, Night 1.*

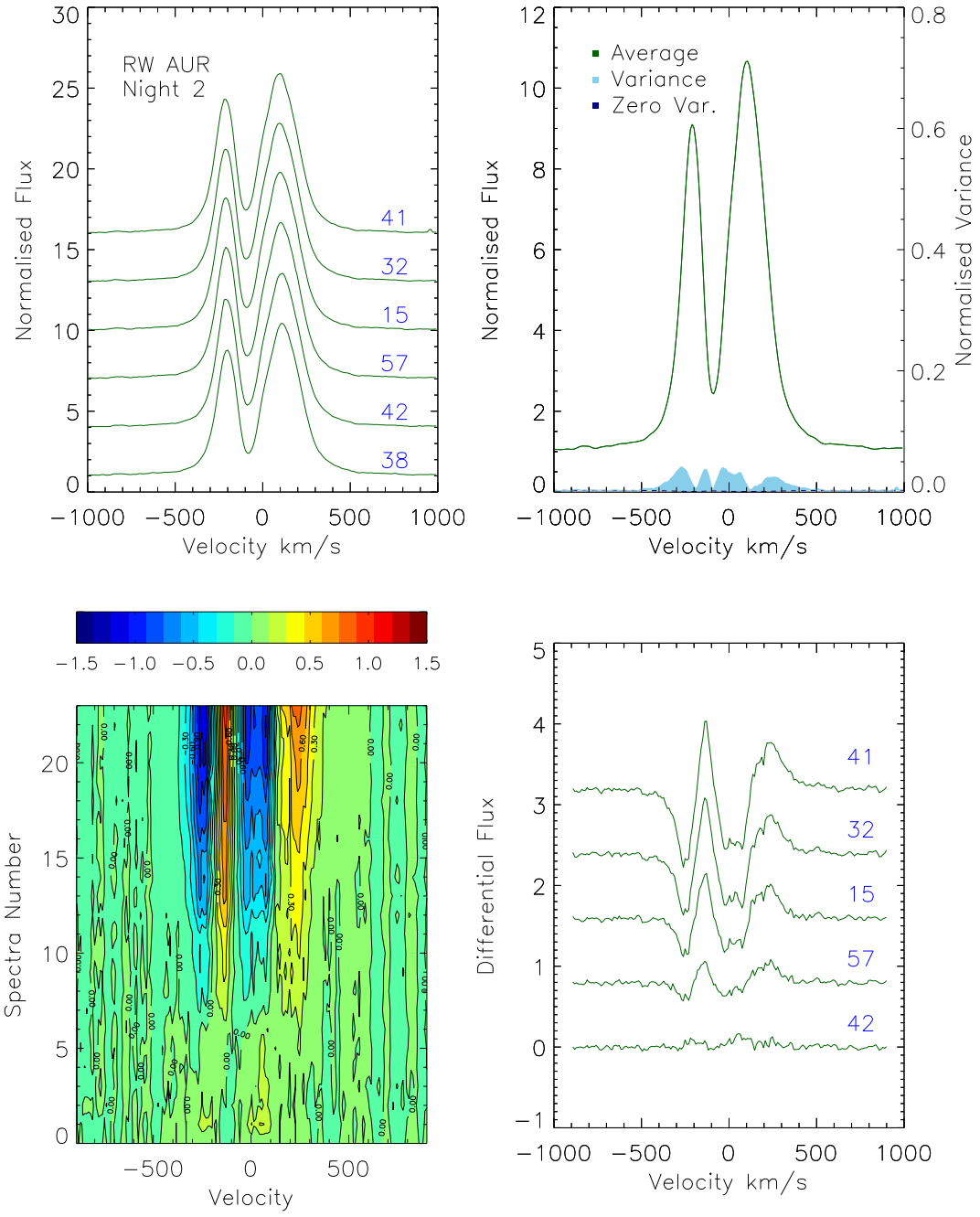

Figure A.3: *RW Aur 2003 observations, Night 2.*

emission peaks within the profile, while the central intensity decreases slightly.
Previous Hα Observations and Variations: A similar Hα profile to these was observed in 1976/77 with an EW of 128Å (Schneeberger et al. 1979a).

RW Aur was also observed in 2001 (Chou et al. 2013), where EW measurements of 80.4, 65.6, 79.7, 72.9 Å were found on November 17^{th}, 21^{st}, 25^{th} and 27^{th} respectively. These measurements are very close to what was observed in the ISIS sample on the 26^{th} December 2001 (mean 74.04 Å). The same magnitude of variations (81.11 - 67.88 Å) was observed with ISIS during the half hour of observations, as Chou et al. (2013) observed in one week. Their variations took the form of a fall in the red peak emission.

Schneeberger et al. (1979b) found evidence for short term flares and changes while photometrically monitoring RW Aur, which they likened to the slow flare events on YZ Cmi. Relatively large photometric variations have also been reported, Petrov et al. (2001b) found over periods of 3 - 4 days changes of 0.2 - 0.7 magnitudes in the V band.

Observations of rapid line profile variability in the spectra of RW Aur, specifically the Hγ profile, have also been observed on time scales as short as 10 mins (Mundt & Giampapa 1982).

A.3 DR Tau

Stellar Properties: DR Tau has a stellar mass of 1.0 $M_\odot$ and a radius of 5.1 $R_\odot$ (Bertout et al. 1988; Gullbring et al. 1998). The period is not very well constrained, Johns & Basri (1995a) found signatures in the emission lines of DR Tau with periods of 5.1 and 7.9 days.
Disk properties: A disc mass of 0.1 $M_\odot$ has been estimated with R_{in} of 0.05 AU (Kitamura et al. 2002). There have been a number of published inclinations for this system, which vary from edge on orientation to a pole on orientation (Alencar et al. 2001; Kitamura et al. 2002; Muzerolle et al. 2001). However, based on the low rotational velocity and a period of 5.1 days (Johns & Basri 1995a), Vink et al. (2005) suggest a pole-on orientation to be more plausible.
Accretion: The lack of photospheric lines in the observed spectra of DR Tau is attributed to high levels of veiling in the continuum (Basri & Batalha 1990; Valenti 1994). Basri & Bertout (1989) have reported an accretion rate of 5×10^{-7} $M_\odot yr^{-1}$ derived by fitting a boundary layer model to the observed emission.
Outflows: It has been suggested that most of the Hα emission is from a stellar wind (Muzerolle et al. 2001). The forbidden emission line [OI] λ6300 has been

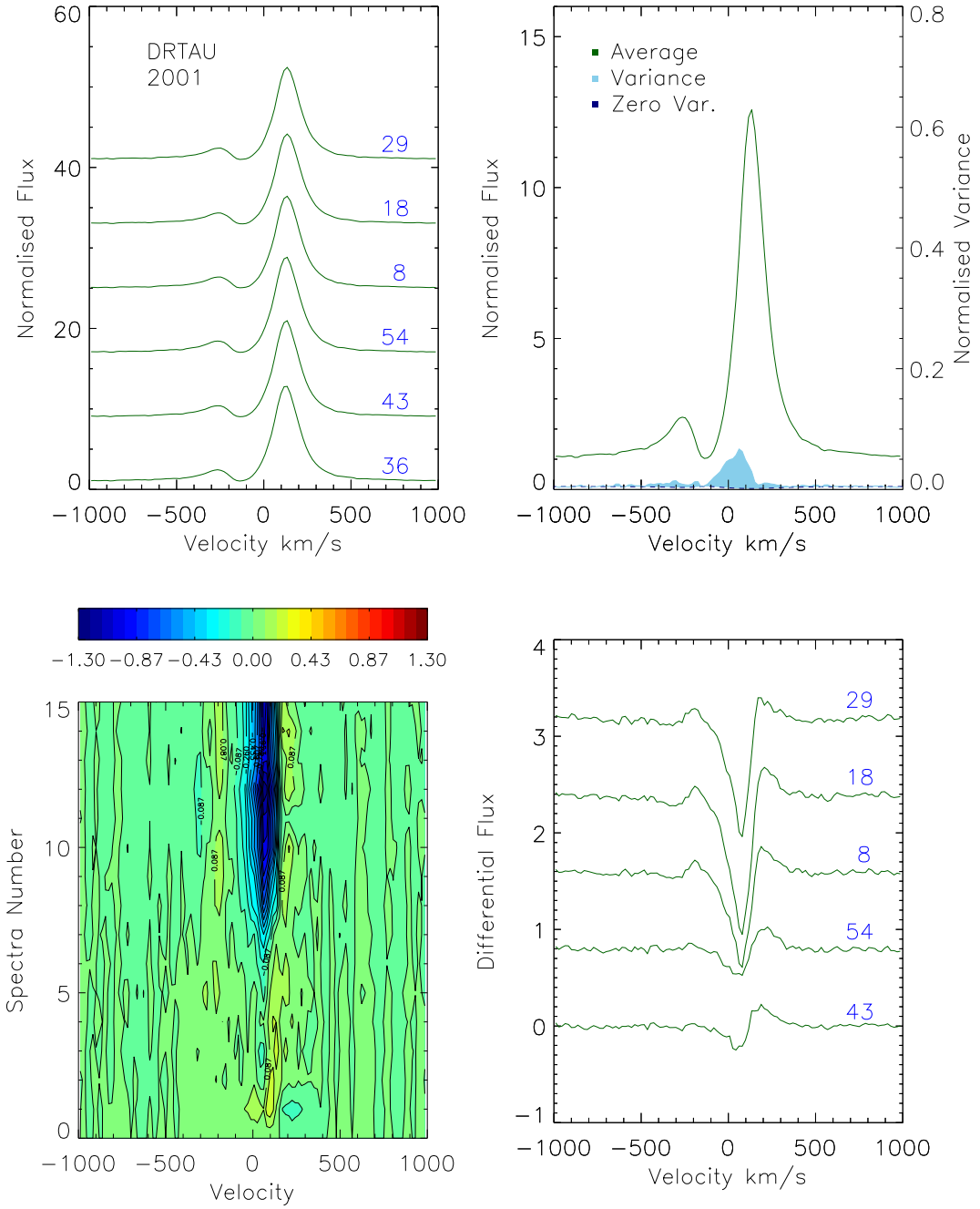

Figure A.4: *DR Tau 2001 observations. Five spectra were observed on the previous day to these observations, but are not shown here.*

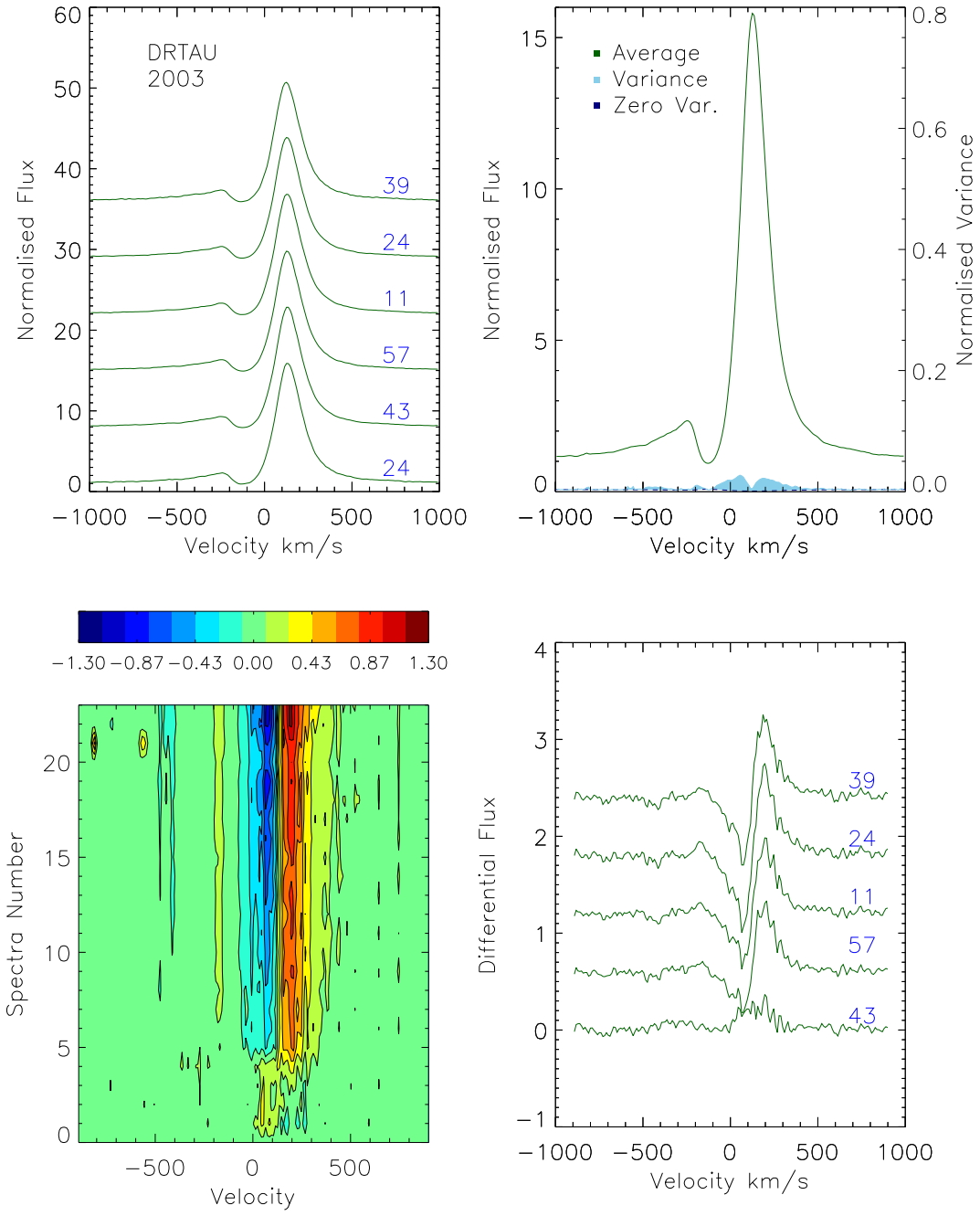

Figure A.5: *DR Tau 2003 Observations.*

observed with profiles composed of two peaks, one at the central wavelength and the second blue-shifted. This is a strong suggestion for a collimated outflow from this source (Hartigan et al. 1995; Hirth et al. 1997).

ISIS Hα Observations: DR Tau shows very similar profiles in both 2001 and 2003 (Fig. A.4 and Fig. A.5). The profile takes the form of a strong red-shifted emission line with extended wings, and a strong blue absorption that extends to below the continuum. In 2001 the blue-shifted 'peak' is more pronounced, suggesting a slightly stronger high-velocity ($> 400\,\mathrm{km\,s^{-1}}$) blue-shifted absorption. The variations in 2001 are contained to a single wavelength range centred at $100\,\mathrm{km\,s^{-1}}$, which is close to the large peak of the profile. No significant variations occur over the time-scale of the observations.

In 2003 the variance profile is different, showing that the changes in the line take the form of a change in emission strength either side of the emission peak (Fig. A.5). The first three spectra in this observation block differ slightly from the rest of the spectra, resulting in a difference of ~ 20Å in EW but no significant change in the 10%w.

Previous Hα Observations and Variations: Alencar et al. (2001) decomposed the Hα emission line for DR Tau into three parts (1) a strong red-shifted emission peak (like the emission line in this work) (2) a blue-shifted wind absorption component and (3) a relatively low amplitude component with a FWHM centred at rest velocity. Most of the variability was found in the blue side of the profile, which was found to be incoherent with changes in the red emission. (Interestingly in the case of the ISIS observations, most variability is found on the red side in emission peak). They attribute the red emission to be a result of emission from a hot inflow.

The large photometric variations of 1 - 3 magnitudes that have been observed have been attributed to hot and cool spots on the surface of DR Tau (Bertout et al. 1977; Bouvier et al. 1993a; Kenyon et al. 1994) and high veiling (see above).

A.4 GW Ori

Stellar Properties: GW Ori is a binary system with a period of 242 days (Murdin & Penston 1977). GW Ori itself has a period of 3.2 days (Bouvier et al. 1986). Signatures of magnetic activity have been observed through X-ray emission from GW Ori (Feigelson & Decampli 1981).

Disc Properties: GW Ori shows a very large IR excess (Cohen 1980) and the strongest sub-millimeter emission found for a T Tauri star (Mathieu et al. 1995)

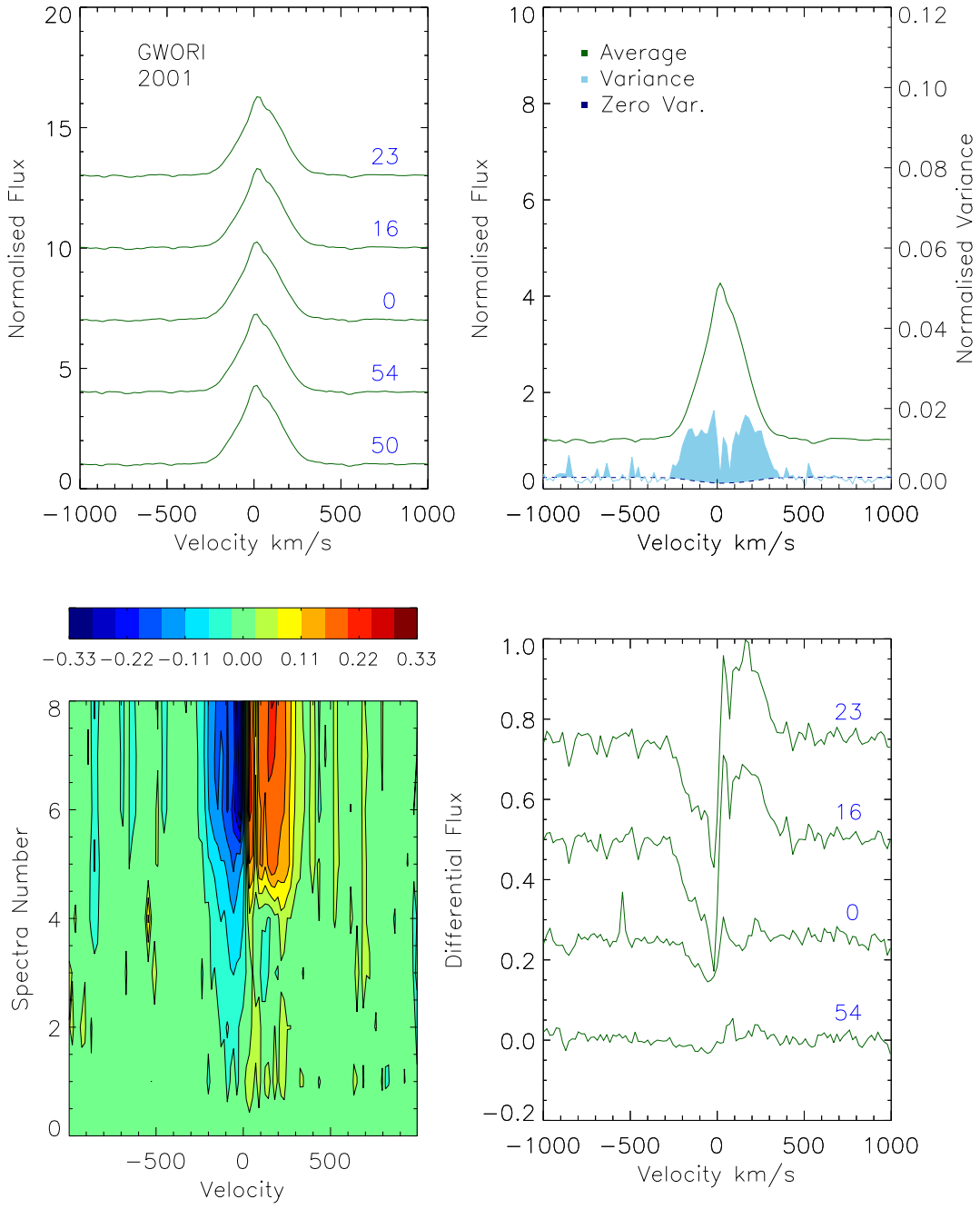

Figure A.6: *GW Ori 2001 observations.*

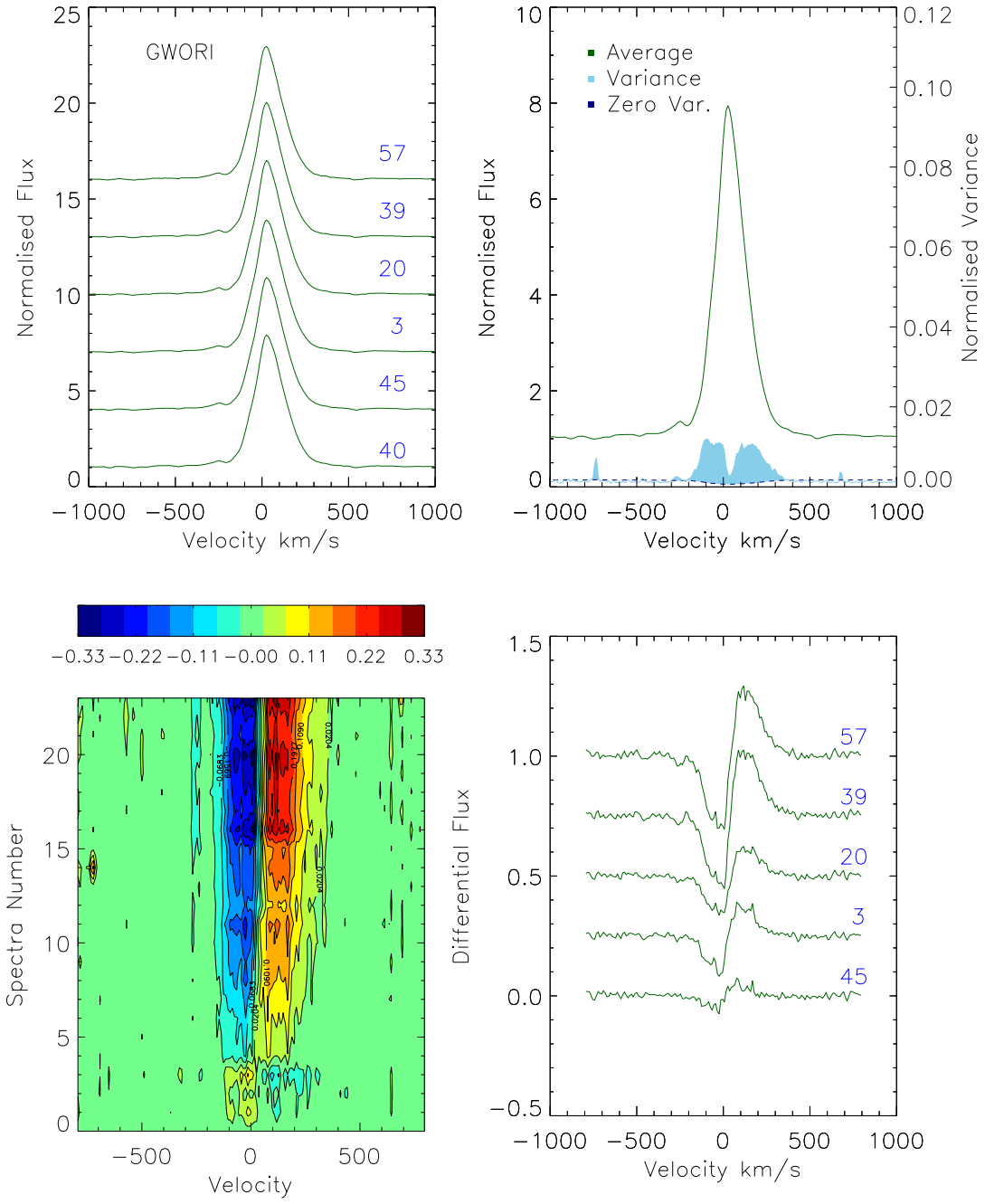

Figure A.7: *GW Ori 2003 observations.*

originating in a circumbinary disc of mass 1.5 $M_\odot$. The inclination of the disc is 15 - 27 ° (Bouvier & Bertout 1989; Mathieu et al. 1991). The disc contains a gap at $\sim$ 0.17 - 3.3 AU (Mathieu et al. 1991) in which the secondary lies.

ISIS Hα Observations: The observations show a roughly symmetric Hα emission profile, that shows small variations in both wings. In 2001 an asymmetry is seen in the wings, with the red wing showing slightly stronger emission (Fig. A.6). Across the observation block this wing grows in strength compared to the blue wing.

In 2003, the two emission wings are more symmetric, and the line is stronger (Fig. A.7). The changes in the emission take a similar form as in 2001. Low amplitude waves are seen in the 2003 time series of Hα EW measurements.

Previous Hα Observations and Variations: Photometric monitoring for flares was carried out over one night for this object, but no flare activity was found (Worden et al. 1981b). A very similar Hα profile was observed in 1977 with an EW of 45 Å (Schneeberger et al. 1979a).

A.5 AB Aur

Stellar Properties: AB Aur is the brightest Herbig star in the sky, and is a very well studied object. It is found to have a stellar mass of 2.5 $M_\odot$ and a stellar radius of 2.5 $R_\odot$ (Bohm & Catala 1993; Praderie et al. 1986). Catala et al. (1999) found a period of 34 hours from the monitoring of photospheric lines. X-ray emission has been observed from AB Aur, however the origin of it is not clear but it is possibly from a magnetic corona (Telleschi et al. 2007)

Disc Properties: Emission from the disc has been observed to extend out to 580 AU, with a double spiral structure within the disk at radii of 200 - 450 AU (Fukagawa et al. 2004). A large 100 AU inner hole in the dust continuum has also been observed in the sub-millimeter emission (Ohashi & Lin 2005). There has been many contradictory reports of inclination angles, which has lead to the belief that the disc is warped. The inclination angle has been reported to be 76° (Mannings & Sargent 1997), <45° (Grady et al. 1999), 27° - 35° (Eisner et al. 2003) which was later revised to 8° - 16° (Eisner et al. 2004). More recently Fukagawa et al. (2004) found an inclination angle of 30° ± 5 ° and large spiral structures within the disc. Modelling of the outer mm emission from the disc suggests a inclination of <30° (Corder et al. 2005; Natta et al. 2001).

ISIS Hα Observations: Across the four nights of observations in 2003, AB Aur shows a strong P-Cygni emission profile. (see Fig. 4.1, 4.2, 4.3 and 4.4).

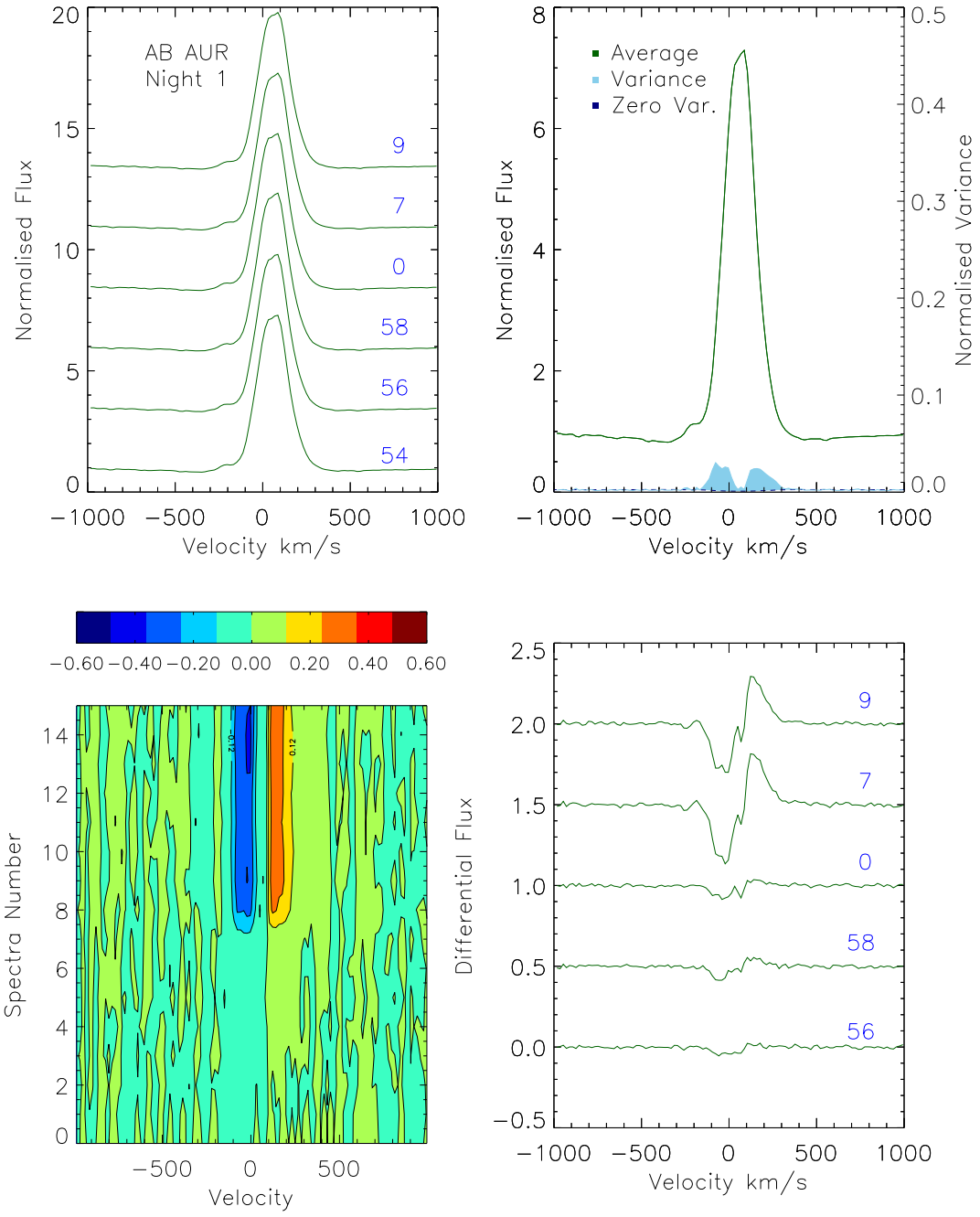

Figure A.8: *AB Aur 2001 observations. Night 1.*

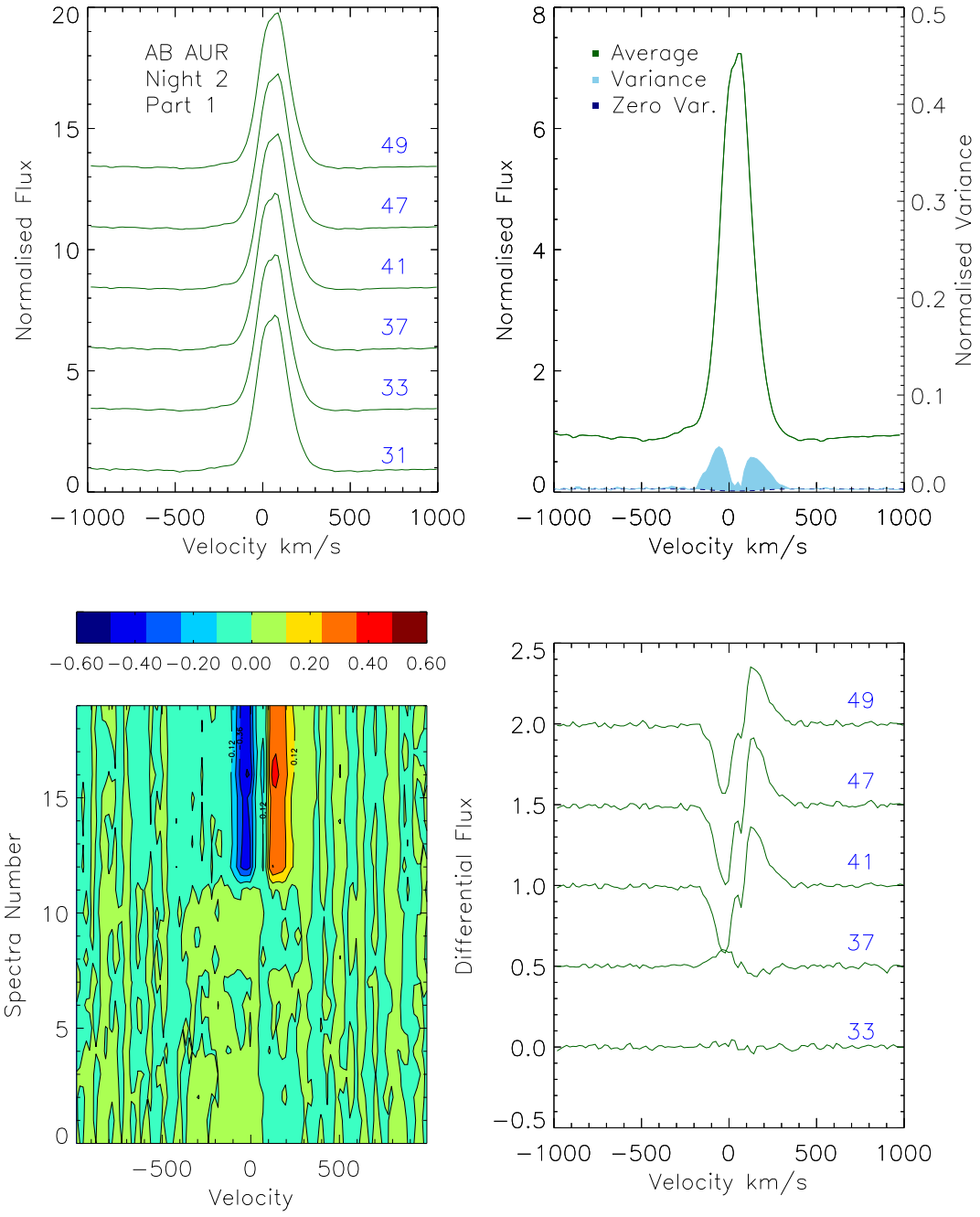

Figure A.9: *AB Aur 2001 observations. First block of observations Night 2.*

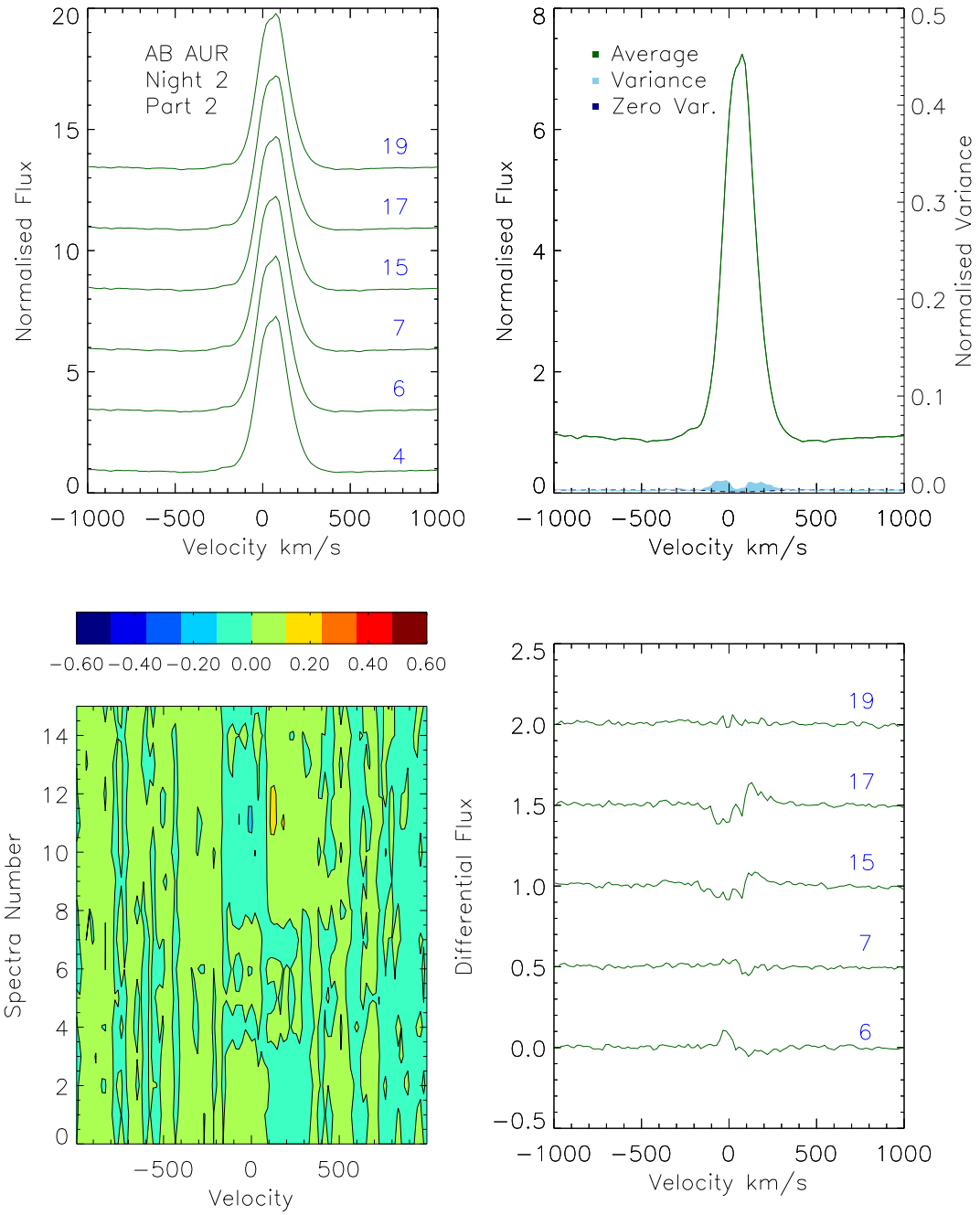

Figure A.10: *AB Aur 2001 observations. Second Block of observations Night 2.*

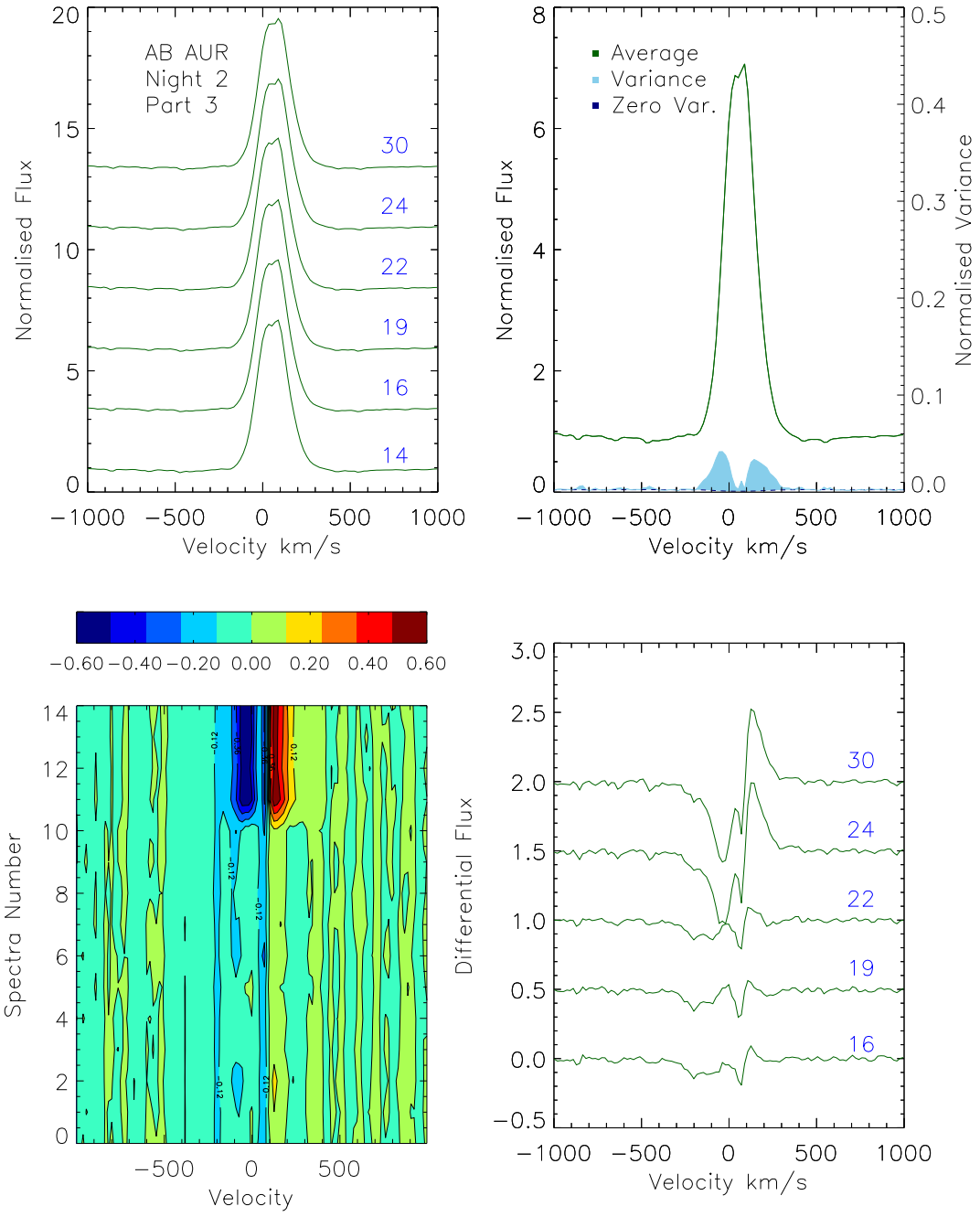

Figure A.11: *AB Aur 2001 observations. Third block of observations Night 2.*

Studying the variance profiles for the first and second night of observations, the changes in the emission line are concentrated in the wings of the profile. On the first night the variations are entirely in the blue wing, and on the second night both wings show variations. No significant variations occur during the fourth night. Within the blue-shifted absorption, a small emission feature can be seen. This changes position between each nights observation. From the first to the second night, the shift is to the blue side, and from the second to the third night it shifts further back to the red side. It cannot be distinguished from the wing or continuum on the fourth night.

On the third night of 2003 large distinctive variations in the Hα emission are seen (Fig. 4.3). The profile decreases in strength and expands a number of times during the observation block. When it increases again it is narrower. These variations manifest themselves as changes in three distinct regions of variations in the variance profiles. This results in not very large changes in the Hα EW of $\sim$ 220 - 234 Å. However during this night there are much more significant variations in the 10%w, $\sim$ 345 - 549 $\mathrm{km\,s^{-1}}$, which is an change of of 60% in 10%w. This bi-modal behaviour can clearly be seen in the surface plot for AB Aur in Fig. 4.3. This is unusual behaviour within this sample: no other object shows such strong, distinct peaks in the variance profile.

During the 2001 observations, AB Aur, does not show the same P-Cygni profile, rather a small emission peak in the blue wing can be seen (Fig A.8, A.9, A.10 and A.11). The emission line does not show any drastic changes as it later does in 2003, the changes are small in 2001, and take place in two velocity ranges one centred at $\pm$ 200 $\mathrm{km\,s^{-1}}$.

Previous Hα Observations: As mentioned in the main text in Chapt. 4, Sect. 4.5.2, Beskrovnaya et al. (1995) have previously observed striking night-to-night variations in Hα profile both in intensity and profile shape. The time sampling of these variations were on longer time-scales than those in the ISIS sample (hours rather than minutes). The authors argue that these P-Cygni variations are connected with the motion of circumstellar inhomogeneities. Large changes in the Hα emission were again recorded between 1987 and 1996, where the line changes more than 100% which is attributed to changes in the wind structure (Bouret & Catala 1998).

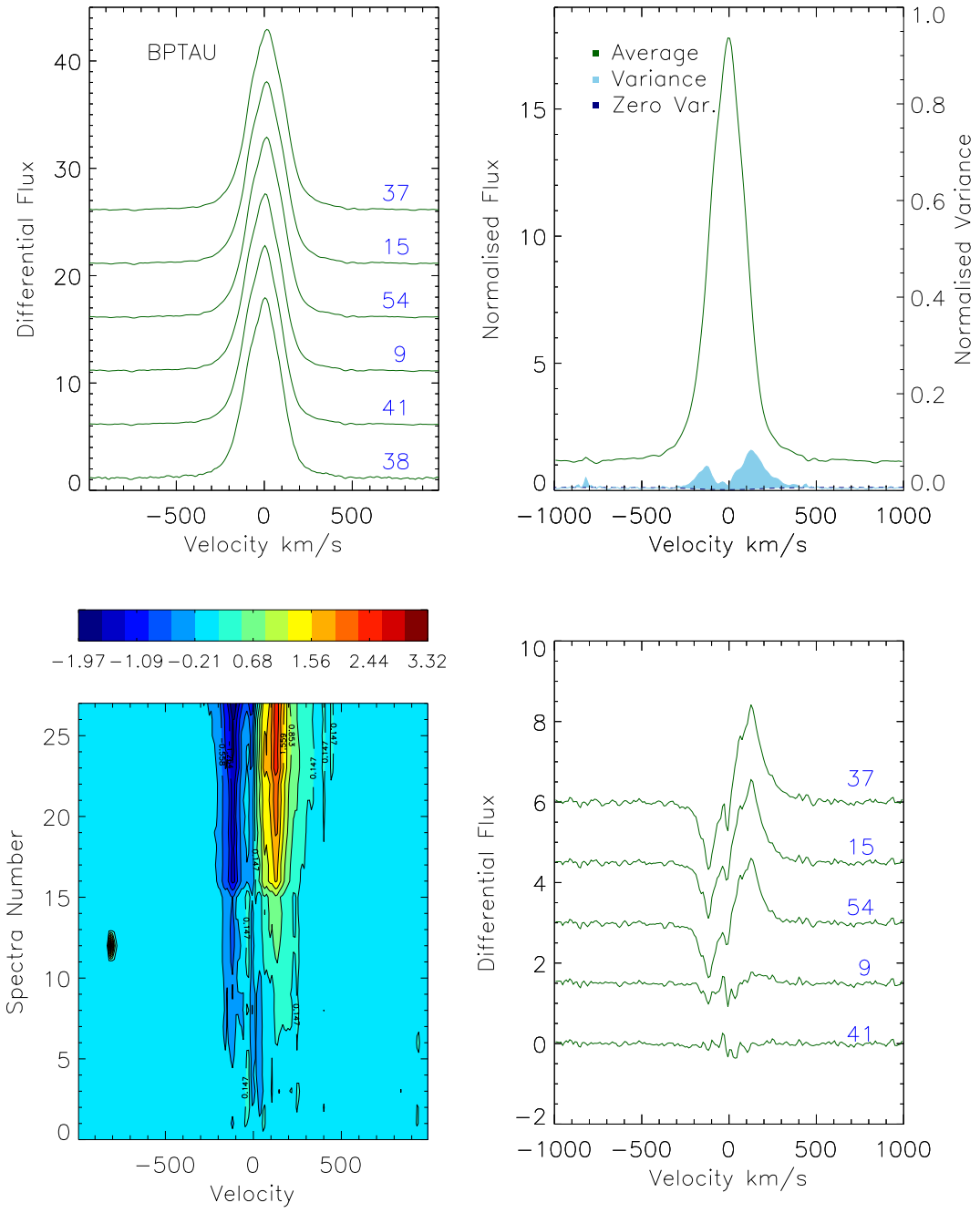

Figure A.12: *BP Tau 2003 observations.*

A.6 BP Tau

Stellar Properties: Observations of BP TAU have revealed that it contains strong magnetic field, both a dipole (1.2 kG) and an octupole (1.6 kG) component, and both are slightly shifted with respect to the rotation axis (20° and 10°, Long et al. 2011). The accretion spots coincide with the two main high-latitude octupole poles and overlap with dark photospheric spots which each cover about 2% of the surface. X-ray emission has also been observed from BP Tau (Neuhaeuser et al. 1995).

Disc Properties: BP Tau has a reported inclination of $\sim 30°$ (Dutrey et al. 2003; Simon et al. 2000). The disc is small with an outer radius of 120 AU, and there are suggestions that BP Tau is in the process of clearing its disc (Dutrey et al. 2003).

Accretion: An accretion rate of $3\,\mathrm{x}\,10^{-8}\mathrm{M}_{\odot}\mathrm{yr}^{-1}$ has been estimated from the UV excess (Gullbring et al. 1998).

ISIS Hα Observations: BP Tau shows a roughly symmetric Hα emission profile across the course of the nights observations (Fig. A.12). The variance profile shows two peaks of variations in the blue and red wings, where the changes in the red side are more pronounced. The time series of the Hα EW measurements shows what looks like a period across the hour of observation, during which the EW changes by about 58 Å. The 10%w does not show the same kind of period as the EW, increasing slightly by $\sim 30\,\mathrm{km\,s^{-1}}$. For BP Tau, four spectra were also observed from the night before the main observations. There is a large difference in EW (70Å) between these two nights observations, with an increase in 10%w over these two nights of $\sim 20\,\mathrm{km\,s^{-1}}$.

Previous Hα Observations and Variations: Donati et al. (2008) have suggested that rotational modulation dominates the observed variability in BP Tau reaching about ± 20 - 25 % for Hβ and ± 10 % for Hα.

Worden et al. (1981b) attributed observed photometric variations on the time-scales of minutes to flare activity. However a later study that carried out simultaneous observations of the optical and X-ray emission, found no correlation between the changes in the two (Gullbring et al. 1997). This led the authors to conclude that there was no flare activity in BP Tau over the course of the observations, and suggested that the interaction between stellar field and circumstellar disc could act to quench any flare activity. They also attributed the variations observed in the optical to changes in the accretion rate (Gullbring et al. 1996).

UV continuum flares have been observed in BP Tau, on time-scales of hours

superimposed on a longer variability pattern which is attributed to rotational modulation of the stellar flux by hot spots on the surface (Gomez de Castro & Franqueira 1997).

A.7 RY Tau

Stellar Properties: RY Tau has a stellar mass 2.2 $M_\odot$ of and a radius 2.7 $R_\odot$ (Bertout et al. 1988). A period of 5.7 days has been found for RY Tau (Herbst & Layden 1987), and it is a confirmed X-ray emitter (Damiani et al. 1995)
Disc Properties: This system has an inclination angle of $\sim$30° (Akeson et al. 2003) with a disk mass 0.2 $M_\odot$. A large cavity has been found in the disc, where the gap is $\sim$ 20 AU, with the outer disc wall lying at 18 AU, and inner wall at 0.42 AU. The disc is classified as a transitional disc (Pott et al. 2010).
Accretion: Observations have suggested that RY Tau has low levels of veiling (Valenti et al. 1993). Basri & Bertout (1989) derived an accretion rate of 7.5×10^{-8} $M_\odot yr^{-1}$.
ISIS Hα Observations: The Hα emission takes the form of a double peaked profile with a central absorption. In the single observation block of 2001, both peaks are of equal strength (Fig. A.13). The red-shifted peak shows an asymmetry, with an excess emission in the wing close to the line centre.

In the 2003 observations the strength of the emission line has dropped, and the excess emission in the red-shifted emission peak becomes more developed (Fig. A.14, A.15, A.16). Comparing the three nights the red emission peak shows more variations. It changes in strength with respect to the blue peak, and also there is a slight change in the morphology of the peak. On the third night the red emission peak becomes a double peak. The changes in the Hα EW on night 1 mainly takes the form of a drop in flux across the emission line. However there are some pronounced changes seen in the variance profile in the red side of the absorption feature. The second and third night have no significant changes, but there are some small changes in the red side of absorption again. From first to second night the Hα EW drops from 245 Å to 203 Å, a change of $\sim$ 17% of original EW.
Previous Hα Observations: RY Tau was also observed in October and November 2010 (Chou et al. 2013), with EW measurements of 10.3, 14.9, 15.5, 14.3, 11.8 Å recorded on October 21^{st}, November 17^{th}, 21^{st}, 25^{th} and 27^{th} respectively. Over the month time-scales of these observations, the profile is similar to what is observed in the ISIS sample. The red peak also shows similar variations in the

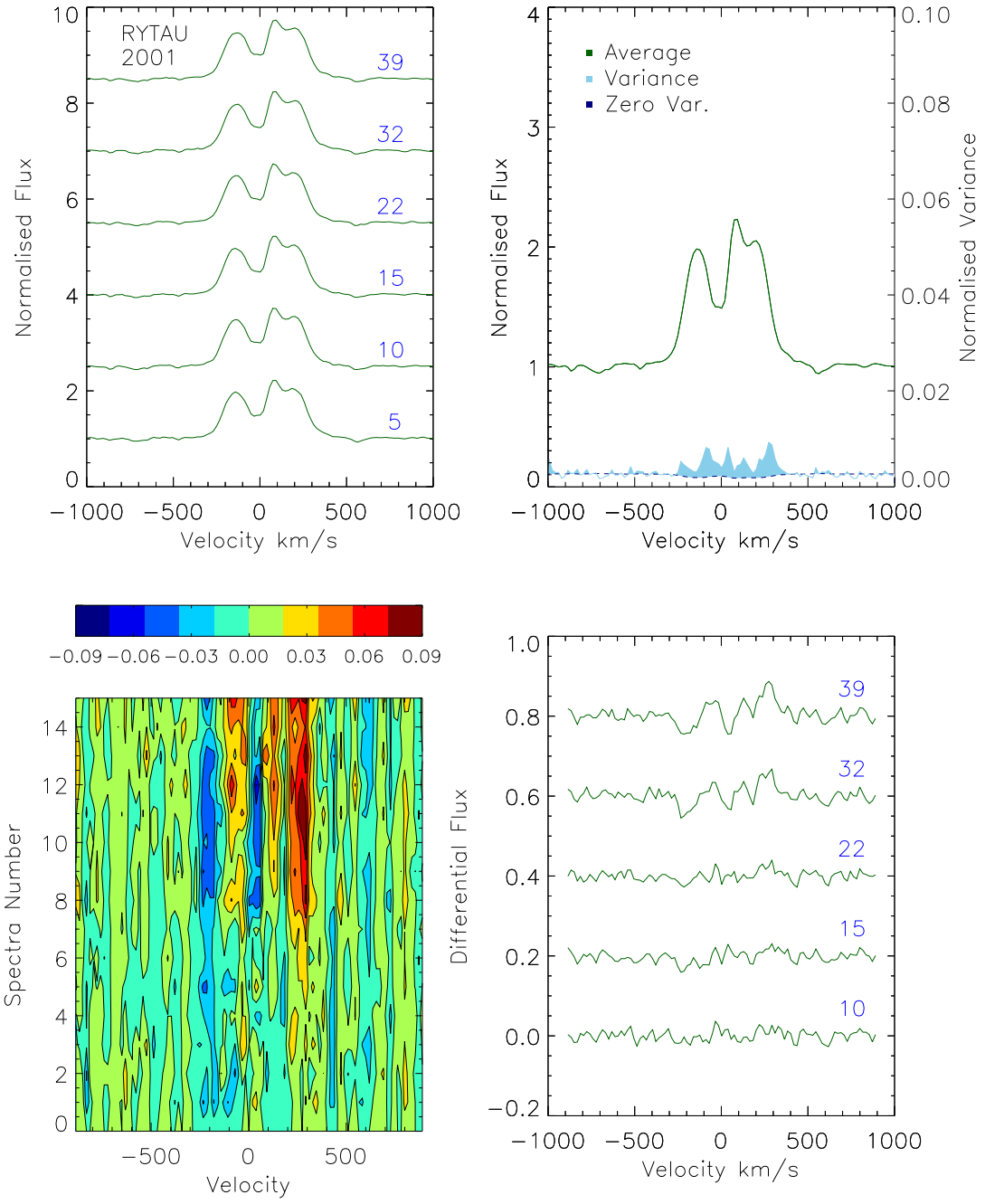

Figure A.13: *RY Tau 2001 observations.*

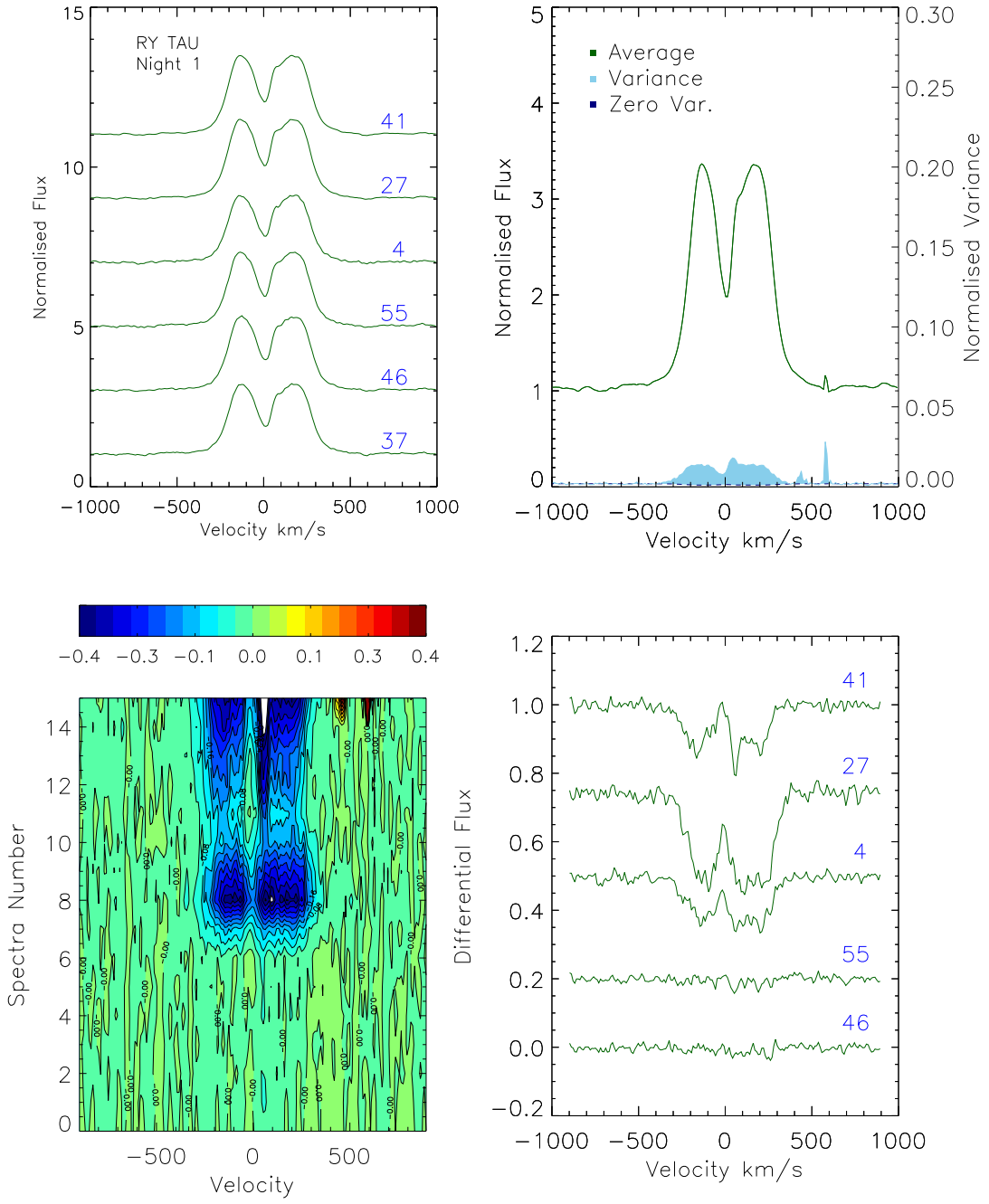

Figure A.14: *RY Tau 2003 observations, Night 1.*

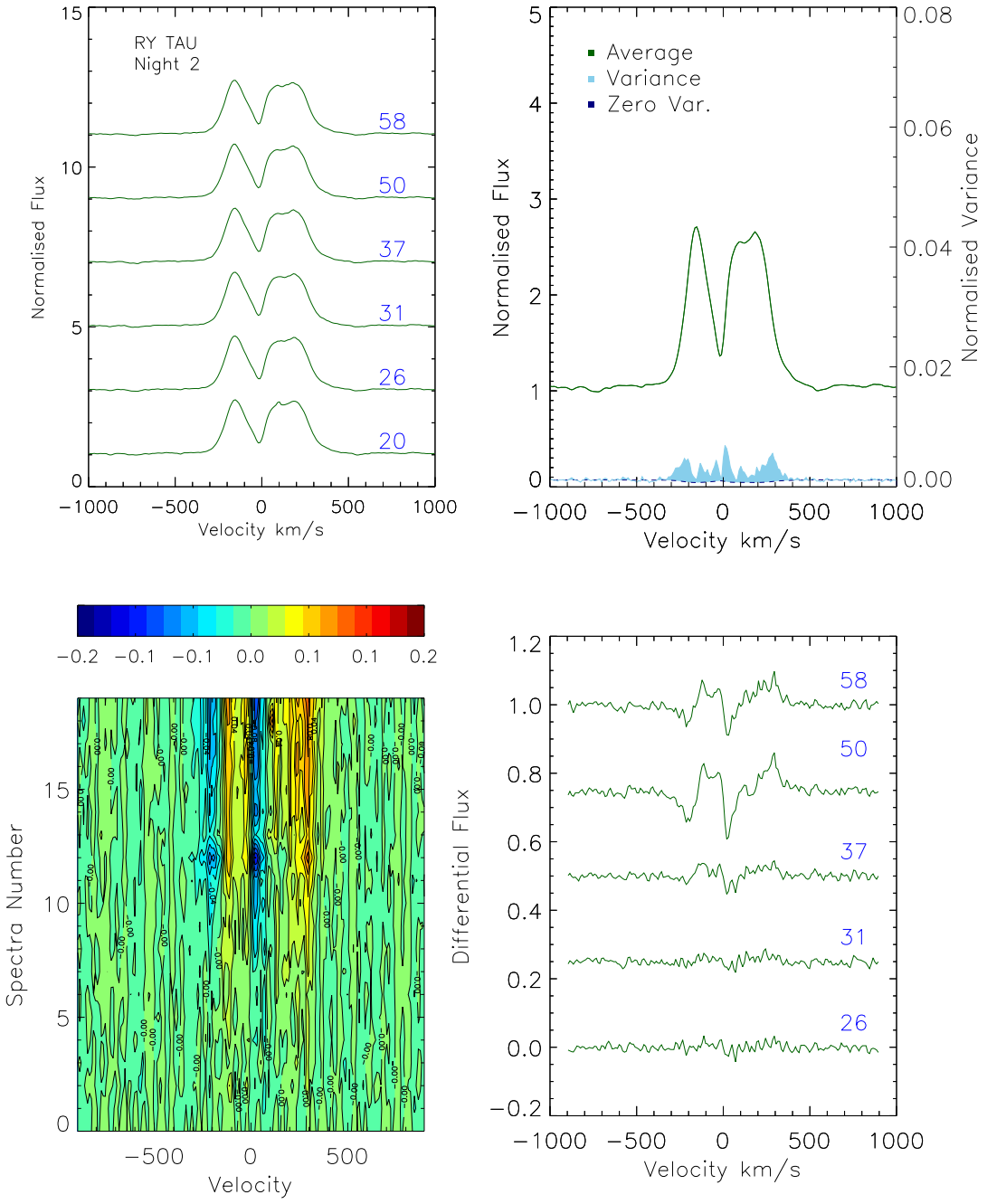

Figure A.15: *RY Tau 2003 observations, Night 2.*

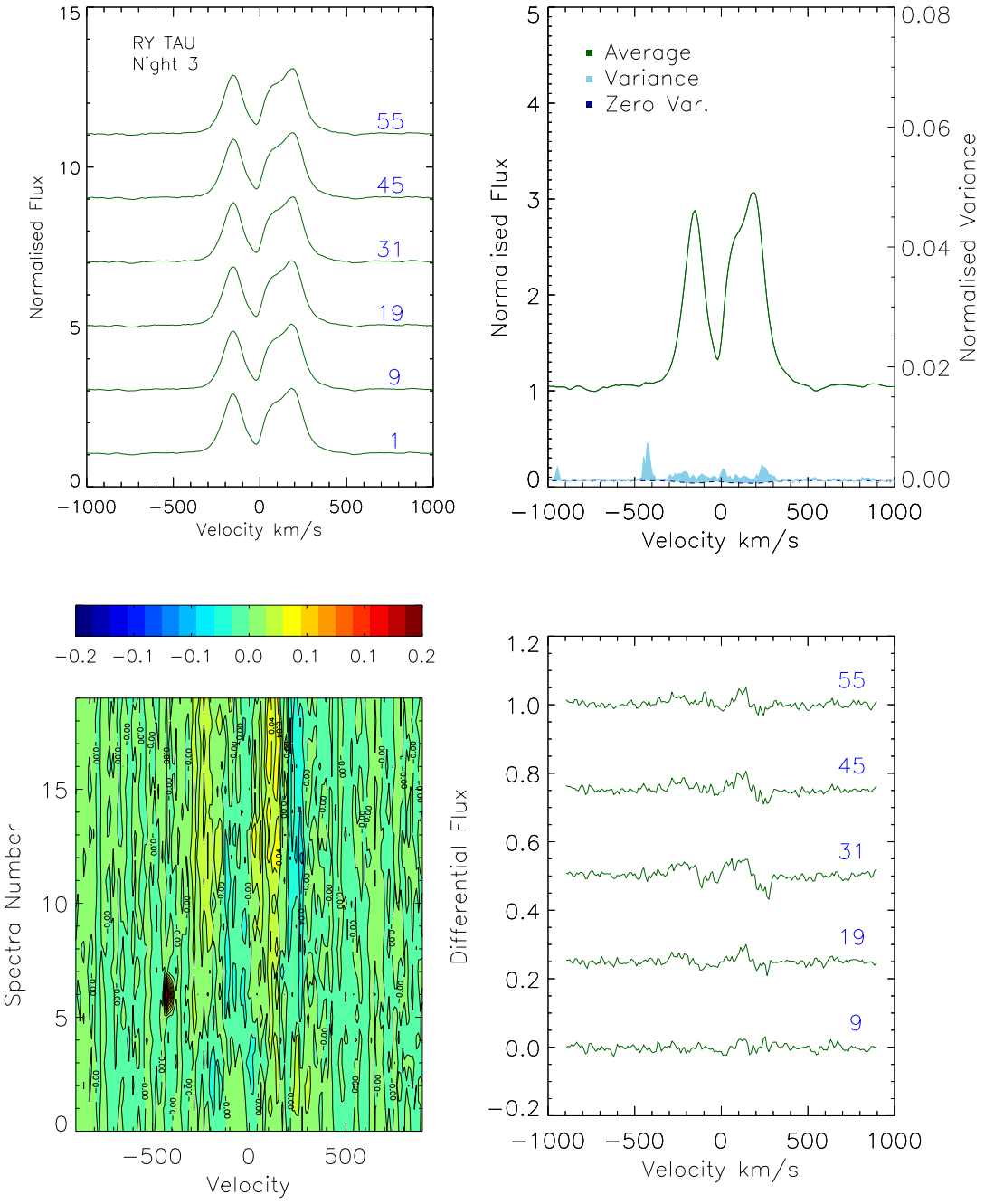

Figure A.16: *RY Tau 2003 observations, Night 3.*

rise and fall, and also the appearance of an extra absorption feature in the red peak (as seen in our 2001 Dec. 26^{th} observation).

Variations in Hα profile have also been found on the time-scales of 10 - 20 mins without variations in the star's brightness in (Kolotilov & Zajtseva 1975). Three separate nights observations took place covering time scales of ∼6.4hrs and 3 hrs. The profiles changed between nights, but in two out of three occasions they were stable through out the night. One night however the profile did go through changes, the EW varying between 19 to 22Å, and absorption features changed in strength, the blue absorption becoming stronger and weaker again, while a red absorption feature appears and disappears. Most spectra where taken with 15 min. exposures and the brightness of the star was lower on the night of the variations than on the other two nights (Kolotilov & Zajtseva 1975). The emission profile in this case is similar to what is observed in the ISIS observations, a double peaked profile, however in this case the blue peak is significantly smaller. Interestingly when this object was observed again in 1976/77 multiple absorption components were observed in Hα emission profile (Schneeberger et al. 1979a).

A.8 SU Aur

Stellar Properties: SU Aur has as stellar mass of $2\,M_\odot$ and a radius of 3.1 $R_\odot$ (Bertout et al. 1988). The period of SU Aur has not been well established, probably lying between 1.7 (DeWarf et al. 2003) and 2.7 days (Herbst & Layden 1987).

Outflows: Evidence has been found of a bipolar outflow from SU Aur (Grady et al. 2001).

Accretion: An accretion rate of $6\,x\,10^{-8}$ $M_\odot yr^{-1}$ was found for this object by Basri & Bertout (1989).

Disc Properties: Interferometric observations found the system inclination to be close to 63° (Akeson et al. 2002) with an inner disc hole of radius 0.05 - 0.08 AU.

ISIS Hα Observations: SU Aur shows one of the most complex profiles in the sample. On the first night of the 2001 observations, the emission line is made up of four peaks (Fig. A.17, A.18). Two are very close together in the line centre, and two lie in either wing at about $200\,km\,s^{-1}$. The peak in the red wing is the most prominent as it is slightly separated from the main emission. During the second night of 2001, this red shifted peak of emission shifts to lower wavelengths and merges with the main emission line. The small variations that do occur in

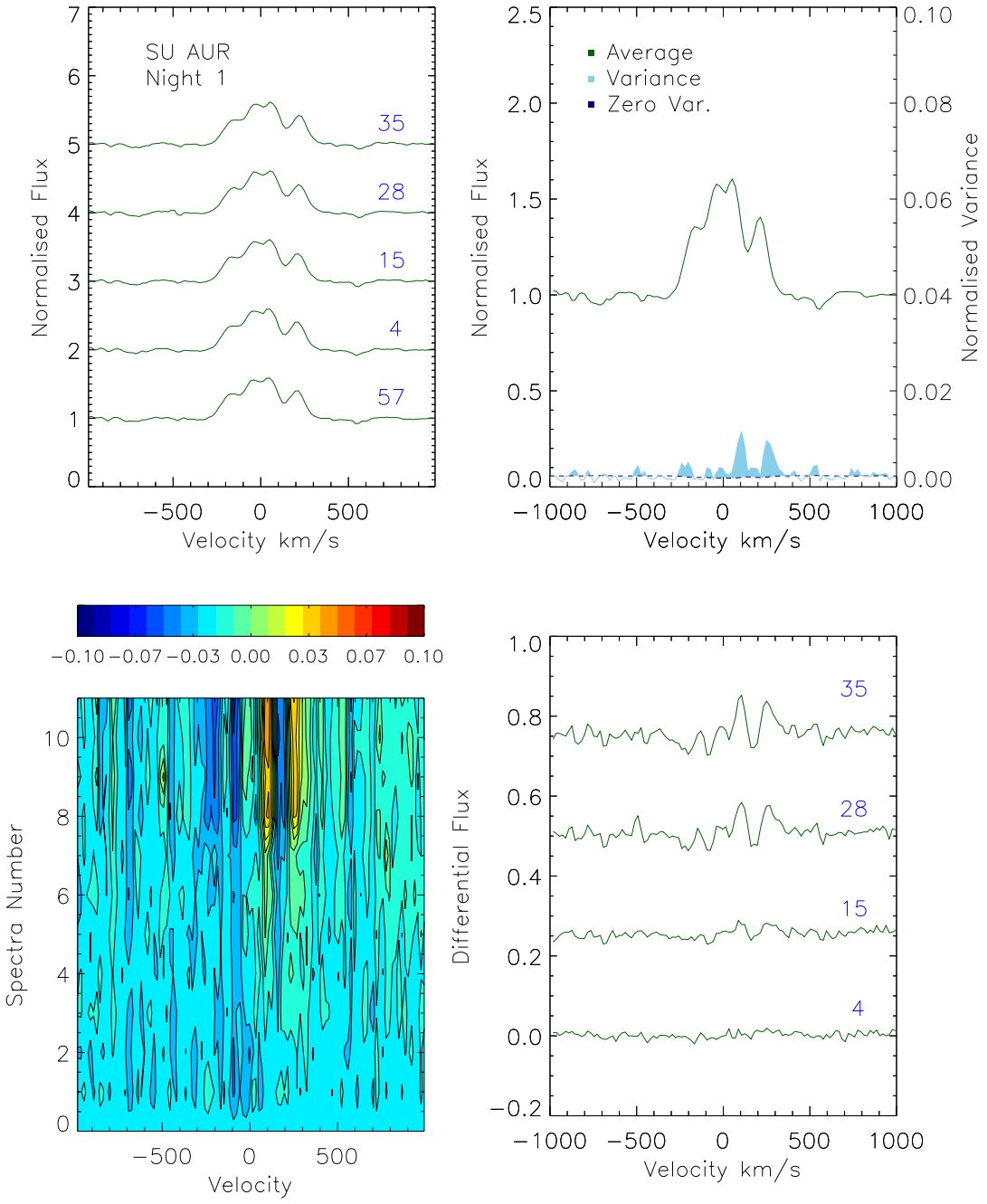

Figure A.17: *SU Aur 2001 observations, Night 1.*

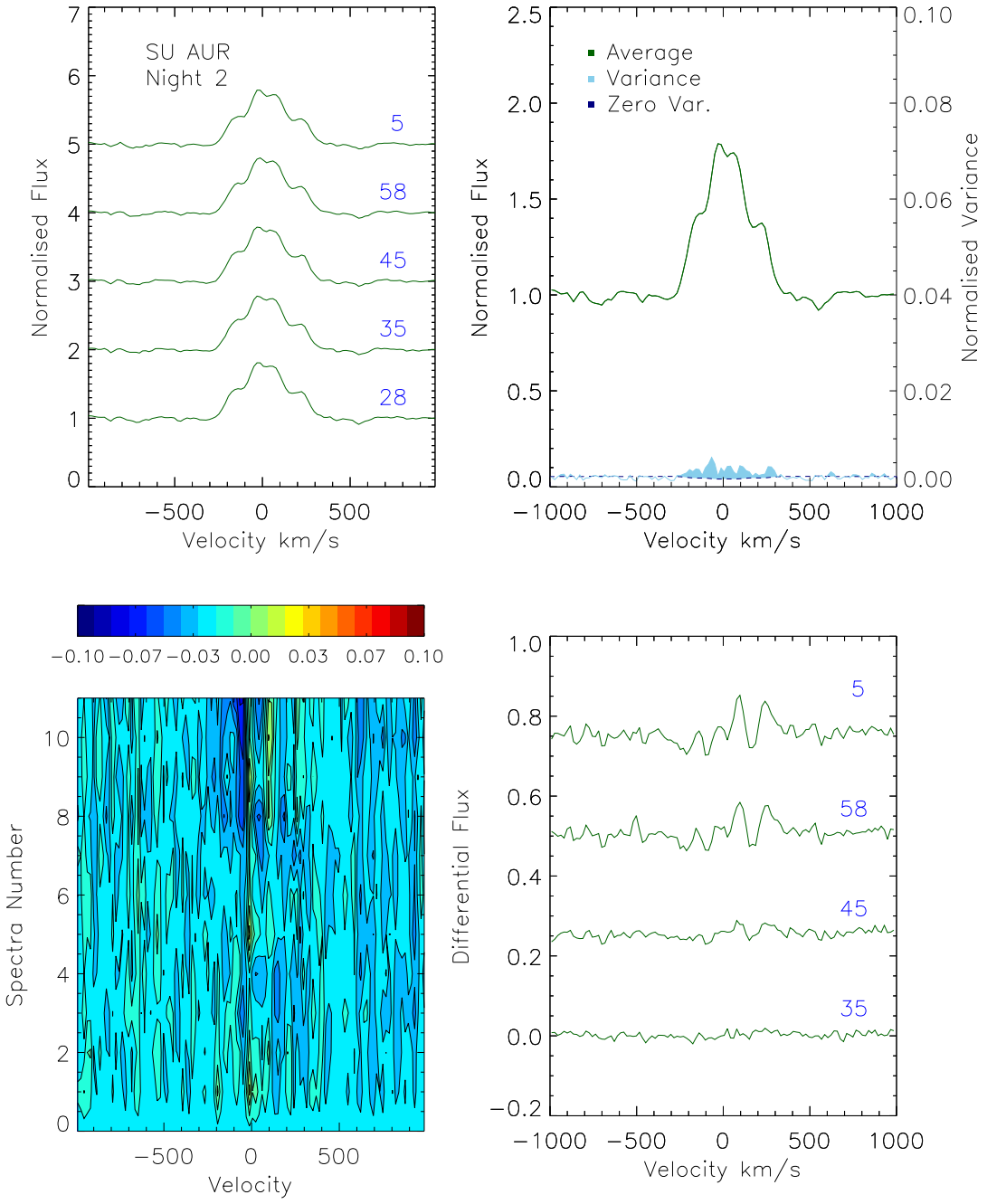

Figure A.18: *SU Aur 2001 observations, Night 2.*

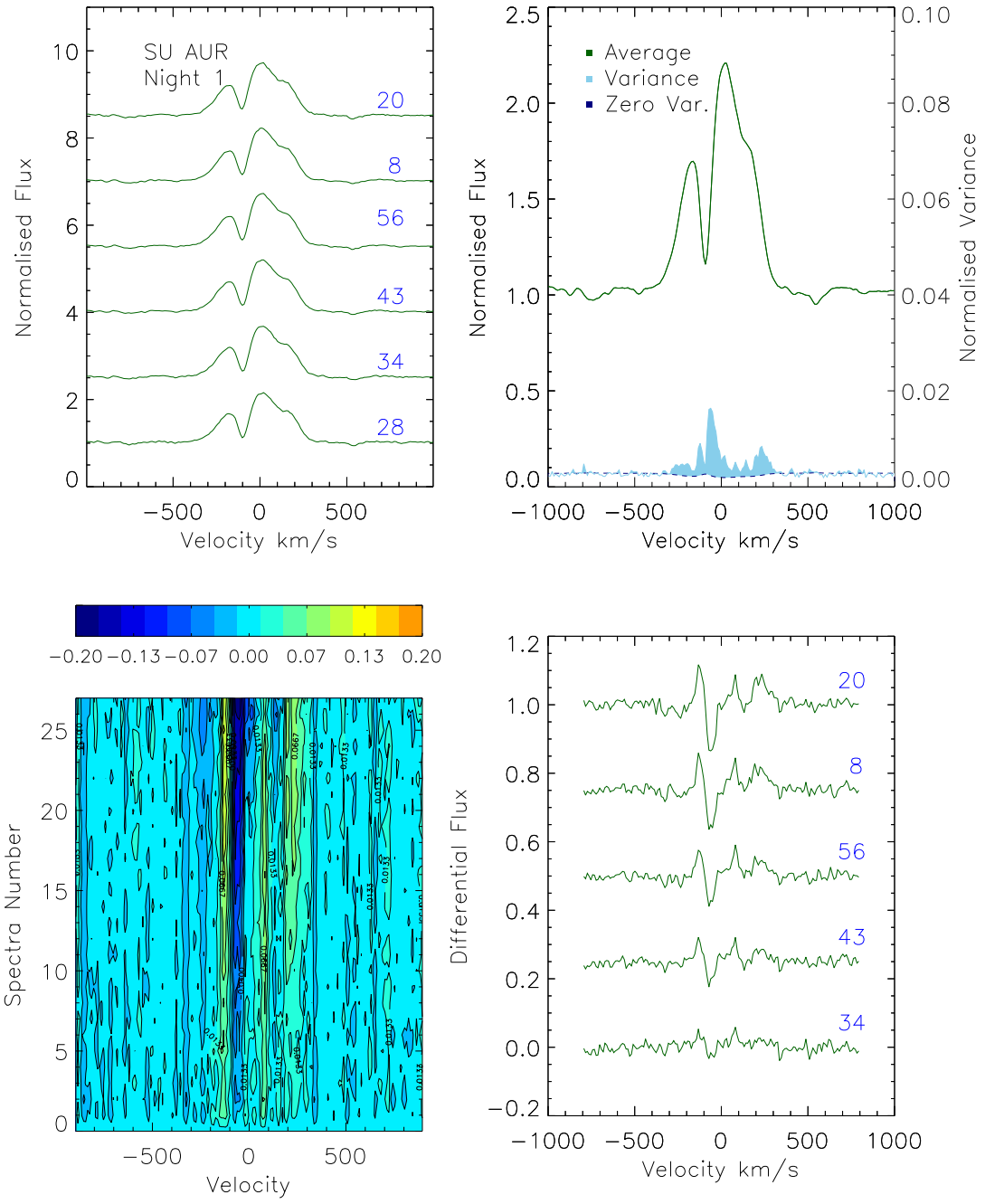

Figure A.19: *SU Aur 2003 observations, Night 1.*

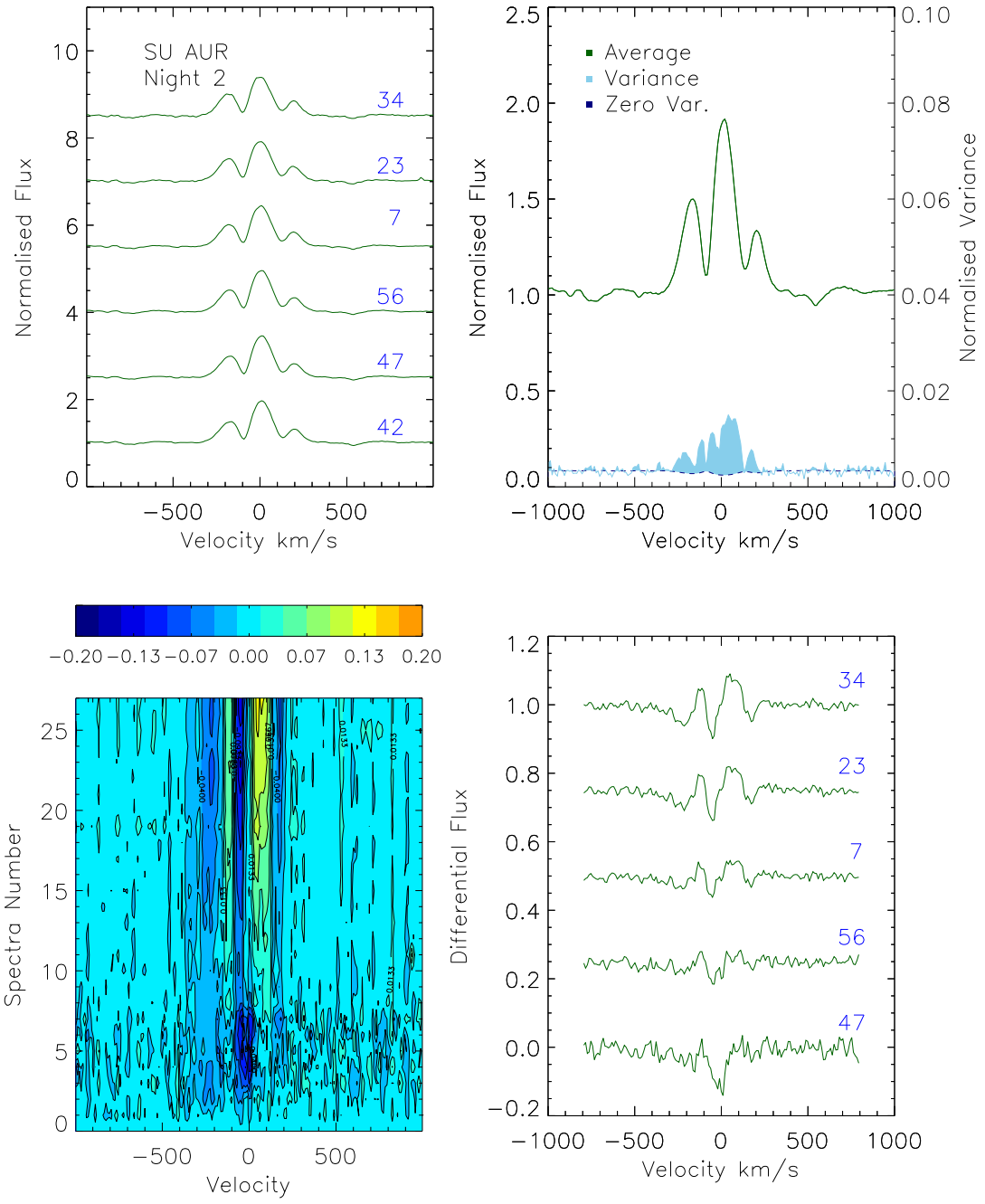

Figure A.20: *SU Aur 2003 observations, Night 2.*

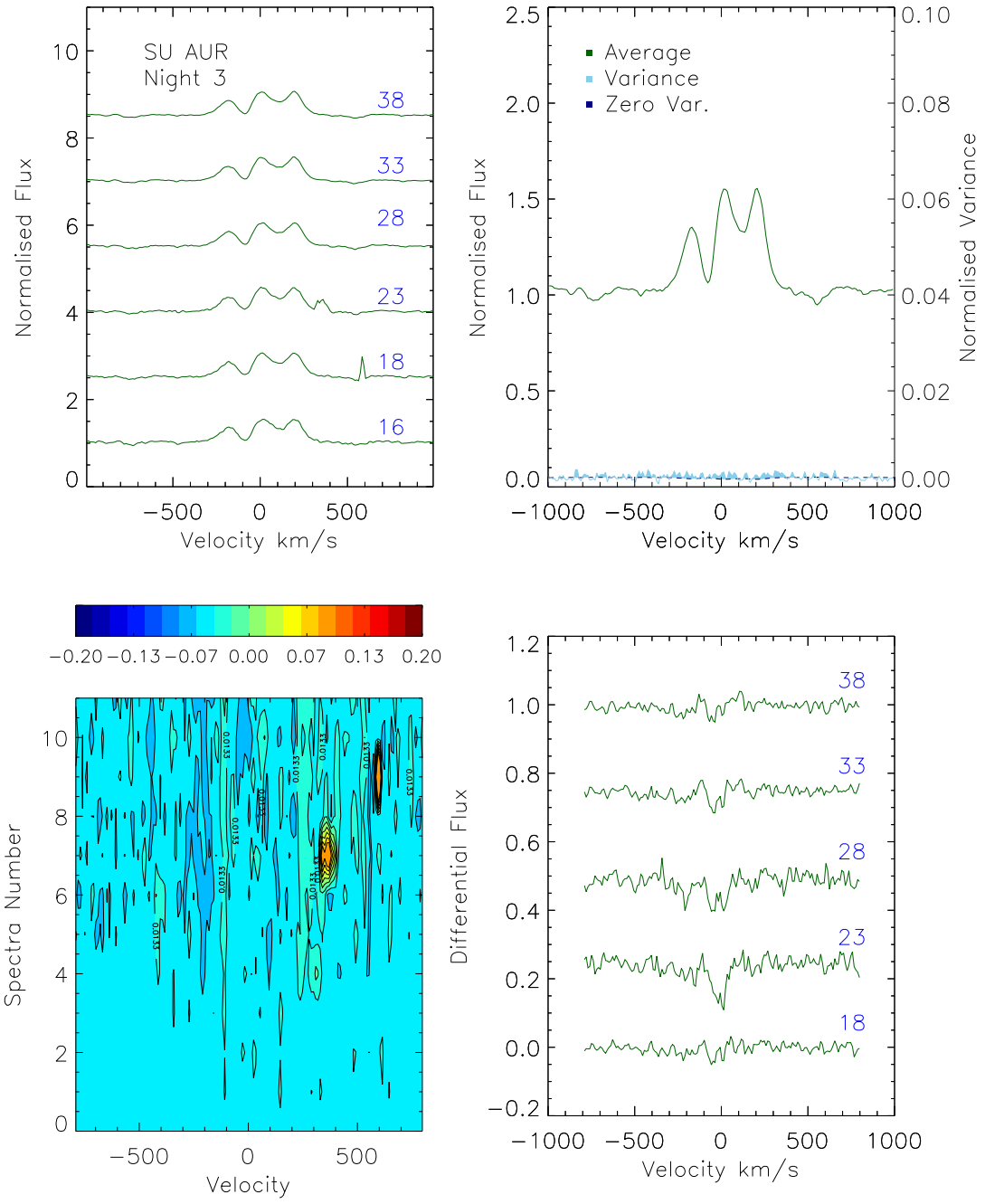

Figure A.21: *SU Aur 2003 observations, Night 3.*

2001 seem to be concentrated on the red side of the line.

On the first night of 2003 the line is composed of two emission peaks, and a blue-shifted central absorption (Fig. A.19). The emission peak on the red side is asymmetric on the first night of observations and separates into a central and red-shifted emission peak for the second and third nights observations (Fig. A.20, A.21). Over the course of the observations, no large variations are seen. On the first night, the changes seem to be concentrated in the blue side of the absorption feature (which is unusual for this sample) and also the red wing of the main emission. The Hα EW falls by half from the first to the second night, from 80Å to 40Å. On the second night of 2003 observations, it is the central peak in the emission line that grows relative to the other two. On the third night the profile shows unchanging steady emission.

Previous Hα Observations: Johns & Basri (1995b) found evidence for unsteady accretion in SU Aur in the form of red displaced absorption feature in Hβ with a period of 3 days, (where each observation was taken within a few hours or few days of each other). The Hα profile shows some similarities to ours. It has two overlying absorption features than grow and weaken over course of observations. However, in the case of Johns & Basri, the blue absorption feature is always the stronger, and below the continuum. In the ISIS observations it is the stronger in two out of three nights in 2003, on the second night it is equal to the depth of the red absorption. Again in 1977 a similar profile to what we observe on the first night of our observations is seen Schneeberger et al. (1979a).

In 1992, SU Aur was observed again showing a very similar profile to our first nights observations in 2003 (Johns et al. 1992). In this case the blue-shifted absorption is shown to vary over the rotation period, and is attributed to an outflow originating in the inner disc and co-rotating with the star.

A.9 T Tau

Stellar Properties: The T Tauri system is one of the best studied pre-main sequence systems. Even though it gave the name to the class of T Tauri stars, it is not a typical one. It is a triple system, where T Tau N is visually bright (V $\sim$ 10), with a strongly IR variable companion, T Tau S which is now known to be a binary. These observations are of the T Tau N, the optical visible T Tauri star in the system. It has stellar mass of 2.0 $M_\odot$ and a radius of 3.3 $R_\odot$ (Bertout et al. 1988). A period of 2.8 days has been found for T Tau N (Herbst et al. 1986). X-ray emission has been observed in T Tau, however Güdel et al. (2007)

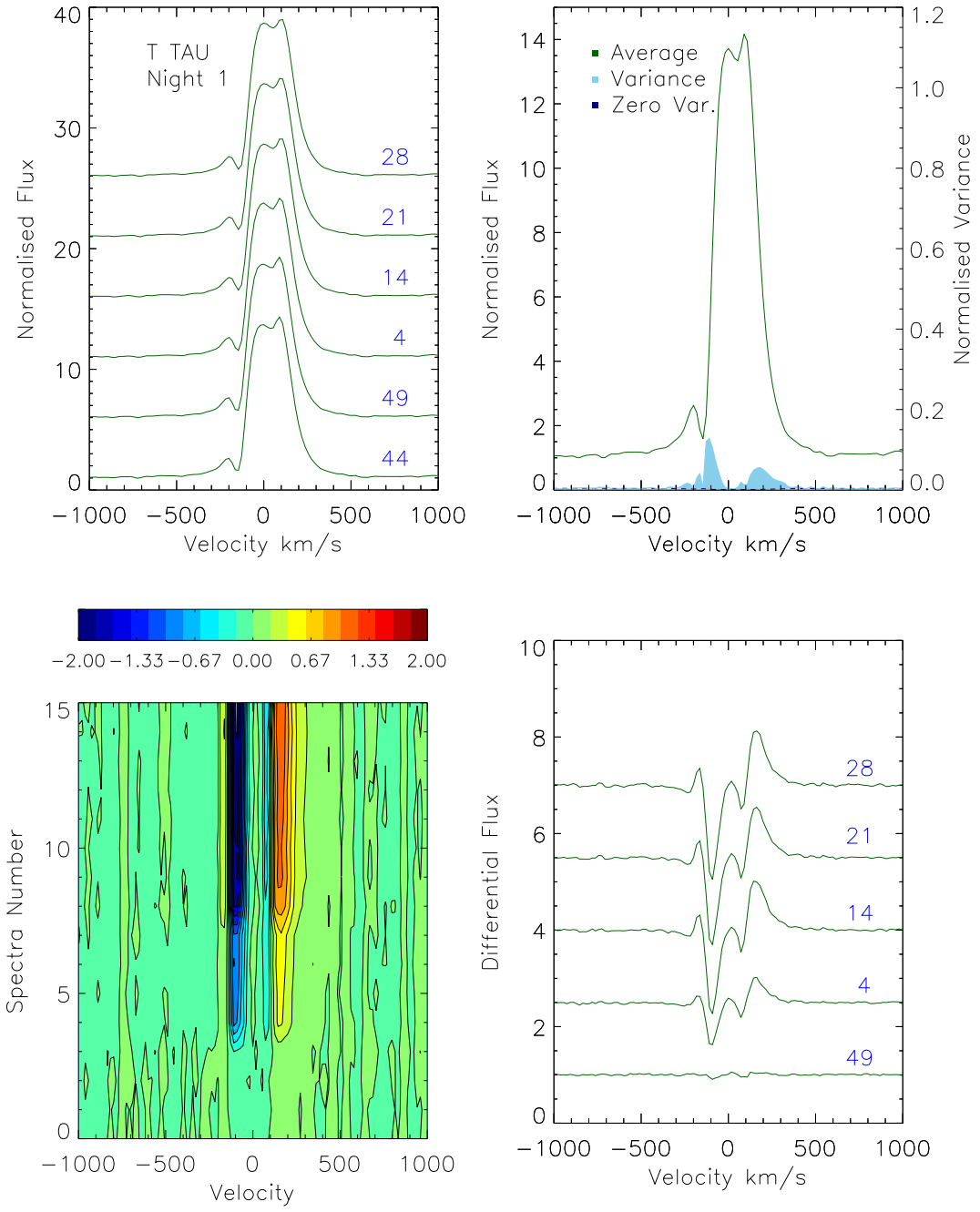

Figure A.22: *T Tau 2001 observations, Night 1.*

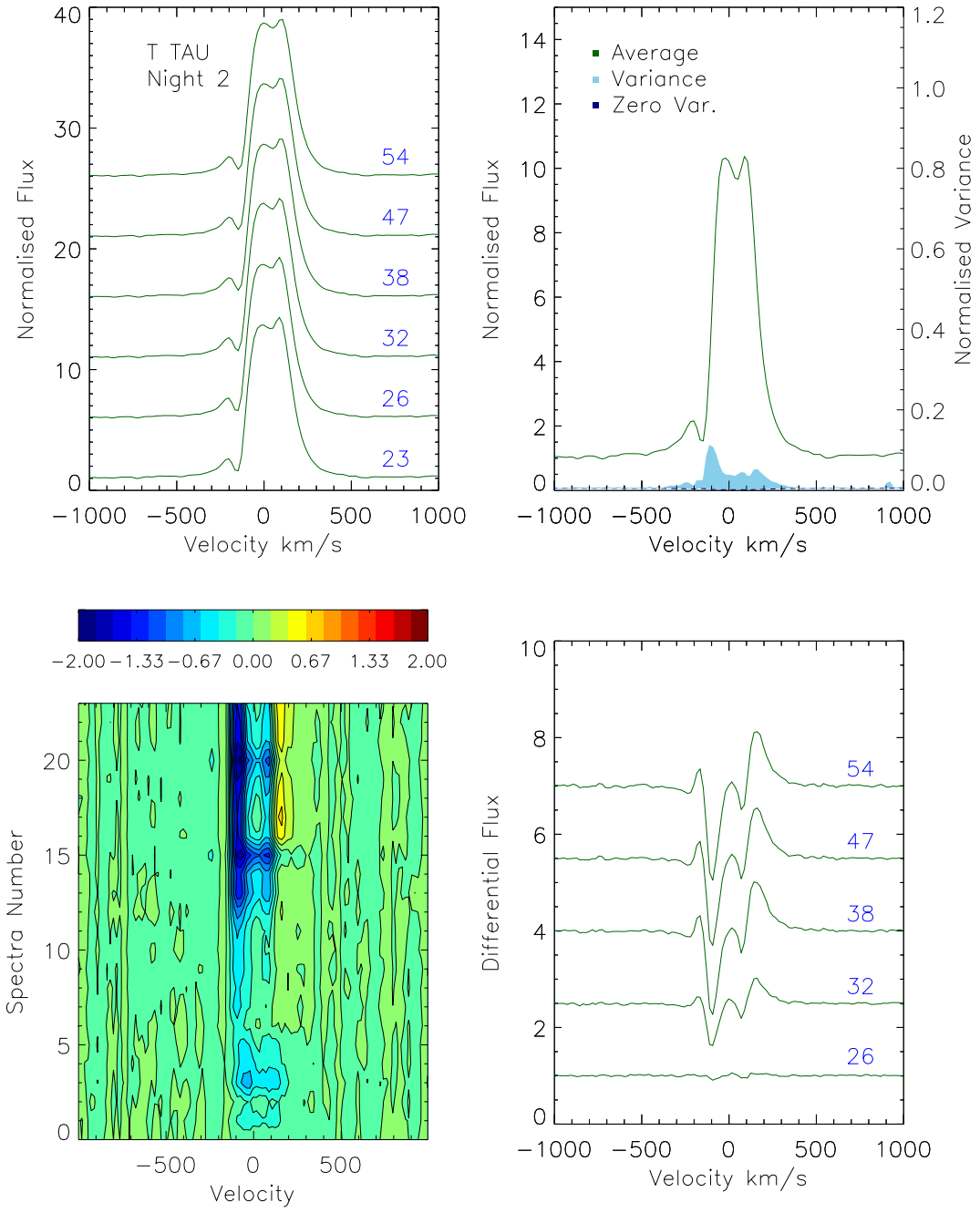

Figure A.23: *T Tau 2001 observations, Night 2.*

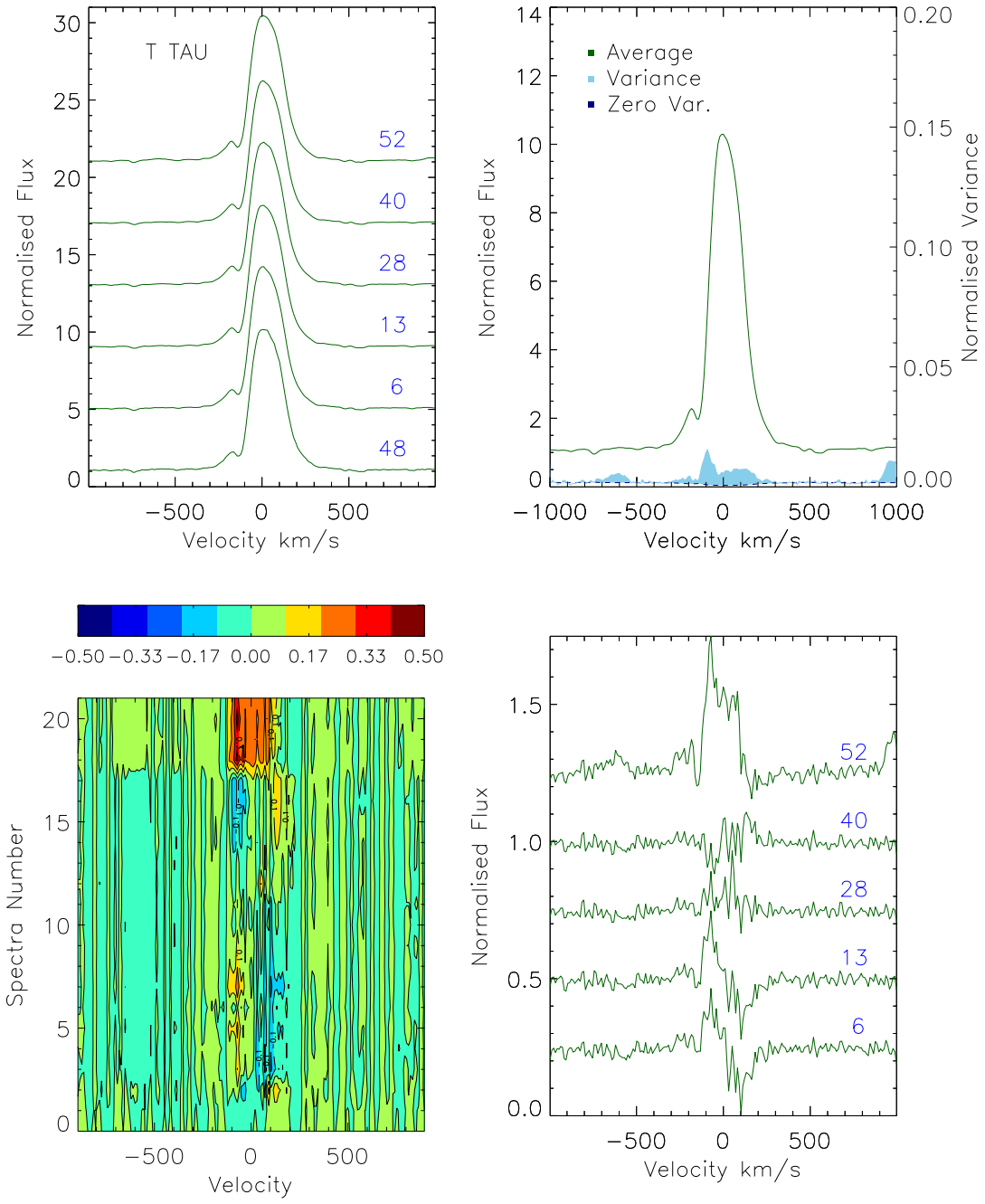

Figure A.24: *T Tau 2003 observations.*

suggest the accretion processes suppresses the emission, and it is lower that what is expected.

Disc Properties: T Tau has a disc mass of 0.008 $M_\odot$ (Andrews & Williams 2005). Akeson et al. (2002) report a system inclination angle of 29° based on interferometric observations.

Accretion: There have been a number of accretion rate estimates found for T Tau. Basri & Bertout (1989) report an accretion rate of $1.1\,\mathrm{x}\,10^{-8} M_\odot \mathrm{yr}^{-1}$, in rough agreement with that found by Calvet et al. (2004) and White & Ghez (2001).

Outflows: T Tau has been observed in the radio, with emission consistent with both an extended outflow and non-thermal emission (Phillips et al. 1993). (Skinner & Brown 1994) found the flux to be consistent with a mass loss rate of $3.7\,\mathrm{x}\,10^{-8} M_\odot \mathrm{yr}^{-1}$.

ISIS Hα Observations: In 2001, T Tau's emission profile is composed of a central emission peak with a small absorption feature in the line centre and with a larger blue-shifted absorption feature in the wing (Fig. A.22, A.23). During both nights, the changes are mostly in the blue wing, very close to the centre of the blue-shifted absorption feature. A smaller strengthening of the emission in the red wing occurs at the same time.

In 2003, T Tau shows weaker emission, and also the central absorption feature has disappeared (Fig. A.24). The variance profile again shows a peak near the blue shifted absorption feature, but the small change that does occur takes the form of a strengthening across the line.

Previous Hα Observations: Multiple observations were taken of T Tau's Hα emission in 1976/77. These observations show a similar profile to what is observed in the ISIS sample, but with a small red-shifted emission feature, that sometimes appears as a knee in the red wing, and sometimes as a distinguished emission feature. During these observations the EW was seen to change by 10% over a three day period (Schneeberger et al. 1979a).

A.10 UX Tau

Stellar Properties: UX Tau is a multiple system (Jones & Herbig 1979), where the primary star UX Tau A is separated from the binary UX Tau b by 5.86" and UX Tau C by 2.63". The primary has a mass of 1.3 $M_\odot$ and a radius of 2.0 $R_\odot$ (Espaillat et al. 2007; Kraus & Hillenbrand 2009).

Disc Properties: The circumstellar disc has been classified as a transitional

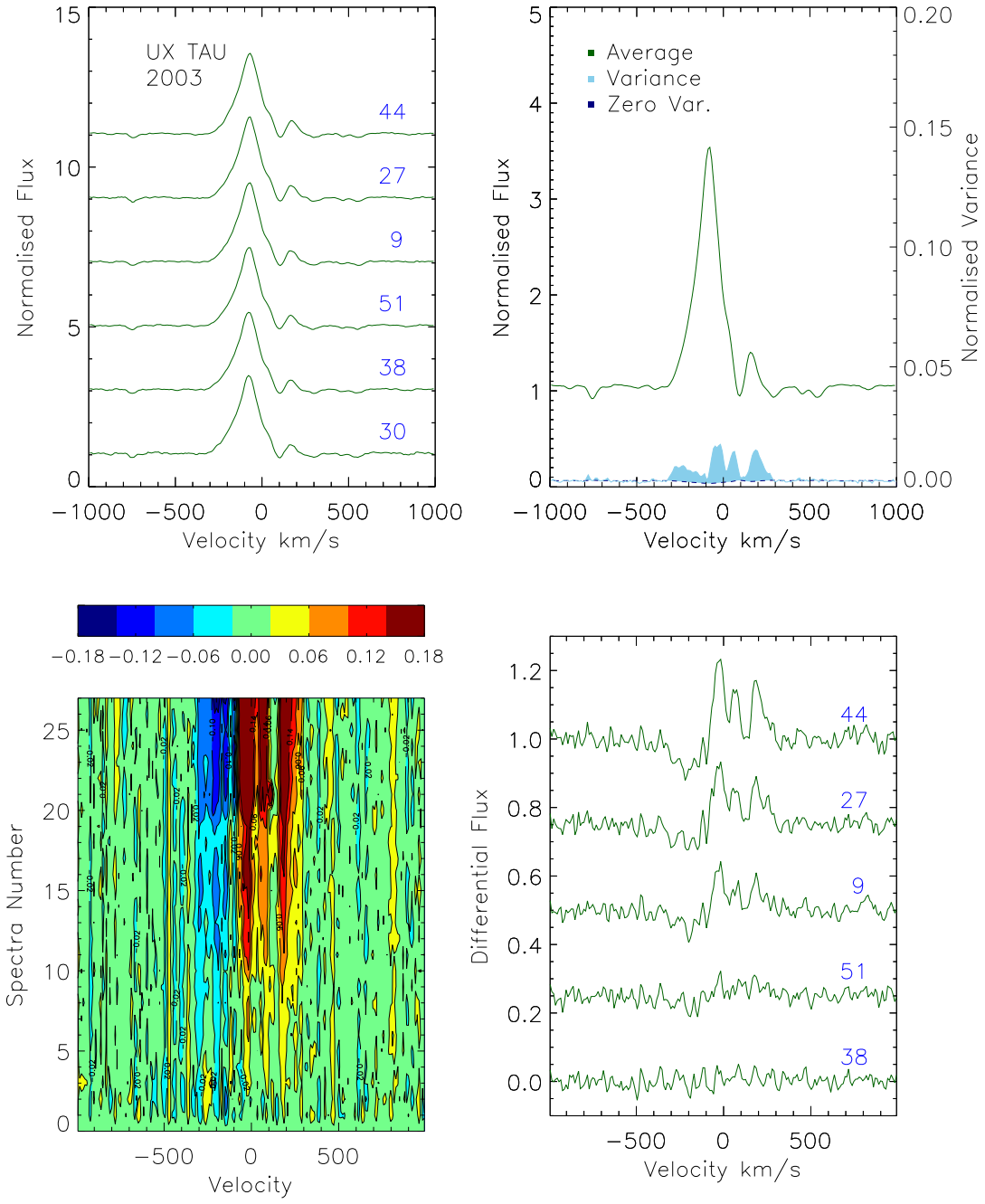

Figure A.25: *UX Tau 2003 observations.*

disc (Pott et al. 2010) and takes the form of an optical thin inner disc separated by a gap from an optically thick outer disc, where the inner wall lies at 0.21 AU and the outer wall at 30 AU. The disc has a mass of 0.005 M$\odot$ (Andrews & Williams 2005) and a tilt angle of $\sim 46^\circ \pm 2^\circ$.

ISIS Hα Observations: UX Tau shows a reverse P-Cgyni profile in these observations (Fig. A.25). Across the hour observation, both emission peaks grow in size. The Hα EW gradually increases by $\sim$ 10Å (12%). The time-series of Hα EW measurements show it increases in a wave like manner. The changes in the profile occur on the blue side of absorption (closer to main peak), and in the wings. This is the only profile with red absorption in this sample.

Previous Hα Observations: Over the course of this work no previous Hα observations of this target were found.

A.11 V773 Tau

Stellar Properties: V773 Tau is a spectroscopic binary (Kraus & Hillenbrand 2009) with an orbit period of 51 days (Boden et al. 2007), with both components having periods of 3.43 days (Rydgren & Vrba 1983). It is highly variable with luminous non-thermal radio emission (Dutrey et al. 1996; O'Neal et al. 1990; Phillips et al. 1991) and very bright, highly variable X-ray emission (Guenther et al. 2000). It is well known for its flaring, particularly around periastron passage, suggesting an interaction of the magnetic fields of the binary (Massi et al. 2002).

Disc Properties: V773 Tau has been found to have a circumstellar disc of mass 0.0005 M$_\odot$ (Andrews & Williams 2005)

ISIS Hα Observations: V773 Tau shows the weakest emission line within the sample, consisting of an asymmetric emission line with enhanced emission in the red wing (Fig. A.26). Across the observations the emission shows no significant variations.

Previous Hα Observations: Guenther et al. (2000) observed V773 Tau in the optical and X-ray simultaneously and found a loose correlation between the Hα EW and X-ray emission strength.

A.12 BF Ori

Stellar Properties: BF Ori has a long history of large amplitude changes and has been classified as an UXors object (Bibo & The 1991). A period of 5.5

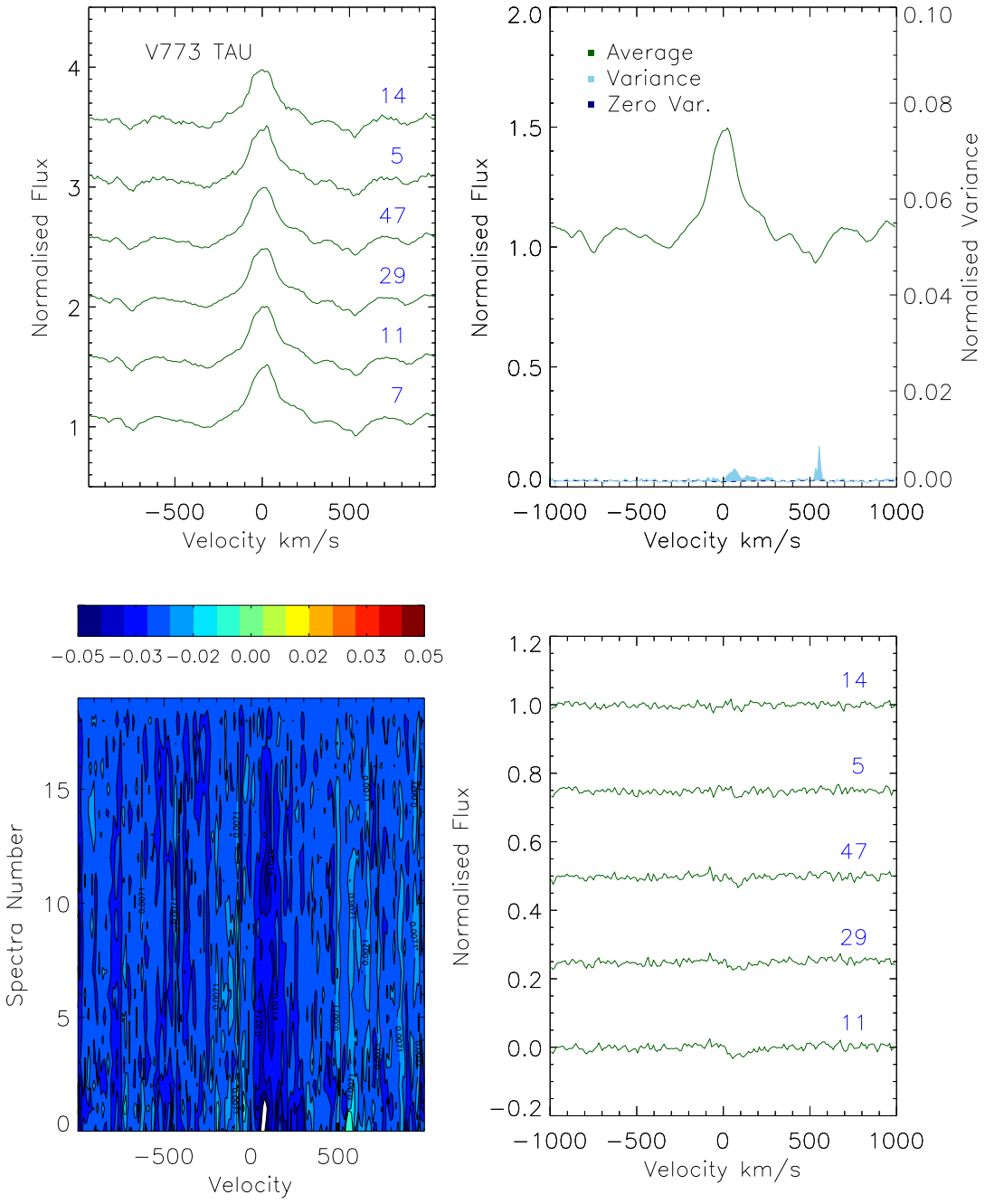

Figure A.26: *V773 Tau 2003 observations.*

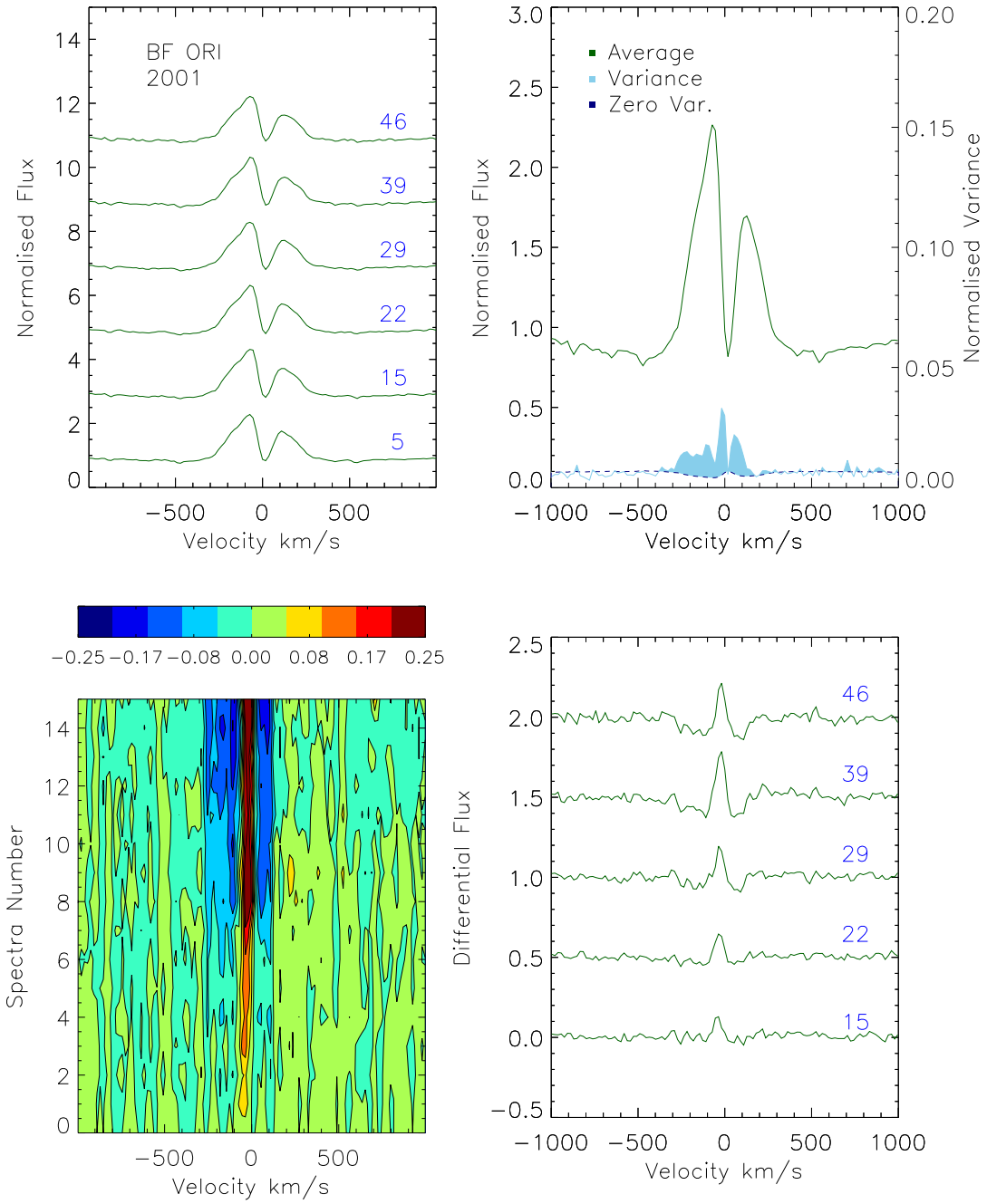

Figure A.27: *BF Ori 2001 observations.*

years has been found in these large variations (Shevchenko et al. 1993). These variations are thought to be a result of viewing the star through the variable circumstellar disc (Grinin & Rostopchina 1996). BF Ori has a stellar mass of 2.5 $M_\odot$ and a radius of 1.3 $R_\odot$ (Hillenbrand et al. 1992; Manoj et al. 2006).

Disc Properties: An inner disc hole of 10 AU was found through SED modelling by Hillenbrand et al. (1992).

Accretion: Using SED modelling, Hillenbrand et al. (1992) derived accretion rate of $1.1\,\mathrm{x}\,10^{-6} M_\odot \mathrm{yr}^{-1}$.

ISIS Hα Observations: BF Ori shows comparatively low levels of variations across the single observation block (Fig. A.27). The Hα profile has two peaks in emission with a central absorption feature. The largest changes take place within the central absorption feature, and take the form of a steady increase in emission in a narrow wavelength range.

Previous Hα Observations: A range of Hα EW measurements have been reported, 10.0Å (Herbig & Bell 1988), 11.30Å (Reipurth et al. 1996), 3.70Å (Corcoran & Ray 1998), 6.70Å (Hernández et al. 2004) and 9.30Å (Acke et al. 2005). The mean EW measured in the ISIS sample in 2001 is on the low end of this range at 3.88Å, but coincides with the dip in strength in 1998 and 2004.

A.13 LkHα 215

Stellar Properties: LkHα 215 is one of the larger stars in this sample, with a mass of 4.8 $M_\odot$ and radius of 5.4 $R_\odot$ (Hillenbrand et al. 1992; Manoj et al. 2006).

Disc Properties: Alonso-Albi et al. (2009) found an uncertain disc outer radius of $\sim 10\,\mathrm{AU}$, and a disc mass of $6\,\mathrm{x}\,10^8$ M$\odot$.

ISIS Hα Observations: The Hα emission in this object takes the form of a double peak profile (Fig. A.28). During the single observation block of this object, only very small changes in emission occur either side of the central absorption feature.

Previous Hα Observations: Previous observations of the Hα emission have found a slightly weaker emission line than is reported here (mean of 3.45 Å), 25 Å (Herbig & Bell 1988), 26.7 Å (Corcoran & Ray 1998) and 25.7 Å (Hernández et al. 2004).

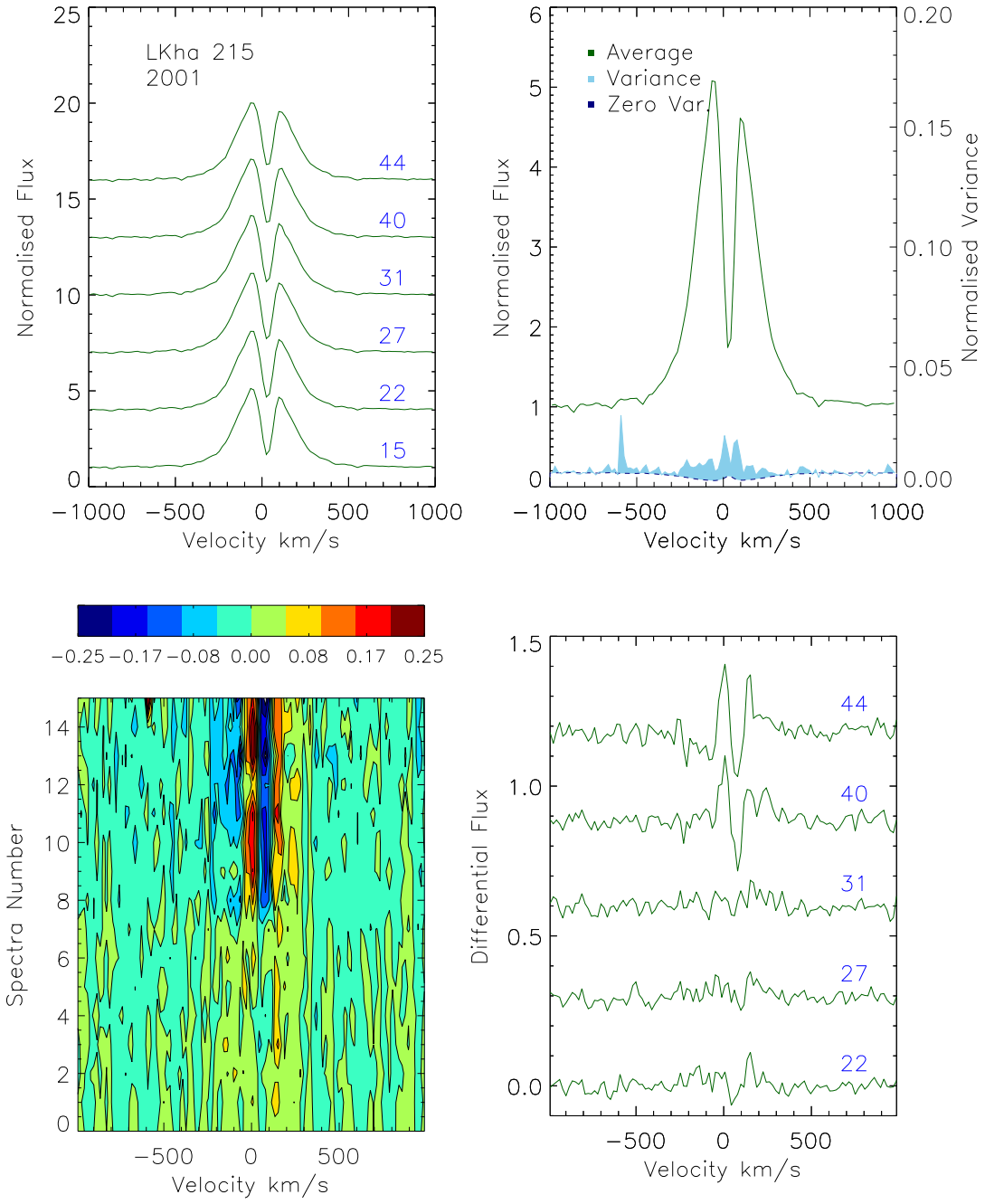

Figure A.28: *LkHα 215 2001 observations.*

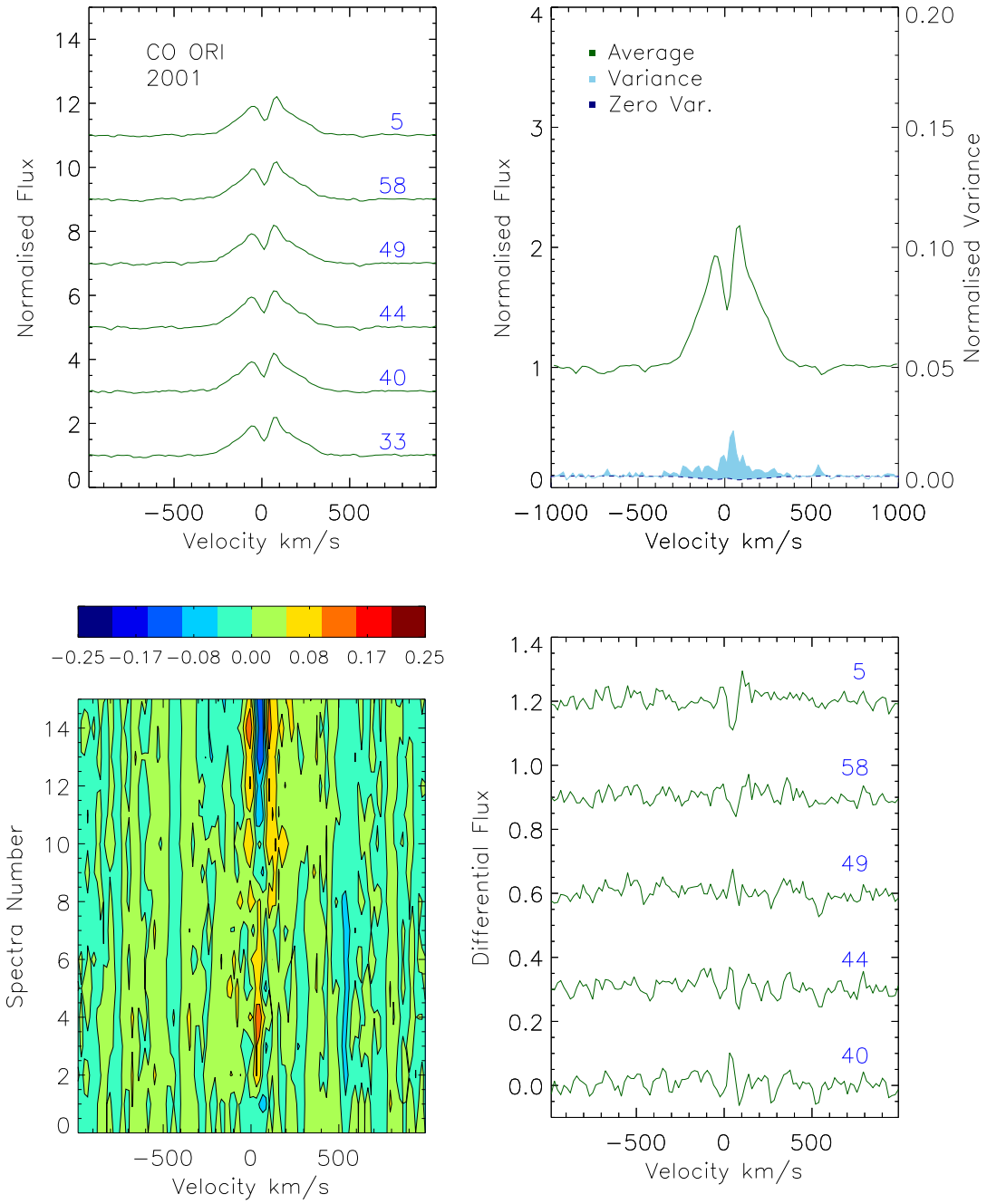

Figure A.29: *CO Ori 2001 observations.*

A.14 CO Ori

Stellar Properties: CO Ori is one of the brightest T Tauri stars, however it has been poorly studied. It has previously shown a high and variable accretion rate (Calvet et al. 2004), and also large photometric variations on time-scales of days (Herbst & Shevchenko 1999), which led the authors to designate is as an UXors object.

ISIS Hα Observations: The Hα emission of CO Ori takes the form of a double peaked profile (Fig. A.29). The small changes in the profile across the hour of observations are concentrated in the two peaks of emission.

Previous Hα Observations: CO Ori has previously been reported to have a weaker Hα emission profile at 4.2 Å and a pronounced P Cygni profile (Reipurth et al. 1996). About 10 years earlier it was observed to have stronger emission at 10 Å (Herbig & Bell 1988).

The Hα profile observed by Calvet et al. (2004), shows quite a different morphology than we observe. Calvet et al. (2004) observed a extremely blue-shifted absorption feature and a single red-shifted emission peak. This suggested that the more central and weaker absorption feature that is observed in the ISIS data sometimes grows in strength and moves more towards the blue.

A.15 MWC 480

Stellar Properties: MWC 480 is a Herbig Ae star with a mass of 2.3 $M_\odot$ and a stellar radius of 2.1 $R_\odot$ (Mannings & Sargent 1997). It is one of the few Herbig Ae stars that have had detections of strong kG magnetic fields on their surfaces (Hubrig et al. 2011).

Accretion and Outflows: Accretion in MWC 480 has been confirmed via both far-UV and X-ray detections. This target also drives a bipolar jet, but the rate of mass loss is lower than is considered normal for Herbig Ae stars (Grady et al. 2010). An accretion rate of 3.8×10^{-8} $M_\odot yr^{-1}$ was derived from the far-UV excess emission by Grady et al. (2010). A higher mean accretion rate was found by Mendigutía et al. (2013), 1.1×10^{-7} $M_\odot yr^{-1}$, by fitting the Balmer excess. Across the few months of observations, they measure accretion rate changes between 5.24×10^{-8} and 1.46×10^{-7} $M_\odot yr^{-1}$. The mean accretion measurement found in the ISIS sample, 4.56×10^{-8} $M_\odot yr^{-1}$, lies within this range of variations.

Disc Properties: A disc inclination angle of 30° has been determined (Eisner

et al. 2004; Mannings & Sargent 1997).

ISIS Hα Observations: The Hα emission is very stable over the three observations blocks that span two nights (Fig. A.30, A.31, A.32 and A.33). There is large blue-shifted absorption that extends below the level of the continuum. The small variations during the first and last observation block take place mainly in the the blue side of the emission peak. Measurements of the 10%w are not taken due to the fact that the entire blue wing of the emission line is in absorption providing no way of telling (without interpolation) where the blue wing lies.

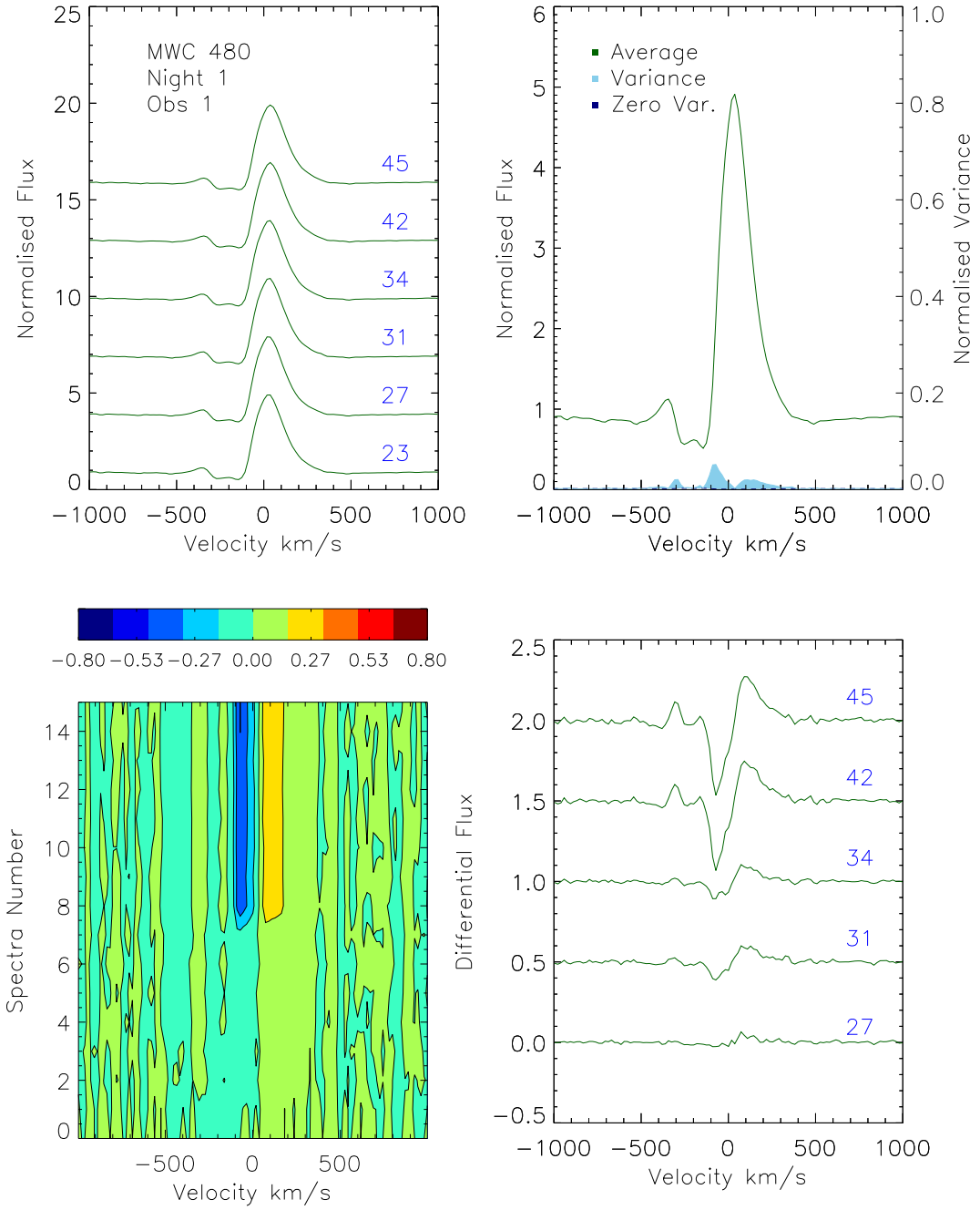

Figure A.30: *MWC 480 2001 observations. First observation block of Night 1.*

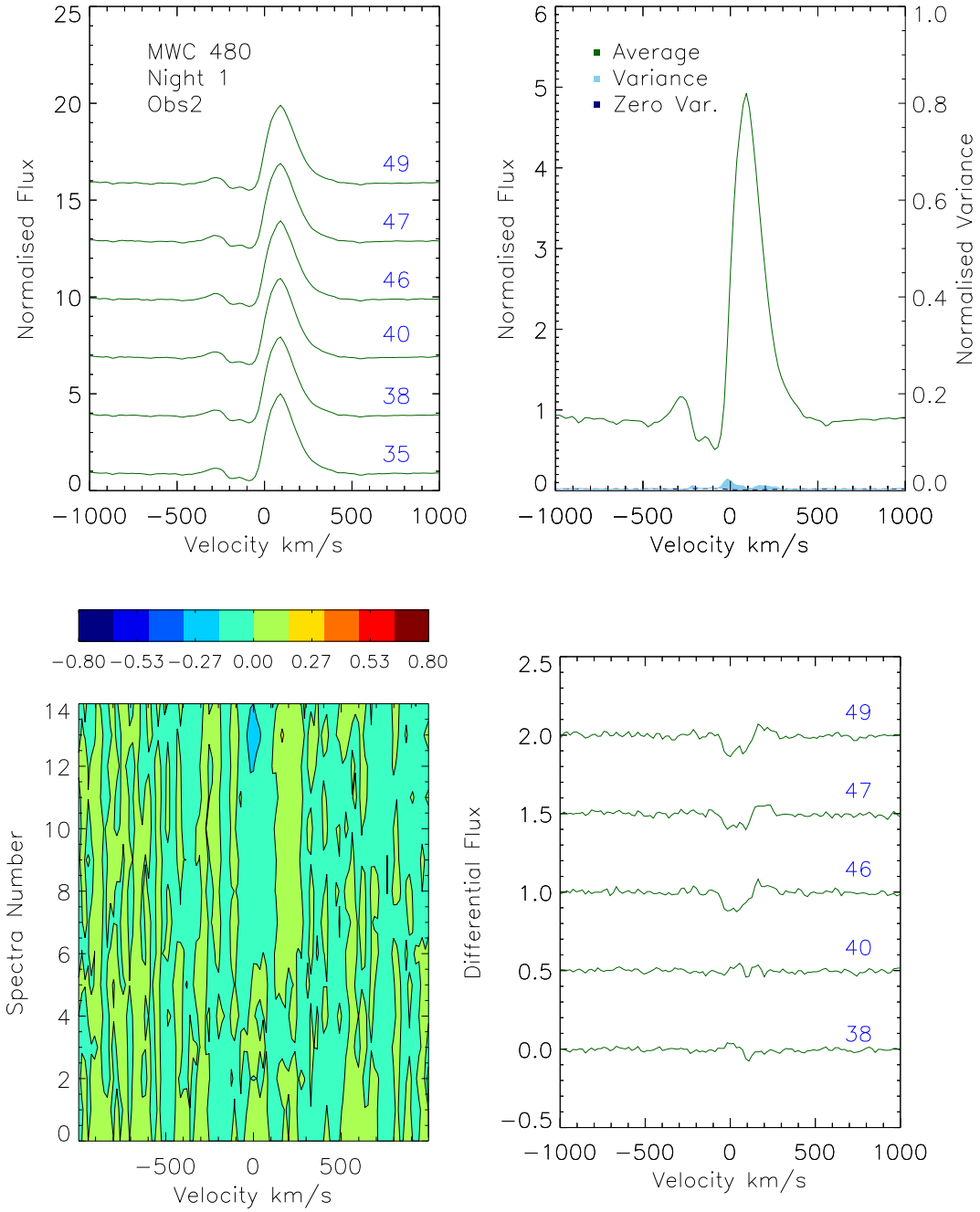

Figure A.31: *MWC 480 2001 observations. Second observation block of Night 1. This block is separated from the first by about 7 hours.*

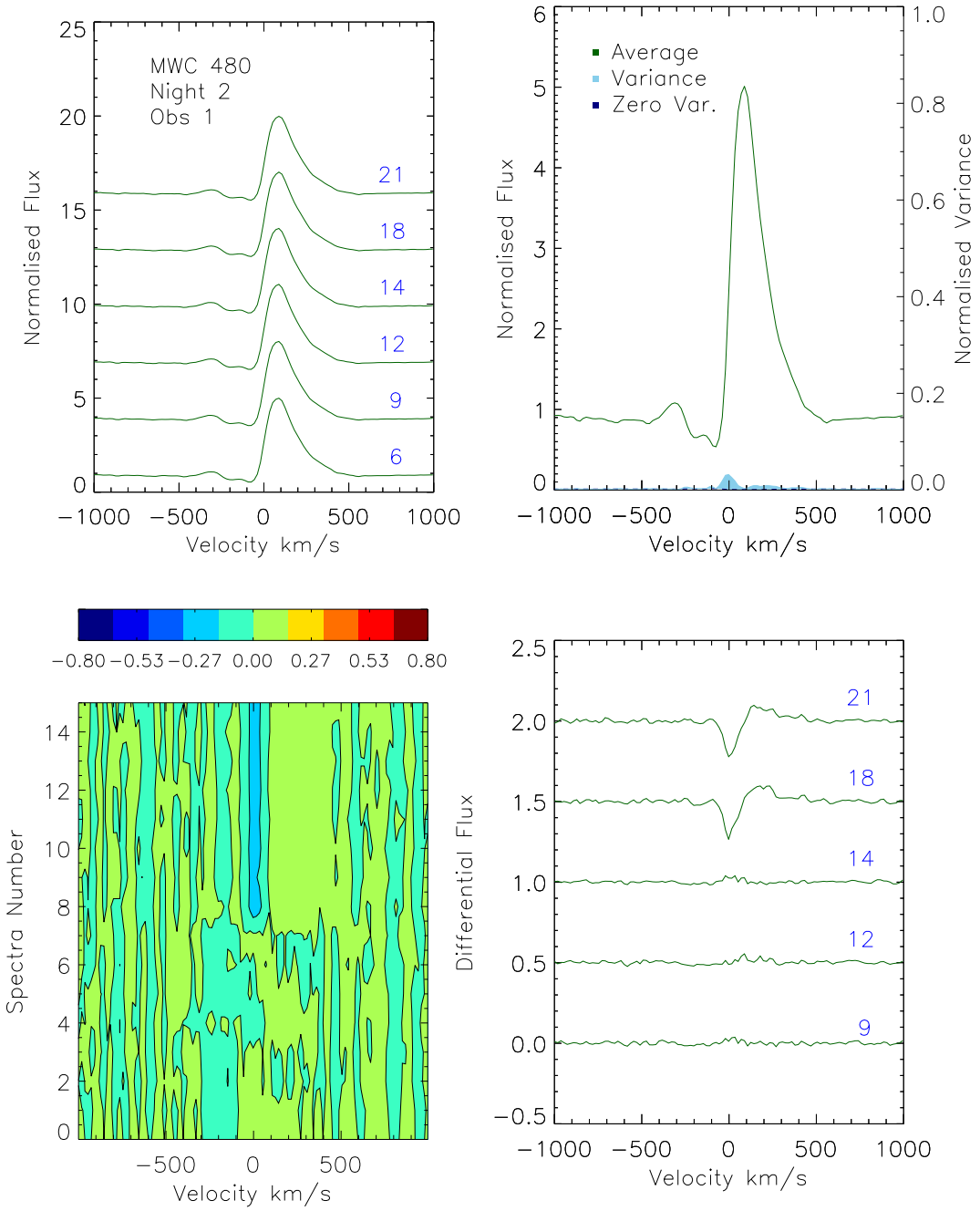

Figure A.32: *MWC 480 2001 observations. First observation block of Night 2.*

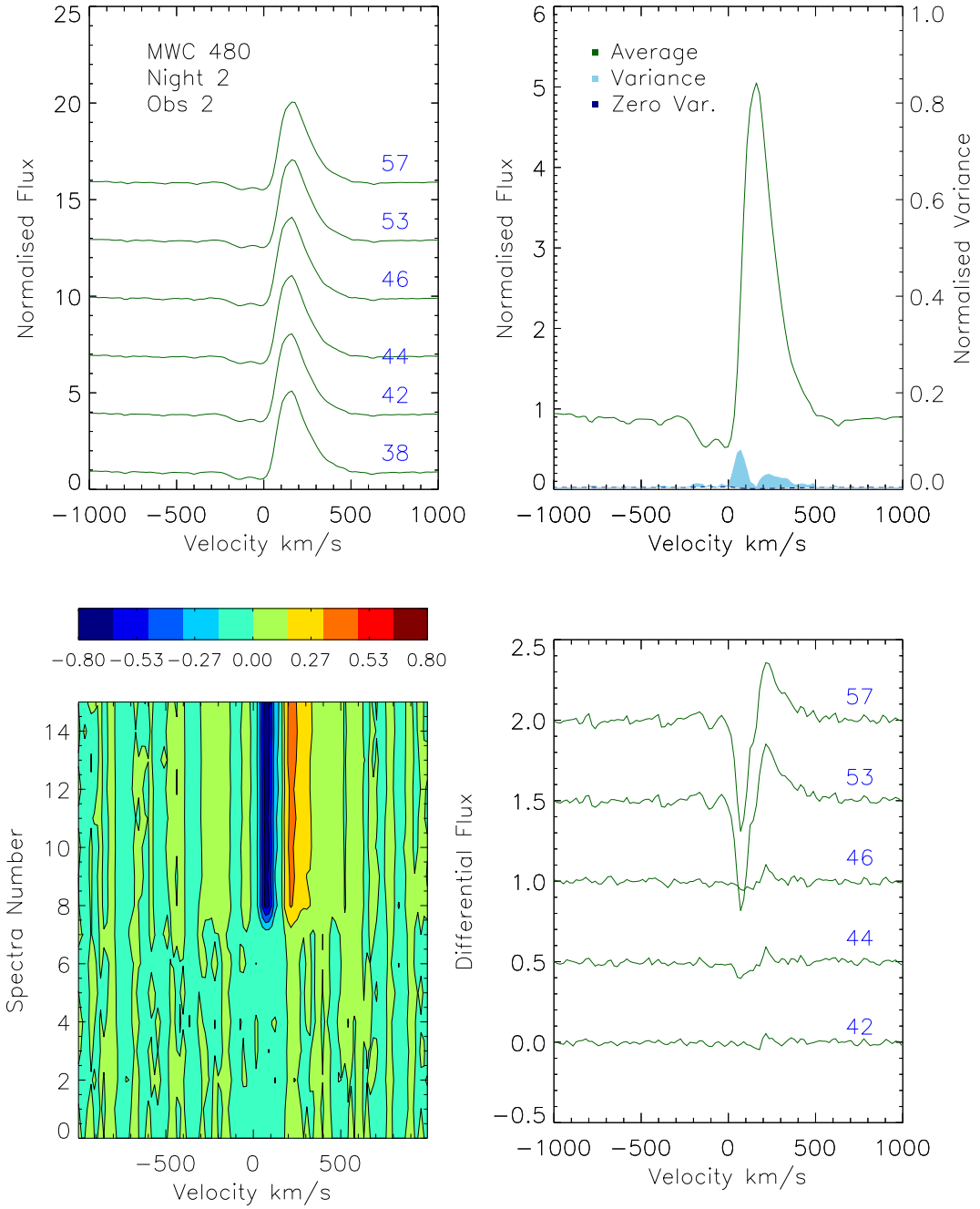

Figure A.33: *MWC 480 2001 observations. Second observation block of night 2. This block is separated from the first by about 8 hours.*

B

Chamaeleon Photometry: Individual Targets

B.1 About this Appendix

The following sections present the lights curves for each object in the photometry sample of Chamaeleon (See Chapt. 5). In each case the goodness of fit is discussed, along with the derived period, amplitude and any remaining variations after the fit is removed (See Table 5.4 for full list of fit parameters).

Two plots are shown for every object, one presenting the light curves and fit and a second presenting the Lomb-Scargle periodogram. The light curve plot is split into three panels. In the top panel of each plot, the data points of the I-band light curve are shown in blue, along with the photometric error. Here the light curves are normalised to the mean magnitude found by the fitting procedure. Over-plotted in a solid red line is the fit to this light curve, with the period and amplitude indicated within the panel. In the middle panel, the R-band light curve is shown in green. The fit to this light curve is plotted as a red dashed line. The last panel shows the residuals of I-band fit, where the dashed blue line indicates the zero point.

The periodogram is also given for each object below the light curve plot. In

each case the max point in the periodogram is indicated. The results of the fit to ChaHα2 have already been presented in Chapt. 5, the following describes those for the remaining 11 variable objects.

B.2 ChaHα6

The sinusoidal fit runs through all data points in the the I-band light (Fig. B.1), apart from the last two and provides and excellent description of the variations observed across the 8 nights observations (χ^2_r of 0.74). The standard deviation in the I-band is reduced to within the errors after fitting a sine curve with a period 4.27 $\pm$ 0.2 days (F-no. of 4.36). The periodogram reaches a peak at 4.09 days, in agreement with that found using the sine fit. This period also describes the R-band variations very well, and considering the error bars, it passes through all the data points within the time series.

The small amplitudes found (0.04 mag. for I-band) suggest the cool spot model is appropriate for modelling the emission variations over this time period. Even though this star was defined as an accretor within the LAMP sample, these observations would suggest no large hot spots are seen on the surface.

ChaHα6 is the second object within the sample for which a period has been measured (where the other object is ChaHα2). The Joergens et al. (2003) period, at 3.6 $\pm$ 0.19 days, lies below the period found here. This difference in the period found in these two studies is addressed in Chapt. 5, Sect. 5.6.1.

B.3 T33

The observations of T33 suggest it has a period longer than is covered by this data set (Fig. B.2). The fit to the I-band data results in a period of 7.85 $\pm$ 0.08 days, which is close to the broad peak of $\sim$ 6.3 days in the periodogram. However further observations over longer periods need to be undertaken to confirm this initial approximation.

The variations are significantly reduced after the fit, though still lie above the background standard deviations (F-no of 14.1). Convincingly, the R-band also follows this fitted period and phase. The R-band variations are found to be slightly larger (0.31 mag.) than the I-band observations (0.28 mag.), but considering the photometric errors are $\sim$ 0.02 mag. they are in rough agreement.

As the variations are relatively small they can be well described by cool spots. In this object we also see significant residuals, at twice the background variations,

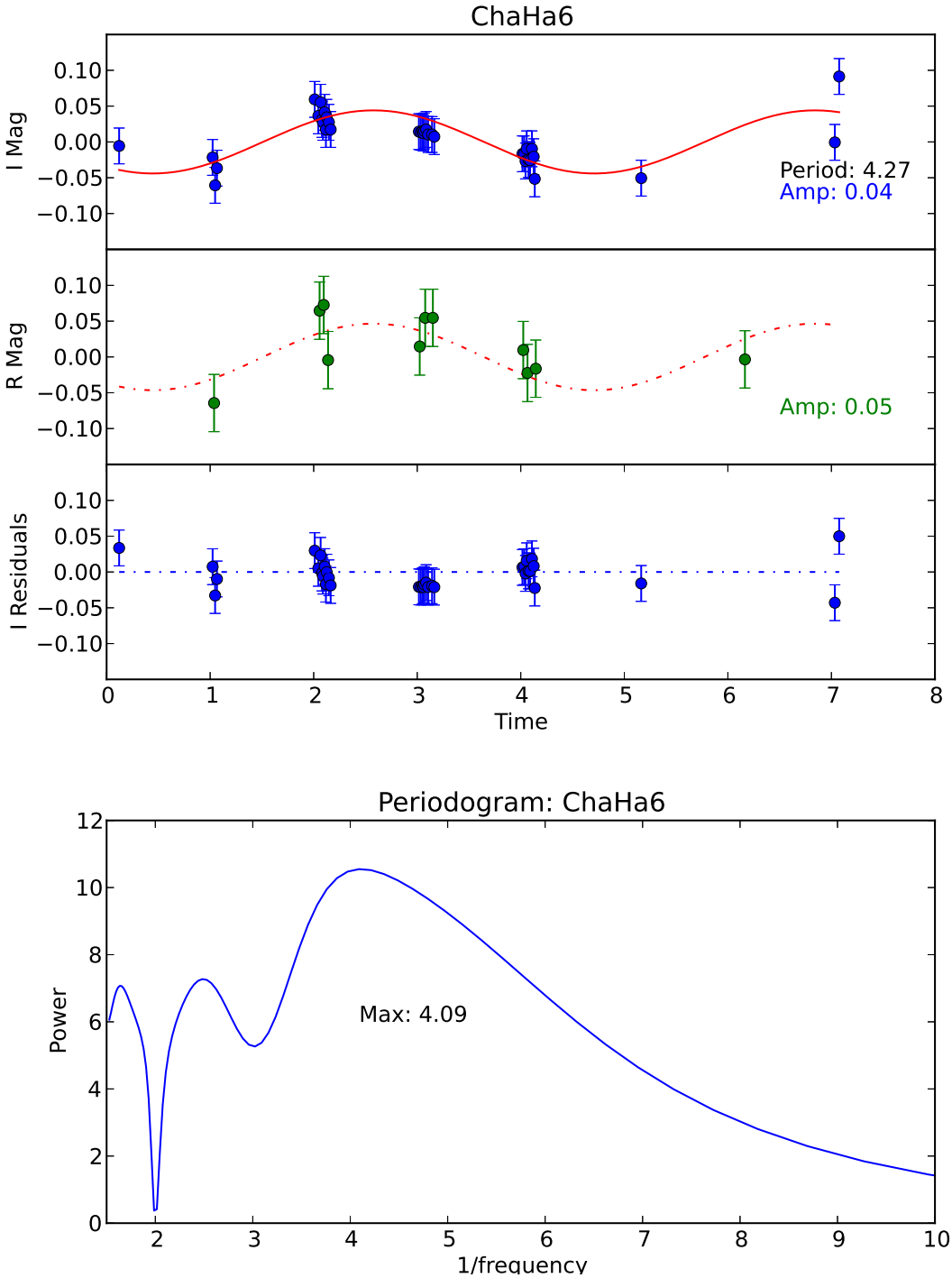

Figure B.1: *Upper Plot: I and R band light curves and I-band residuals for ChaHα6. Lower Plot: Lomb-Scargle periodogram.*

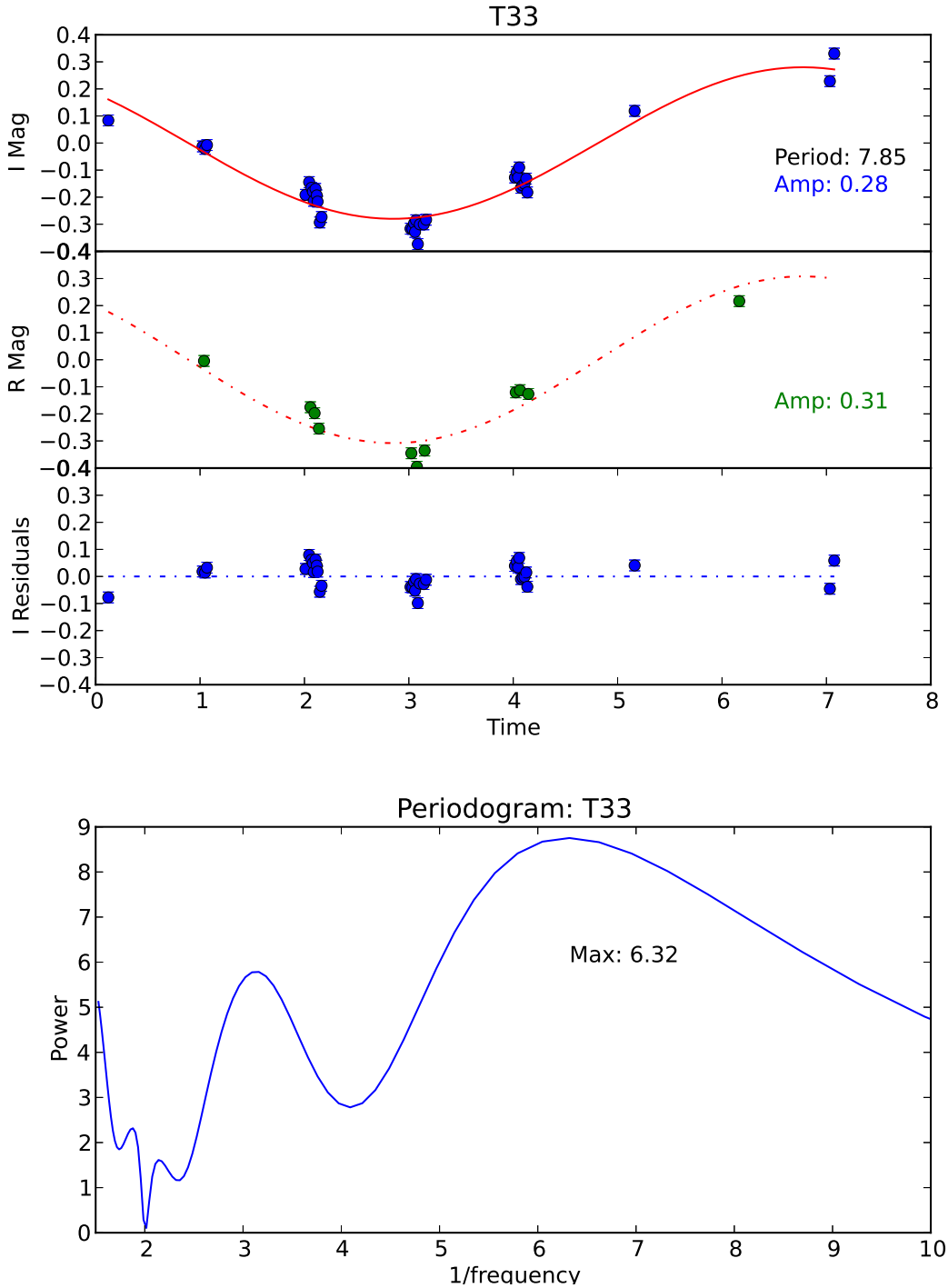

Figure B.2: *Upper Plot: I and R band light curves and I-band residuals for T33. Lower Plot: Lomb-Scargle periodogram.*

during each nights observations. This suggests there is some further activity on the surface of this star, which could take the form of a hot spot or accretion event, which is likely as this target is classified as an accretor in the LAMP sample.

B.4 T31

The observed variations of T31 cannot be described using a sinusoidal fit (Fig. B.3). The F-number in this case (0.75) is at the level of 80% false alarm probability. The light curve that is observed monotonically falls across the observation period. Over the course of the eight nights, the magnitude drops by 0.3 mag. The periodogram for this object shows no valid peaks. When a fit is attempted to the data, the standard deviation of the residuals of the fit remains higher than the original light curve.

These data suggest that T31 has a much longer observation period than is covered in this sample. Alternatively the star could be passing behind a denser part of the molecular cloud or undergoing a disc accretion event. The observations of Carpenter et al. (2001), suggest that there are larger amplitude variations occurring in the J band than observed here in the I or R band. This is not consistent with spot modulation of the light curve, but more likely to come from a change in the disc emission. However these J-band observations were observed years before the observations here, and so, while not conclusive suggest that some other source of variability is occurring in this system.

B.5 ISO143

The derived period for ISO143 is the longest in the sample at 8.82 ± 0.92 days. In fact, it is too long to be adequately constrained with this data set. However, the variations observed are well described by the sinusoidal fit, even though a full period was not observed (Fig. B.4). The F-number of 30.84 shows the residuals in the I-band after the fit are significantly smaller, and lie within the assumed errors. The data points at either end of the time-series play a significant role in determining the fit, and unfortunately these are few in number.

The R-band light curve does not show a clear periodic variation. Though the period found from the I-band light curve does roughly follows the data points, it is a poor fit and the high amplitude of variations found in the R-band light curve should not be trusted. The periodogram peaks at 6.3 days, the peak however is extremely wide spanning about four days. Further observations are necessary to

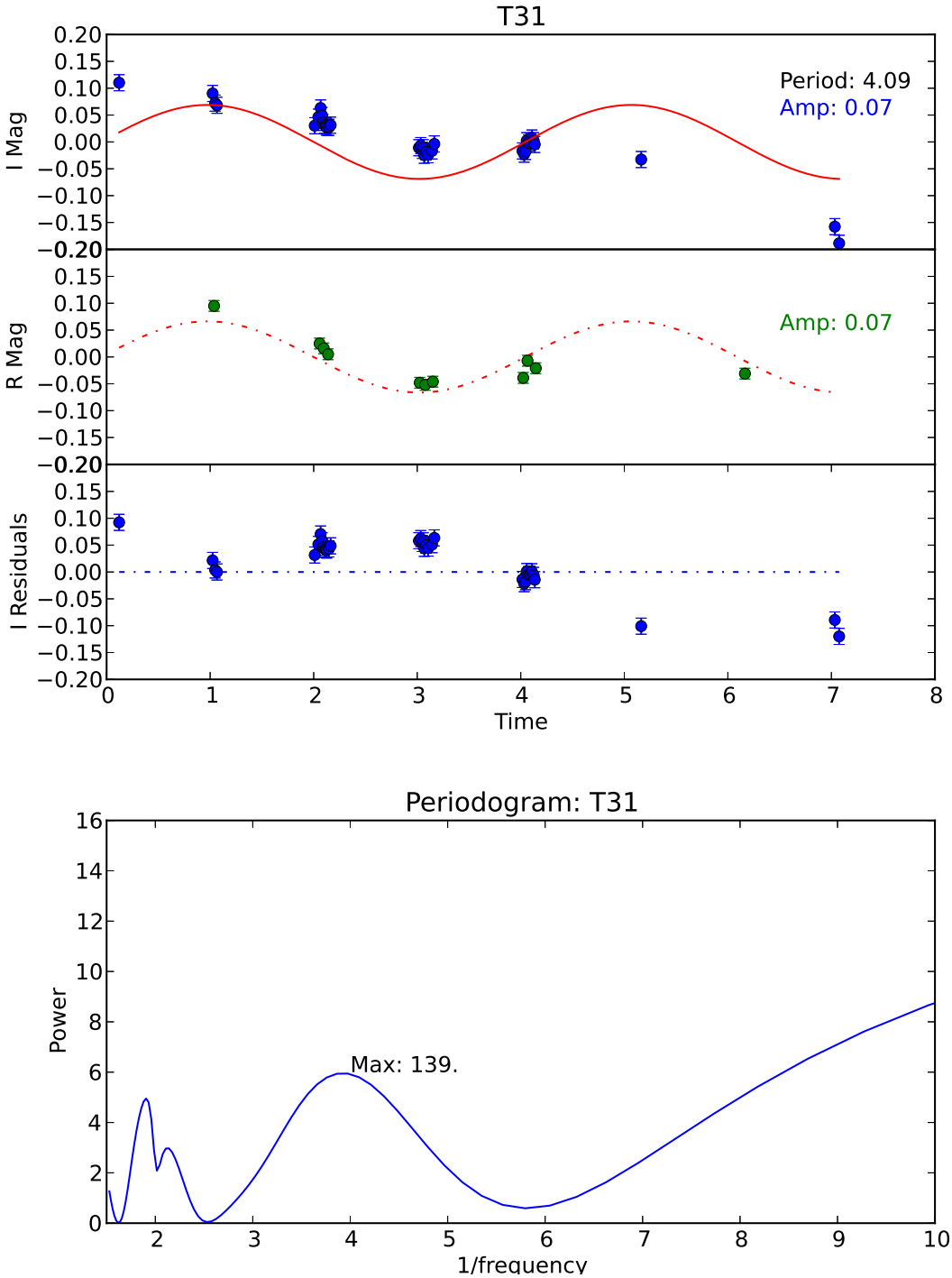

Figure B.3: *Upper Plot: I and R band light curves and I-band residuals for T31. Lower Plot: Lomb-Scargle periodogram.*

confirm this period.

The amplitudes of variation (I-band 0.05 mag.) are consistent with cool spots alone. However, as this object is classified as an accretor it is likely that there is a hot spot on the surface.

B.6 ISO126

The sharp peak at 3.66 days in the Lomb-Scargle periodogram for ISO126 suggests this is one of the best constrained periods in the sample (Fig. B.5). The fitting procedure to the I-band suggests a period of 3.72 days. There remains some residual variations after the fit (F-no. 8.24), which could be due to either a more complicated cool spot coverage than is allowed for by a simple sin fit, the presence of a hot spot along side the cool spot or accretion rate variations.

The R-band roughly follows the period and phase found in the I-band fit. In this case the R-band amplitude (0.09 mag.) is lower than the I-band amplitude (0.15 mag). However the fit in Fig. B.5 does not go through the first and the last data point, which would pull the amplitude up, suggesting that the R-band amplitude is higher than is measured here.

B.7 CHXR27

The light curve of the CHXR27 is convincingly reproduced by a sine curve with period of 6.92 days (Fig. B.6). The F-number is high 29.92 showing that the majority of the variations can be described with a simple cool spot model. The periodogram however does not show a significant peak. After reaching a maximum at 3.97 days, it decays slowly. However the R-band observations follow the fit for the most part.

In both the I-band and the R-band there are some remaining residuals, again suggesting more activity than simple cool spot models. This is one of the targets that is not covered within the LAMP sample, and so it is not known whether this object is accreting or not.

B.8 B43

In the case of B43, the max peak in the periodogram and the fitted period agree nearly exactly at 3.09 ± 0.03 days and 3.08 days. However a visual inspection of the fit is less convincing (Fig. B.7). Both the χ^2_r (10.23) and the F-number

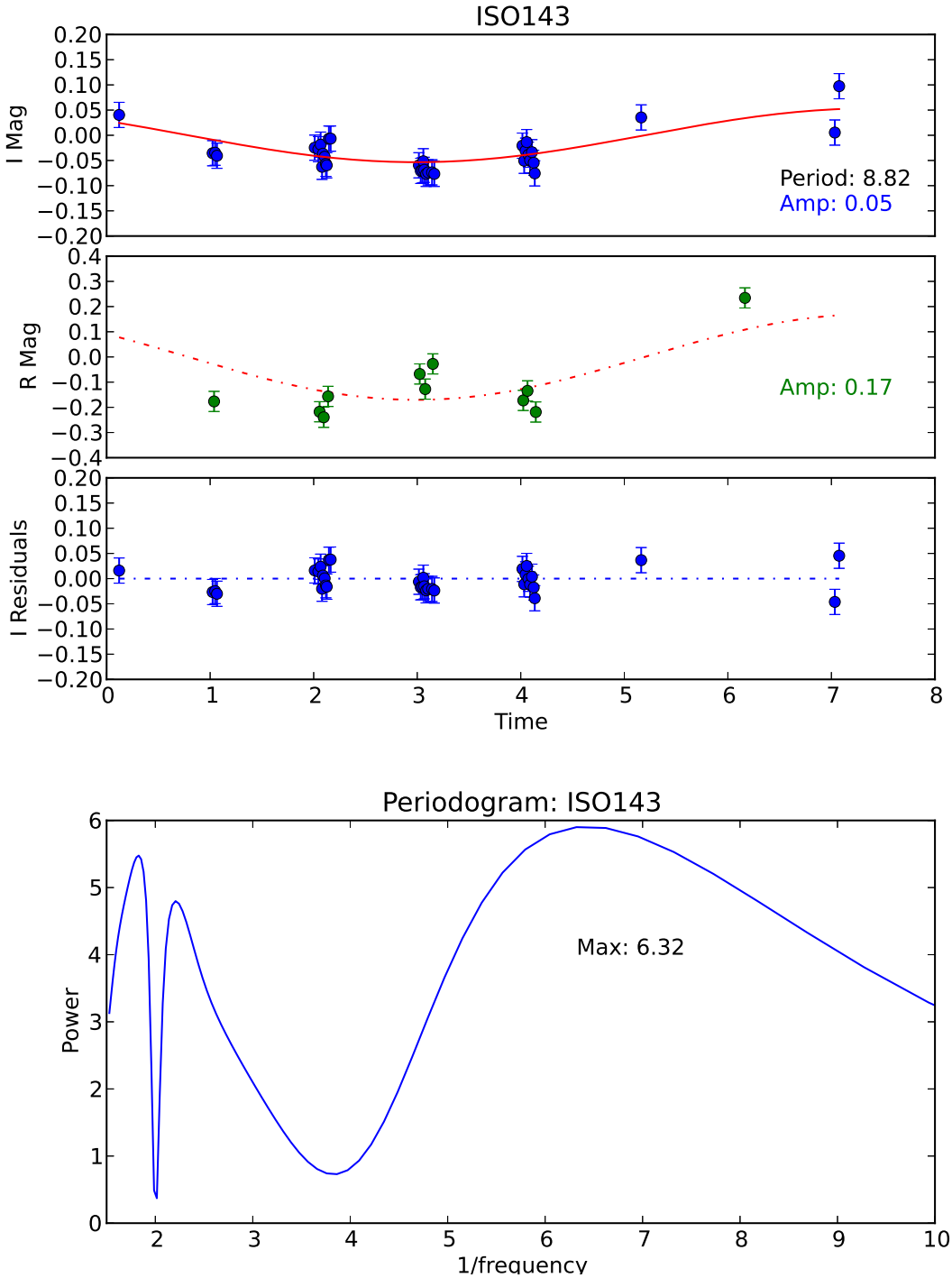

Figure B.4: *Upper Plot: I and R band light curves and I-band residuals for ISO143. Lower Plot: Lomb-Scargle periodogram.*

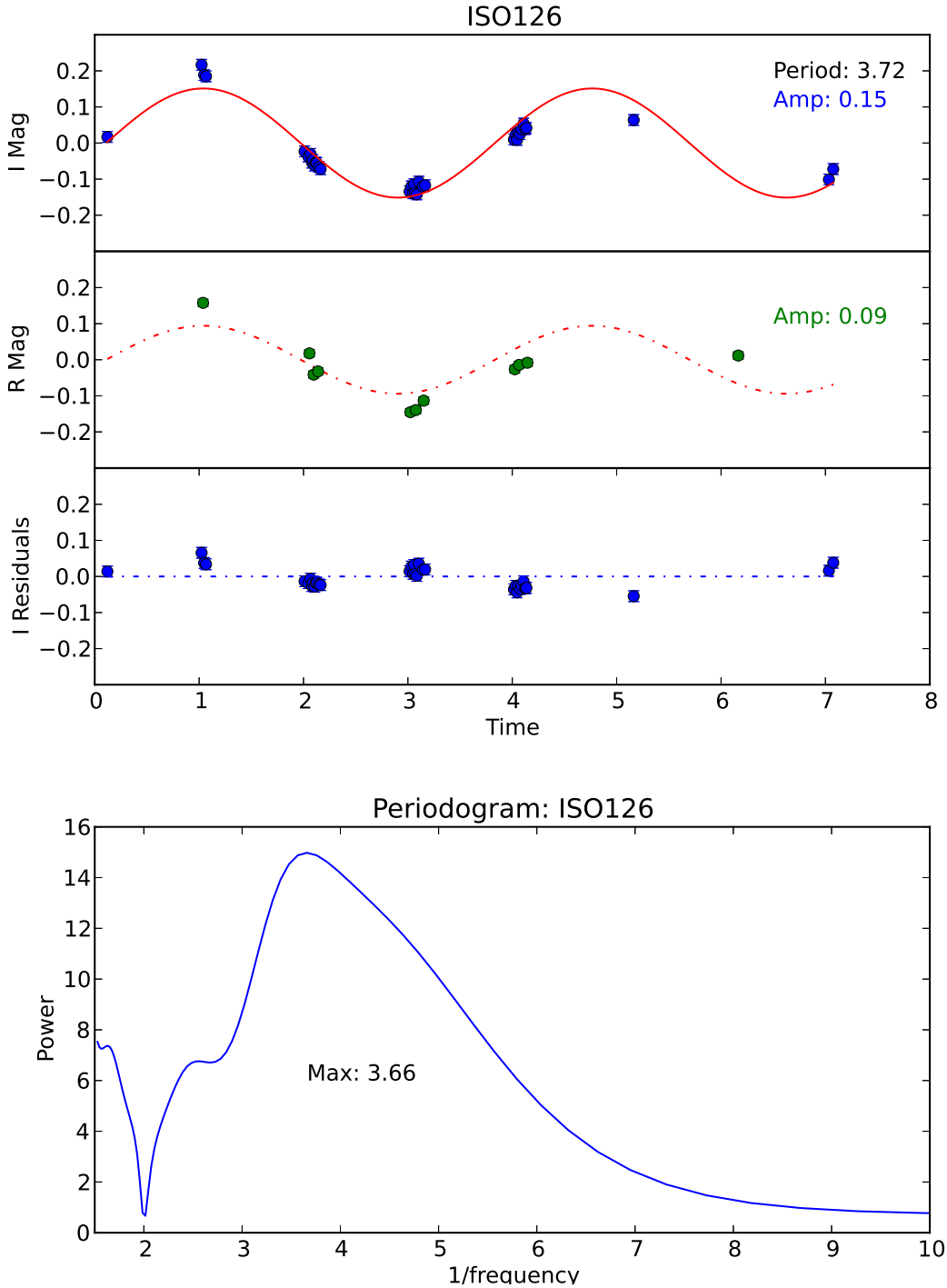

Figure B.5: *Upper Plot: I and R band light curves and I-band residuals for ISO126. Lower Plot: Lomb-Scargle periodogram.*

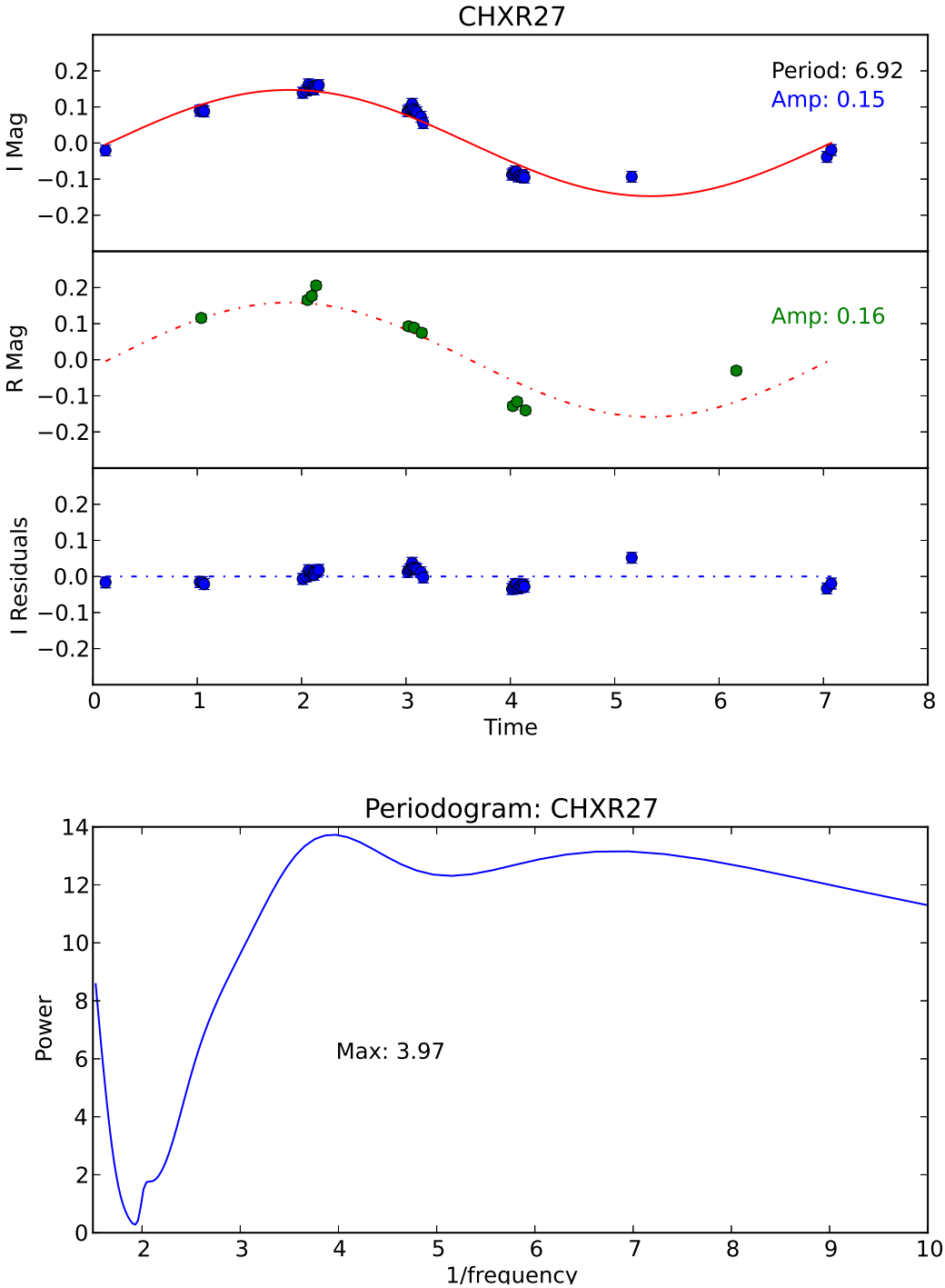

Figure B.6: *Upper Plot: I and R band light curves and I-band residuals for CHXR27. Lower Plot: Lomb-Scargle periodogram.*

(7.42) show that it is a reasonable fit to the data, and the variations are reduced. However in both the I-band and the R-band there are still significant variations remaining after the fit. On top of these variations that occur within a night, the mean magnitude in the I-band seems to fall across the observations. This suggests that while the variability is consistent with cool spot rotating with the surface, there may also be some other source of variations, and possibly with a longer term gradient.

This is another case where the R-band variations are larger than the I-band variations. In fact the fit to the R-band does not go through the highest magnitude points in the light curve, and so the amplitudes of the variations could be even larger.

B.9 CHXR22E

The period fit of 4.91 ± 0.19 days follows the variations within the I-band light curve well, and also agrees with the maximum found in the periodogram (Fig. B.8). The large F-number shows the reduction in the variations after the fit. The residual variations are on the same level as those of the non-varying stars in the field. The R-band variations are not as well described by this fit, and many points lie off the line. However there is a rough agreement.

CHXR22E was classified as a non-accretor in the LAMP sample. There are no strong indications of extra variations on top of what is expected of cool spots. However as we have seen many accretors show low amplitude variations well described by a simple sin fit, there can be ongoing accretion without strong indications of large hot spots.

B.10 T30

The light curve of can be modelled with a period of 4.81 days and 5.81 days (Fig. B.9). Both cases result in a high χ^2_r of ~ 79. Conversely there is also a reasonably high F-number in both cases of 10.78. This shows that though the fit does significantly reduce the variations, it is not a good model for the variations. The periodogram reaches a maximum at 4.21 days, but does not show a significant peak.

The residuals of the fit still have a high standard deviation at 0.12, and there are clear variations within each night's observations.

On visual inspection, the fit probably gives a reasonable estimate of the am-

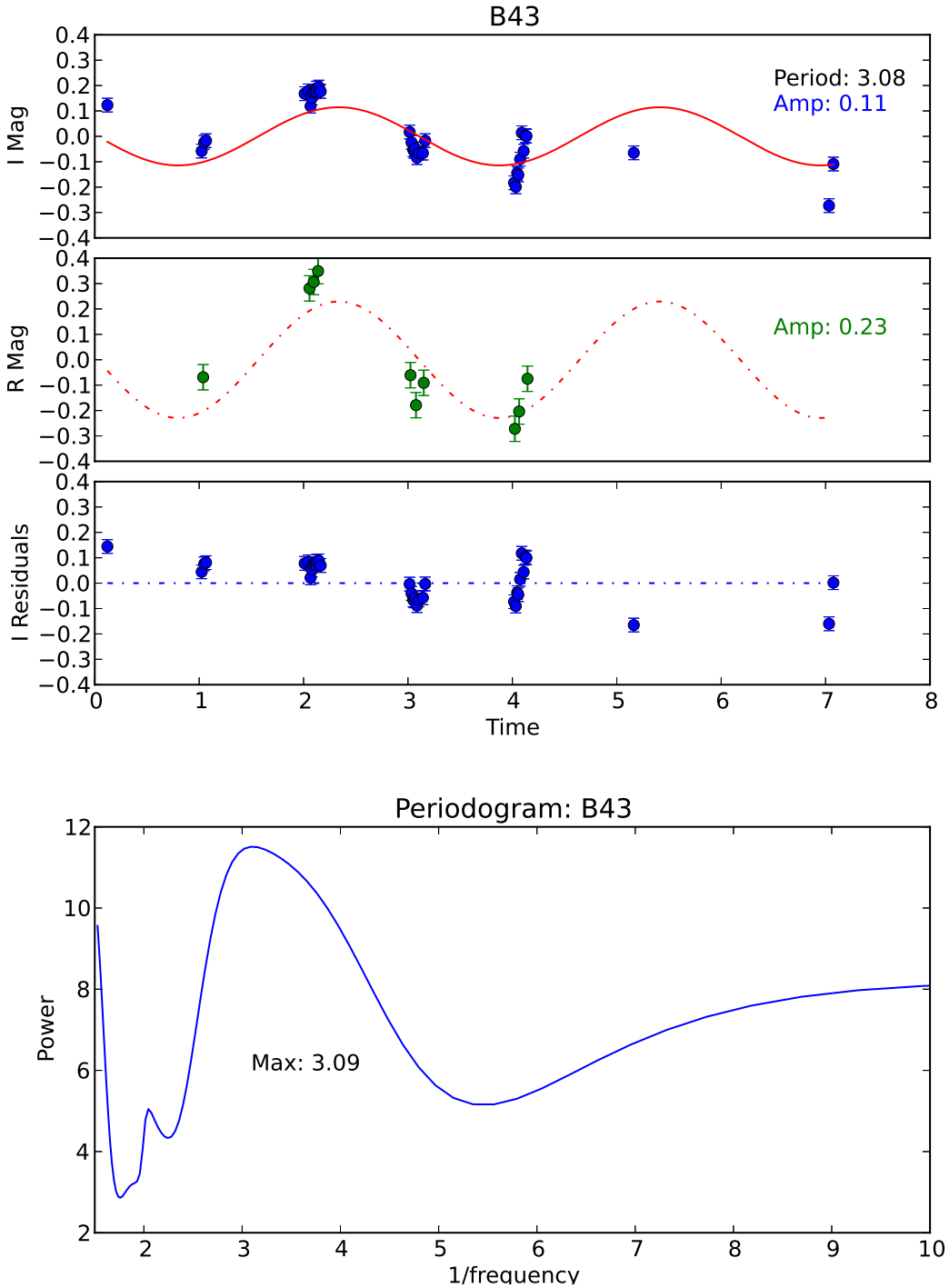

Figure B.7: *Upper Plot: I and R band light curves and I-band residuals for B43. Lower Plot: Lomb-Scargle periodogram.*

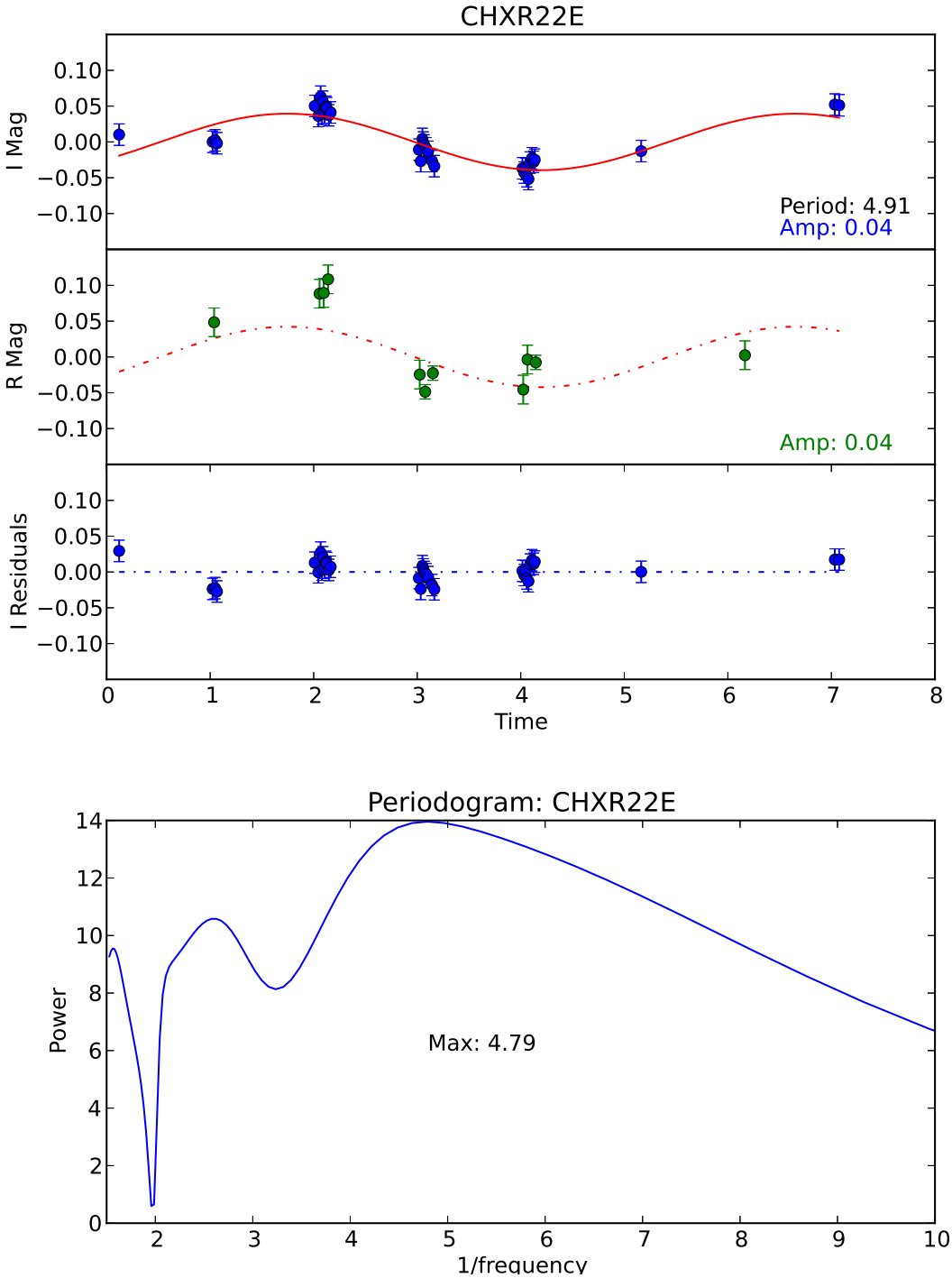

Figure B.8: *Upper Plot: I and R band light curves and I-band residuals for CHXR22E. Lower Plot: Lomb-Scargle periodogram.*

plitude of variations in the I-band, which at 0.28 mag. are one of the highest in this sample. It is most likely that there are multiple spots on the surface of this object, and quite possibly both hot and cool spots. The true rotation period of T30 most likely lies within the range of 4 - 6 days, but further observations are necessary to disentangle the rotation signatures from the other sources of variations in this object.

B.11 T45

On visual inspection, the sine fit to the T45 light curve agrees quite well with the data (Fig. B.10). The χ^2_r of 1.13 and the F-number of 4.54 show that while not all the variations are covered with a single sinusoidal fit, the major variations are. There are still some residual variations within each nights observations, suggesting again that there is more than a cool rotating spot on the surface.

The period of 5.41 $\pm$ 0.9 days agrees well with the max peak of 5.34 in the periodogram. However the R-band observations are not well described by the fit. The last point in the R-band time-series is much lower than the fit predicts, and the other points are too spread to properly fit for the amplitude.

B.12 ChaHα1

This brown dwarf was also not covered in the LAMP sample. There is a reasonable amount of spread in the I-band light curve. So although the period found through the fit (3.24 $\pm$ 0.07 days) is in agreement with the sharp peak in the periodogram (3.31 days), and the fit runs through the majority of data points considering the errors, the χ^2_r of the fit is still relatively high at 2.46 (Fig. B.11). The F-number (15.44) shows that there is a large reduction in the variations after the fit, and the remaining residuals do lie around the zero point. There are large variations during each nights observations, however they are not significantly above the background level of variations (See Table 5.4).

There is also a significant spread within the R-band light curve, and in this case the errors are also larger. The R-band light curve does follow the general trend of the I-band fit. The amplitude of the R-band fit (0.16 mag.) is significantly higher than the I-band amplitude of 0.08 mag. However, this is an affect of the large nightly variations which, in the case of the sparse R-band sampling, mask the period change running through the light curve.

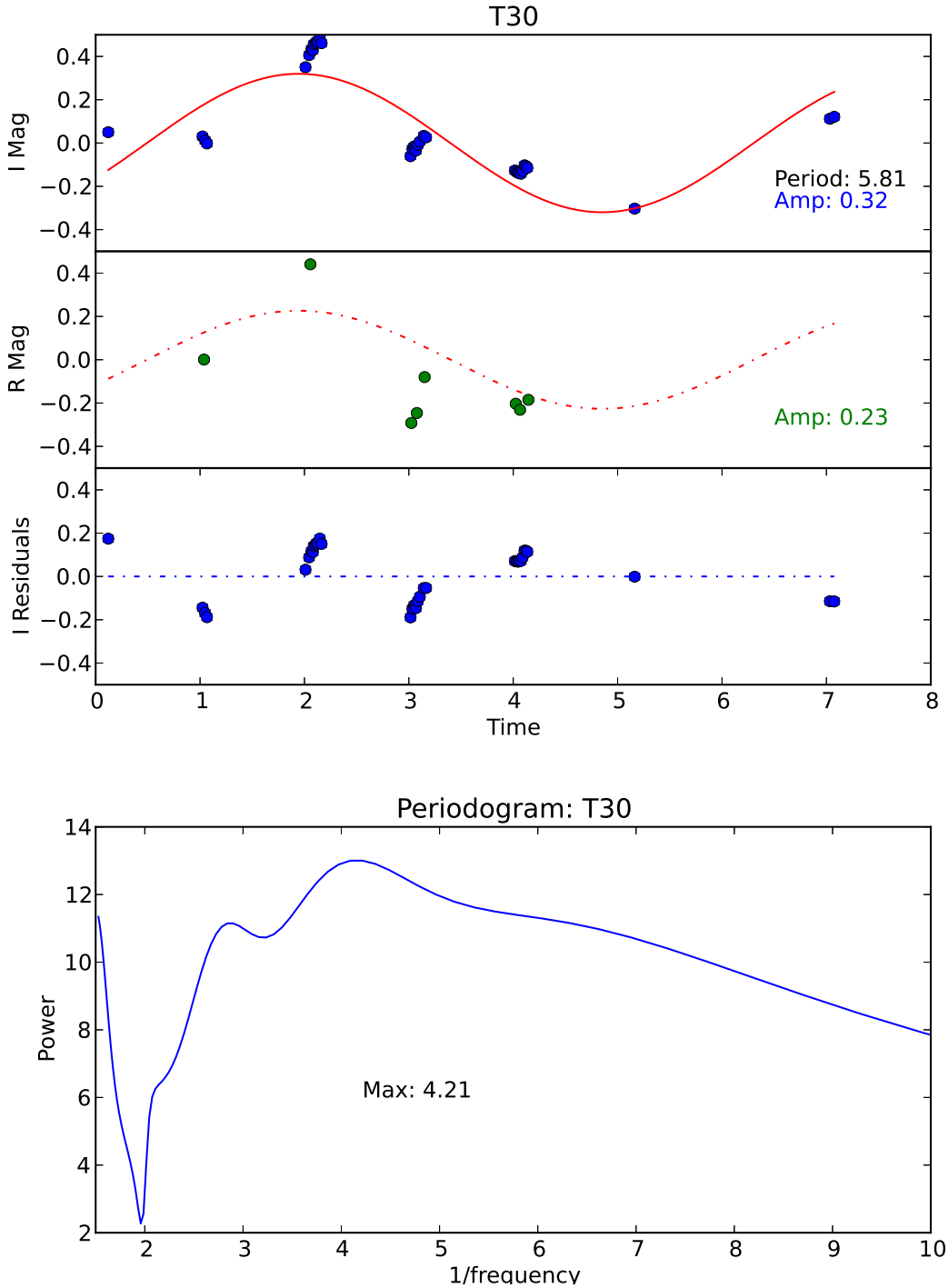

Figure B.9: *Upper Plot: I and R band light curves and I-band residuals for T30. Lower Plot: Lomb-Scargle periodogram.*

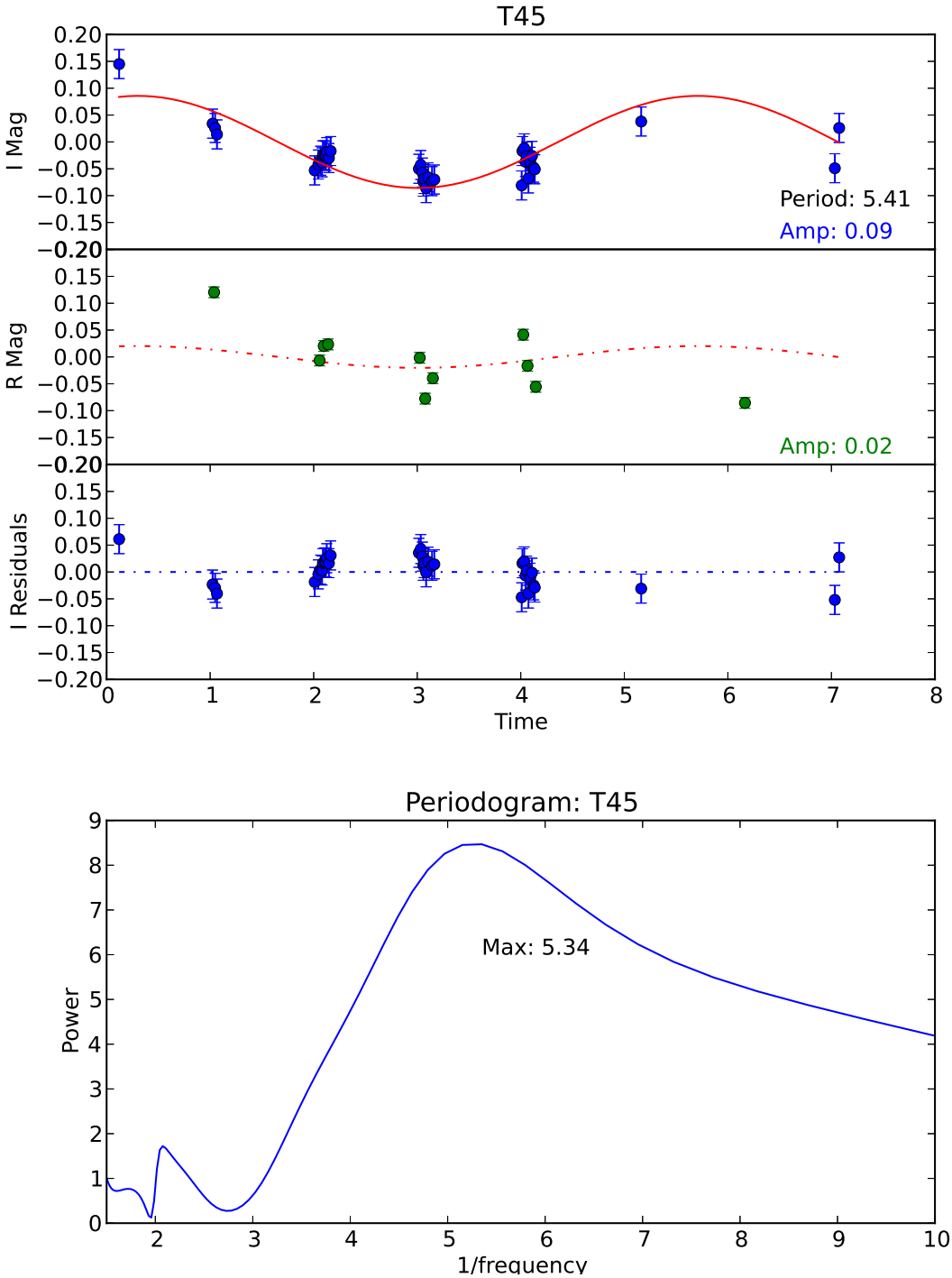

Figure B.10: *Upper Plot: I and R band light curves and I-band residuals for T45. Lower Plot: Lomb-Scargle periodogram.*

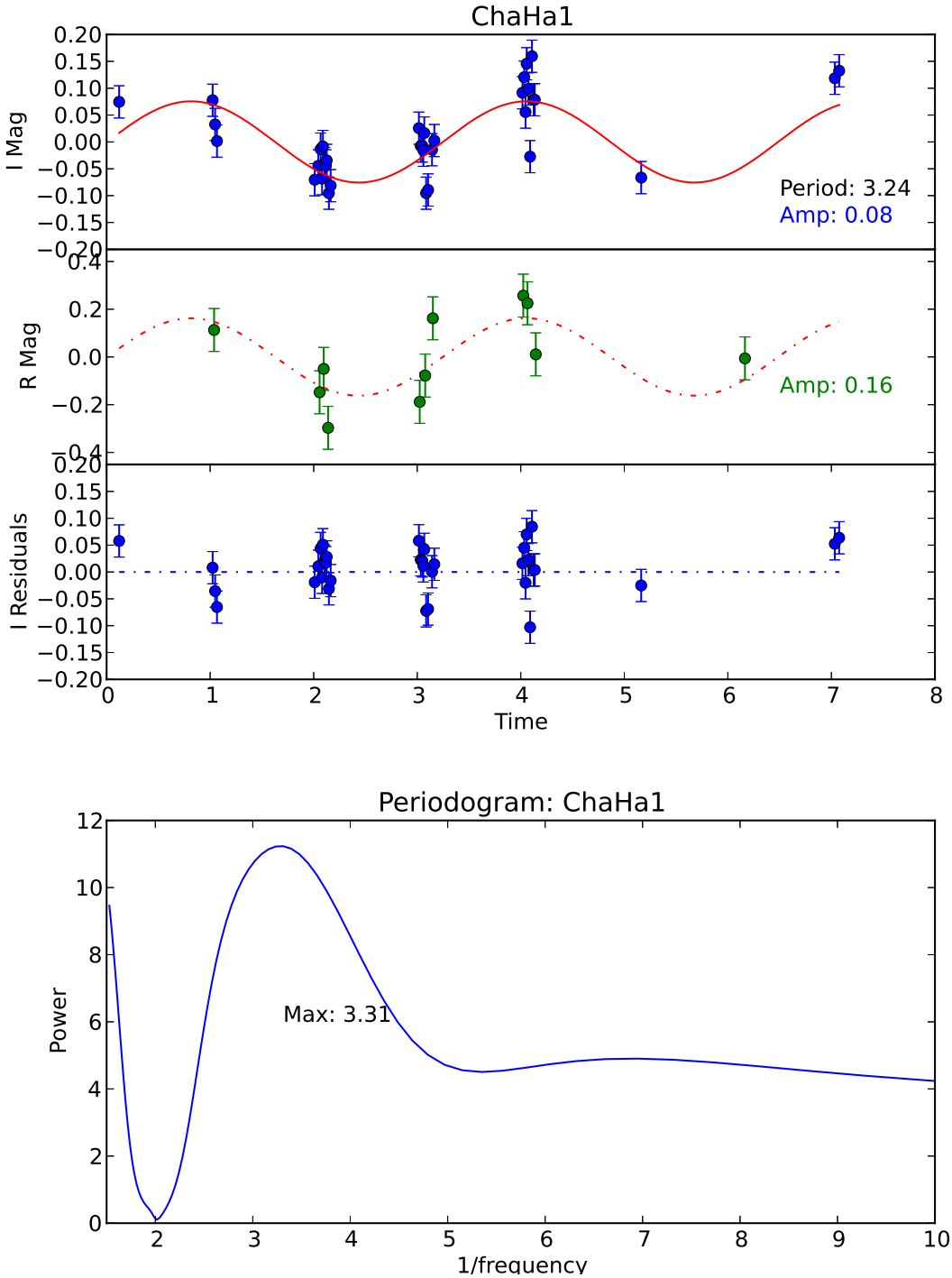

Figure B.11: *Upper Plot: I and R band light curves and I-band residuals for ChaHα1. Lower Plot: Lomb-Scargle periodogram.*

Bibliography

Acke, B., van den Ancker, M. E., & Dullemond, C. P. 2005, A&A, 436, 209

Adams, F. C. & Gregory, S. G. 2012, ApJ, 744, 55

Akeson, R. L., Ciardi, D., & van Belle, G. T. 2003, in Society of Photo-Optical Instrumentation Engineers (SPIE) Conference Series, Vol. 4838, Society of Photo-Optical Instrumentation Engineers (SPIE) Conference Series, ed. W. A. Traub, 1037–1042

Akeson, R. L., Ciardi, D. R., van Belle, G. T., & Creech-Eakman, M. J. 2002, ApJ, 566, 1124

Alecian, E., Peralta, R., Oksala, M. E., & Neiner, C. 2012, in SF2A-2012: Proceedings of the Annual meeting of the French Society of Astronomy and Astrophysics, ed. S. Boissier, P. de Laverny, N. Nardetto, R. Samadi, D. Valls-Gabaud, & H. Wozniak, 401–404

Alencar, S. H. P., Basri, G., Hartmann, L., & Calvet, N. 2005, A&A, 440, 595

Alencar, S. H. P., Bouvier, J., Walter, F. M., et al. 2012, A&A, 541, A116

Alencar, S. H. P., Johns-Krull, C. M., & Basri, G. 2001, AJ, 122, 3335

Alexander, R. D. & Armitage, P. J. 2006, ApJ, 639, L83

Allard, F., Hauschildt, P. H., Alexander, D. R., Tamanai, A., & Schweitzer, A. 2001, ApJ, 556, 357

Alonso-Albi, T., Fuente, A., Bachiller, R., et al. 2009, A&A, 497, 117

Andre, P., Ward-Thompson, D., & Barsony, M. 1993, ApJ, 406, 122

Andrews, S. M. & Williams, J. P. 2005, ApJ, 631, 1134

Antoniucci, S., García López, R., Nisini, B., et al. 2011, A&A, 534, A32

Ardila, D. R. & Basri, G. 2000, ApJ, 539, 834

Armitage, P. J. 1995, MNRAS, 274, 1242

Attridge, J. M. & Herbst, W. 1992, ApJ, 398, L61

Bai, X.-N. 2013, ApJ, 772, 96

Bally, J. 2008, Overview of the Orion Complex (Reipurth, B.), 459

Baraffe, I., Chabrier, G., Allard, F., & Hauschildt, P. H. 1998, A&A, 337, 403

Barentsen, G., Vink, J. S., Drew, J. E., et al. 2011, MNRAS, 415, 103

Barrado y Navascués, D. & Martín, E. L. 2003, AJ, 126, 2997

Basri, G. 1987, in Lecture Notes in Physics, Berlin Springer Verlag, Vol. 291, Cool Stars, Stellar Systems and the Sun, ed. J. L. Linsky & R. E. Stencel, 411

Basri, G. & Batalha, C. 1990, ApJ, 363, 654

Basri, G. & Bertout, C. 1989, ApJ, 341, 340

Basri, G., Marcy, G. W., & Valenti, J. A. 1992, ApJ, 390, 622

Baud, B., Beintema, D. A., Wesselius, P. R., et al. 1984, ApJ, 278, L53

Bertout, C., Basri, G., & Bouvier, J. 1988, ApJ, 330, 350

Bertout, C., Krautter, J., Moellenhoff, C., & Wolf, B. 1977, A&A, 61, 737

Bertout, C., Robichon, N., & Arenou, F. 1999, A&A, 352, 574

Beskrovnaya, N. G., Pogodin, M. A., Najdenov, I. D., & Romanyuk, I. I. 1995, A&A, 298, 585

Biazzo, K., Alcalá, J. M., Covino, E., et al. 2012, A&A, 547, A104

Bibo, E. A. & The, P. S. 1991, A&AS, 89, 319

Boden, A. F., Torres, G., Sargent, A. I., et al. 2007, ApJ, 670, 1214

Bohm, T. & Catala, C. 1993, A&AS, 101, 629

Boss, A. P. 2000, ApJ, 536, L101

Bouret, J.-C. & Catala, C. 1998, A&A, 340, 163

Bouvier, J., Alencar, S. H. P., Boutelier, T., et al. 2007a, A&A, 463, 1017

Bouvier, J., Alencar, S. H. P., Harries, T. J., Johns-Krull, C. M., & Romanova, M. M. 2007b, Protostars and Planets V, 479

Bouvier, J. & Bertout, C. 1989, A&A, 211, 99

Bouvier, J., Bertout, C., Benz, W., & Mayor, M. 1986, A&A, 165, 110

Bouvier, J., Cabrit, S., Fernandez, M., Martin, E. L., & Matthews, J. M. 1993a, A&AS, 101, 485

Bouvier, J., Cabrit, S., Fernandez, M., Martin, E. L., & Matthews, J. M. 1993b, A&A, 272, 176

Bouvier, J., Chelli, A., Allain, S., et al. 1999, A&A, 349, 619

Bouvier, J., Covino, E., Kovo, O., et al. 1995, A&A, 299, 89

Bouvier, J., Grankin, K. N., Alencar, S. H. P., et al. 2003, A&A, 409, 169

Bouwman, J., Lawson, W. A., Dominik, C., et al. 2006, ApJ, 653, L57

Cabrit, S. & Andre, P. 1991, ApJ, 379, L25

Cabrit, S., Edwards, S., Strom, S. E., & Strom, K. M. 1990, ApJ, 354, 687

Cabrit, S., Pety, J., Pesenti, N., & Dougados, C. 2006, A&A, 452, 897

Calvet, N. & Gullbring, E. 1998, ApJ, 509, 802

Calvet, N., Hartmann, L., & Strom, S. E. 2000, Protostars and Planets IV, 377

Calvet, N., Muzerolle, J., Briceño, C., et al. 2004, AJ, 128, 1294

Carpenter, J. M., Hillenbrand, L. A., & Skrutskie, M. F. 2001, AJ, 121, 3160

Carpenter, J. M., Hillenbrand, L. A., Skrutskie, M. F., & Meyer, M. R. 2002, AJ, 124, 1001

Catala, C., Donati, J. F., Böhm, T., et al. 1999, A&A, 345, 884

Chandler, C. J., Koerner, D. W., Sargent, A. I., & Wood, D. O. S. 1995, ApJ, 449, L139

Chatterjee, S. & Tan, J. C. 2013, ArXiv e-prints

Chen, H., Grenfell, T. G., Myers, P. C., & Hughes, J. D. 1997, ApJ, 478, 295

Chen, H., Myers, P. C., Ladd, E. F., & Wood, D. O. S. 1995, ApJ, 445, 377

Chou, M.-Y., Takami, M., Manset, N., et al. 2013, ArXiv e-prints

Clarke, C. J., Gendrin, A., & Sotomayor, M. 2001, MNRAS, 328, 485

Clarke, C. J. & Pringle, J. E. 2006, MNRAS, 370, L10

Cohen, M. 1980, MNRAS, 191, 499

Cohen, M. & Kuhi, L. V. 1979, ApJS, 41, 743

Cohen, R. E., Herbst, W., & Williams, E. C. 2004, AJ, 127, 1602

Corcoran, M. & Ray, T. P. 1998, A&A, 331, 147

Corder, S., Eisner, J., & Sargent, A. 2005, ApJ, 622, L133

Costigan, G., Scholz, A., Stelzer, B., et al. 2012, MNRAS, 427, 1344

Curran, R. L., Argiroffi, C., Sacco, G. G., et al. 2011, A&A, 526, A104

Damiani, F., Micela, G., Sciortino, S., & Harnden, Jr., F. R. 1995, ApJ, 446, 331

D'Angelo, C. R. & Spruit, H. C. 2012, MNRAS, 420, 416

D'Antona, F. & Mazzitelli, I. 1997, MEMSAI, 68, 807

DeWarf, L. E., Sepinsky, J. F., Guinan, E. F., Ribas, I., & Nadalin, I. 2003, ApJ, 590, 357

Donati, J.-F., Bouvier, J., Walter, F. M., et al. 2011a, MNRAS, 412, 2454

Donati, J.-F., Gregory, S. G., Montmerle, T., et al. 2011b, MNRAS, 417, 1747

Donati, J.-F., Jardine, M. M., Gregory, S. G., et al. 2008, MNRAS, 386, 1234

Donati, J.-F., Skelly, M. B., Bouvier, J., et al. 2010, MNRAS, 409, 1347

Donehew, B. & Brittain, S. 2011, AJ, 141, 46

Drew, J. E., Busfield, G., Hoare, M. G., et al. 1997, MNRAS, 286, 538

Dullemond, C. P. & Monnier, J. D. 2010, ARA&A, 48, 205

Dullemond, C. P., Natta, A., & Testi, L. 2006, ApJ, 645, L69

Dupree, A. K., Brickhouse, N. S., Cranmer, S. R., et al. 2012, ApJ, 750, 73

Dutrey, A., Guilloteau, S., Duvert, G., et al. 1996, A&A, 309, 493

Dutrey, A., Guilloteau, S., & Simon, M. 2003, A&A, 402, 1003

Dworetsky, M. M. 1983, MNRAS, 203, 917

Edwards, S., Fischer, W., Kwan, J., Hillenbrand, L., & Dupree, A. K. 2003, ApJ, 599, L41

Edwards, S., Hartigan, P., Ghandour, L., & Andrulis, C. 1994, AJ, 108, 1056

Eiroa, C., Oudmaijer, R. D., Davies, J. K., et al. 2002, A&A, 384, 1038

Eisloffel, J., Davis, C. J., Ray, T. P., & Mundt, R. 1994, ApJ, 422, L91

Eisner, J. A., Lane, B. F., Akeson, R. L., Hillenbrand, L. A., & Sargent, A. I. 2003, ApJ, 588, 360

Eisner, J. A., Lane, B. F., Hillenbrand, L. A., Akeson, R. L., & Sargent, A. I. 2004, ApJ, 613, 1049

Espaillat, C., Calvet, N., D'Alessio, P., et al. 2007, ApJ, 670, L135

Evans, I. N. J., Dunham, M. M., Jørgensen, J. K., et al. 2009, ApJS, 181, 321

Fang, M., van Boekel, R., Wang, W., et al. 2009, A&A, 504, 461

Favata, F., Reale, F., Micela, G., et al. 2000, A&A, 353, 987

Fedele, D., van den Ancker, M. E., Henning, T., Jayawardhana, R., & Oliveira, J. M. 2010, A&A, 510, A72

Feigelson, E. D. & Decampli, W. M. 1981, ApJ, 243, L89

Feigelson, E. D. & Lawson, W. A. 2004, ApJ, 614, 267

Feigelson, E. D. & Montmerle, T. 1999, ARA&A, 37, 363

Feigelson, E. D., Welty, A. D., Imhoff, C., et al. 1994, ApJ, 432, 373

Flaherty, K. M., Muzerolle, J., Rieke, G., et al. 2012, ApJ, 748, 71

Fuhrmeister, B., Liefke, C., Schmitt, J. H. M. M., & Reiners, A. 2008, A&A, 487, 293

Fukagawa, M., Hayashi, M., Tamura, M., et al. 2004, ApJ, 605, L53

Gagné, M., Skinner, S. L., & Daniel, K. J. 2004, ApJ, 613, 393

Garcia Lopez, R., Natta, A., Testi, L., & Habart, E. 2006, A&A, 459, 837

Ghez, A. M., Neugebauer, G., & Matthews, K. 1993, AJ, 106, 2005

Ghosh, P. & Lamb, F. K. 1978, ApJ, 223, L83

Giampapa, M. S., Basri, G. S., Johns, C. M., & Imhoff, C. 1993, ApJS, 89, 321

Gizis, J. E., Reid, I. N., & Hawley, S. L. 2002, AJ, 123, 3356

Gomez de Castro, A. I. & Franqueira, M. 1997, ApJ, 482, 465

Gómez de Castro, A. I. & Verdugo, E. 2003, ApJ, 597, 443

Goodson, A. P., Böhm, K. H., & Winglee, R. M. 1998, in American Institute of Physics Conference Series, Vol. 431, American Institute of Physics Conference Series, ed. S. S. Holt & T. R. Kallman, 533–536

Grady, C., Stapelfeldt, K., Clampin, M., et al. 2001, in Bulletin of the American Astronomical Society, Vol. 33, American Astronomical Society Meeting Abstracts, 1396

Grady, C. A., Hamaguchi, K., Schneider, G., et al. 2010, ApJ, 719, 1565

Grady, C. A., Woodgate, B., Bruhweiler, F. C., et al. 1999, ApJ, 523, L151

Grankin, K. N., Melnikov, S. Y., Bouvier, J., Herbst, W., & Shevchenko, V. S. 2007, A&A, 461, 183

Greene, T. P., Wilking, B. A., Andre, P., Young, E. T., & Lada, C. J. 1994, ApJ, 434, 614

Grinin, V. P. & Rostopchina, A. N. 1996, Astronomy Reports, 40, 171

Grinin, V. P., The, P. S., de Winter, D., et al. 1994, A&A, 292, 165

Güdel, M., Skinner, S. L., Mel'Nikov, S. Y., et al. 2007, A&A, 468, 529

Guenther, E. & Ball, M. 1998, in Astronomical Society of the Pacific Conference Series, Vol. 154, Cool Stars, Stellar Systems, and the Sun, ed. R. A. Donahue & J. A. Bookbinder, 1701

Guenther, E. W., Stelzer, B., Neuhäuser, R., et al. 2000, A&A, 357, 206

Gullbring, E. 1994, A&A, 287, 131

Gullbring, E., Barwig, H., Chen, P. S., Gahm, G. F., & Bao, M. X. 1996, A&A, 307, 791

Gullbring, E., Barwig, H., & Schmitt, J. H. M. M. 1997, A&A, 324, 155

Gullbring, E., Calvet, N., Muzerolle, J., & Hartmann, L. 2000, ApJ, 544, 927

Gullbring, E., Hartmann, L., Briceno, C., & Calvet, N. 1998, ApJ, 492, 323

Günther, H. M., Matt, S. P., Schmitt, J. H. M. M., et al. 2010, A&A, 519, A97

Haisch, Jr., K. E., Jayawardhana, R., & Alves, J. 2005, ApJ, 627, L57

Hamann, F. & Persson, S. E. 1992, ApJS, 82, 247

Haro, G. & Herbig, G. H. 1955, Boletin de los Observatorios Tonantzintla y Tacubaya, 2, 33

Hartigan, P., Edwards, S., & Ghandour, L. 1995, ApJ, 452, 736

Hartigan, P. & Kenyon, S. J. 2003, ApJ, 583, 334

Hartigan, P., Kenyon, S. J., Hartmann, L., et al. 1991, ApJ, 382, 617

Hartigan, P., Morse, J. A., & Raymond, J. 1994, ApJ, 436, 125

Hartmann, L. 1998, Accretion Processes in Star Formation

Hartmann, L., Hewett, R., & Calvet, N. 1994, ApJ, 426, 669

Hartmann, L., Hewett, R., Stahler, S., & Mathieu, R. D. 1986, ApJ, 309, 275

Hartmann, L. & Kenyon, S. J. 1996, ARA&A, 34, 207

Hayashi, M. R., Shibata, K., & Matsumoto, R. 1996, ApJ, 468, L37

Henize, K. G. 1963, AJ, 68, 280

Herbig, G. H. 1977, ApJ, 217, 693

Herbig, G. H. 2007, AJ, 133, 2679

Herbig, G. H. & Bell, K. R. 1988, Third Catalog of Emission-Line Stars of the Orion Population : 3 : 1988 (Lick Observatory)

Herbst, W., Bailer-Jones, C. A. L., Mundt, R., Meisenheimer, K., & Wackermann, R. 2002, A&A, 396, 513

Herbst, W., Booth, J. F., Chugainov, P. F., et al. 1986, ApJ, 310, L71

Herbst, W., Eislöffel, J., Mundt, R., & Scholz, A. 2007, Protostars and Planets V, 297

Herbst, W., Herbst, D. K., Grossman, E. J., & Weinstein, D. 1994, AJ, 108, 1906

Herbst, W., Holtzman, J. A., & Klasky, R. S. 1983, AJ, 88, 1648

Herbst, W. & Layden, A. C. 1987, AJ, 94, 150

Herbst, W. & Shevchenko, V. S. 1999, AJ, 118, 1043

Herczeg, G. J. & Hillenbrand, L. A. 2008, ApJ, 681, 594

Hernández, J., Calvet, N., Briceño, C., Hartmann, L., & Berlind, P. 2004, AJ, 127, 1682

Hillenbrand, L. A. 2008, Physica Scripta Volume T, 130, 014024

Hillenbrand, L. A., Strom, S. E., Vrba, F. J., & Keene, J. 1992, ApJ, 397, 613

Hirth, G. A., Mundt, R., & Solf, J. 1997, A&AS, 126, 437

Hirth, G. A., Mundt, R., Solf, J., & Ray, T. P. 1994, ApJ, 427, L99

Hoffmeister, C. 1962, ZAp, 55, 290

Hoffmeister, C. 1965, Veroeffentlichungen der Sternwarte Sonneberg, 6, 97

Høg, E., Fabricius, C., Makarov, V. V., et al. 2000, A&A, 355, L27

Hubrig, S., Schöller, M., Ilyin, I., et al. 2011, A&A, 536, A45

Hubrig, S., Schöller, M., & Yudin, R. V. 2004, A&A, 428, L1

Hussain, G. A. J. 2002, Astronomische Nachrichten, 323, 349

Jardine, M., Collier Cameron, A., Donati, J.-F., Gregory, S. G., & Wood, K. 2006, MNRAS, 367, 917

Jaschek, M., Jaschek, C., & Andrillat, Y. 1988, A&AS, 72, 505

Jayawardhana, R., Coffey, J., Scholz, A., Brandeker, A., & van Kerkwijk, M. H. 2006, ApJ, 648, 1206

Jayawardhana, R., Mohanty, S., & Basri, G. 2003, ApJ, 592, 282

Joergens, V., Fernández, M., Carpenter, J. M., & Neuhäuser, R. 2003, ApJ, 594, 971

Johns, C. M. & Basri, G. 1995a, AJ, 109, 2800

Johns, C. M. & Basri, G. 1995b, ApJ, 449, 341

Johns, C. M., Basri, G. S., Giampapa, M. S., & Defonso, E. 1992, in Astronomical Society of the Pacific Conference Series, Vol. 26, Cool Stars, Stellar Systems, and the Sun, ed. M. S. Giampapa & J. A. Bookbinder, 441

Johnstone, R. M. & Penston, M. V. 1986, MNRAS, 219, 927

Jones, B. F. & Herbig, G. H. 1979, AJ, 84, 1872

Jørgensen, J. K., van Dishoeck, E. F., Visser, R., et al. 2009, A&A, 507, 861

Joy, A. H. 1945, ApJ, 102, 168

Kenyon, S. J., Gómez, M., & Whitney, B. A. 2008, Low Mass Star Formation in the Taurus-Auriga Clouds (Reipurth, B.), 405

Kenyon, S. J. & Hartmann, L. 1987, ApJ, 323, 714

Kenyon, S. J. & Hartmann, L. 1995, ApJS, 101, 117

Kenyon, S. J., Hartmann, L., Hewett, R., et al. 1994, AJ, 107, 2153

Kenyon, S. J. & Hartmann, L. W. 1991, ApJ, 383, 664

Kenyon, S. J., Hartmann, L. W., Strom, K. M., & Strom, S. E. 1990, AJ, 99, 869

Kitamura, Y., Momose, M., Yokogawa, S., et al. 2002, ApJ, 581, 357

Kolotilov, E. A. & Zajtseva, G. V. 1975, Peremennye Zvezdy, 20, 153

Königl, A. 1991, ApJ, 370, L39

Konigl, A. & Pudritz, R. E. 2000, Protostars and Planets IV, 759

Kraus, A. L. & Hillenbrand, L. A. 2009, ApJ, 704, 531

Kraus, S., Hofmann, K.-H., Benisty, M., et al. 2008, A&A, 489, 1157

Kuerster, M. & Schmitt, J. H. M. M. 1996, A&A, 311, 211

Kurosawa, R., Harries, T. J., & Symington, N. H. 2006, MNRAS, 370, 580

Kurosawa, R. & Romanova, M. M. 2013, MNRAS, 431, 2673

Kurosawa, R., Romanova, M. M., & Harries, T. J. 2008, MNRAS, 385, 1931

Kurucz, R. L. 1979, ApJS, 40, 1

Kurucz, R. L. 1993, VizieR Online Data Catalog, 6039, 0

Lada, C. J. & Wilking, B. A. 1984, ApJ, 287, 610

Lai, D. 1999, ApJ, 524, 1030

Lamm, M. H., Bailer-Jones, C. A. L., Mundt, R., Herbst, W., & Scholz, A. 2004, A&A, 417, 557

Laughlin, G. & Bodenheimer, P. 1994, ApJ, 436, 335

Liefke, C., Fuhrmeister, B., & Schmitt, J. H. M. M. 2010, A&A, 514, A94

Lomb, N. R. 1976, Ap&SS, 39, 447

Long, M., Romanova, M. M., Kulkarni, A. K., & Donati, J.-F. 2011, MNRAS, 413, 1061

López-Martín, L., Cabrit, S., & Dougados, C. 2003, A&A, 405, L1

Luhman, K. L. 2007, ApJS, 173, 104

Luhman, K. L. 2008, Chamaeleon, ed. B. Reipurth, 169

Luhman, K. L., Allen, L. E., Allen, P. R., et al. 2008, ApJ, 675, 1375

Lynden-Bell, D. & Pringle, J. E. 1974, MNRAS, 168, 603

Malbet, F., Benisty, M., de Wit, W.-J., et al. 2007, A&A, 464, 43

Malbet, F., Berger, J.-P., Colavita, M. M., et al. 1998, ApJ, 507, L149

Malbet, F., Lachaume, R., Berger, J.-P., et al. 2005, A&A, 437, 627

Manara, C. F., Testi, L., Rigliaco, E., et al. 2013, A&A, 551, A107

Mandel, G. N. & Herbst, W. 1991, ApJ, 383, L75

Mannings, V. & Sargent, A. I. 1997, ApJ, 490, 792

Manoj, P., Bhatt, H. C., Maheswar, G., & Muneer, S. 2006, ApJ, 653, 657

Martin, S. C. 1996, ApJ, 470, 537

Massi, M., Menten, K., & Neidhöfer, J. 2002, A&A, 382, 152

Mathieu, R. D. 2008, The λ Orionis Star Forming Region, ed. B. Reipurth, 757

Mathieu, R. D., Adams, F. C., Fuller, G. A., et al. 1995, AJ, 109, 2655

Mathieu, R. D., Adams, F. C., & Latham, D. W. 1991, AJ, 101, 2184

Matt, S. & Pudritz, R. E. 2005, MNRAS, 356, 167

Matt, S. & Pudritz, R. E. 2008, ApJ, 681, 391

Matt, S. P., MacGregor, K. B., Pinsonneault, M. H., & Greene, T. P. 2012, ApJ, 754, L26

Mendigutía, I., Brittain, S. D., Eiroa, C., et al. 2013, ArXiv e-prints

Mendigutía, I., Calvet, N., Montesinos, B., et al. 2011, A&A, 535, A99

Mendigutía, I., Eiroa, C., Montesinos, B., et al. 2011, A&A, 529, A34

Mendigutía, I., Mora, A., Montesinos, B., et al. 2012, A&A, 543, A59

Mentuch, E., Brandeker, A., van Kerkwijk, M. H., Jayawardhana, R., & Hauschildt, P. H. 2008, ApJ, 689, 1127

Mizuno, A., Hayakawa, T., Tachihara, K., et al. 1999, PASJ, 51, 859

Mohanty, S., Ercolano, B., & Turner, N. J. 2013, ApJ, 764, 65

Mohanty, S., Jayawardhana, R., & Basri, G. 2005, ApJ, 626, 498

Montes, D., Saar, S. H., Collier Cameron, A., & Unruh, Y. C. 1998, in Astronomical Society of the Pacific Conference Series, Vol. 154, Cool Stars, Stellar Systems, and the Sun, ed. R. A. Donahue & J. A. Bookbinder, 1508

Mora, A., Merín, B., Solano, E., Montesinos, B., & et al. 2001, A&A, 378, 116

Morales-Calderón, M., Stauffer, J. R., Rebull, L., et al. 2009, ApJ, 702, 1507

Mundt, R. & Giampapa, M. S. 1982, ApJ, 256, 156

Murdin, P. & Penston, M. V. 1977, MNRAS, 181, 657

Murphy, S. J., Lawson, W. A., Bessell, M. S., & Bayliss, D. D. R. 2011, MNRAS, 411, L51

Muzerolle, J., Calvet, N., & Hartmann, L. 2001, ApJ, 550, 944

Muzerolle, J., D'Alessio, P., Calvet, N., & Hartmann, L. 2004, ApJ, 617, 406

Muzerolle, J., Hartmann, L., & Calvet, N. 1998a, AJ, 116, 2965

Muzerolle, J., Hartmann, L., & Calvet, N. 1998b, AJ, 116, 455

Muzerolle, J., Hillenbrand, L., Calvet, N., Briceño, C., & Hartmann, L. 2003, ApJ, 592, 266

Natta, A., Prusti, T., Neri, R., et al. 2001, A&A, 371, 186

Natta, A., Testi, L., Muzerolle, J., et al. 2004, A&A, 424, 603

Natta, A., Testi, L., & Randich, S. 2006, A&A, 452, 245

Neuhaeuser, R., Sterzik, M. F., Schmitt, J. H. M. M., Wichmann, R., & Krautter, J. 1995, A&A, 297, 391

Nguyen, D. C., Jayawardhana, R., van Kerkwijk, M. H., et al. 2009a, ApJ, 695, 1648

Nguyen, D. C., Scholz, A., van Kerkwijk, M. H., Jayawardhana, R., & Brandeker, A. 2009b, ApJ, 694, L153

Ohashi, N. & Lin, S. 2005, in Astronomical Society of the Pacific Conference Series, Vol. 344, The Cool Universe: Observing Cosmic Dawn, ed. C. Lidman & D. Alloin, 168

Oliveira, J. M., Foing, B. H., van Loon, J. T., & Unruh, Y. C. 2000, A&A, 362, 615

O'Neal, D., Feigelson, E. D., Mathieu, R. D., & Myers, P. C. 1990, AJ, 100, 1610

Onishi, T., Mizuno, A., Kawamura, A., Ogawa, H., & Fukui, Y. 1998, ApJ, 502, 296

Osterbrock, D. E., Fulbright, J. P., Martel, A. R., et al. 1996, PASP, 108, 277

Persi, P., Marenzi, A. R., Kaas, A. A., et al. 1999, AJ, 117, 439

Petrov, P. P., Gahm, G. F., Gameiro, J. F., et al. 2001a, A&A, 369, 993

Petrov, P. P., Gullbring, E., Ilyin, I., et al. 1996, A&A, 314, 821

Petrov, P. P., Pelt, J., & Tuominen, I. 2001b, A&A, 375, 977

Phillips, R. B., Lonsdale, C. J., & Feigelson, E. D. 1991, ApJ, 382, 261

Phillips, R. B., Lonsdale, C. J., & Feigelson, E. D. 1993, ApJ, 403, L43

Pickles, A. J. 1998, PASP, 110, 863

Pogodin, M. A., Hubrig, S., Yudin, R. V., et al. 2012, Astronomische Nachrichten, 333, 594

Pott, J.-U., Perrin, M. D., Furlan, E., et al. 2010, ApJ, 710, 265

Praderie, F., Catala, C., Simon, T., & Boesgaard, A. M. 1986, ApJ, 303, 311

Pringle, J. E. 1981, ARA&A, 19, 137

Pudritz, R. E., Wilson, C. D., Carlstrom, J. E., et al. 1996, ApJ, 470, L123

Ray, T., Dougados, C., Bacciotti, F., Eislöffel, J., & Chrysostomou, A. 2007, Protostars and Planets V, 231

Reipurth, B. & Aspin, C. 2004, ApJ, 608, L65

Reipurth, B. & Bally, J. 2001, ARA&A, 39, 403

Reipurth, B., Pedrosa, A., & Lago, M. T. V. T. 1996, A&AS, 120, 229

Rigliaco, E., Natta, A., Randich, S., Testi, L., & Biazzo, K. 2011, A&A, 525, A47

Rigliaco, E., Natta, A., Testi, L., et al. 2012, A&A, 548, A56

Robinson, R. D., Cram, L. E., & Giampapa, M. S. 1990, ApJS, 74, 891

Rodriguez, J. E., Pepper, J., Stassun, K., et al. 2013, in Giants of Eclipse, 40103

Romanova, M. M., Ustyugova, G. V., Koldoba, A. V., & Lovelace, R. V. E. 2002, ApJ, 578, 420

Romanova, M. M., Ustyugova, G. V., Koldoba, A. V., & Lovelace, R. V. E. 2004, ApJ, 616, L151

Romanova, M. M., Ustyugova, G. V., Koldoba, A. V., & Lovelace, R. V. E. 2005, ApJ, 635, L165

Romanova, M. M., Ustyugova, G. V., Koldoba, A. V., Wick, J. V., & Lovelace, R. V. E. 2003, ApJ, 595, 1009

Rydgren, A. E., Strom, S. E., & Strom, K. M. 1976, ApJS, 30, 307

Rydgren, A. E. & Vrba, F. J. 1983, ApJ, 267, 191

Salyk, C., Herczeg, G. J., Brown, J. M., et al. 2013, ApJ, 769, 21

Scargle, J. D. 1982, ApJ, 263, 835

Schisano, E., Covino, E., Alcalá, J. M., et al. 2009, A&A, 501, 1013

Schmitt, J. H. M. M. & Favata, F. 1999, Nature, 401, 44

Schneeberger, T. J., Wilkerson, M. S., & Worden, S. P. 1979a, ApJS, 41, 369

Schneeberger, T. J., Worden, S. P., & Africano, J. L. 1979b, in Bulletin of the American Astronomical Society, Vol. 11 (Bulletin of the American Astronomical Society), 439

Scholz, A., Coffey, J., Brandeker, A., & Jayawardhana, R. 2007, ApJ, 662, 1254

Scholz, A. & Eislöffel, J. 2004, A&A, 419, 249

Scholz, A. & Jayawardhana, R. 2006, ApJ, 638, 1056

Scholz, A., Jayawardhana, R., Eislöffel, J., & Froebrich, D. 2005, Astronomische Nachrichten, 326, 895

Scholz, A., Xu, X., Jayawardhana, R., et al. 2009, MNRAS, 398, 873

Schulz, N. S. 2005, From Dust To Stars Studies of the Formation and Early Evolution of Stars

Shevchenko, V. S., Grankin, K. N., Ibragimov, M. A., Melnikov, S. Y., & Yakubov, S. D. 1993, APSS, 202, 137

Shu, F. H., Najita, J. R., Shang, H., & Li, Z.-Y. 2000, Protostars and Planets IV, 789

Sicilia-Aguilar, A., Hartmann, L. W., Szentgyorgyi, A. H., et al. 2005, AJ, 129, 363

Simon, M., Dutrey, A., & Guilloteau, S. 2000, ApJ, 545, 1034

Skinner, S. L. & Brown, A. 1994, AJ, 107, 1461

Skrutskie, M. F., Meyer, M. R., Whalen, D., & Hamilton, C. 1996, AJ, 112, 2168

Spezzi, L., Alcalá, J. M., Frasca, A., Covino, E., & Gandolfi, D. 2007, A&A, 470, 281

Stelzer, B., Scholz, A., & Jayawardhana, R. 2007, ApJ, 671, 842

Takami, M., Bailey, J., & Chrysostomou, A. 2003, A&A, 397, 675

Telleschi, A., Güdel, M., Briggs, K. R., et al. 2007, A&A, 468, 541

Terquem, C. & Papaloizou, J. C. B. 2000, A&A, 360, 1031

Ungerechts, H. & Thaddeus, P. 1987, ApJS, 63, 645

Ustyugova, G. V., Koldoba, A. V., Romanova, M. M., & Lovelace, R. V. E. 2006, ApJ, 646, 304

Valenti, J. A. 1994, PhD thesis, UNIVERSITY OF CALIFORNIA, BERKELEY.

Valenti, J. A., Basri, G., & Johns, C. M. 1993, AJ, 106, 2024

Vink, J. S., Drew, J. E., Harries, T. J., & Oudmaijer, R. D. 2002, MNRAS, 337, 356

Vink, J. S., Drew, J. E., Harries, T. J., Oudmaijer, R. D., & Unruh, Y. 2005, MNRAS, 359, 1049

Vink, J. S., Drew, J. E., Harries, T. J., Oudmaijer, R. D., & Unruh, Y. C. 2003, A&A, 406, 703

Vogel, S. N. & Kuhi, L. V. 1981, ApJ, 245, 960

Vorobyov, E. I. & Basu, S. 2010, ApJ, 719, 1896

Vrba, F. J., Rydgren, A. E., Chugainov, P. F., Shakovskaia, N. I., & Zak, D. S. 1986, ApJ, 306, 199

Vrba, F. J., Rydgren, A. E., Zak, D. S., Chugainov, P. F., & Shakhovskaya, N. I. 1984, in Bulletin of the American Astronomical Society, Vol. 16, Bulletin of the American Astronomical Society, 998

Wade, G. A., Drouin, D., Bagnulo, S., et al. 2005, A&A, 442, L31

Walker, M. F. 1972, ApJ, 175, 89

Ward-Thompson, D., André, P., Crutcher, R., et al. 2007, Protostars and Planets V, 33

Welty, A. D. 1995, AJ, 110, 776

Whelan, E. T., Ray, T. P., & Bacciotti, F. 2009, ApJ, 691, L106

White, R. J. & Basri, G. 2003, ApJ, 582, 1109

White, R. J. & Ghez, A. M. 2001, ApJ, 556, 265

White, R. J. & Hillenbrand, L. A. 2004, ApJ, 616, 998

Whittet, D. C. B., Prusti, T., Franco, G. A. P., et al. 1997, A&A, 327, 1194

Williams, J. P. & Andrews, S. M. 2006, ApJ, 653, 1480

Worden, S. P., Schneeberger, T. J., & Giampapa, M. S. 1981a, ApJS, 46, 159

Worden, S. P., Schneeberger, T. J., Kuhn, J. R., & Africano, J. L. 1981b, ApJ, 244, 520

Young, K. E., Harvey, P. M., Brooke, T. Y., et al. 2005, ApJ, 628, 283

Zacharias, N., Urban, S. E., Zacharias, M. I., et al. 2004, AJ, 127, 3043